

**MULTIWALLED CARBON NANOTUBES AND THEIR
COMPOSITES AS ALCOHOL SENSORS AND FIELD
ELECTRON EMISSION CATHODES**

FARIDAH BINTI ABDUL RAZAK

**FACULTY OF SCIENCE
UNIVERSITY OF MALAYA
KUALA LUMPUR**

2016

**MULTIWALLED CARBON NANOTUBES AND THEIR
COMPOSITES AS ALCOHOL SENSORS AND FIELD
ELECTRON EMISSION CATHODES**

FARIDAH BINTI ABDUL RAZAK

**THESIS SUBMITTED IN FULFILMENT OF THE
REQUIREMENTS FOR THE DEGREE OF DOCTOR OF
PHILOSOPHY**

**FACULTY OF SCIENCE
UNIVERSITY OF MALAYA
KUALA LUMPUR**

2016

UNIVERSITY OF MALAYA
ORIGINAL LITERARY WORK DECLARATION

Name of Candidate: **Faridah Binti Abdul Razak**

Registration/Matric No: **SHC100020**

Name of Degree: **Doctor of Philosophy (Except Mathematics & Science Philosophy)**

Title of Project Paper/Research Report/Dissertation/Thesis ("this Work"): **Multiwalled Carbon Nanotubes and their Composites as Alcohol Sensors and Field Electron Emission Cathodes**

Field of Study: **Advanced Material/Nanotechnology**

I do solemnly and sincerely declare that:

- (1) I am the sole author/writer of this Work;
- (2) This Work is original;
- (3) Any use of any work in which copyright exists was done by way of fair dealing and for permitted purposes and any excerpt or extract from, or reference to or reproduction of any copyright work has been disclosed expressly and sufficiently and the title of the Work and its authorship have been acknowledged in this Work;
- (4) I do not have any actual knowledge nor do I ought reasonably to know that the making of this work constitutes an infringement of any copyright work;
- (5) I hereby assign all and every rights in the copyright to this Work to the University of Malaya ("UM"), who henceforth shall be owner of the copyright in this Work and that any reproduction or use in any form or by any means whatsoever is prohibited without the written consent of UM having been first had and obtained;
- (6) I am fully aware that if in the course of making this Work I have infringed any copyright whether intentionally or otherwise, I may be subject to legal action or any other action as may be determined by UM.

Candidate's Signature

Date:

Subscribed and solemnly declared before,

Witness's Signature

Date:

Name: **ASSOC. PROF. DR ROSLAN MD NOR**

Designation:

ABSTRACT

Composites of multiwalled carbon nanotubes (MWCNTs) with polyethylene oxide and hybrid films of MWCNT with oxide materials (TiO_2 and ZnO) were prepared for alcohol vapor sensing and field electron emission studies. The justification for fabricating such materials was to overcome the problem associated with using pure MWCNTs where adhesions to substrates surfaces were generally poor. Poly(ethylene oxide)/multiwalled carbon nanotube (PEO/MWCNT) composites were fabricated using the solution cast technique and characterized using field emission scanning electron microscopy (FESEM), fourier transform infrared spectroscopy (FTIR), thermogravimetric analysis (TGA) and conductivity analyses. Results of the analysis showed good distribution of MWCNT in the composite which were used as alcohol vapor sensors. It was discovered that a poly(ethylene oxide)/multiwalled carbon nanotube (PEO/MWCNT) composite provided the best sensitivity for both ethanol and methanol vapor with detection limits down to 10 ppm. The effect of MWCNT loading the composites on the sensitivity to ethanol and acetone sensing showed an increase in the sensitivity with decreasing loading and increasing in dynamic range with increase loading. This shows that the amount of MWCNT loading will determine the application trade off, either for high sensitivity or high dynamic range. Hybrid material films of TiO_2 and ZnO with MWCNT were fabricated using the electrophoresis process on silver substrates. FESEM and Raman spectroscopy were used to analyze the deposited composite materials. Field electron emission properties were studied as a function film thickness and compared with pure MWCNT results. For all films, the maximum current densities were observed with the thinnest films deposited for 1 minute. This was due to the shielding effect in the thicker films. Also, the inclusion of the oxide materials into the films resulted in significant increase in the maximum current densities compare to

the corresponding pure MWCNT films. This is evident that the oxide particles acted as spacers which spread the MWCNT and reduced the shield effect.

University of Malaya

ABSTRAK

Komposit tiub nano dengan polimer polyethylene oksida dan filem bahan hibrid daripada tiub nano dengan bahan-bahan oksida (TiO_2 dan ZnO) diuji melalui pengesan wap alkohol dan ruang pancaran elektron. Justifikasi bagi fabrikasi bahan-bahan tersebut adalah untuk mengatasi masalah yang berkaitan dengan penggunaan tiub nano yang asli di mana pelekatan kepada permukaan bahan-bahan tersebut adalah sedikit. Komposit tiub nano/PEO difabrikasikan menggunakan cara larutan tuangan dan dianalisis menggunakan FESEM, FTIR, TGA dan analisa konduktiviti. Hasil penemuan menunjukkan bahawa komposit tiub nano/PEO mempunyai kepekaan yang terbaik untuk kedua-dua wap etanol dan methanol melalui had pengesan jatuh ke paras 10 ppm. Kesan komposit tiub nano memuatkan komposit kepada sensitiviti pengesan wap etanol dan aseton yang menunjukkan kepada peningkatan dalam sensitiviti dengan mengurangkan muatan dan semakin meningkat dalam julat dinamik maka semakin meningkat muatan. Ini menunjukkan bahawa jumlah komposit tiub nano yang ada akan menentukan aplikasi di dalam penukar-tambah, sama ada untuk sensitivity atau julat yang dinamik tinggi. Filem bahan hibrid komposit TiO_2 dan ZnO beserta tiub nano difabrikasikan dengan menggunakan proses elektrolisis di atas bahan perak. FESEM dan spektroskopi raman digunakan bagi menganalisis penghasilan bahan-bahan komposit. Ciri ruang pancaran elektron dikaji dengan lebih mendalam melalui ketebalan fungsi filem dan dibandingkan dengan keputusan tiub nano yang tulen. Bagi semua filem, ketumpatan arus maksimum diperhatikan melalui filem nipis yang telah disimpan selama 1 minit. Ini disebabkan oleh kesan perisai dalam filem tebal. Juga, kemasukan bahan-bahan oksida ke dalam filem menyebabkan peningkatan ketara dalam ketumpatan arus maksimum berbanding dengan filem komposit tiub nano tulen yang sepadan. Ini terbukti bahawa zarah oksida bertindak sebagai pengatur jarak yang akan meliputi ke semua bahagian komposit tiub nano dan akan mengurangkan kesan perisai.

ACKNOWLEDGEMENTS

Foremost, I would like to express my sincere gratitude to my supervisor Assoc. Prof. Dr Roslan Md. Nor for the continuous support of my Ph.D study and research, for his patience, motivation, enthusiasm and immense knowledge. His guidance helped me in all the time of research and writing of this thesis. I could not have imagined having a better advisor and mentor for my Ph.D study.

I would like to thank the members of my family who assisted me with this project, my father Hj Abdul Razak Tampi and my mother Hjh Fatimah Hj Abdullah who assisted in the construction of the display board.

I am also grateful to University of Malaya for providing me a seat to pursue my higher studies and Ministry of Higher Education (MOHE) for the financial support.

A special note of thanks to my friends and laboratory mates for their expert guidance.

TABLE OF CONTENTS

Abstract.....	iii
Abstrak.....	v
Acknowledgements.....	vi
Table of Contents.....	vii
List of Figures.....	x
List of Tables.....	xvii
List of Abbreviations.....	xviii
CHAPTER 1: INTRODUCTION	1
1.1 Introduction	1
1.2 Objective of the Thesis.....	3
1.3 Outline of the Research.....	3
CHAPTER 2: LITERATURE REVIEW.....	5
2.1 Carbon and Its Allotropes.....	5
2.2 Individual Carbon Nanotubes.....	8
2.3 The vector and Chiral Angle of SWCNT	10
2.4 Single-Wall Carbon Nanotube Conductivity.....	13
2.5 Carbon Nanotubes, Unique Properties and Potential Applications	16
2.5.1 CNTs and Electronic industry	18
2.5.2 CNTs and Electrical Conductivity	20
2.5.3 CNTs Biomedical Applications.....	21
2.5.4 CNTs Applications due to Mechanical Properties.....	24
2.5.5 CNTs applications in the Chemical Field.....	25
2.5.6 CNTs and Heat Conductivity.....	26

CHAPTER 3: MWCNT AND MWCNT COMPOSITES AS FIELD ELECTRON	
EMITTERS CATHODES.....	29
3.1 Introduction	29
3.2 Carbon Nanotubes as Field Electron Emitters	30
3.3 Surface Potential Barrier Lowering (Schottky Lowering)	34
3.4 Fowler-Nordheim Field Electron Emission Model.....	35
3.5 Mechanism of Electrophoresis	39
3.6 Experimental Details	43
3.6.1 Fabrication of MWCNT/PEO Composites.....	43
3.6.2 FEE Measurement Techniques.....	44
3.7 Electrophoresis Deposition and characterized of MWCNT/ZnO and MWCNT/TiO ₂	46
3.8 Experimental results.....	48
3.8.1 Thin Films Characterization.....	50
3.8.2 Thin Films Field Electron Emission.....	56
3.8.3 Thick Films Characterization.....	62
3.8.4 Thick Films Field Electron Emission.....	73
3.9 MWCNT/ZnO and MWCNT/TiO ₂ Hybrid Films as Electrophoretic Deposition.....	79
3.9.1 Introduction.....	79
3.9.2 Field Emission Scanning Electron Microscope (FESEM).....	80
3.9.3 Raman Spectroscopy	84
3.10 Field Electron Emission Properties of MWCNT, MWCNT/ZnO and MWCNT/TiO ₂ Films.....	85
3.11 Conclusions.....	90

CHAPTER 4: MWCNT/PEO COMPOSITES AS ACETONE AND

ETHANOL SENSORS.....92

4.1	Introduction to Volatile Organic Compound Sensors.....	92
4.2	Types of Sensors.....	93
4.3	Carbon Nanotubes Based Sensors.....	95
4.4	Detection of Acetone or Propanone	97
4.5	Experimental Details.....	99
4.5.1	Fabrication of MWCNT/PEO Composites Sensors.....	100
4.5.2	Sensing Measurement Techniques	100
4.5.3	Fourier Transform Infrared Spectroscopy (FTIR) Basics.....	102
4.6	Thick Films Characterization	105
4.6.1	Raman Characterization.....	105
4.6.2	Fourier Transform Infra-Red (FTIR) Characterization.....	106
4.7	Results and Discussion.....	114
4.7.1	Acetone Sensing Results and Discussion.....	114
4.7.2	Water Vapor Sensing Results and Discussion.....	122
4.7.3	Sensing Mechanism	124
4.8	Conclusions.....	126

CHAPTER 5: CONCLUSIONS.....128

References.....130

List of Publications and Papers Presented.....146

Appendix

147

LIST OF FIGURES

Figure 2.1: Comparison of diameters of various forms of graphitic carbon (Ebbesen, 1997).....	6
Figure 2.2: The structures of eight allotropes of carbon:(a) Diamond (b) Graphite (c)Lonsdaleite (d) C ₆₀ (Buckminsterfullerene) (e) C540 Fullerene (f) C ₇₀ Fullerene (g) Amorphous carbon (h) Single-walled carbon nanotube	7
Figure 2.3: The average bond length and carbon separation values of the hexagonal lattice.	9
Figure 2.4: A graphene sheet showing the chiral vector with the unit vectors.....	10
Figure 2.5: (a) Graphene sheet with carbon atoms labeled using the (n, m) notation....	11
Figure 2.6: (a) Three-dimensional view of the graphene π / π^* bands and its 2D projection. (b) Example of the allowed 1D subbands for a metallic tube. Schematic depicts (9,0). (c) Example of the quantized 1D subbands for a semiconducting tube. Schematic shows (10,0). The white hexagon defines the first Brilluion zone of graphene, and the green dots in the corners are the graphene K points (Odom, Huang et al. 2000).....	14
Figure 2.7: A chart to show the diversity of applications possible using the various attributes of carbon nanotubes.....	17
Figure 2.8: CNT transistor schema (Do, Truong et al. 2013).	18
Figure 2.9: CNT thin-film transistors in integrated circuits on a flexible and transparent substrate. (Zhang, Hu et al. 2007)	19

Figure 2.10: Carbon nanotube based device which can convert laser to heat and To electricity, the laser can power devices through living tissue (Adio 2009)	21
Figure 2.11: “carbon nano-bottles” loaded with antitumor agents and C60 using a controlled nanoextraction strategy. C60 filled at the extremities of CNTs could act as “cap” to seal the CNTs (Ren and Pastorin 2008).....	23
Figure 2.12: Artificial muscles from carbon nanotube yarns (Schulz 2012)	25
Figure 2.13: Carbon nanotube fountain pen.....	27
Figure 2.14: Carbon nanotube rackets (Kuroyanagi, Ueno et al. 1990).....	28
Figure 3.1: Schematic of Schottky Lowering: (a) without image potential and external field, (b) without image potential but with external field, (c) with image potential but without external field, and (d) with both image potential and external field.	35
Figure 3.2: Illustration of electrophoresis.....	39
Figure 3.3: Illustration of electrophoresis retardation.....	42
Figure 3.4: A schematic diagram of FEE chamber used in the experiments.	45
Figure 3.5: Composites of (a) CNT/ZnO and (b) CNT/TiO ₂	46
Figure 3.6: The samples of CNT/ZnO and CNT/TiO ₂ for 1 minute, 2 minutes and 3 minutes respectively.....	47
Figure 3.7: SEM images of films sintered in argon	48
Figure 3.8: Field electron emission measurements	48
Figure 3.9: The stability of IV curve.....	49
Figure 3.10: The effect of burn out process (Initial measurements from fresh sample).	49

Figure 3.11: The effect of burn out process after continuous run at 1 kV and 30 minutes.....	50
Figure 3.12: Raman spectroscopy of MWCNT/PEO thin films. (a) Before FEE measurements (b) After FEE measurements.	53
Figure 3.13: SEM micrographs of the six thin films composites (a) 5%, (b) 15%, (c) 25%, (d) 33%, (e) 40% and (f)50% MWCNT/PEO thin films.	55
Figure 3.14: Current density versus the electric field applied for the thin films with different MWCNTs weight concentrations.	56
Figure 3.15: Fowler- Nordheim plot for the thin films with different MWCNTs weight concentrations.....	57
Figure 3.16: Enhancement factors of the thin films with different MWCNTs weight concentrations.....	59
Figure 3.17: Current stability in about 34 min period time for the thin films with different MWCNTs weight concentrations.....	61
Figure 3.18: Current density versus applied electric field for before and after stability test of 15% MWCNT/PEO thin film.....	62
Figure 3.19: Raman spectroscopy of MWCNT/PEO thick films. (a) Before FEE measurements. (b)After FEE measurements.....	65
Figure 3.20: SEM micrographs of the six thick films composites (a) 5%, (b) 15%, (c) 25%, (d) 33%, (e) 40% and (f) 50% MWCNT/PEO thin films.	67
Figure 3.21: TG curves of the pure PEO and 5wt%, 15wt%, 25wt%, 33wt%, 40wt% and 50 wt% of MWCNT/PEO composites.....	68
Figure 3.22: TG and its DTG curves of pure PEO.....	69
Figure 3.23: The TG and DTG curves of each MWCNT/PEO composite.	72

Figure 3.24: Current density versus the electric field applied for Thick films with different MWCNTs weight concentrations.....	73
Figure 3.25: Fowler- Nordheim plot of Thick films with different MWCNTs weight concentrations.....	75
Figure 3.26: Enhancement factors for films with different MWCNTs weight concentrations.....	76
Figure 3.27: Current stability in about 34 min period time for thick films with different MWCNTs weight concentrations.....	77
Figure 3.28: Current density versus applied electric field for before and after stability test for 33wt% thick film.....	78
Figure 3.29: FESEM images of (a) 1 minute of MWCNT, (b) 2 minutes of MWCNT, (c) 3 minutes of MWCNT, (d) 1 minute of MWCNT/ZnO, (e) 2 minutes of MWCNT/ZnO, (f) 3 minutes of MWCNT/ZnO (g) 1 minute of MWCNT/TiO ₂ , (h) 2 minutes of MWCNT/TiO ₂ and (i) 3 minutes of MWCNT/TiO ₂ , were deposited on silver.....	81
Figure 3.30: Figure 3.30 (a), (b) and (c) shows the EDX spectra of MWCNT/ZnO. The spectra exhibited the existence of carbon, oxygen, titanium and argentum. Argentum is the major composition and has the highest concentration comparing it to other elements. Zinc and oxygen are resulted from the using of Zinc Oxide. Figure 3.30 (d), (e) and (f) shows the EDX spectra of MWCNT/TiO ₂ . The highest concentration and the major composition is still Argentum. Titanium and oxygen are produced from the using of Titanium Oxide.....	82

Figure 3.31: EDS spectra of MWCNT/ZnO hybrid film of (a) 1 minute, (b) 2 minutes (c) 3 minutes and EDS spectra of MWCNT/ZnO hybrid film of (d) 1 minute, (e) 2 minutes (f) 3 minutes respectively.....	83
Figure 3.32: Typical raman spectra of (a) MWCNT (b) MWCNT/ZnO (c) MWCNT/TiO ₂	85
Figure 3.33: Typical field emission current density vs. the applied electric field for (a) MWCNT film (b) MWCNT/ZnO and (c) MWCNT/TiO ₂	87
Figure 3.34: The corresponding Fowler-Nordheim (F-N) plots ($\ln(J/E^2)-(1/E)$) with the field emission characteristics of the (a) MWCNT film (b) MWCNT/ZnO hybrid film and (c) MWCNT/TiO ₂ hybrid film.....	89
Figure 4.1: Carbon nanotube based sensor in acetone and water vapor environment. ..	96
Figure 4.2: Acetone chemical structure (2013).....	98
Figure 4.3: A scheme for vapor delivery and gas sensitivity measuring systems.....	101
Figure 4.4: Schematic illustration of FTIR system	103
Figure 4.5: A typical FT-IR spectrum(2012).	105
Figure 4.6: Raman spectroscopy of MWCNT/PEO films (a) Before sensing measurements. (b) After sensing measurements.....	106
Figure 4.7: FTIR spectra before sensing measurements (a) Obtained for MWCNT, SDS, PEO, and (5%, 15%, 25%, 33%, 40% and 50%) MWCNT/PEO composites in the wavenumber range 650 to 4000 cm ⁻¹ . (b) A clearer picture of PEO, and (5%, 15%, 25%, 33%, 40% and 50%) MWCNT/PEO composites in the wavenumber range 650 to 1600 cm ⁻¹	108

Figure 4.8: FTIR spectroscopy of (a) 5%,15%, 25%, 33%, 40% and 50% MWCNT/PEO after sensing. (b) 5%, 15% and 25% MWCNT/PEO composites before and after sensing (c) 33%, 40% and 50% MWCNT/PEO composites before and after sensing.	113
Figure 4.9: Five rounds of electrical response of (a) 5wt%, (b) 15wt% (c) 25wt% (d) 33wt%, (e) 40wt% and (f) 50wt MWCNT/PEO films. Each composite was exposed to three acetone vapor concentrations (The numbers given within the graphs represent the acetone vapor ppm concentration).....	115
Figure 4.10: Five successive rounds of electrical response of: 5wt%, 15wt% and 25wt%, 33wt%, 40wt% and 50wt MWCNT/PEO films in (a) low concentration (113 ppm) acetone and (b) high concentration (14900 ppm) acetone. Some adjustments were made in the Y axis in order to obtain a clear view are mentioned at the right side of the curves.	116
Figure 4.11: Sensing response rates of (5%, 15%, 25%, 33%, 40% and 50%) MWCNTs/PEO thick films versus acetone four ranges of concentration (ppm).....	118
Figure 4.12: Response logarithm of (5%, 15%, 25%, 33%, 40% and 50%) MWCNTs/PEO composites versus acetone four ranges of concentrations (ppm).....	119
Figure 4.13: Sensitivity versus carbon nanotubes concentration in four ranges of acetone vapour ppm concentrations.....	120

Figure 4.14: Five successive rounds of electrical response of: 5wt%, 15wt% and 25wt%. 33wt%, 40wt% and 50wt MWCNT/PEO film sin 160 ppm water vapour. Some adjustments were made in the Y axis in order to obtain a clear view are mentioned at the right side of the curves.	122
Figure 4.15: Response of MWCNT/PEO sensors to H ₂ O vapour (a) Response versus water concentration. (b) Response logarithm versus water concentration.	123
Figure 4.16: Sensitivity versus carbon nanotubes concentration in the range (160-1560 ppm) water vapour.....	124

University of Malaysia

LIST OF TABLES

Table 2.1: Typical properties of CNTs.	16
Table 2.2: Physical properties of different carbon materials (P: in-plane; c: axis).....	16
Table 3.1: Electric field threshold for 10 mA/cm ² current density emission for different materials (Cheng and Zhou 2003).	31
Table 3.2: Characteristics of field emission of PEO/MWCNT composites thin films. ..	58
Table 3.3: Summary of the prepared composites along with pure PEO thermal degradation.	70
Table 3.4: Field emission characteristics of PEO/MWCNT thick films composites.....	74
Table 3.5: β value for MWCNT, MWCNT/ZnO and MWCNT/TiO ₂	89
Table 4.1: The assignment of the vibrational bands of SDS, H ₂ O, PEO and Acetone.	109
Table 4.2: Acetone concentration ranges related to figure 4.11 corresponding graphs.	117
Table 4.3: The resistance and its rise and fall time in MWCNT/PEO composites (565 ppm).	121

LIST OF ABBREVIATIONS

CH ₂	Ethylene
CH ₄	Methane
C ₃ H ₆ O	Acetone
CNT	Carbon nanotube
CO	Carbon monoxide
CVD	Chemical vapor deposition
DOC	Sodium deoxycholate
DTG	Dependence thermogravimetric analysis
DWCNT	Double-walled carbon nanotube
EDX	Energy dispersed x-ray spectroscopy
FEE	Field emission electron
FESEM	Field emission scanning electron microscopy
FET	Field effect transistor
FN	Fowler-Nordheim
FTIR	Fourier transform infrared spectroscopy
FWHM	Full width half maximum
ITO	Indium tin oxide
InGaN	Indium gallium nitride
LaB ₆	Lanthanum hexaboride
MWCNT	Multiwalled carbon nanotube
NH ₃	Ammonia
NO ₂	Nitrogen dioxide
PCB	Printed circuit board
PDDA	Poly(diallyldimethyl-ammonium chloride)

PEO	Poly(ethylene oxide)
PET	Poly(ethyleneterephthalate)
PMMA	Poly(methyl methacrylate)
PS	Polystrene
PU	Polyurethane
PVA	Poly(vinyl alcohol)
RBM	Radial breathing mode
SB	Schottky barrier
SDS	Sodium dodecyl sulfate
SEM	Scanning electron microscopy
SO ₂	Sulfur dioxide
SnO ₂	Tin dioxide
SWCNT	Singlewalled carbon nanotube
TG	Thermogravimetric
TGA	Thermogravimetric analysis
TiO ₂	Titanium oxide
WO ₃	Tungsten trioxide
ZnO	Zinc oxide

CHAPTER 1: INTRODUCTION

1.1 Introduction

Since the discovery of carbon nanotubes (CNTs) (Iijima 1991), fundamental research on CNTs and their applications have made rapid progresses (Moniruzzaman 2006). CNTs are considered potential candidates in nanoelectronics, field emission devices, gas storage and sensors, for fabricating CNT reinforced composites in many matrices, such as polymers, metals and ceramic materials. (Jin, Bower et al. 1998).

CNTs are long cylinders of covalently bonded carbon atoms with a diameter ranging from a few angstroms to several tens of nanometers across. These tubes have an extremely desirable combination of mechanical, thermal and electrical properties. They exhibit extraordinary strength and unique electrical properties, and are efficient thermal conductors. Specifically, they have an elastic stiffness comparable to that of diamond (1000 GPa), but they are ten times as strong (yield strength 100 GPa).

There are two basic types of CNTs, namely single-walled CNTs (SWCNTs) and multi-walled CNTs (MWCNTs). SWCNTs consist of a single layer of carbon atoms in the form of a graphite sheet (graphene) that wraps around to form a seamless tube. These tubes may be open at both ends or capped at one or both ends. SWCNTs can be metallic or semiconducting. MWCNTs are of two types, single walled carbon nanotubes arranged concentrically or a graphene sheet that is wrapped around onto itself, like a scroll.

The nature of the bonding of a nanotube is described by applied quantum chemistry, specifically, orbital hybridization. The chemical bonding of nanotubes are composed entirely of sp^2 bonds, similar to those of graphite. This bonding structure, which is stronger than the sp^3 bonds found in diamond, provides the molecules with

their unique strength. Nanotubes naturally align themselves into “ropes” held together by van der Waals forces.

CNTs are promising additives to polymeric materials. Due to their excellent structural, mechanical and electronic properties, CNTs are considered as potentially useful reinforcements for structural and multi-functional composites (Thostenson, Chou et al. 2001). One of the first studies of polymer/CNT composites was initially reported by (Ajayan 1994). In their research, MWCNTs were dispersed randomly in a liquid epoxy resin by mechanical mixing. Since then, many other reports have addressed the fact that incorporating a small percentage of CNTs by weight into polymer matrices could improve mechanical (Andrews 2003) and electrical (Kymakis, Amaratunga et al. 2002) properties of polymer composites.

The gas-sensing property in particular is very attractive as their small size, high surface area, good environmental stability, and excellent mechanical and electronic properties (Meyyappan 2005). The large surface area provided by the hollow cores and outside walls of nanotubes gives them a very large gas absorptive capacity. Therefore, CNTs show faster response and higher sensitivity at lower operating temperature compared to other sensor materials such as zinc oxide. (Philip, Chandrasekhar et al. 2003). The principle of CNT gas sensors for the detection and quantization of gases is based on changes in electrical properties induced by charge transfer with gas molecules or changes in adsorption (Cantalini, Armentano et al. 2003). Much work has been done to estimate the hydrogen storage capacity of CNTs either by physisorption or chemisorption process (Shen, Jiang et al. 2004). Cheng et al. have been reported that hydrogen is a completely deformable fluid that fills the space between CNTs and can be absorbed on inner walls as well as in the interstitial volume of CNTs (Cheng 2001). The formation of polymer/CNTs composites has been explored for possible improvement in electrical as well as the gas sensing properties of polymers. The focus of the proposed work is to fabricate polymer/CNTs composites for the application of gas sensor.

1.2 Objective of the Thesis

Since the discovery of CNTs, fundamental research on CNTs and their applications have made rapid progress. CNTs are considered potential candidates in nanoelectronics, field emission devices, gas storage and sensors, for fabricating CNTs reinforced composites in many matrices, such as polymers, metals and ceramic materials. The objective for application of polymer composites is to adhere with MWCNT. And these objectives will be achieved by:

1. Fabrication, characterization of PEO/MWCNT films by the solution casting method and its applications as organic vapor sensors and field electron emission cathodes.
2. Fabrication and characterization of pure MWCNT, MWCNT/ZnO and MWCNT/TiO₂ films using electrophoresis deposition and its application as field electron emission cathodes.

The instruments used for characterization of CNT composites are Fourier transform infrared (FTIR), field emission scanning electron microscopy (FESEM), X-ray energy dispersive x-ray spectroscopy (EDS), ethanol/methanol sensing behaviour and field emission electron (FEE).

1.3 Outline of the Research

The opening of the thesis highlights an introduction of carbon nanotube reinforced polymer composites and the objective of the research. Chapter 2 will present the literature review on CNTs and CNT/polymer composites. Various methods for preparation of carbon nanotube/polymer composites will be described, with particular emphasis on the preparation of aligned nanocomposite materials. Characterization of CNT composites using transmission electron microscopy (TEM), field emission

scanning electron microscopy (FESEM), X-ray energy dispersive x-ray spectroscopy (EDS) and fourier transform infrared (FTIR) are presented in this chapter.

The MWCNT and MWCNT composites as field electron emitters cathodes will be investigated in chapter 3. The field electron emission of MWCNT/ZnO and MWCNT/TiO₂ hybrid films as electrophoretic deposition will be investigated using the electrophoresis technique.

Chapter 4 describes the experimental setup for the MWCNT/polymer composites (PVA/PEO/PS) as alcohol sensor. The fabrication of composites of carbon nanotubes using the dispersion method will be described in this chapter and also its use the alcohol sensor technique. Lastly, the results and discussions of the ethanol sensing properties of the MWCNT/PEO, MWCNT/PVA and MWCNT/PS composites will be presented.

Finally, chapter 5 outlines the conclusion of the experimental results.

CHAPTER 2: LITERATURE REVIEW

2.1 Carbon and Its Allotropes

Carbon is one of the most fascinating elements in particular because of the variety of materials it forms. In its many forms it can appear as a hard and transparent crystal and also as black amorphous soot, all due to the way the carbon atoms are bonded to each other. Carbon can have several very stable crystalline forms, with widely different properties. Diamond is composed of sp^3 bonded carbon atoms arranged in tetrahedrons, and is an insulator, transparent and one of the hardest materials known. In contrast, graphite appears as layered sheets of sp^2 bonded carbon atoms arranged in a hexagonal network, and is semi-metallic, shiny grey and with one of the highest melting points. Another form of diversity is the way graphitic carbon formed allotropes of diverse dimensions. Figure 2.1 shows some of these carbon materials on the basis of their size. The structures of eight allotropes of carbon are illustrated in figure 2.2.

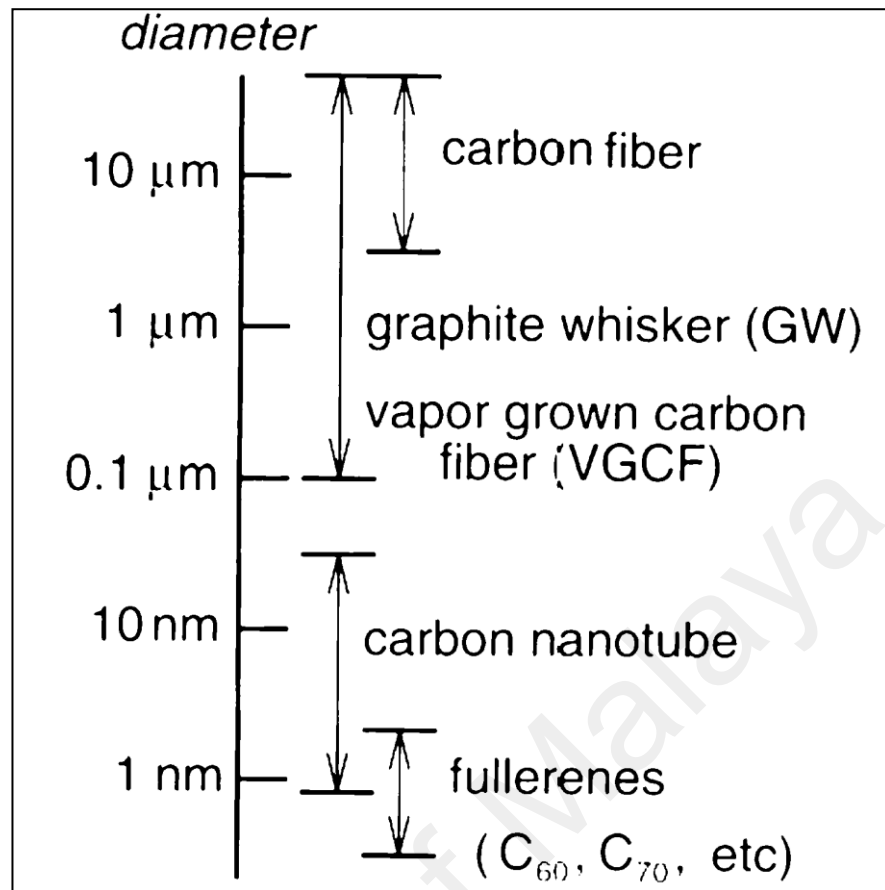


Figure 2.1: Comparison of diameters of various forms of graphitic carbon (Ebbesen, 1997).

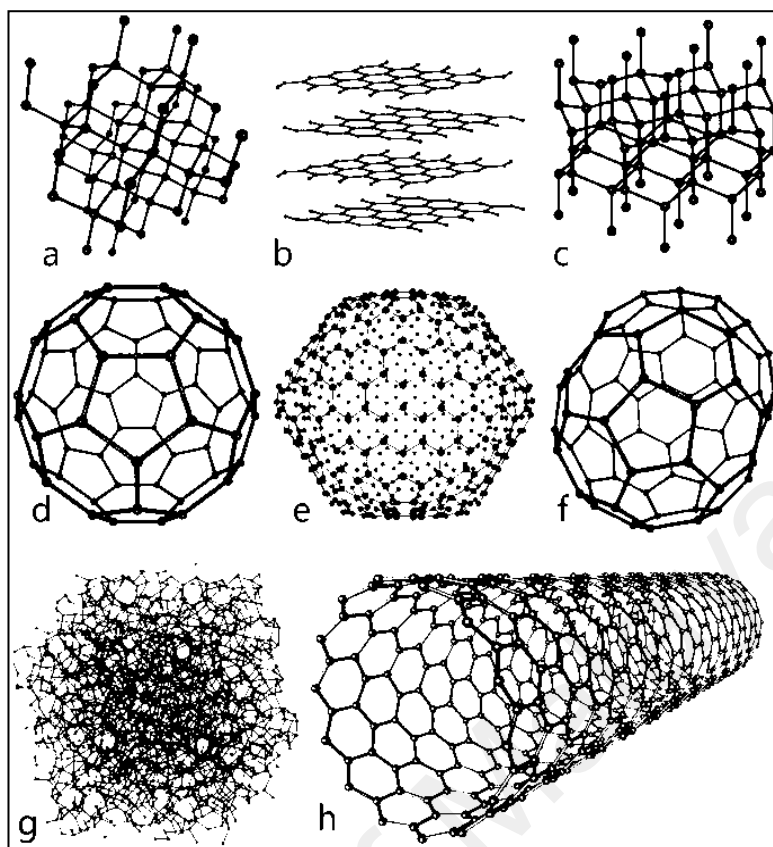


Figure 2.2: The structures of eight allotropes of carbon:

- (a) Diamond (b) Graphite (c) Lonsdaleite
 (d) C₆₀ (Buckminsterfullerene) (e) C₅₄₀ Fullerene
 (f) C₇₀ Fullerene (g) Amorphous carbon
 (h) Single-walled carbon nanotube.

Recent years have shown an intense renewal of interest for carbon science, provoked by the discovery in 1985 of buckminsterfullerene or C₆₀ by *Kroto, Curl, Smalley and co-workers* (Kroto, Heath et al. 1985). Fullerene are a family of molecules composed entirely of carbon, in the form of a hollow sphere, ellipsoid, or tube. Spherical fullerenes are also called buckyballs, and they resemble the balls used in the game of soccer. Fullerenes are similar in structure to graphite, which is composed of stacked graphene sheets of linked hexagonal rings; but they may also contain pentagonal (or sometimes heptagonal) rings.

Single walled carbon nanotubes are an allotrope of sp² hybridized carbon, similar to fullerenes. The structure can be thought of as a cylindrical tube comprised of 6-membered carbon rings, as in graphite. The cylindrical tubes may have one or both

ends capped with a hemisphere of the buckyball or fullerene structure. In 1991, Iijima discovered closed tubular structures, consisting of nested cylindrical graphitic layers capped by fullerene-like ends with a hollow internal cavity (Iijima 1991).

Nanotubes can be found in several forms; single-wall (having one single shell), double-wall and multi-wall. Depending on the growth process, single-wall, double-wall or multi-wall nanotubes can be selectively produced. Carbon nanotubes come in a variety of diameters and lengths, depending on the growth process and treatment. Carbon nanotubes, can be metallic as well as semiconducting, depending on the tube geometry (Wildöer, Venema et al. 1998), (Odom, Huang et al. 1998). They show promising prospects for applications: they are mechanically extremely stiff and resistant to bending (Falvo, Clary et al. 1997), and their suitability as a tip for scanning probe microscopy has also been demonstrated (Dai et al. 1996 and Hafner et al. 1996). Furthermore, they have proven to be very good electron field emitters (De Heer, Chatelain et al. 1995) (Rinzler, Hafner et al. 1995) (Collins, Zettl et al. 1996) (Bonard, Maier et al. 1998) (Wang, Corrigan et al. 1997).

2.2 Individual Carbon nanotubes

Nanotubes can be thought of layers of the conventional graphite structure rolled up into a cylinder, the lattice of carbon atoms remains continuous around the circumference. The number of shells varies from one a single-walled CNT to as many as fifty with the spacing between the layers matching closely the layer spacing in graphite around 0.34 nm. MWCNTs were defined as, the concentric graphite layers spaced 0.34 nm apart, with diameters from 10 to 200 nm and lengths up to hundreds of microns (Dai 2002). A single-wall carbon nanotube is best described as a rolled-up tubular shell of graphene sheet which is made of benzene type hexagonal rings of carbon atoms (Dresselhaus, Dresselhaus et al. 1996). The average diameter of a SWCNT is 1.2 nm (Spires and Brown 1996) and their lengths are typically several

microns, but recent advancements have made the nanotubes much longer, and measured in centimeters and lengths up to 1.5 cm have been reported (Huang, Woodson et al. 2004).

In 2004 a length of 4 cm was recorded by a group of scientists, the single-wall carbon nanotubes (SWCNTs) synthesized at a high growth rate of $11\mu\text{ms}^{-1}$ by catalytic chemical vapour deposition (Zheng, O'Connell et al. 2004). The result suggested the possibility of growing SWCNTs continuously without any apparent length limitation. Thus, resulting in an aspect ratio (length/diameter) significantly larger than 1000. However, nanotubes can vary in size, and they aren't always perfectly cylindrical. The larger nanotubes, such as a (20,20) tube, tend to bend under their own weight. The diagram (figure 2.3) below shows the average bond length and carbon separation values of the hexagonal lattice. The average bond length of 1.42 \AA was measured by Spires and Brown in 1996 and later confirmed by Wildöer in 1998 (Wildöer, Venema et al. 1998). The C-C tight bonding overlap energy is in the order of 2.5 eV. Wilder et al. estimated it to be between 2.6 eV-2.8 eV (Wildöer, Venema et al. 1998), while at the same time, Odom et al. estimated it to be 2.45 eV (Odom, Huang et al. 1998).

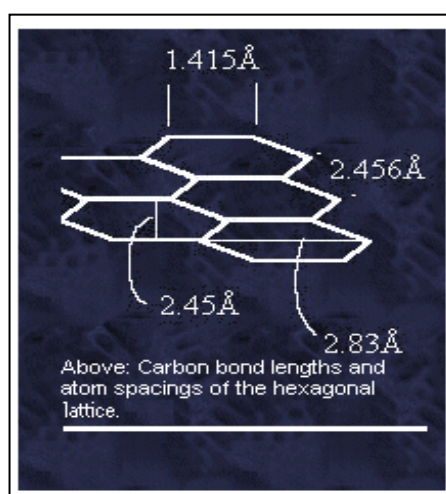


Figure 2.3: The average bond length and carbon separation values of the hexagonal lattice.

2.3 The vector and chiral angle of SWCNT

The structure of a SWCNT can be conceptualized by wrapping a one-atom-thick layer of graphite called graphene into a seamless cylinder. The structure of carbon nanotube is identified in three parameters such as diameter, chiral angle (twist angle) and spiral direction. The diameter of carbon nanotube and chiral angle can be unambiguously measured by the chiral vector. Thus, chiral laps a circumference of a nanotube cylinder and identifies tube structure. Figure 2.2(b) shows a graphene sheet. A nanotube is cut and opened. The vector OA is chiral, and the point O laps over the point A when forming a tube. The chiral vector \vec{C}_h is expressed by \vec{a}_1, \vec{a}_2 using primitive translation vectors: $\vec{C}_h = n\vec{a}_1 + m\vec{a}_2$ of primitive lattice of graphene, where n and m are integer numbers. The magnitude of \vec{C}_h corresponds to the circumference around the nanotube.

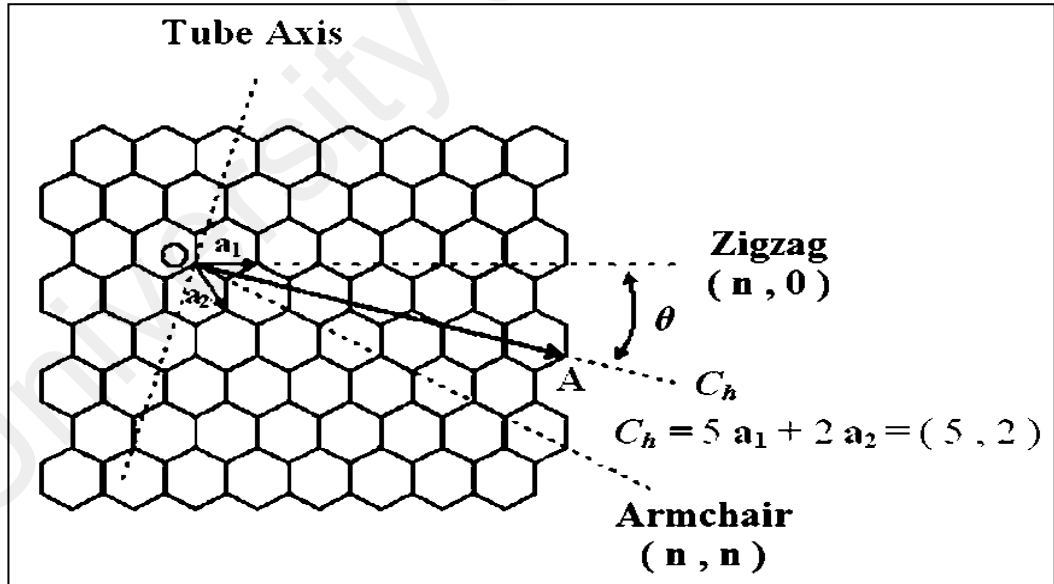


Figure 2.4: A graphene sheet showing the chiral vector with the unit vectors.

Basically, one can roll up the sheet along one of the symmetry axis: this gives either a zig-zag tube or an armchair tube. It is also possible to roll up the sheet in a direction that differs from a symmetry axis: one obtains a chiral nanotube, in which the

equivalent atoms of each unit cell are aligned on a spiral. Besides the chiral angle, the circumference of the cylinder can also be varied. In general, the whole family of nanotubes is classified as zigzag, armchair, and chiral tubes of different diameters.

According to the chiral angles and chiral vectors, the chiral angle and C_h of zigzag nanotubes is 0° and $(n,0)$ respectively. The chiral angle is 30° and C_h is (n,n) for armchair nanotubes. The chiral SWNTs have $C_h = (n,m)$ where n is not equal to m , and a chiral angle which is greater than 0° and less than 30° (see figure 2.4). The electronic properties of nanotubes depend greatly on their structure. For example, it is known that (n,m) nanotubes are metallic if $(2n + m)$ is a multiple of 3 and that other nanotube structures are semiconducting (Dresselhaus, Dresselhaus et al. 1996).

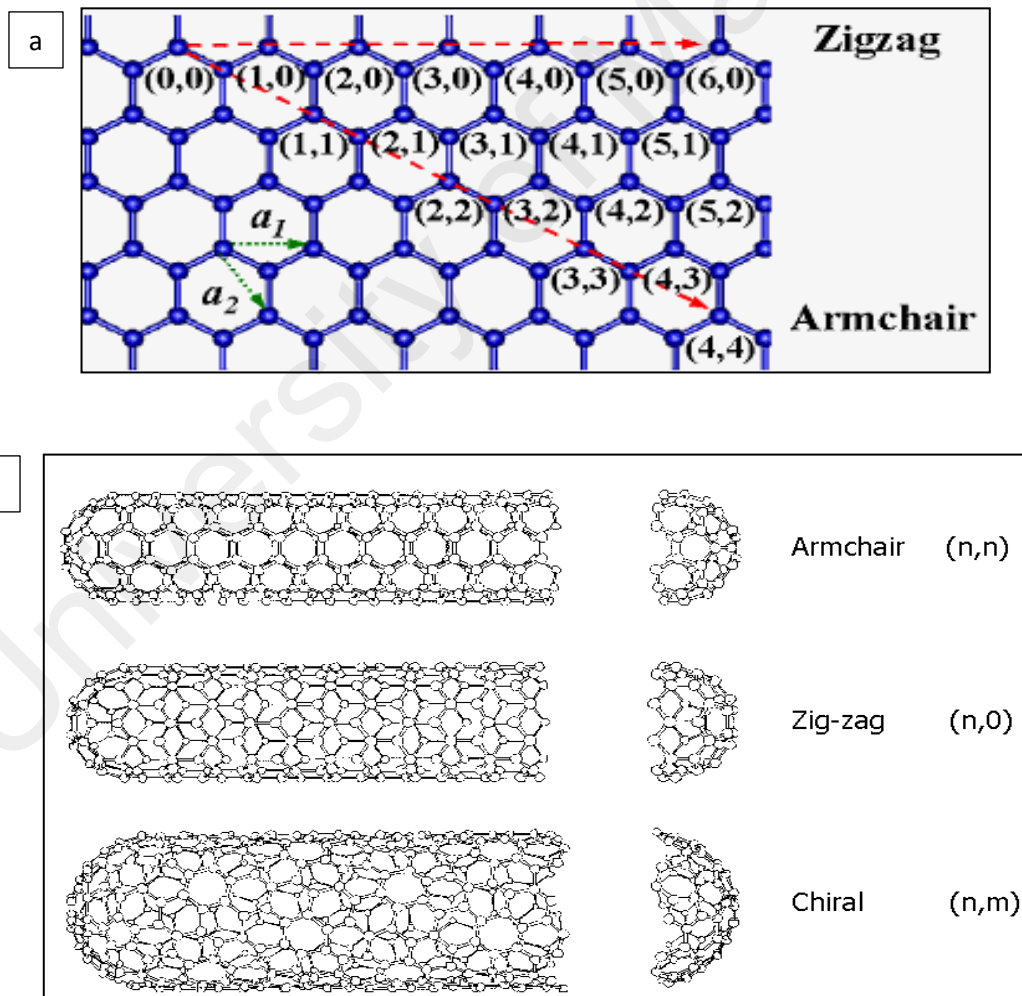


Figure 2.5: (a) Graphene sheet with carbon atoms labeled using the (n, m) notation (b) Models of different singlewall nanotubes.

As mentioned above, the chiral vector \vec{C}_h is defined by the use of the real space unit vectors \vec{a}_1 and \vec{a}_2 of the hexagonal lattice as follows:

$$\vec{C}_h = n\vec{a}_1 + m\vec{a}_2 \quad 2-1$$

Here the angle between the unit vectors \vec{a}_1 and \vec{a}_2 is 60 degree and:

$$|\vec{a}_1| = |\vec{a}_2| = a = \sqrt{3}a_{cc} \quad 2-2$$

Where the constant a_{cc} (0.142 nm) represents the nearest neighbor C-C distance (Charlier, Blase et al. 2007).

The magnitude of chiral vector \vec{C}_h can be given by the following equation;

$$|\vec{C}_h| = a\sqrt{n^2 + m^2 + nm} \quad 2-3$$

Since the single wall carbon nanotube is formed by rolling up the sheet along the direction of the chiral vector \vec{C}_h , the circumference of a cylindrical carbon nanotube equals to the length of the chiral vector \vec{C}_h . For a given pair of integers (n,m) , the diameter (d) of a carbon nanotube may be derived from the length of the chiral vector \vec{C}_h as follows:

$$d = \frac{|\vec{C}_h|}{\pi} = \frac{\sqrt{3}}{\pi} a_{cc} \sqrt{m^2 + nm + n^2} \quad 2-4$$

The angle (θ) between the chiral vector \vec{C}_h and the primitive lattice translation vector \vec{a}_1 is called the chiral angle, which is in the range of 0 to 30 degree and can be expressed by the pair of integers (n,m) , and defined by using the scalar product of the vectors \vec{a}_1 and \vec{C}_h :

$$\cos(\theta) = \frac{\vec{a}_1 \cdot \vec{C}_h}{|\vec{a}_1| |\vec{C}_h|} = \frac{2n+m}{2\sqrt{n^2+m^2+nm}} \quad 2-5$$

The chiral angle θ , can be given in tangential form as well by the vector and scalar product of the vectors \vec{a}_1 and \vec{C}_h as follows:

$$\tan(\theta) = \frac{|\vec{a}_1 \otimes \vec{C}_h|}{|\vec{a}_1 \cdot \vec{C}_h|} = \frac{\sqrt{3}m}{2n+m} \quad 2-6$$

The chiral angle (θ) can be expressed as (Hamada, Sawada et al. 1992):

$$\theta = \tan^{-1}\left(\frac{\sqrt{3}m}{2n+m}\right) \quad 2-7$$

Furthermore, it may be useful to specify the unit cell of a carbon nanotube (CNT), which is a part of a nanotube containing non-equivalent atoms.

2.4 Single-wall carbon nanotube conductivity

An individual SWCNT exhibits metallic or semiconducting behavior depending on the diameter and spiral conformation (helicity) of the carbon rings. These structure function relations are a consequence of graphite being a ‘semi-metal’, example a semiconductor with a zero band gap, where structural distortion of the planar graphene sheet can either increase the overlap between the conductance and valence bands, (creating a metallic SWCNT) or open a wider band-gap, forming a semiconducting SWCNT. In graphite, the valence and conduction bands touch and are degenerate at six \mathbf{K} (k_F) points; these six positions define the corners of the first Brilluion zone (Figure

6(a)). When wrapping up a graphene sheet to an SWNT the electron's k vector gets quantized in the circumferential direction because of the periodic boundary conditions of the nanotube.

$$\vec{C}_h \cdot \vec{k} = 2\pi q$$

2-8

where q is an integer. If one of these allowed subbands passes through one of the K points, the nanotube will be metallic and otherwise semiconducting.

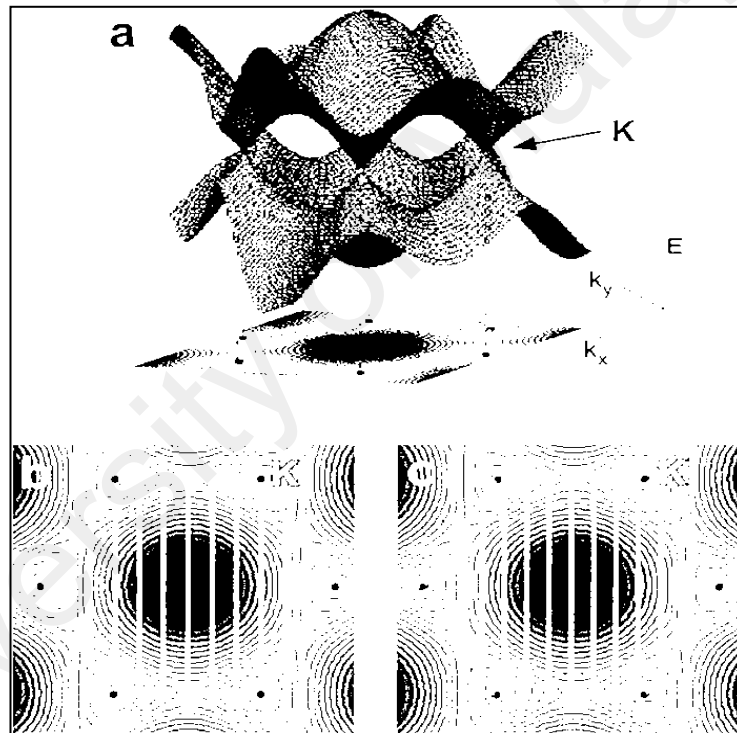


Figure 2.6: (a) Three-dimensional view of the graphene π / π^* bands and its 2D projection. (b) Example of the allowed 1D subbands for a metallic tube. Schematic depicts (9,0). (c) Example of the quantized 1D subbands for a semiconducting tube. Schematic shows (10,0). The white hexagon defines the first Brilluion zone of graphene, and the green dots in the corners are the graphene K points (Odom, Huang et al. 2000).

Figures 6(b), 6(c) show the allowed subbands for two zigzag tubes, (9,0) and (10,0), respectively. Notice that the (9,0) subbands contain a K point while none of the (10,0) subbands do. The condition for metallic tubes is (Odom, Huang et al. 2000) :

$$\vec{C}_h \cdot \vec{k}_F = 2\pi q$$

2-9

Thus to first order, zigzag $(n,0)$ or chiral (n,m) SWNTs are metallic when $(n - m)/3$ is an integer and otherwise semiconducting.

The density of states for the nanotubes at the Fermi energy, E_f located at $E_f = 0$, is zero for semi-conducting nanotubes, and is non-zero for metallic tubes. The energy gap E_g for semi-conducting nanotubes depends on the reciprocal of the nanotube diameter d , and is given by:

$$E_g = \frac{4\hbar v_F}{3d}$$

2-10

Where v_F is the Fermi velocity. Bandgaps vary from about 10 meV to 1 eV (Stetter 2004).

The chirality defines many of the properties of the individual SWCNT. One of the important things which plays an essential role on electronic properties, is the energy gap which can inform us about metallic and semi-metallic properties of nanotubes. A variety of probes predict that armchair single-wall carbon nanotubes are always metallic (Dresselhaus, Dresselhaus et al. 1996) and all the other tubes (zigzag and chiral), depend on whether they satisfy $n-m=3i$ or not (where i is an integer), are metallic or semi-conducting (Wildöer, Venema et al. 1998).

2.5 Carbon nanotubes, unique properties and potential applications

CNTs have attracted the fantasy of many scientists worldwide; they are an example of true nanotechnology. The small dimensions, strength and the remarkable physical properties of these structures make them a very unique material with a whole

range of promising applications. CNTs exhibit excellent mechanical, electrical, thermal and magnetic properties (Treacy, Ebbesen et al. 1996), (Saito, Dresselhaus et al. 1998). The exact magnitude of these properties depends on the diameter and chirality of the nanotubes and whether they are single-walled, double-walled or multi-walled form. Typical properties of CNTs as well as different carbon materials are collected in table 2.1 (Sahoo, Rana et al. 2010) and table 2.2 (Ma, Siddiqui et al. 2010).

Table 2.1: Typical properties of CNTs.

Property	SWNT	DWNT	MWNT
Tensile strength (GPa)	50-500	23-63	10-60
Elastic modulus (TPa)	~1	-	0.3-1
Elongation at break (%)	5.8	28	-
Density (g/cm ³)	1.3-1.5	1.5	1.8-2.0
Electrical conductivity (S/m)		~10 ⁶	
Thermal stability		>700°C (in air)	
Typical diameter	1 nm	~5 nm	~20 nm
Specific surface area		10-20m ² /g	

Table 2.2: Physical properties of different carbon materials (P: in-plane; c: axis).

Property	C material				
	Graphite	Diamond	Fullerene	SWCNT	MWCNT
Specific gravity (g/cm ³)	1.9-2.3	3.5	1.7	0.8	1.8
Electrical conductivity (S/cm)	4000 ^P , 3.3 ^c	10 ⁻² -10 ⁻¹⁵	10 ⁻⁵	10 ² -10 ⁶	10 ³ -10 ⁵
Electron mobility (cm ² /V s)	2.0 × 10 ⁴	1800	0.5-6	~10 ⁵	10 ⁴ -10 ⁵
Thermal conductivity (W/(m.K))	298 ^P , 2.2 ^c	900-2320	0.4	6000	2000
Coefficient of thermal expansion (K ⁻¹)	-1 × 10 ^{-6p} 2.9 × 10 ^{-5c}	(1~3)×10 ⁻⁶	6.2 × 10 ⁻⁵	Negligible	Negligible
Thermal stability in air (°C)	450-650	<600	~600	>600	>600

Carbon nanotubes have potential applications in fields such as nanotechnology, electronics, optics, materials science, and architecture. They have been used for diversified applications such as sensing, gas storage, biomedicine, field emission displays, energy-storage devices and functional fillers in composites (Vashist, Zheng et

al. 2011), (Endo, Hayashi et al. 2004). The chart in figure 2.7, illustrates the diversity of applications possible using the various attributes of carbon nanotubes.

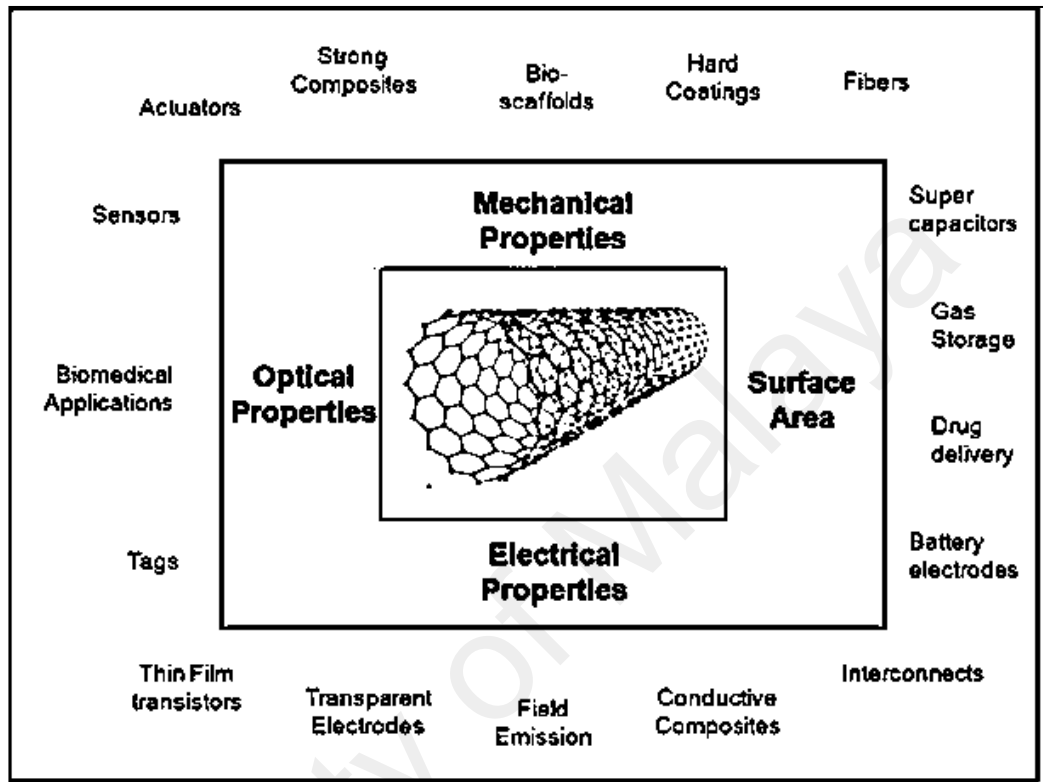


Figure 2.7: A chart to show the diversity of applications possible using the various attributes of carbon nanotubes.

At present, researchers are working on the following areas in order to apply carbon nanotubes in emerging technologies.

- (i) Production of defect-free and high-purity carbon nanotubes.
- (ii) Establishment of useful techniques for quantifying the number of defects (their types, where they are, etc.) in the nanotube structure.
- (iii) Development of effective purification techniques (below the parts per million level) the metal particles within carbon nanotubes, especially for biological and electronic applications.
- (iv) Achieving homogeneous carbon nanotube dispersions in polymer composites.

Over the years new applications have taken advantage of the carbon nanotubes properties, the following is the overall applications of this exciting material.

2.5.1 CNTs and Electronic Industry

The unique electronic properties of nanotubes make them good candidates in the electronics industry for replacing silicon-based technologies with those based on nanocarbons (Collins and Avouris 2000). The electronic properties of MWNT are rather similar to those of SWNT, due to the weak coupling between the cylinders. The wonderful CNTs are expected to serve as active components in electronic nano-switches and nano-transistors, electron emission sources, act as molecular wires connecting components in nano-devices, and as chemical sensors (Szeleifer and Yerushalmi-Rozen 2005). Figure 2.8 (Do, Truong et al. 2013), and figure 2.9 (Zhang, Hu et al. 2007) show a CNT transistor schema and CNT thin-film transistors in integrated circuits on a flexible and transparent substrate.

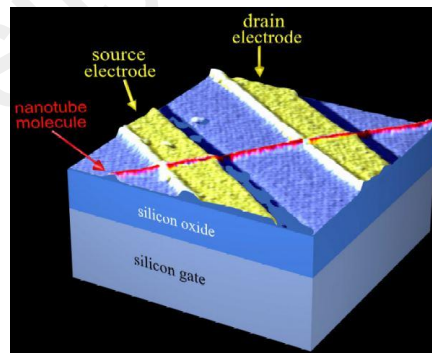


Figure 2.8: CNT transistor schema (Do, Truong et al. 2013).

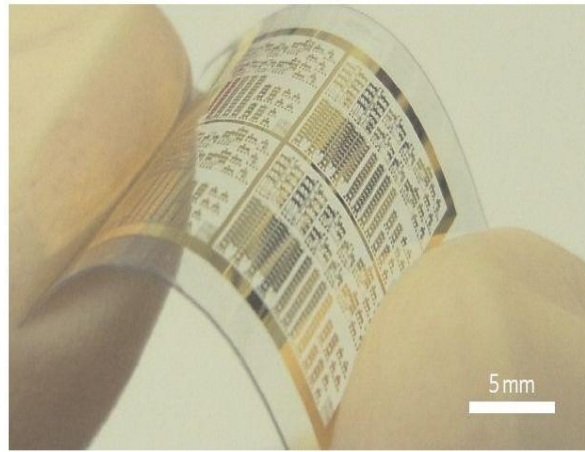


Figure 2.9: CNT thin-film transistors in integrated circuits on a flexible and transparent substrate (Zhang, Hu et al. 2007).

Nanodiodes based on CNT, which are very stable in ambient environment, were successfully fabricated (Chai, Zhou et al. 2005). Sheets of SWNTs can be used as electromechanical actuators, mimicking the actuator mechanism present in natural muscles. Devices made from stretchable electronic materials could be incorporated into clothing or attached directly to the body. A class of wearable and stretchable devices fabricated from thin films of aligned single-walled carbon nanotubes was reported. When stretched, the nanotube films fracture into gaps and islands, and bundles bridging the gaps. This mechanism allows the films to act as strain sensors capable of measuring strains up to 280% (50 times more than conventional metal strain gauges), with high durability, fast response and low creep. The carbon-nanotube sensors were assembled on stockings, bandages and gloves to fabricate devices that can detect different types of human motion, including movement, typing, breathing and speech (Yamada, Hayamizu et al. 2011). SWCNTs can be joined to form the 'X', 'Y' or 'T' shaped junctions, by introducing pentagon/heptagon defects at joining regions (Menon, Andriotis et al. 2003). These nanotube junctions can be constructed to form two and three dimensional (2D, 3D) CNTs networks (Dag, Senger et al. 2004). These networks can be used to form thin film transistors (Snow, Campbell et al. 2005) and many other nanodevices

which would facilitate forming and integrating potential complex networks in rectenna. CNTs are the best known field emitters of any material. An immediate application of this behavior receiving considerable interest is in field-emission flat-panel displays. Instead of a single electron gun, as in a traditional cathode ray tube display, in CNT-based displays there is a separate electron gun (or even many of them) for each individual pixel in the display.

2.5.2 CNTs and Electrical Conductivity

The conductivity of SWCNT bundles was found to vary between 1×10^4 (Kim, Choi et al. 1998) and 3×10^6 S/m (Fischer, Dai et al. 1997), (Bozhko, Sklovsky et al. 1998) at room temperature, depending on sample type and entanglement state. These values approach that for the in-plane conductivity of graphite (2.5×10^6 S/m) (Charlier and Issi 1996). Conductivities of individual MWCNTs have been reported to range between 20 and 2×10^7 S/m (Ebbesen, Lezec et al. 1996), depending on the helicities of the outermost shells (Lee, Park et al. 2000) or the presence of defects (Dai, Wong et al. 1996). It is well-established that the higher the aspect ratio of filler particles, the lower the loading required needed to achieve a given level of conductivity. CNTs are ideal in this sense, since they have the highest aspect ratio of any carbon fiber. In addition, their natural tendency to form ropes provides inherently very long conductive pathways even at ultra-low loadings.

The semi-one-dimensional structure of SWNT leads to ballistic transport in metallic SWNT, where the electrons can be considered as moving freely through the structure, without any scattering from atoms or defects. Experimental results showed that metallic single wall nanotubes can carry up to 10^9 A/cm² with essentially no heating, compared to current densities for normal metals being only 10^5 A/cm² (Wei, Vajtai et al. 2001), making them more conductive than copper (Wei, Vajtai et al. 2001), (Durkop, Kim et al. 2004). The image below in figure 2.10, shows a device based on

carbon nanotubes wrapped with poly(3-hexylthiophene) and dispersed in poly(dimethylsiloxane) sheets can effectively convert laser light into thermal energy and subsequently to electricity. The converter can be transmitted through living tissue.

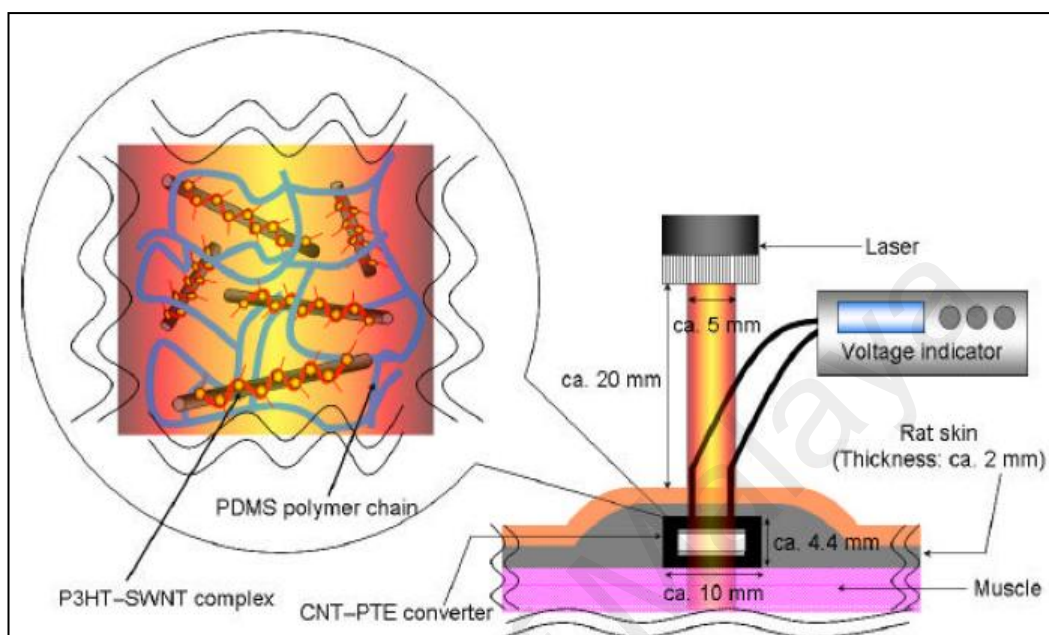


Figure 2.10: Carbon nanotube based device which can convert laser to heat and to electricity, the laser can power devices through living tissue (Adio 2009).

2.5.3 CNTs Biomedical Applications

Carbon nanotubes (CNTs) have been explored for potential applications in biological and biomedical fields ever since the discovery of them (Huang, Li et al. 2009). They could be one of the most advanced nano vectors for the highly efficient delivery of drugs and biomolecules due to their unique optical and electrical properties. They can be conjugated non-covalently or covalently with drugs, biomolecules and nanoparticles towards the development of a new-generation delivery system for drugs and biomolecules. There have been significant advances in the field of CNT based drug delivery, especially in the specific targeting of anticancer and anti-inflammatory drugs for tissues and organs in the body, where their therapeutic effect is highly required.

Other promising applications are the delivery of DNA, RNA and proteins (Vashist, Zheng et al. 2011).

SWCNTs absorb light strongly in the near-infrared (NIR) range (800–1600 nm), which contains the tissue transparent region of electromagnetic wavelengths (800–1400 nm). Therefore, they are extensively employed in photothermal therapy (Chakravarty, Marches et al. 2008), (Kam, O'Connell et al. 2005) and photoacoustic imaging (De La Zerda, Zavaleta et al. 2008).

The optical properties of SWCNTs can also be used for Raman detection and imaging (Heller, Baik et al. 2005), (Rao, Richter et al. 1997).

Interactions between specific types of DNA and CNT enabled visualization of DNA (Guo, Sadler et al. 1999). Drugs and biomolecules can be stored inside CNTs, which can then be bound to targeting molecules such as antibodies or contrast agents. Hexamethylmelamine (HMM), an antitumor agent, can be incorporated inside C₆₀ capped SWCNT/double wall carbon nanotubes (DWCNT), results in a “carbon nano-bottle” structure, obtained by sealing CNT opened ends using C₆₀ after loading HMM (Ren and Pastorin 2008) (See figure 2.11).

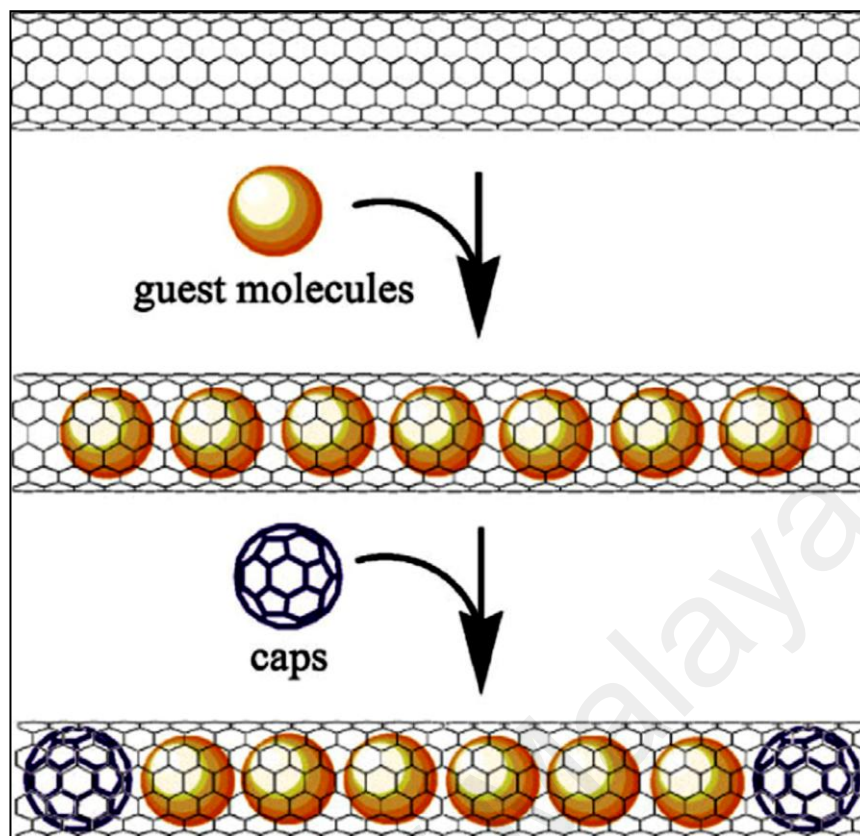


Figure 2.11: “carbon nano-bottles” loaded with antitumor agents and C60 using a controlled nanoextraction strategy. C60 filled at the extremities of CNTs could act as “cap” to seal the CNTs (Ren and Pastorin 2008).

It is worthwhile to be aware of probable environmental and health issues that would arise by using CNTs. These issues will be indirectly governing the commercialization process. Raffaele et al. (Raffaele, Landi et al. 2005) indicated that nanotubes would be more toxic than other carbon particles or quartz dust when being absorbed into the lung tissue. Riviere et al. (Riviere, Nemanich et al. 2005) stated that the nanotubes are capable of intracellular localization and consequently cause irritation in human epidermal keratinocytes (superficial layer of the skin). However, functionalized CNTs have been considered biocompatible and safe for drug and biomolecular delivery applications as they are soluble in physiological media and nontoxic. They have shown no accumulation in the tissues; conversely, once functionalized, they can be readily excreted through the renal route (Vashist, Zheng et

al. 2011). Overall, the use of CNTs for delivery of drugs and biomolecules is a significant development in the field of therapeutic nanomedicine.

2.5.4 CNTs Applications due to Mechanical Properties

Carbon nanotubes can replace steel industry with more efficiency and wider range of application. Individual SWNTs are significantly stronger than steel. Calculated values for tensile strengths of SWNTs are ~ 100 times greater than steel at 1/16th the weight (Jansen and Wallis 2009) and are very resistant to damage from physical forces. Pressing on the tip of a nanotube will cause it to bend, but without damage to the tip. When the force is removed, the tip returns to its original state (elastic behavior).

Due to the very large aspect ratio and the high rigidity of SWNTs, they exhibit exceptional strength and stiffness as manifested by an elastic Young's modulus of ≈ 1 TPa and strength of few tens of GP. In addition, because of their flexibility, nanotubes can also be used in scanning probe instruments. Since MWNT tips are conducting, they can be used in STM and AFM instruments. Advantages are the improved resolution in comparison with conventional Si or metal tips and the tips do not suffer from crashes with the surfaces because of their high elasticity. However, nanotube vibration, due to their large length, will remain an important issue until shorter nanotubes can be grown controllably. A pair of nanotubes can be used as tweezers to move nanoscale structures on surfaces (Baughman, Zakhidov et al. 2002). CNT-based nanocomposites form a new class of lightweight super strong functional materials for air and space applications. Recently, UT Dallas researchers have made artificial muscles from carbon nanotube yarns that have spun from carbon nanotubes and soaked in paraffin wax (Schulz 2012) (figure 2.12).

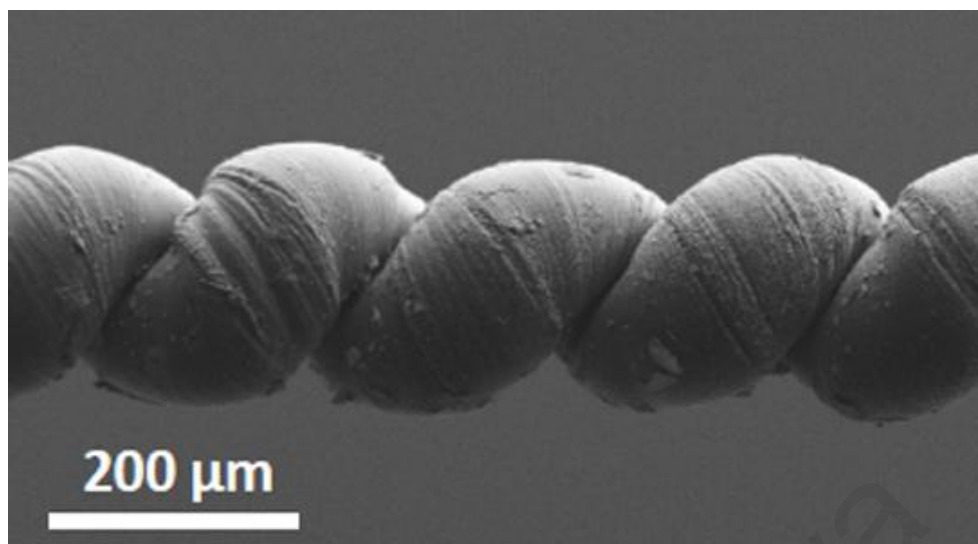


Figure 2.12: Artificial muscles from carbon nanotube yarns (Schulz 2012).

2.5.5 CNTs applications in the Chemical field

The properties of strain reversibility at room temperature (Pham, Park et al. 2008), in addition to a smooth surface topology; perfect surface specificity (Ajayan and Zhou 2001). The mechanical robustness (Wang and Cao 2001) makes carbon nanotubes highly compatible regarding thermo-mechanical and chemical properties.

SWNTs may be used as miniaturized chemical sensors. On exposure to environments, which contain NO_2 , NH_3 , CH_4 or O_2 (Nguyen and Huh 2006), the electrical resistance changes.

If it becomes possible to keep fluids inside nanotubes, it could also be possible to perform chemical reactions inside their cavities especially organic solvents which wet nanotubes easily. In this case we could speak of a nonreactor. Because of their smaller pore sizes, filling of SWNTs is more difficult than filling of MWNTs. Hydrogen can be electrochemically stored in CNTs, lithium also can be stored in CNTs by electrochemical intercalation (Frackowiak and Béguin 2002), (Yang and Wu 2001). Outstanding capacitance and good stability have been obtained from the electrodes prepared from CNT/conducting polymer. For example 606 F g^{-1} for CNT/polyaniline (Sivakkumar, Kim et al. 2007).

2.5.6 CNTs and Heat Conductivity

High thermal conductivity (κ) is one of the most attractive intrinsic properties of carbon nanotubes (Baughman, Zakhidov et al. 2002). Such a high κ is mainly attributed to the large mean free path of phonons in CNT (Mingo and Broido 2005, (Yu, Shi et al. 2005). Because of their small size, quantum effects are important, and the low-temperature specific heat and thermal conductivity show direct evidence of 1-D quantization of the phonon bandstructure (Hone 2004). Many theoretical and experimental studies on the thermal transport property of a single CNT have been conducted (Lin, Shang et al. 2012). The theoretical work predicts a room-temperature thermal conductivity that is larger than graphite or diamond. By molecular dynamic simulations, Berber et al. determined κ of an isolated single-walled CNT at room temperature to be $\sim 6600 \text{ W m}^{-1} \text{ K}^{-1}$ (Berber, Kwon et al. 2000). Thermal conductivity of individual CNTs was predicted to be dependent on tube diameter, length, chirality, defect and temperature (Lin, Shang et al. 2012). Measurements show a room-temperature thermal conductivity of over 200 W/m K for bulk samples of single-walled nanotubes (SWNTs), and over 3000 W/m K for individual multiwalled nanotubes (MWNTs) (Hone 2004) and $\kappa \approx 3500 \text{ W/mK}$ for an individual single-wall carbon nanotube (SW-CNT) (Pop, Mann et al. 2006). The room temperature values of the thermal conductivity of up to 5300 W/mK were extracted for a single-layer graphene from the dependence of the Raman G peak frequency on the excitation laser power. The extremely high values of the thermal conductivity suggest that graphene can outperform carbon nanotubes (CNTs) in heat conduction (Balandin, Ghosh et al. 2008). Very interesting is the fact that once graphene layers are stacked in graphite, the interlayer (van der Waals) interactions quench the thermal conductivity of this system by nearly 1 order of magnitude (Berber, Kwon et al. 2000).

The high thermal conductivity of nanotubes may be useful for a number of thermal management applications, such as heat sinking of silicon processors, or to increase the thermal conductivity of plastics in such areas as housing for electric motors. Carbon nanotubes with their light weight and high thermal conductivity value have the potential to be used as thermal interface materials. The high intrinsic thermal conductivity of CNT suggests many heat transfer enhancement applications. Thus the CNT can play a significant role in reducing the thermal resistance by lowering or eliminating the micro-gaps at the same time providing a high thermal conductivity path through them (Shaikh, Lafdi et al. 2007).

In overall, there is a wealth of other potential applications for CNTs, such as solar collection; nano-porous filters, catalyst supports and coatings of all sorts. There are almost certainly many unanticipated applications for this remarkable material that will come to utilization in the years ahead, and which may prove to be the most important and valuable ones of all. Figure 2.13 shows a carbon nanotube fountain pen, it can make three-dimensional structures, with metal atoms ink.

Figure 2.14 presents carbon nanotubes wonderful characteristics rackets, currently existing in the market (Kuroyanagi, Ueno et al. 1990).

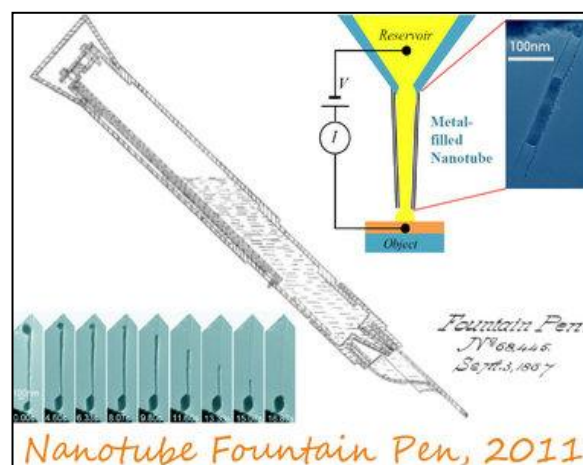


Figure 2.13: Carbon nanotube fountain pen.



Figure 2.14: Carbon nanotube rackets (Kuroyanagi, Ueno et al. 1990).

University of Malaysia

CHAPTER 3: MWCNT AND MWCNT COMPOSITES AS FIELD ELECTRON EMITTERS CATHODES

3.1 Introduction

One of the first applications of CNTs was as field electron emitters. The small size and high aspect ratio of CNTs combined with the high electrical conductivity are expected to yield efficient field emission currents, due to high field enhancement factors. Numerous studies has been conducted on the applications of CNTs as field emitters (Murphy 1956, Gomer 1961, Xu and Huq 2005).

The first theories attempted to describe field electron emission were in the 1920's by Schottky (Yamamoto 2006). In 1928, Fowler and Nordheim reported a theoretical analysis with experimental electron field emission data (Fowler and Nordheim 1928). Currently, the basic physics of field electron emission is reasonably well understood for flat metal surfaces and the emission current from a metal surface can be described by the Fowler–Nordheim (FN) equation. Experimental observations of FEE from flat metal surfaces and rough surfaces differed significantly. However, the basic theory that describes field electron emissions from flat metal surfaces have often been adopted to describe emissions from rough surfaces including nanostructures surfaces. Such adoption of the FN equation was normally done with some small modification to accommodate the structure effects since the morphology of a field emitting surface was found to play a crucial role in determining the field emission properties (Nilsson, Groening et al. 2000, Smith, Forrest et al. 2005).

In a field electron emission situation, the electric field is applied across two electrodes. For electrode surfaces that are ideally smooth, the electric field on the

surface equals the macroscopic electric field applied. It is the local field at the emission site that governs electron emission,

For rough electron surfaces with micro- and nano scaled protrusions the local field at the field emission sites are the points closest to the anode, for example at the tips of the protrusions itself. The electric field strength can be greatly enhanced at these sites resulting in significant enhancement of the field emission currents compare to that from flat surfaces. There are other factors that renders a materials applicable as field electron emitters. Arguably, the most important factors are low work function and materials durability. Considering a common material used in field emitter equipment, LaB₆, has a work function value of about 2.7 eV which is much lower that of tungsten at 4.55 eV. Furthermore LaB₆ is much more durable under emission conditions in the sense of low volatility and materials integrity. As such, very small sized LaB₆ field electron emission cathodes are commonly used in applications where high brightness and fine focused electron beams are required.

However, the major drawback to field emission cathodes is the limited lifetime associated with the devices. The nano or micro-scale protrusions were fragile and lost their features under a high electrostatic field. In this view, researchers were looking for the ideal field emitter, which should be very long, very thin, made of a conductive material with high mechanical strength, robust, cheap and easy to process. When researchers were still looking for the ideal material, most of the previous properties were discovered in carbon nanotubes and their composites.

3.2 Carbon Nanotubes as Field Electron Emitters

In flat metals, an abundance of electrons exist, but the absence of surface geometric enhancement factor coupled with a high surface potential barrier (work function) make it not easy to extract electrons applying fields lower than 200 V/ μm . In

addition, the metallic emitters are instable even at the lowest residual gas pressure (Fransen, Van Rooy et al. 1999). On the other hand, CNT has the combined some excellent properties as field emission material: nanometer-size diameter, structural integrity, high electrical and thermal conductivity, and chemical stability (Dresselhaus, Dresselhaus et al. 2000). Moreover, its high aspect ratio makes it possible to significantly strengthen electric fields into the vicinity of nanotubes tips. Thus, provides a reason why much effort has been invested in the study of CNTs application for electron field emission (Saito, Uemura et al. 1998, Choi, Chung et al. 1999, Bonard, Stöckli et al. 2001, Somani, Somani et al. 2007, Giubileo, Di Bartolomeo et al. 2012), after first demonstrated in 1995 (De Heer, Chatelain et al. 1995, Rinzler, Hafner et al. 1995).

Table 3.3: Electric field threshold for 10 mA/cm² current density emission for different materials (Cheng and Zhou et al. 2003).

Table 3.1	
Threshold electric field required for a 10 mA/cm ² emission current density for different materials	
Cathode material	Threshold field (V/μm) for a current density of 10 mA/cm ²
Mo tips	50–100
Si tips	50–100
p-type diamond	160
Defective CVD diamond	30–120
Amorphous diamond	20–40
Cesium-coated diamond	20–30
Graphite powders	10–20
Nano-diamond	3–5 (unstable >30 mA/cm ²)
Assorted carbon nanotubes	1–2 (stable >4000 mA/cm ²)

Field electron emission has been observed from both single-walled and multi-walled carbon nanotubes, individual or in an ensemble (CNT films). Current densities of over 1 Acm⁻² at macroscopic applied fields of few V/μm have been reported (Bonard,

Kind et al. 2001, Bonard, Croci et al. 2002, Cheng and Zhou 2003, Shakir, Nadeem et al. 2006). Another research revealed that a single MWNT tip was capable of emitting stably for more than 100 hours at $\sim 2 \mu\text{A}$ current (Bonard, Maier et al. 1998). However, SWNTs generally have a smaller diameter and higher degree of structural perfection, therefore they are found to have better field electron emission properties than multiwalled carbon nanotubes and a longer life time (Bonard, Salvétat et al. 1998, (Zhu, Bower et al. 1999, Zhang, Fu et al. 2005). A theoretical study predicted that an open-ended SWNT has much better field-emission properties than a closed SWNT (Zhou, Duan et al. 2001).

CNT films differ for tube type, shape, dimension, density, substrate, etc. They have been proposed for applications in devices using CNTs as field emitters. Such as flat panel displays (De Heer, Chatelain et al. 1995, Rinzler, Hafner et al. 1995), lighting devices (Bonard, Stöckli et al. 2001), klystrons, X-ray tubes (Yue, Qiu et al. 2002), electron guns (De Jonge, Allieux et al. 2005), microwave power tube amplifiers and electron microscopy (Bower, Zhu et al. 2002, De Jonge and Bonard 2004, Milne, Teo et al. 2006).

In addition to these results, scientists were looking for further field emission enhancement by surface modification; using nano-coatings (Cha, Kim et al. 2006, Zhang, Qin et al. 2006) or plasma treatment (Chen, Den Engelsen et al. 2005, Cha, Kim et al. 2006) (nitrogen, oxygen and inert gas plasma) or both techniques. Promising results were attained.

The exceptional properties of carbon nanotubes have stimulated researchers to investigate the preparation and properties of polymer carbon nanotube composite materials. Thus, polymer composite materials are more applied than granular or ceramic composites for their higher tensile strength and elastic modulus (flexibility), the latest will be an important requirement for transparent electrodes and displays in the near

future. Moreover, integrating CNTs in polymers will lower the cost of devices production, as it was reported that the high cost was the major factor that keeps away the CNT from effective usage (Shaffer and Kinloch 2004). In 2012 prices were advertised for \$250/g for SWCNTs and \$25/g for MWCNTs. Prices of both MWCNT and SWCNT are a function of purity.

The concept of an emitter based material embedded in a host matrix can be originally traced back to the pioneering work of Latham (Latham 1981). Recently, randomly oriented CNTs, mixed with non-conducting epoxies field emitters were reported (Collins and Zettl 1997). Efficient field emitters based on MWCNTs embedded in a conjugated polymer host Poly(m-phenylenevinylene-co-2,5-dioctyloxy-p-phenylenevinylene) were also fabricated, the threshold field decreased with increasing CNTs loading (Smith, Carey et al. 2005). PANI-CNTs and PPy-CNTs composites with enhanced electronic properties were also studied (Khomeenko, Frackowiak et al. 2005). In addition, a considerable amount of researches has focused on integrating CNT emitters into flexible devices (Jung, Kar et al. 2006, Lyth and Silva 2007, Sim, Lau et al. 2007).

Although, FEEs from CNTs has been demonstrated by many researchers industrial applications remains difficult. One of the most challenging issues with macroscopic CNT cathodes is the emission uniformity. Due to variations in CNT structure and overall sample uniformity, only a very small fraction of the CNTs emit at a given time. For example, for flat-panel displays, an emission site density of $\sim 10^5 \text{ cm}^{-2}$ is often required which is not easy to accomplish. In addition, screening effects due to the proximity of neighboring nanotubes results in high threshold fields (Nilsson, Groening et al. 2000). Another weakness of CNTs is oxidation, which makes them less applicable. Damage to CNTs has been observed via field evaporation, ion bombardment, oxidation, thermal failure due to excessive emission current, and arcing

(Bonard, Kind et al. 2001, Bonard, Klinke et al. 2003). However, various methods have been developed to improve the field emission performance of CNTs, such as thermal oxidation (Wang, Zeng et al. 2006), laser treatment (Chen, Chen et al. 2006), Ar neutral beam treatment (Kyung, Park et al. 2008), ultraviolet laser ablation (Kim, Ahn et al. 2003), in addition to plasma treatment (Zhi, Bai et al. 2002, Zhu, Cheong et al. 2005, Feng, Zhang et al. 2007, Lee, Lim et al. 2008).

3.3 Surface Potential Barrier Lowering (Schottky Lowering)

An electron in front of a metal surface induces a rearrangement of the charge carriers in the metal. Therefore, a positive charge on the surface of the conducting plane is created. As it moves around, the electron experiences a potential imposed by its image charge. The electrostatic attractive force between the electron and its image is:

$$F(x) = eE_i = \frac{-e^2}{16\pi\epsilon_0 x^2} \quad 3-11$$

The electron and its image are both a distance x , away from the interface ($x = 0$).

The corresponding potential equals:

$$\phi(x) = -\int_x^{\infty} E_i(x)dx = \frac{e}{16\pi\epsilon_0 x} \quad 3-12$$

Where ϵ_0 is the permittivity of empty space. When an external electrical field is applied, the surface potential is reduced by the quantity eE_x and deformed into a triangular finite thickness barrier. The triangular barrier is further lowered and rounded at its tip due to the image force (see figure 3.1). Field electron emission occurs when the vacuum level bending is so much that the barrier width is small enough for the electrons

inside the metal to tunnel through the barrier. Most of the emission will occur from the vicinity of the Fermi level where the barrier is thinnest.

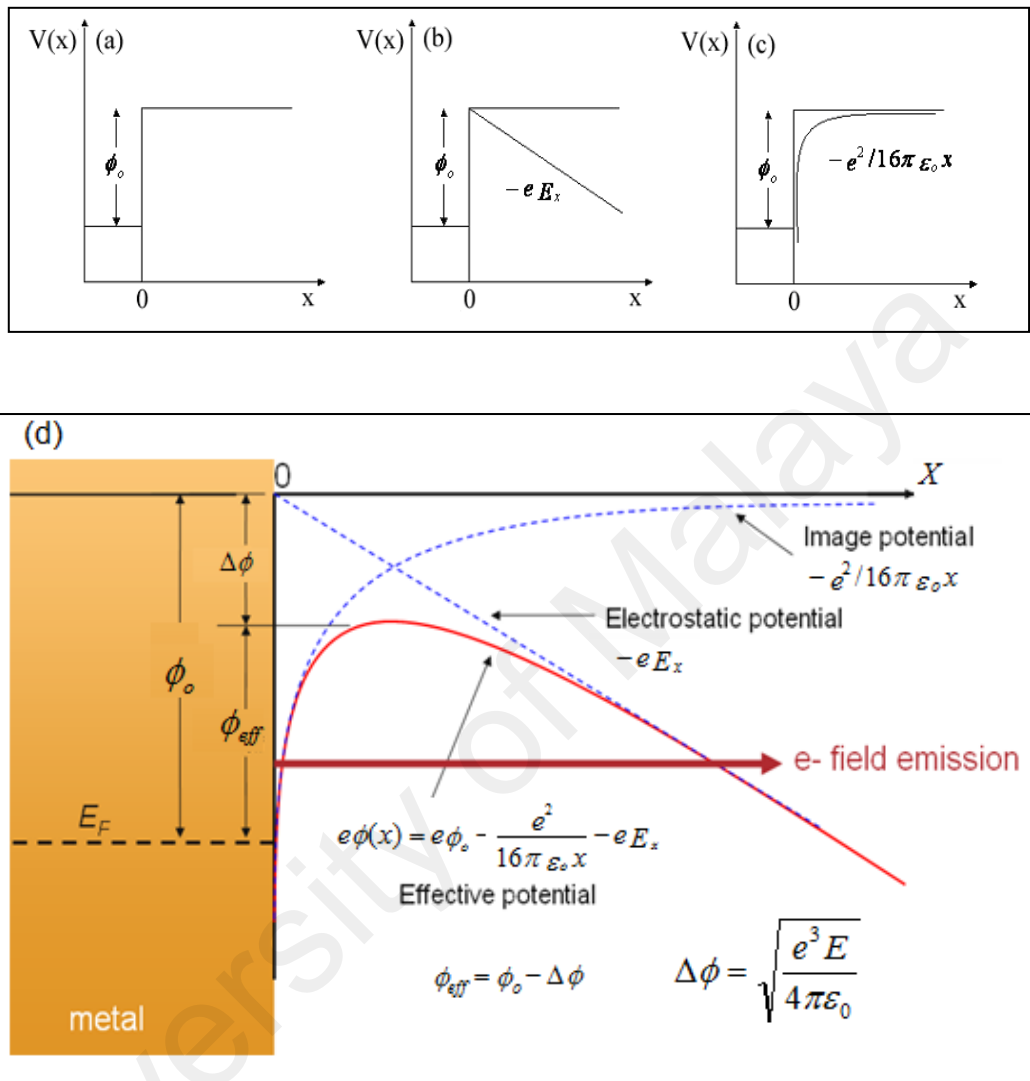


Figure 3.1: Schematic of Schottky Lowering: (a) without image potential and external field, (b) without image potential but with external field, (c) with image potential but without external field, and (d) with both image potential and external field.

3.4 Fowler-Nordheim Field Electron Emission Model

The following field electron emission theory is derived for a metal. Here the conduction electrons are treated as a gas of free particles obeying the Fermi-Dirac statistics. The metal surface assumed to be planar and the calculation is performed for the temperature of $T=0$ K. However, Fowler-Nordheim theory can be also applied to

carbon nanotubes; the only difference is in the work function. FEE process involves calculating the current density as a function of the electric field.

If $N(W)$ is the number of electrons per second having energies between W and $W+dW$ incident on 1cm^2 of the barrier surface, $W = P^2/2m$ is the electron kinetic energy carried by the momentum component W normal to the surface, m is free electron rest mass. $D(W,E)$ is the probability of transmission through the barrier, E is the local electric field.

The product $D(W,E) N(W) dW$ gives the number of electrons within dW that emit from the metal per second per unit area. Hence the current density $J(E)$ through the barrier is given by:

$$J(E) = e \int_0^{\infty} N(W) D(W, E) dW \quad 3-13$$

Using Wentzel-Kramers-Brillouin (WKB) approximation (Fröman and Fröman 1965); the barrier transparency is given by:

$$D(W, E) = \exp\left[-\frac{8\pi(2m)^{1/2}}{3he}\right] \frac{|W|^{3/2}}{E} \mathcal{G}(y) \quad 3-14$$

Where $\mathcal{G}(y)$ is the Nordheim function.

$$\mathcal{G}(y) = 2^{-1/2} \left[1 + (1 - y^2)^{1/2}\right]^{1/2} \cdot \left[F(k) - \left\{1 - (1 - y^2)^{1/2}\right\} K(k)\right] \quad 3-15$$

Having for an argument

$$y = \frac{(e^3 E)^{1/2}}{\phi}$$

Where ϕ is the work function and,

$$F(k) = \int_0^{\pi/2} \frac{d\alpha}{(1-k^2 \sin^2 \alpha)^{1/2}} \quad , \quad K(k) = \int_0^{\pi/2} (1-k^2 \sin^2 \alpha)^{1/2} d\alpha \quad \mathbf{3-16}$$

are complete elliptic integrals of the first and second kinds, with

$$k^2 = \frac{2(1-y^2)^{1/2}}{1+(1-y^2)^{1/2}}$$

Using (3.4) , the well-known FN equation is obtained:

$$J(E) = \frac{e^3 E^2}{16\pi^2 \hbar \phi t^2(y)} \exp\left[-\frac{4}{3e} \left(\frac{2m}{\hbar^2}\right)^{1/2}\right] \mathcal{G}(y) \frac{\phi^{3/2}}{E} \quad \mathbf{3-17}$$

$$\text{Where } y = 3.79 \cdot 10^{-4} \cdot \frac{\sqrt{E}}{\phi} \quad , \quad t(y) = \mathcal{G}(y) - \frac{2y}{3} \frac{d\mathcal{G}(y)}{dy} .$$

$\mathcal{G}(y)$ and $t(y)$ are tabulated functions (Choi, Chung et al. 1999). Equation (3.7)

can be written as follows:

$$J(E) = A \frac{E^2}{\phi} \exp\left(-B \frac{\phi^{3/2}}{E}\right) \quad \mathbf{3-18}$$

The other form of FN equation in terms of current is:

$$I(E) = J(E) \cdot S = A \cdot S \frac{E^2}{\phi} \exp\left(-B \frac{\phi^{3/2}}{E}\right) \quad 3-19$$

Where I is the tunneling current through the barrier, S is the emitting area, $E = \beta E_o$ is the local electric field (E_o is the applied electric field, $E_o = V/d$, V is the applied voltage and d is the gap dimension) and β is the field amplification factor. A and B are constants (When S , ϕ and E are expressed in cm^2 , eV , and V/cm , respectively, the constants A and B assume the values: $A = 1.54 \times 10^{-6} \text{ A.eV/V}^2$, $B = 6.83 \times 10^7 \text{ V}/(\text{cm} \cdot (\text{eV})^{3/2})$).

From equation (3.8):

$$\ln\left(\frac{J(E)}{E^2}\right) = \ln\left(\frac{A}{\phi}\right) - B \frac{\phi^{3/2}}{E} \quad 3-20$$

The FN plot, $\ln(J/E_o^2)$ vs $(1/E_o)$, yields a straight line, with a slope $(-\frac{B\phi^{3/2}}{\beta})$ and intercept $(\ln(A\beta^2/\phi))$. The slope can be used to evaluate the field enhancement factor.

3.5 Mechanism of Electrophoresis

Electrophoresis is the motion of dispersed particles relative to a fluid under the influence of a spatially uniform electric field. This electro kinetic phenomenon was observed for the first time in 1807 by Ferdinand Frederic Reuss (Moscow State University), who noticed that the application of a constant electric field caused clay particles dispersed in water to migrate. It is ultimately caused by the presence of a charged interface between the particle surface and the surrounding fluid.

Electrophoresis of positively charged particles (cations) is called cataphoresis, while electrophoresis of negatively charged particles (anions) is called anaphoresis.

MOTION BY ELECTROPHORESIS OF A CHARGED PARTICLE

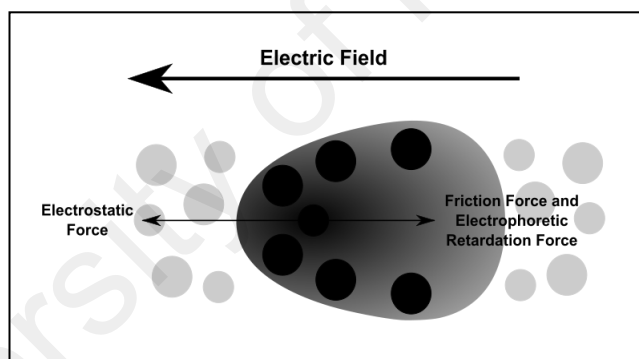


Figure 3.2: Illustration of electrophoresis.

An electric field surrounds electrically charged particles and time-varying magnetic fields. The electric field depicts the force exerted on other electrically charged objects by the electrically charged particle the field is surrounding.

The mechanism of electrophoresis on suspended particles had an electric surface charge, strongly affected by surface adsorbed species, on which an external electric field exerts an electrostatic Coulomb force. According to the double layer theory, all surface charges in fluids are screened by a diffuse layer of ions, which has the same absolute charge but opposite sign with respect to that of the surface charge. The electric field also exerts a force on the ions in the diffuse layer which has a direction opposite to that acting on the surface charge. This latter force is not actually applied to the particle, but to the ions in the diffuse layer located at some distance from the particle surface, and part of it is transferred all the way to the particle surface through viscous stress. This part of the force is also called electrophoretic retardation force. When the electric field is applied and the charged particle to be analyzed is at steady movement through the diffuse layer, the total resulting force is zero:

$$F_{tot} = 0 = F_{el} + F_f + F_{ret} \quad 3-11$$

Considering the drag on the moving particles due to the viscosity of the dispersant, in the case of low Reynolds number and moderate electric field strength E , the velocity of a dispersed particle v is simply proportional to the applied field, which leaves the electrophoretic mobility μ_e defined as:

$$\mu_e = \frac{v}{E}. \quad 3-12$$

The most known and widely used theory of electrophoresis was developed in 1903 by Smoluchowski.

$$\mu_e = \frac{\epsilon_r \epsilon_0 \zeta}{\eta} \quad 3-13$$

where ϵ_r is the dielectric constant of the dispersion medium, ϵ_0 is the permittivity of free space ($C^2 N^{-1} m^{-2}$), η is dynamic viscosity of the dispersion medium (Pa s), and ζ is the zeta potential (i.e., the electrokinetic potential of the slipping plane in the double layer).

The Smoluchowski theory is very powerful because it works for dispersed particles of any shape at any concentration. Unfortunately, it has limitations on its validity. It follows, for instance, from the fact that it does not include Debye length κ^{-1} . However, Debye length must be important for electrophoresis. Increasing the thickness of the double layer (DL) leads to removing point of retardation force further from the particle surface. The thicker DL, the smaller the retardation force must be.

Detailed theoretical analysis proved that the Smoluchowski theory is valid only for sufficiently thin DL, when particle radius a is much greater than the Debye length:

$$a\kappa \gg 1 \quad \text{3-14}$$

This model of "thin Double Layer" offers tremendous simplifications not only for electrophoresis theory but for many other electrokinetic theories. This model is valid for most aqueous systems because the Debye length is only a few nanometers there. It breaks only for nano-colloids in solution with ionic strength close to water.

The Smoluchowski theory also neglects contribution of surface conductivity. This is expressed in modern theory as condition of small Dukhin number:

$$Du \ll 1 \quad \text{3-15}$$

In the effort of expanding the range of validity of electrophoretic theories, the opposite asymptotic case was considered, when the Debye length is larger than the particle radius:

$$a\kappa < 1. \quad 3-16$$

Under this condition of a "thick Double Layer", Hückel predicted the following relation for the electrophoretic mobility:

$$\mu_e = \frac{2\varepsilon_r\varepsilon_0\zeta}{3\eta} \quad 3-17$$

This model can be useful for some nanoparticles and non-polar fluids, where Debye length is much larger than in the usual cases.

RETARDATION FORCE

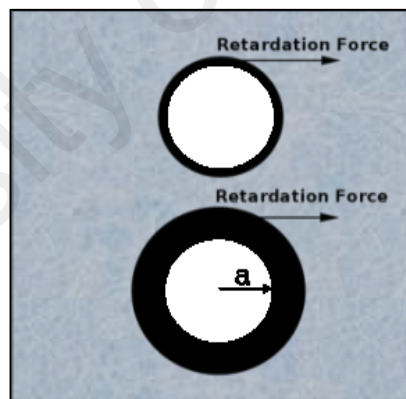


Figure 3.3: Illustration of electrophoresis retardation.

Retardation is the act or result of delaying; the extent to which anything is retarded or delayed, that which retards or delays.

3.6 Experimental Details

This part presents an overview of the experimental techniques and technological pathways used in this work to obtain MWCNT/PEO composites and fabricate samples with forms suitable for Field Electron Emission measurements. The instrumentation employed for the extraction and quantification of the emitted electrons are introduced.

Eventually, the MWCNT/PEO composites were analyzed for various properties using a variety of techniques, including Raman and TGA techniques. Various peaks of the composites by Fourier Transform Infra-red Spectrum (FTIR) technique and morphology of these samples by Field Electron Scanning Electron Microscopy (SEM) have been studied.

3.6.1 Fabrication of MWCNT/PEO composites

Specimens were made using MWCNT of 95% purity, >50 nm diameter and lengths between 10 and 15 μm were purchased from Chengdu Organic Chemicals Limited, China, and was used as received. Poly(ethylene oxide) (PEO), is white, hydrophilic powder has a typical M_v 1,000,000, was purchased from Sigma Aldrich. Sodium dodecyl sulfate (SDS) white powder designated for high quality chemical for laboratory use $\geq 99.0\%$, was from Sigma Aldrich as well.

The fabrication of the PEO/MWCNT composite was by the solution casting method. It was as follows:

- The MWCNT was dispersed ultrasonically using SDS solution. Typically 1wt% MWCNT was sonicated for 1 hour at 25 W to obtain stable suspension.
- Typically 1g PEO was dissolved in 50 ml D.I. water under ultrasonication.
- PEO/MWCNT solutions containing different masses of MWCNT were prepared. Each composite was thoroughly mixed, when it was subjected to ultrasonic agitation at 25 W for two hours.

Dispersion by ultra-sonication is a well-known technique for protecting the CNTs from their aggregated state. On the other hand wrapping nanotubes with, sodium dodecyl sulfate (SDS) anionic surfactant guarantees that tubes previously separated by sonication will not rejoin (O'connell, Bachilo et al. 2002).

Solutions with 5%, 15%, 25%, 33%, 40% and 50% loadings of MWCNT were fabricated. Then, two groups of MWCNT/PEO composite were fabricated:

Group 1 (Thin films): A small drop of each solution was spread on a one side mirror polished N-type Si (100) substrate with $5 \Omega\text{cm}^{-1}$ resistivity. The spread drop left to dry in air; forming thin film with typical dimension of 0.36 cm^2 surface area.

Group 2 (Thick films): - Each liquid composite was poured in a Petri dish and left for several days to dry in air and room temperature. Dried thick films of about $60 \mu\text{m}$ thickness were obtained and cut in rectangular shapes with surface areas between 0.13 and 0.32 cm^2 .

3.6.2 FEE measurement techniques

The Si substrates were previously cleaned with acetone in an ultrasonic cleaner for 30 min. The substrates were pasted to the cathode holder using silver paste. The diameter of the stainless steel anode is 1.5 cm, and the anode-cathode spacing can be adjusted using a micrometer in the range of 0 – 1 cm. In this work, the measuring gap is constituted by the sample as a cathode and a stainless steel as the anode was fixed to $100 \mu\text{m}$. A schematic diagram is presented in figure 3.4.

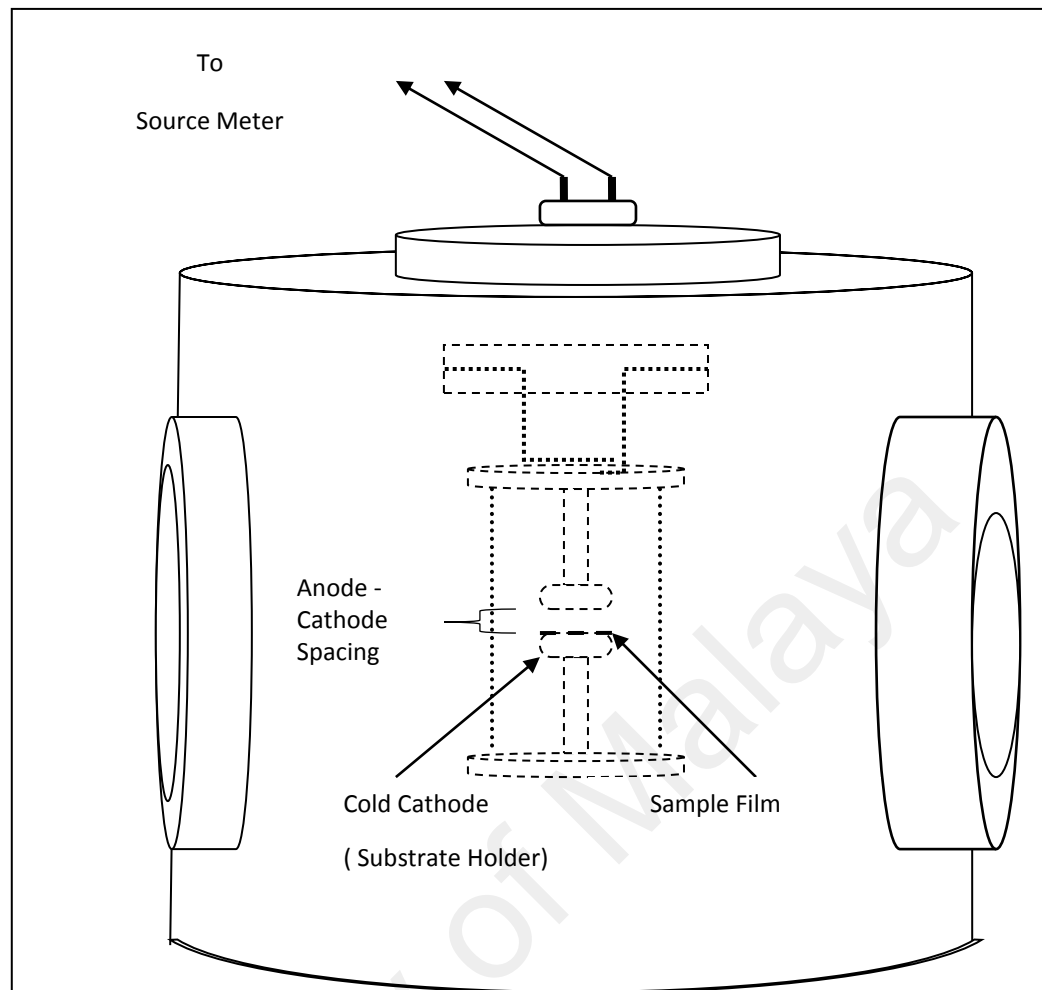


Figure 3.4: A schematic diagram of FEE chamber used in the experiments.

Electron field emission measurement from each prepared sample was conducted in 7.10^{-6} mbr atmosphere. The anode and sample were placed in a stainless steel vacuum chamber having about 9.5 cm maintained by a turbo pump. The instrument employed was a Keithley-Model 2410 high-voltage source meter. The data acquisition was performed using the Lab tracer 2.0 software. The field electron emission I - V curve and corresponding F-N plot could be obtained and displayed on the computer screen. The tension between the anode and the cathode was increased from 100 V to 1100 V in 100 V steps. Then, the graphs were analyzed and data was extracted using Fowler-Nordheim equation. The error analysis for the determination of threshold and turn-on fields and the field enhancement factor, β , is given in Appendix A.

3.7 Electrophoresis deposition and characterization of MWCNT/ZnO and MWCNT/ TiO₂ hybrid films

2.5 g ZnO and TiO₂ were ball milled in DI water for 4 hours to reduce the particulate size. The suspensions of the metal oxide were centrifuged for 30 minutes at 1000 rpm to separate large particles. The MWCNTs of about 30 nm diameter and 10-30 μm in length were added to the metal oxide suspension the desired mass ratio. The mixtures were vigorously stirred for 1 hour. After that the suspensions were used for electrophoresis deposition on silver substrates. Silver was chosen to minimize the formation of substrate material oxides and corrosion. Deposition was conducted in using parallel plate silver electrodes. The length of the 1 cm wide electrodes immerse in the suspension were about 2 cm. A constant dc voltage of about 20 V was applied to the electrodes which was separated at about 1 cm. Different thickness of MWCNT/ZnO and MWCNT/TiO₂ films were deposited on the surface of the anode by varying the deposition time at 1, 2 and 3 mins. Figure 3.5 shows an example of films produced at a 3 minute deposition run.

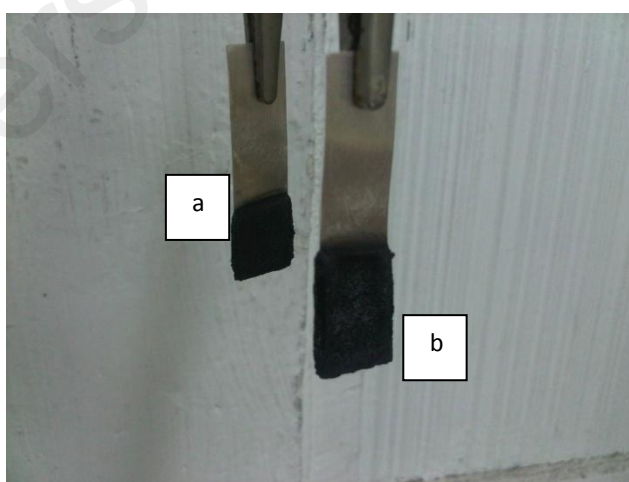


Figure 3.5: Composites of (a) CNT/ZnO and (b) CNT/TiO₂.

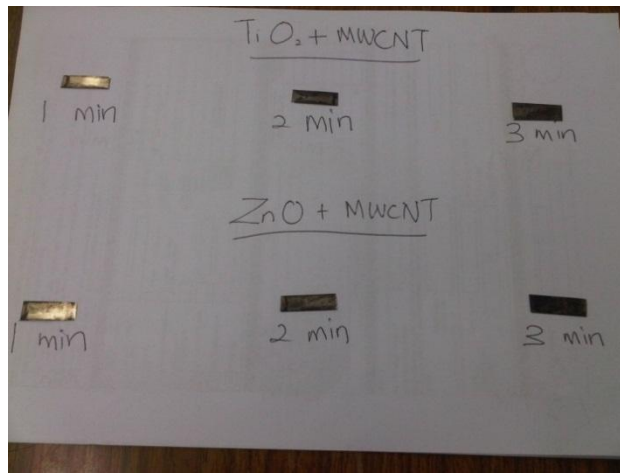


Figure 3.6: The samples of CNT/ZnO and CNT/TiO₂ for 1 minute, 2 minutes and 3 minutes respectively.

The films were analyzed using FESEM, EDX and Raman spectroscopy and were used as cathodes in field electron emission studies.

Field electron emission measurements was done in a vacuum of less than 10^{-7} mbar using a diode configuration (Figure 3.8). The oxide-MWCNT hybrid samples were mount at the earthed cathode. The dimension of the cathode was 5 mm x 5 mm measured using a caliper micrometer and the inter-electrode spacing was set at 100 μm , adjusted using a micrometer screw gauge with a resolution of 10 μm . The IV characteristics (Figure 3.9) of the emission current was measured using a source meter unit (Keithley 2410 SMU) that can deliver a voltage of up to 1100 V while simultaneously measuring the current. Initial measurement gave unstable results as shown in Figure 3.10 where effects of small MWCNT protrusions in the sample caused current instabilities. This was overcome by a burnt out process where the cathode was allowed to emit current while under a bias of 1000 V for an hour. This will cause the small protrusions to be burnt away resulting in a more stable IV curves as shown in Figure 3.11.

3.8 Experimental Results

Thin and thick films characterization and FEE Characteristics

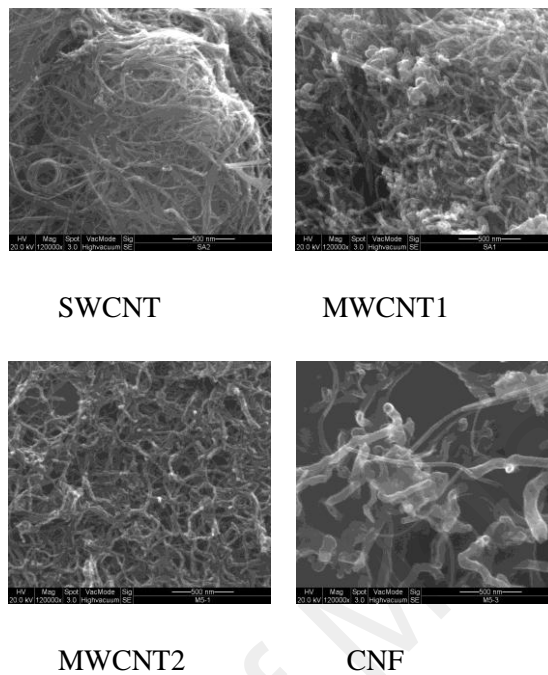


Figure 3.7: SEM images of films sintered in argon.

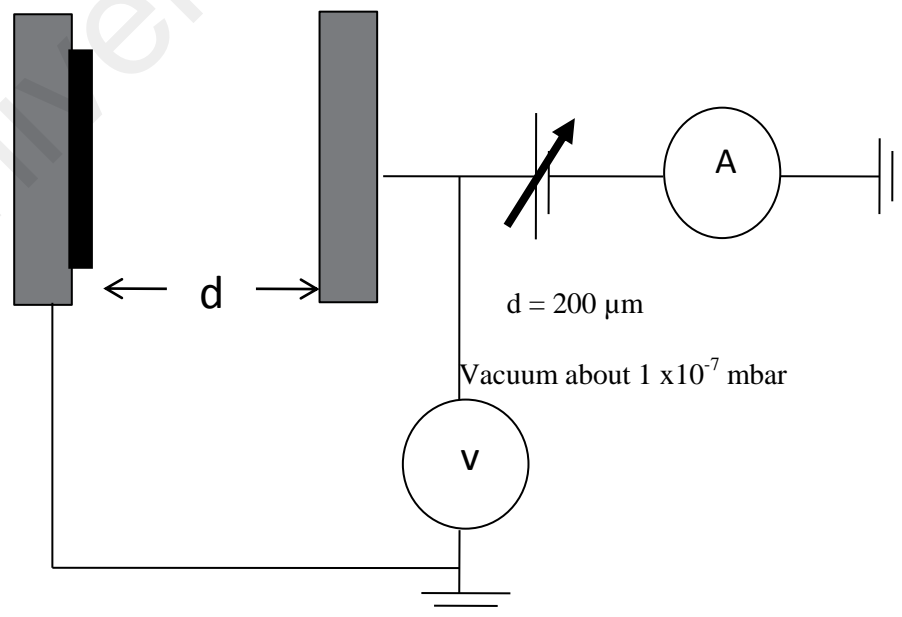


Figure 3.8: Field electron emission measurements.

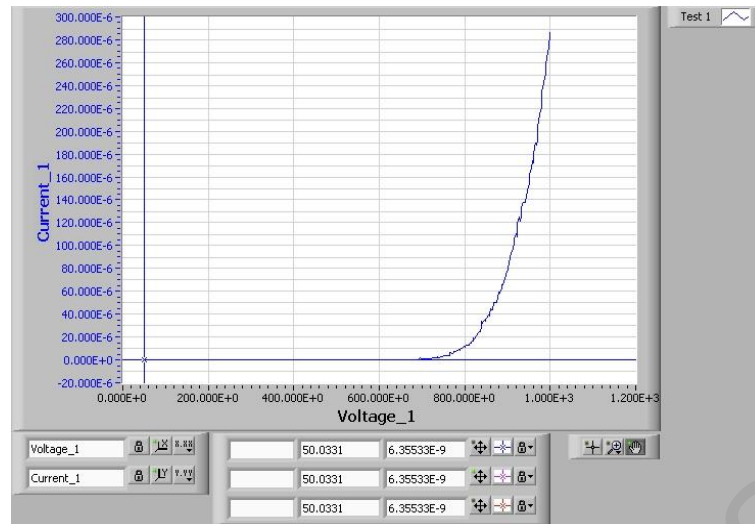


Figure 3.9: The stability of IV curve.

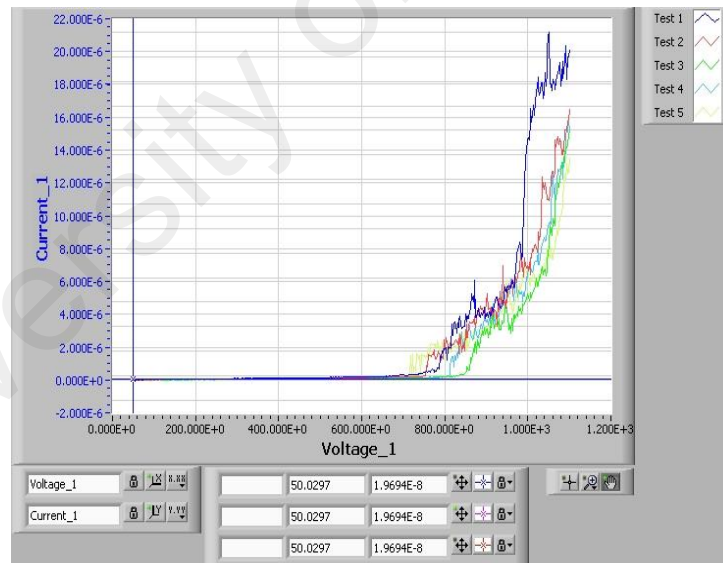


Figure 3.10: The effect of burn out process (Initial measurements from fresh sample).

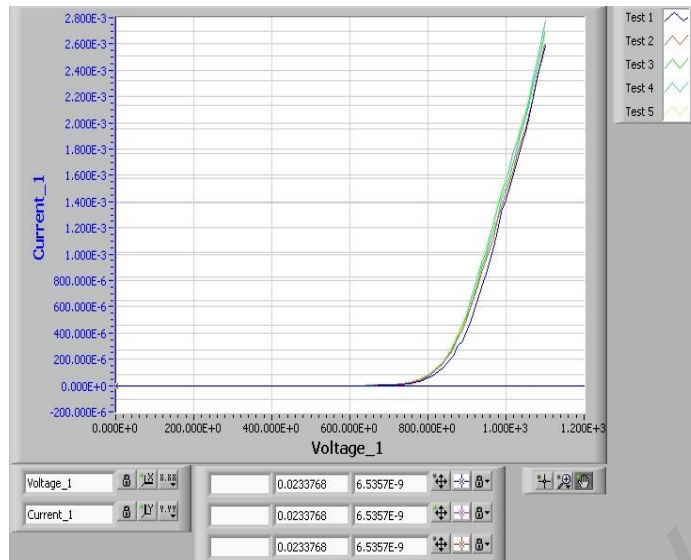


Figure 3.11: The effect of burn out process after continuous run at 1 kV and 30 minutes.

3.8.1 Thin films characterization

Figure 3.12 shows the Raman spectra for PEO/MWCNT thin films before FEE measurement (figure 3.12(a)) and after FEE measurement (figure 3.12(b)). The pattern of Raman scattering for MWCNT is analogous for the single-walled CNT (Ritter, Scharff et al. 2006). The first two lowermost curves in figure 3.8(a) show the PEO and SDS row materials spectra. Several number of peaks are present, two characteristic vibrational modes linked to PEO, a skeletal (C-O) stretching vibration band at around 848 cm^{-1} and a disordered longitudinal acoustic mode at 365 cm^{-1} region. The Raman spectra at around 304 cm^{-1} , 523 cm^{-1} and 964 cm^{-1} are relevant to Si, substrate (Zdrojek, Gebicki et al. 2004). The third trace in figure 3.12(a) shows the spectrum obtained from composite sample with 5% MWCNT loading, the D, G and G' peaks are present in addition to C-H stretching bands of PEO between 2800 and 3000 cm^{-1} , their intensities are lower than the G' band intensity. The fourth trace in figure 3.12(a) shows the spectrum of 15% MWCNT loading, it shows the same features as 5% with a lower

intensity in C-H stretching bands. The same thing can be said for 15%, 25%, 33% and 40% where the C-H bands have lower intensities compared to G' whenever the carbon portion increases; except for 50% which could be related to the high presence of SDS in the spot since it has a strong peak in the same position. The gradual depletion of the polymer with the increment of MWCNT concludes the well dispersion of the prepared composites. This result is emphasized by SEM micrographs.

Eventhough, it was mentionned that the RBM mode is hard to be seen in MWCNTs since the RBM signal from large diameter tubes is usually too weak to be observable and the ensemble average of inner tube diameter broadens the signal (Dresselhaus, Dresselhaus et al. 2005, Costa, Borowiak-Palen et al. 2008), a low peak is observed around 116 cm^{-1} we believe that is illustrating the RBM band from the inner layers in all MWCNT samples. Three peaks are related to MWCNTs at 1338.8 cm^{-1} , 2677.7 cm^{-1} and at 1571.7 cm^{-1} are defect band peak D-band peak, first overtone of it (G' band peak) and the G-band peak respectively. G-band frequencies have up shifted from 1571.7 to 1580.04 (15%) and above in all composites. The shifting of the G band peak to higher frequencies can be explained by the disentanglement of the MWCNTs and subsequent dispersion in the PEO matrix as a consequence of polymer penetration and interaction with the MWCNT bundles during ultra sonication. An up-shifting of the G band, was reported for SWCNT reinforced epoxy resins and polypropylene (McNally, Pötschke et al. 2005).

Most of the composites present a D-peak at about 1347.2 cm^{-1} or insignificantly higher. Thus this peak has up-shifted by 8.4 cm^{-1} from what it was in the MWCNTs. The up-shifting of the D and G bands is a consequence of strong compressive forces associated with PEO chains on MWCNT (McNally, Pötschke et al. 2005). In this experiment, the ratio I_D/I_G was found to be 0.55 for the MWCNTs. This ratio has increased after samples preparation in all composites except for 33% loading.

The high disorder is related to the influence of the ultrasonication as well as the nanotubes-matrix interaction. The gradual depletion of the polymer with the increment of MWCNT in addition to the augmentation of defects in the tubes, concludes the well dispersion of the prepared composites. This result is emphasized by SEM micrographs.

University of Malaya

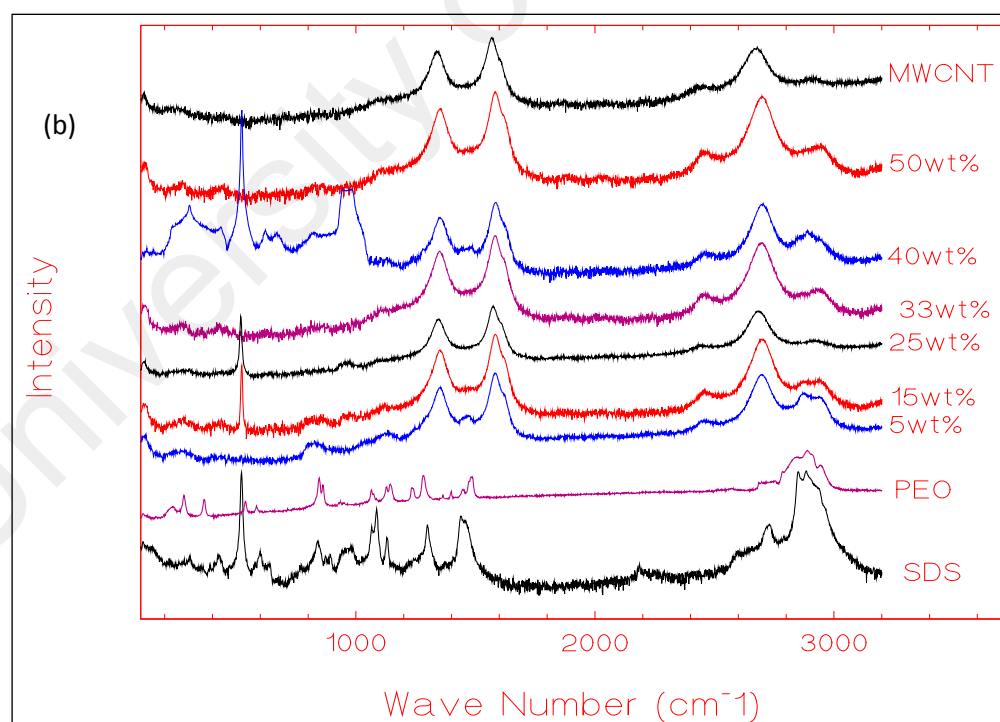
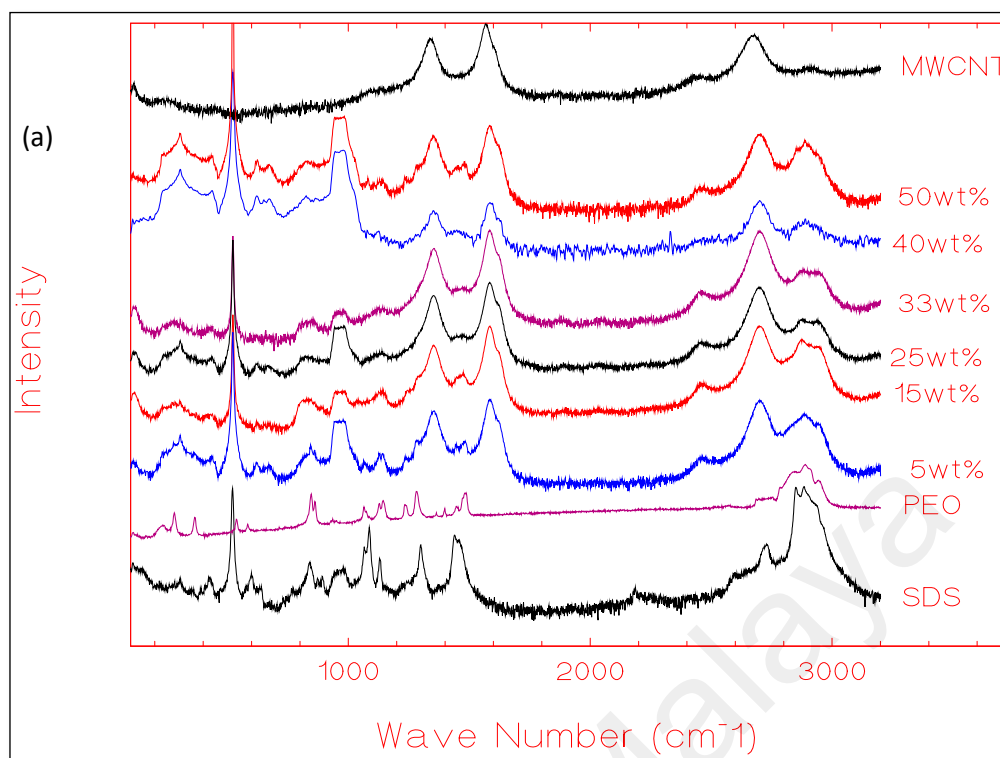
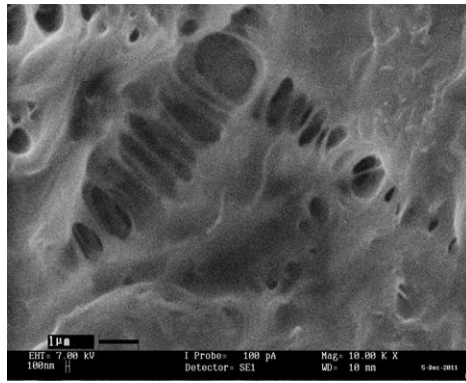


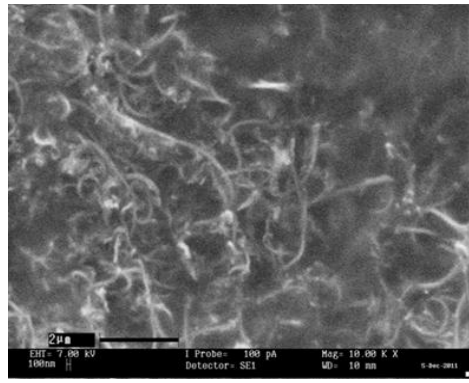
Figure 3.12: Raman spectroscopy of MWCNT/PEO thin films. (a) Before FEE measurements (b) After FEE measurements.

After FEE measurement (figure 3.12 (b)), almost the same band features with the same characteristics were obtained. However, the C-H stretching bands of PEO between 2800 and 3000 cm^{-1} decrement with the increment of the MWCNT loading is partially disrupted. The range within 1000 cm^{-1} after FEE test is smoother as the majority of peaks have disappeared. An up shift of G-band frequency from 1580.04 to 1588.36 for 15wt% composite after exposed to the FEE test. Whereas the rest of the thin films showed a down-shift, for instance 1588.36 band became 1582.33 in 40wt% filler. Some of the composites had D-band shift to lower frequencies, whereas others to higher. The I_D/I_G ratio was reduced after the FEE test in five out of six samples, where the majority of the films after the field emission measurement, showed a better quality of nanotubes than the MWCNT used. We relate the changes in Raman spectra after FEE measurement to the influence of low pressure and high voltage which induced out gassing and evaporation of the radicals produced.

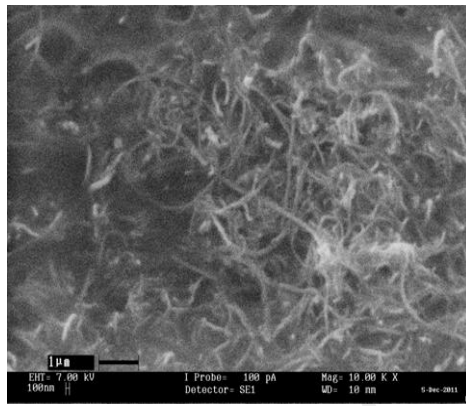
Figure 3.13 (a)-(f) depicts SEM micrographs of the six composites (5%, 15%, 25%, 33%, 40% and 50%) MWCNT/PEO thin films respectively. Figure 3.9 (a) has a smooth surface, which is expected since 95% of the mixture is PEO, it reveals pores with size reaching to almost 8 μm . Figure 3.9(b) shows a rougher surface with the nanotubes well dispersed in the matrix. Figure 3.9(c)-(e), illustrates rough surfaces with more compacted nanotubes whenever the concentration increases. The MWCNTs seem to be well wetted by the PEO. This suggests good adhesion and dispersion of the filler in the polymer. No aggregation formation in the MWCNT/PEO nanocomposites, could also be indicative of the effects of functionalization on the enhancements of the CNT compatibility to PEO matrix (Liu, Chang et al. 2008). TGA and Raman implied a good adhesion as well.



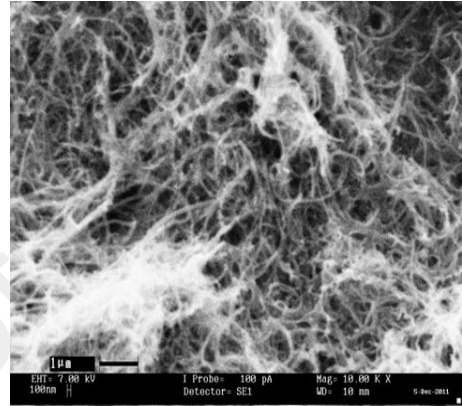
(a)



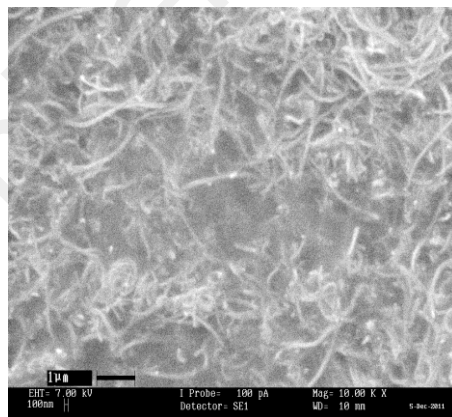
(b)



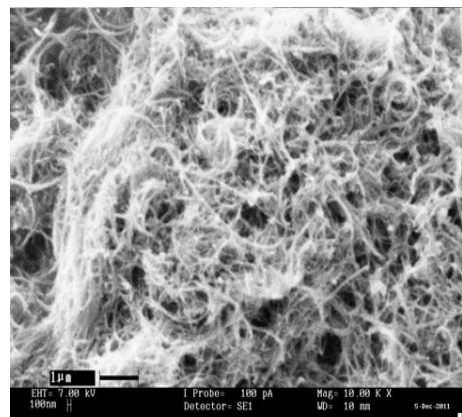
(c)



(d)



(e)



(f)

Figure 3.13: SEM micrographs of the six thin films composites (a)5%, (b) 15%, (c) 25%, (d) 33%, (e) 40% and (f) 50% MWCNT/PEO thin films.

The sizes of the nanotubes seem to be in the range of 50 nm-100 nm. The bright dots such as shown in figure 3.13(c), are the ends of broken carbon nanotubes. This phenomenon was reported before and related either to composite method of preparation or to nanotube chemical modification (Zaragoza-Contreras, Lozano-Rodríguez et al. 2009). In figure 3.13(f) corresponding 50%, some MWCNT agglomerates can be seen as not all the bundles were dispersed.

3.8.2 Thin Films Field Electron Emission

The typical field electron emission J - E curves and the corresponding Fowler-Nordheim plot for 5%, 15%, 25%, 33%, 40% and 50% loading MWCNT/PEO thin films are illustrated in figures 3.14 and 3.15.

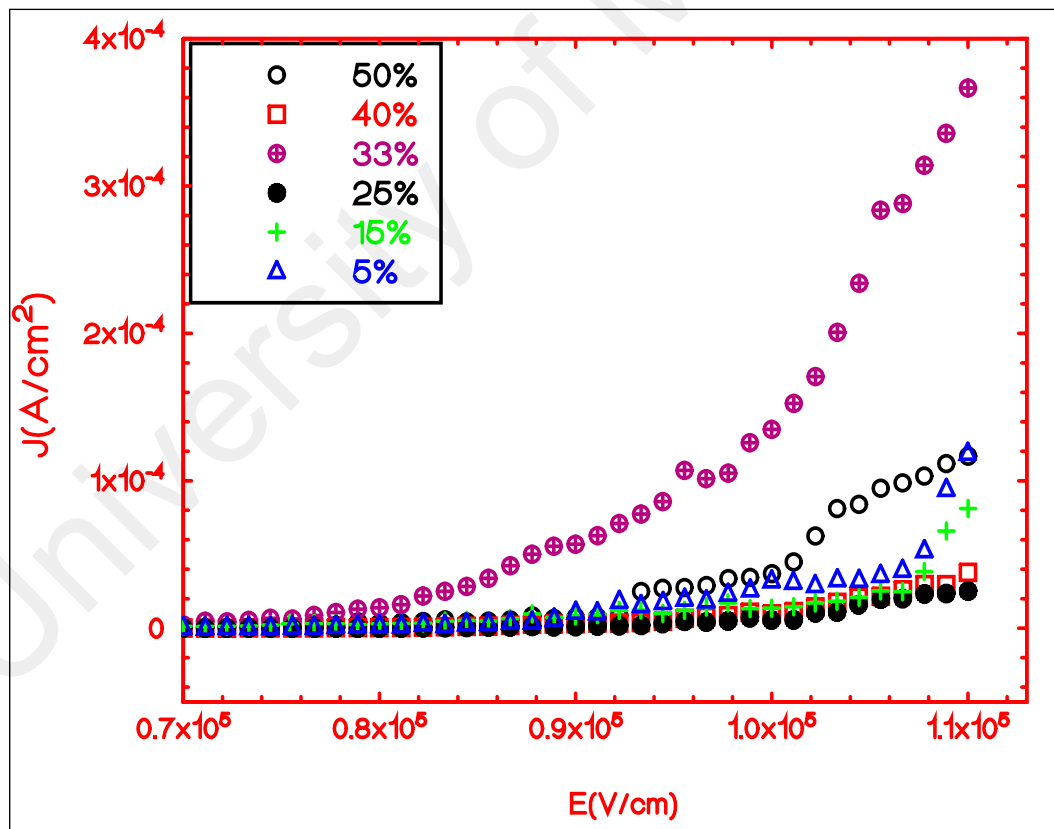


Figure 3.14: Current density versus the electric field applied for the thin films with different MWCNTs weight concentrations.

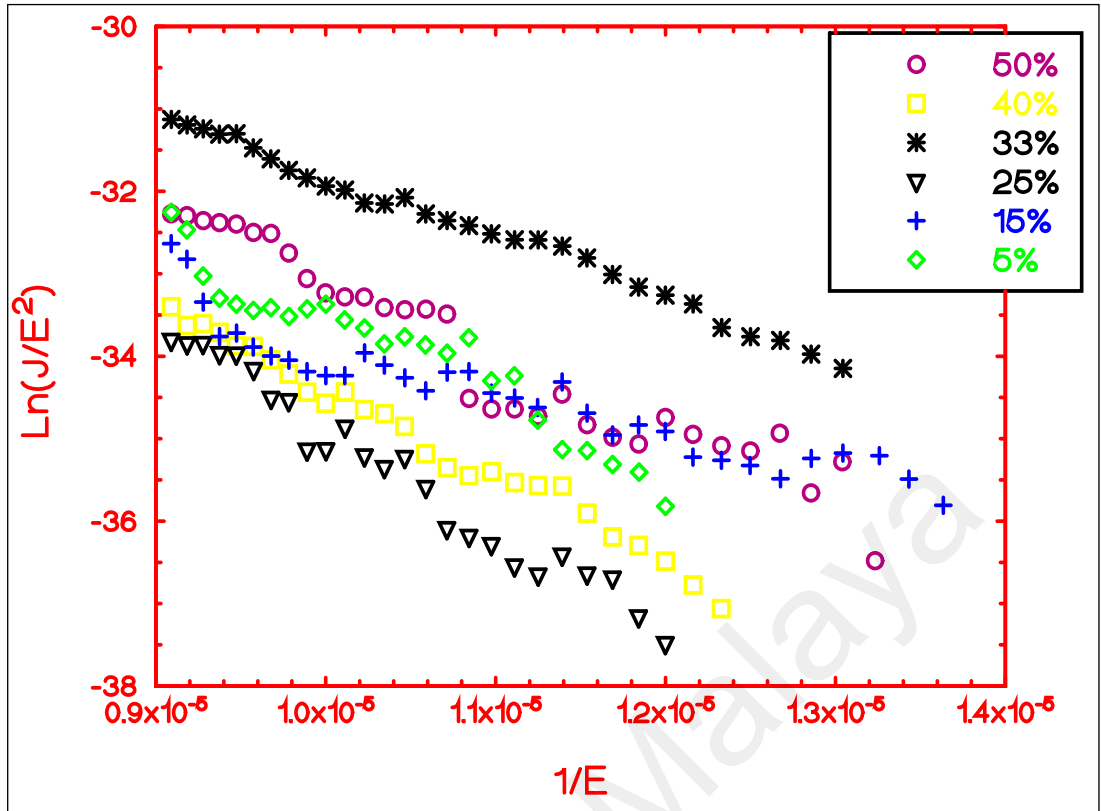


Figure 3.15: Fowler- Nordheim plot for the thin films with different MWCNTs weight concentrations.

The turn-on field and threshold fields are usually reported for electron emitters, which are defined as the macroscopic fields needed to extract current densities respectively of $10 \mu\text{A}\cdot\text{cm}^{-2}$ and $10 \text{mA}\cdot\text{cm}^{-2}$ (which are the current densities required to light or saturate a pixel in a display). Since the current densities in our data did not cover $10\text{mA}\cdot\text{cm}^{-2}$ range, we defined here the turn-on field as the applied field at an emission current density of $0.1\text{mA}\cdot\text{cm}^{-2}$.

The turn on field (defined here as the applied field at an emission current density of $10 \mu\text{A}\cdot\text{cm}^{-2}$), the threshold field (defined here as the applied field at an emission current density of $0.1\text{mA}/\text{cm}^{-2}$), and the field enhancement factor (β) which was derived from the F-N plot slope assuming a work function of 5 eV, the enhancement factor is proportional to $\phi^{3/2}$. However, its impact remains small enough when the ϕ value is in the range 4-5 eV are stated in table 3.2.

Table 3.2: Characteristics of field emission of PEO/MWCNT composites thin films.

Thin films wt. %	Turn on field (V/ μm) ($10 \mu\text{A. cm}^{-2}$)	Threshold field (V/ μm) (0.1mA.cm^{-2})	$\hat{\alpha}$
5%	8.99 \pm 1.35	10.91 \pm 1.64	786 \pm 120
15%	9.25 \pm 1.39	/	1509 \pm 226
25%	10.21 \pm 1.53	/	601 \pm 90
33%	7.66 \pm 1.15	9.72 \pm 1.46	1037 \pm 160
40%	9.97 \pm 1.50	/	727 \pm 110
50%	9.25 \pm 1.39	10.71 \pm 1.61	853 \pm 130

From the results, we found that the composite with 33wt% displayed the lowest turn on field 7.66 V/ μm with the highest current density of 0.36 mAcm⁻². The approximately linear behavior of the F-N curves confirm that the observed current is generated by field emitted electrons. Deviations from Fowler–Nordheim behavior are usually attributed to space-charge effects which induce a diminution of the F–N slope (Bonard, Croci et al. 2002).

Figure 3.16 illustrates the enhancement factors versus CNT portion in the six composites. It is obvious that there is a non-linear relationship between the FEE properties of the devices and the increasing MWCNT filler loading fractions, which can be attributed to the non-homogeneous dispersion of MWCNTs within polymer matrices, in addition to the surface morphology and the work function of the different composites prepared. A study on field emission characteristics of polymer-based MWCNT–PMMA composite for application to a flexible substrate; showed a certain degree of linearity with polymer ratio. As the PMMA ratio increased from 0.3 to 2.4, the turn-on field

(defined as the electric field for a current density of $10 \mu\text{A}/\text{cm}^2$) gradually decreased from 1.54 to $1.20 \text{ V}/\mu\text{m}$. The value of β gradually increased from 1892 to 2216.

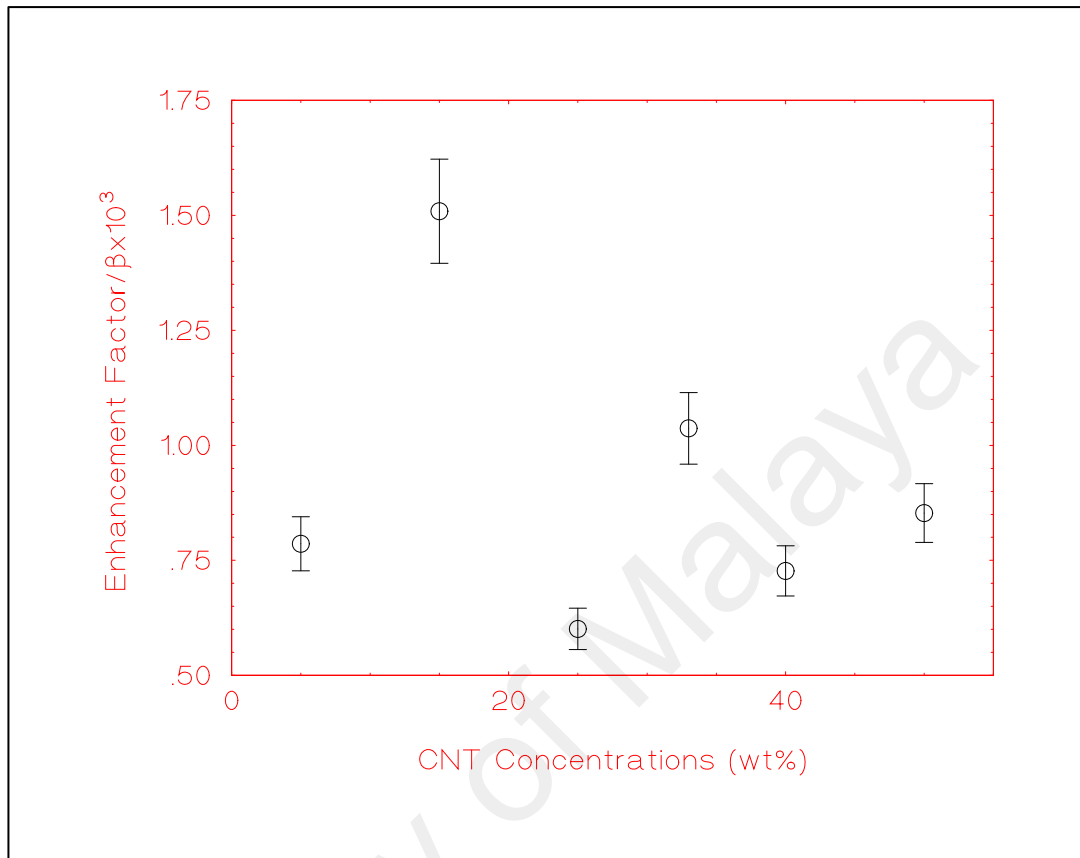


Figure 3.16: Enhancement factors of the thin films with different MWCNTs weight concentrations.

Field emission properties of CNTs are greatly influenced by the geometry and characteristics of microstructures present on the surface, adsorption of gas atoms on the surface and geometry of the nanostructures are the key factors influencing the emission.

It is difficult to have a direct comparison of our results with other reported in past, this is due to the fact that, different preparation and measurement techniques were used. However, it is preferable to have an overview of other emitters characteristics. In previous studies, the turn-on and the threshold fields (field needed to produce a current density $10 \mu\text{A cm}^{-2}$ and 10 mA cm^{-2}) were found to be typically, $E_{\text{to}} = 2.6 \text{ V}/\mu\text{m}$, $E_{\text{th}} =$

4.6 V/ μm in MWCNT films and in the range $E_{\text{to}} = 1.5\text{--}4.5$ V/ μm and $E_{\text{th}} = 3.9\text{--}7.8$ V/ μm regarding SWCNT films (Bonard, Salvetat et al. 1998).

Diamond films synthesized using 1% CH₄ can be turned on at 20 V/ μm and the emission current reached 0.12 μA at 26 V/ μm . However, with the increase of methane concentration, the field electron emission performances of diamond films were improved (Lu 2006). A DWCNT film on ITO substrate, showed turn-on field, threshold field enhancement factor β at about 0.8 V/ μm , 1.8 V/ μm and 1715 respectively. Here, the turn-on field and threshold field are defined as the fields at which the emission current density reaches 1 nA/cm² and 1 $\mu\text{A}/\text{cm}^2$, respectively (Somani, Somani et al. 2007). Another study on InGaN nanowires fabricated by chemical vapor deposition. The InGaN nanowires had a turn-on electric field of 10 V/ μm at a current density of 2.83 $\mu\text{A}/\text{cm}^2$ and a high field emission current density of 2.9 mA/cm² at an applied field of about 24 V/ μm (Ye, Cai et al. 2007).

The stability of the field emission can be evaluated by monitoring the evolution of total emission current at a fixed electric field. In the 2000 s (~34min) current stability test where the voltage was set to a constant for each sample and the correspondent current intensity is depicted. The result in figure 3.17 shows that current of 50%, 15% and 25% have a good stability, except for some slight fluctuations in the first quarter of the time period. The sample with 40%wt had a current intensity jump from 28 μA to 39 μA after 30 min, which most probably was the result of gas desorption. Generally, all the samples exhibited a satisfaction in stability.

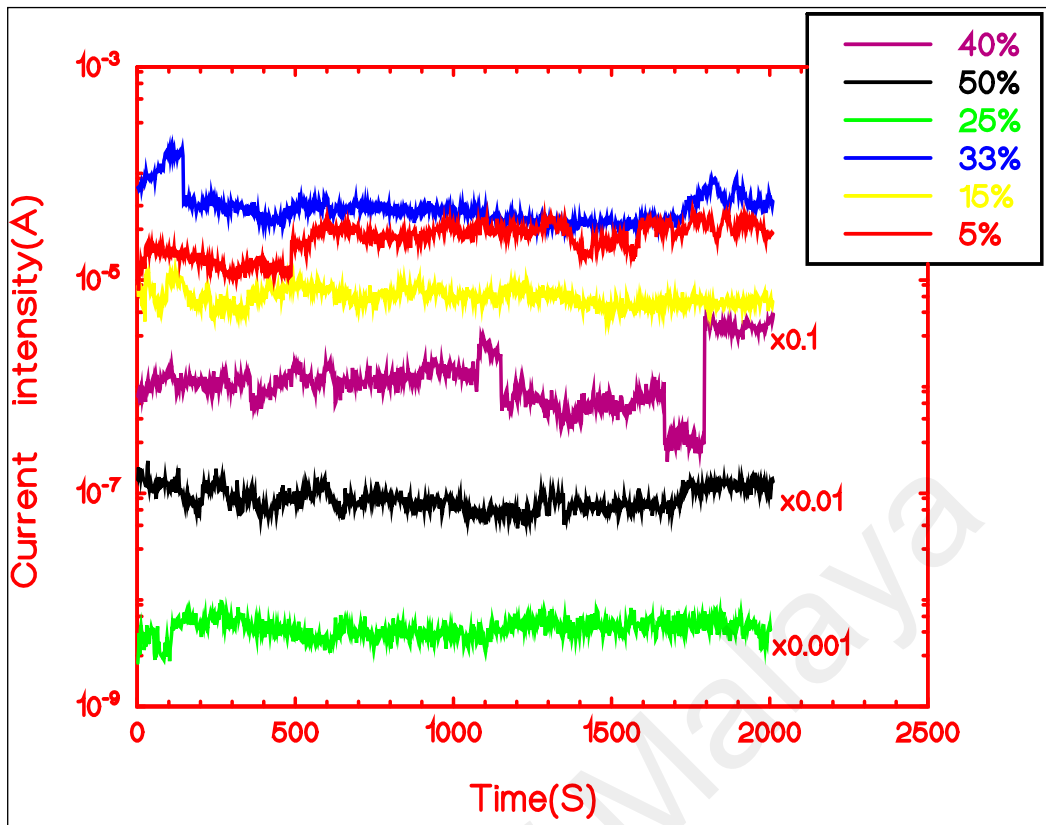


Figure 3.17: Current stability in about 34 min period time for the thin films with different MWCNTs weight concentrations.

The 15% composite provided the greatest enhancement factor of 1509. The measurement of the current density versus the electric field of the latest sample, for before and after the stability test of 2000 s (~ 34 min) time is plotted in figure 3.18.

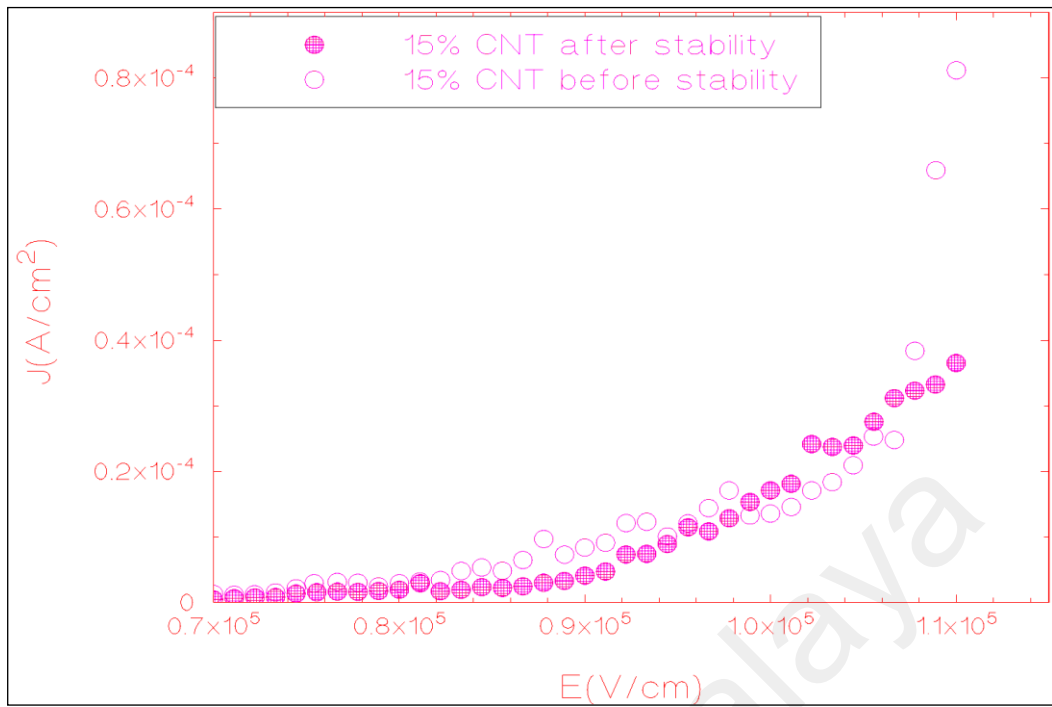


Figure 3.18: Current density versus applied electric field for before and after stability test of 15% MWCNT/PEO thin film.

It is obvious that the yield of the current density was affected and decreased from to $81 \mu\text{A}/\text{cm}^2$ to $36 \mu\text{A}/\text{cm}^2$ stability test. On the other hand, the turn on field has slightly increased from $9.25 \text{ V}/\mu\text{m}$ to $9.54 \text{ V}/\mu\text{m}$ whereas the threshold of $0.1 \text{ mA}/\text{cm}^2$ was not reached, neither before nor after the stability test. We conclude that The strong electrostatic force exerted during the emission and the local Joule heating produced, in addition to the low pressure, have partially deteriorated the function of the emitter primarily through ion bombardment.

3.8.3 Thick films characterization

Figure 3.19 shows the raman spectra for PEO/MWCNT field electron emitter thick film composites before electrons extraction (figure 3.19(a)) and after electrons extraction (figure 3.19(b)). In figure 3.19(a) the uppermost plot obtained from pure MWCNT used in fabricating the composites, showed the typical spectrum for MWCNT. The three distinct peaks attributed to the D-line at about 1338.8 cm^{-1} , the G-line at 1571.7 cm^{-1} and the G'-line at 2677.7 cm^{-1} are clearly visible.

The second trace in figure 3.19(a) shows the spectrum obtained from composite sample with 50% MWCNT loading. The D, G and G' peaks are present in addition to C-H stretching bands of PEO, their intensities are much lower than the G' band intensity. The third trace in figure 3.19(a) shows the spectrum of 40% MWCNT loading, it shows the same features as 50% with a higher intensities in C-H stretching bands. The same thing can be said for 33%, 25%, 15% and 5% where the C-H bands have higher intensities compared to G' whenever the carbon portion was less, except for 25%. PEO skeletal vibrations between 400 and 1500 cm^{-1} and far infrared region below 400 cm^{-1} appear clearly in the low loading samples, with reduced intensities when the MWCNTs goes higher.

The G-peak has up-shifted in all prepared thick films, this shifting was as high as 16.66 cm^{-1} in 40% and 50% composites. The same thing can be said for the D-band, where all the band have up-shifted whether to 1355.51 cm^{-1} or 1357.19 cm^{-1} . Thus, the dispersion and the interaction of the polymer, filler is achieved. In addition, a strong compressive force is exerted on the nanotubes, is inferred from D and G bands up-shifting. Interestingly, I_D/I_G ratios slightly changed to higher values in 5%, 10% and 15% loading in the thick films after preparation, whereas the rest showed a significant decrease compared to I_D/I_G of raw MWCNTs. Probably, the radicals and the dangling bonds produced in the low concentration composites have reacted with polymer molecules since their portions are much higher.

After FEE measurement in the thick films figure 3.19(b), the same band features with slight characteristics differences were obtained. However, the spectra appear smoother than before FEE measurement. Particularly in 5% and 40% loadings, which presented a very few peaks. In the rest of the composites, the decrement of PEO C-H stretching bands intensities compared to G' bands whenever the MWCNTs concentration is elevated was almost verified. Four G-band frequencies were observed

in the composites; 1580 cm^{-1} in all the thick films after FEE test except for 5wt%, which had a peak at 1588.3 cm^{-1} . Thus indicates a G-band down-shift in 5%, 40% and 50% composites reached to 8 cm^{-1} in the latest two samples. Meanwhile no change in this band was recorded for the other composites. D-band showed a down-shift in three out of the six samples (5%, 25%, 33%), no change in two (40%, 50%) and a slight increase in one composite (5%). The D and G bands down shifting infer that less compressive force is exerted on the carbon tubes after exposure to FEE measurement. We relate the down shifting of the bands to the evaporation of the cathode material (prepared composites) to the anode side during exposure to high voltage, low pressure.

All the thick films exhibited higher disorder after the FEE measurement, except for 25% film. For instance, 5% and 40% increased from 0.56 to 0.87 and from 0.52 to 0.64 respectively. This indicates the influence of the high voltage and the heat accompanied on the morphology of the prepared samples.

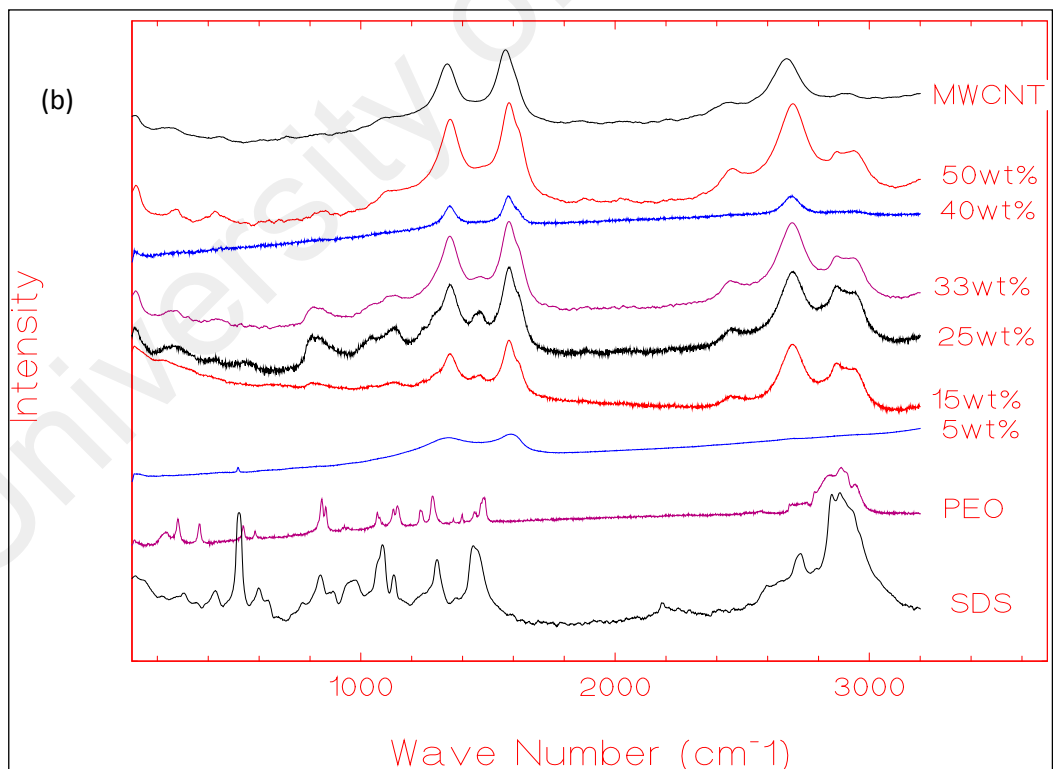
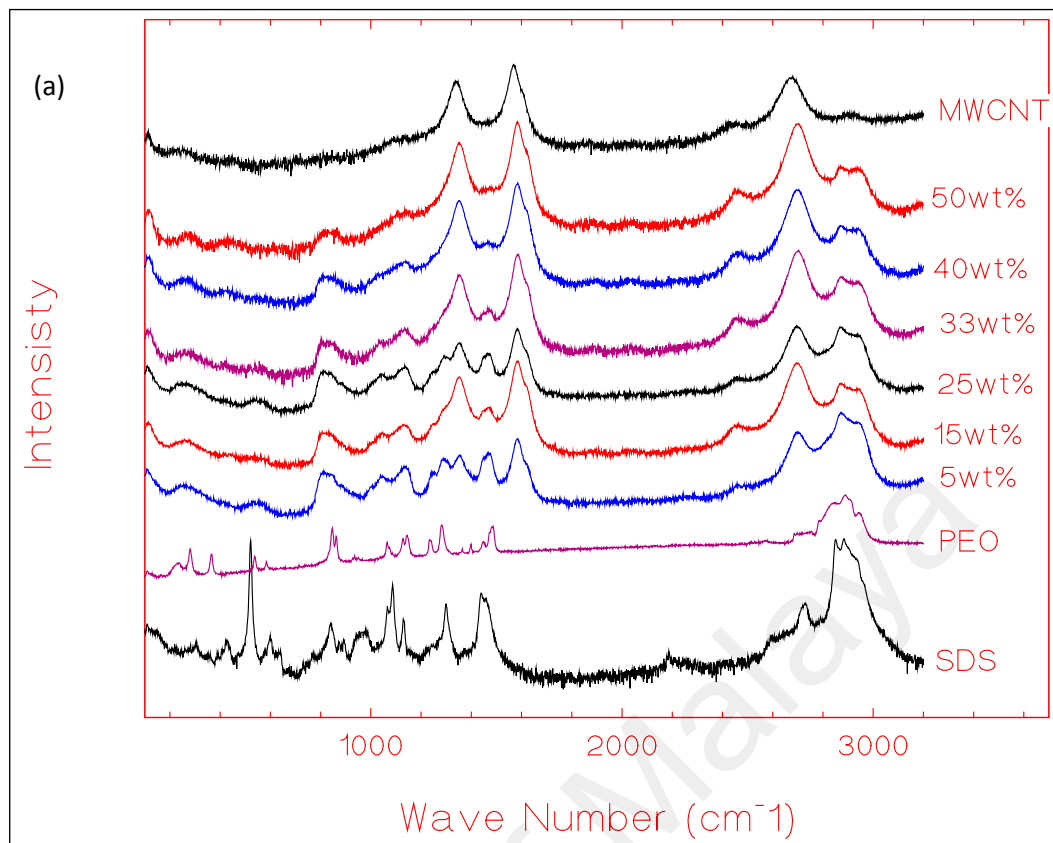
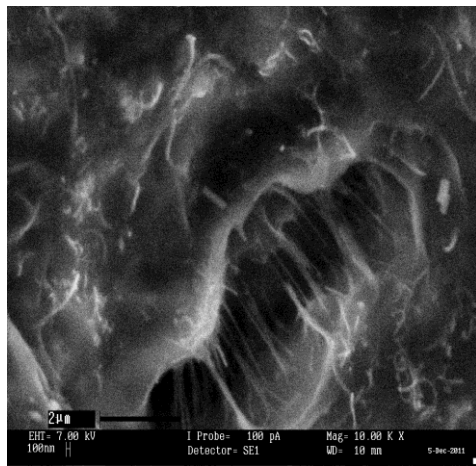
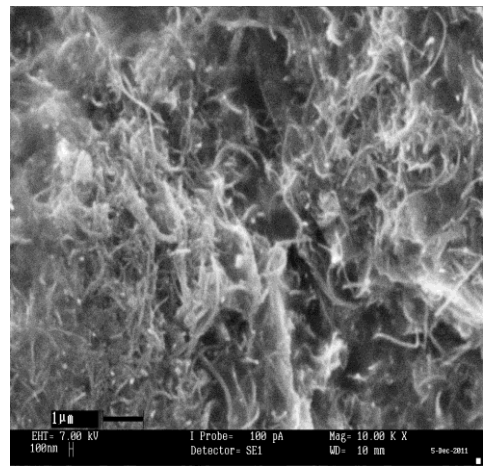


Figure 3.19: Raman spectroscopy of MWCNT/PEO thick films. (a) Before FEE measurements. (b) After FEE measurements.

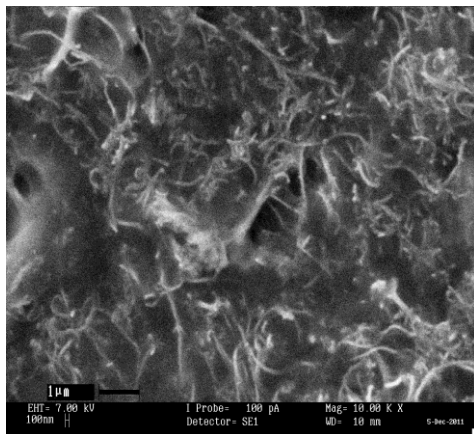
SEM micrographs 5%, 15%, 25%, 33%, 40% and 50% composites, respectively are shown in figure 3.20 (a)-(f). 5% MWCNT/PEO micrograph has a smooth surface and reveals pores about 8 μm long and 2 μm width. Figure 3.20 (b) shows a rougher surface with the nanotubes well dispersed in the matrix. The pores in 15% are smaller compared to 5% composite. Figure 3.20 (c)-(e), illustrates rough surfaces with more compacted nanotubes whenever the concentration increases. Figure 3.20 (f), corresponding to 50%, some MWCNT agglomerates can be found in the PEO matrix resulted from the van der Waals interaction. Apparently, in 50% the CNTs could not be wrapped perfectly and totally, due to the high quantity of CNTs. Generally the SEM micrographs indicate that a well and homogeneous dispersion was achieved. This result is reinforced by Raman and TGA analysis. The dispersion of MWNTs in polymer is one of the most important topics for fabricating high performance MWNTs/polymer composites. A homogeneous dispersion of MWNTs and strong interfacial interactions between polymer matrix and nanotubes can effectively improve the mechanical, electrical, and thermal properties of polymer composites (Xu, Niu et al. 2010).



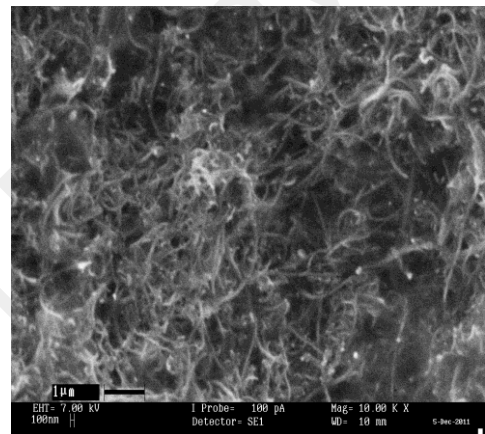
(a)



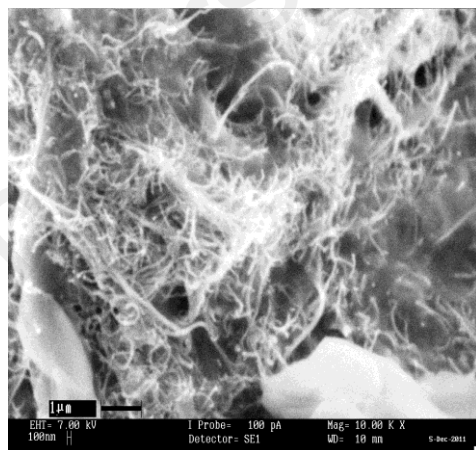
(b)



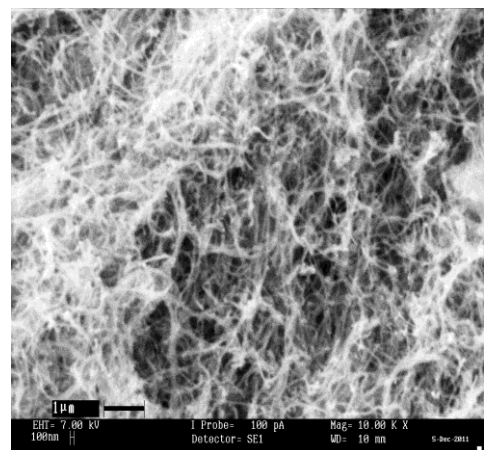
(c)



(d)



(e)



(f)

Figure 3.20: SEM micrographs of the six thick films composites (a)5%, (b) 15%, (c) 25%, (d) 33%, (e) 40% and (f) 50% MWCNT/PEO thin films.

Figure 3.21 shows the TG curves of the pure PEO and (5%, 15%, 25%, 33%, 40% and 50%) MWCNT/PEO composites. In the PEO curve, the mass initially remained constant, up to 334°C, then turned and decreased abruptly. The pure PEO (see figure. 3.18) started an abrupt degradation at about 335°C and lost 95.5% of its weight at 401 °C, the DTG curve displayed a sharp intensive and symmetric peak at 346°C. Thus the decomposition of the polymer appeared in only one stage.

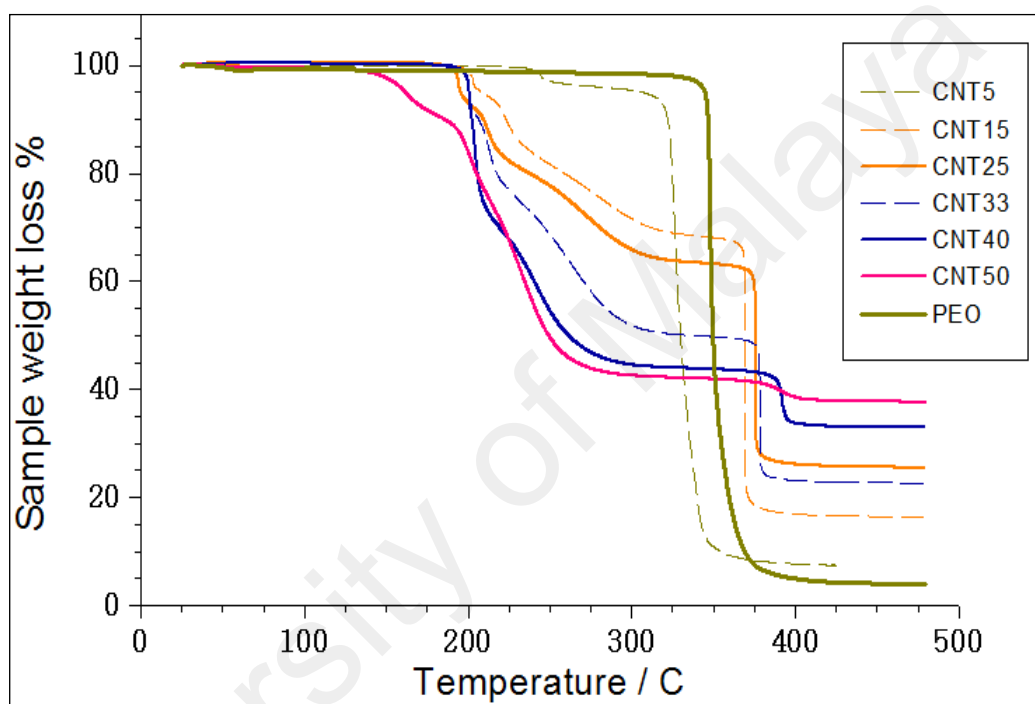


Figure 3.21: TG curves of the pure PEO and 5wt%, 15wt%, 25wt%, 33wt%, 40wt% and 50 wt% of MWCNT/PEO composites.

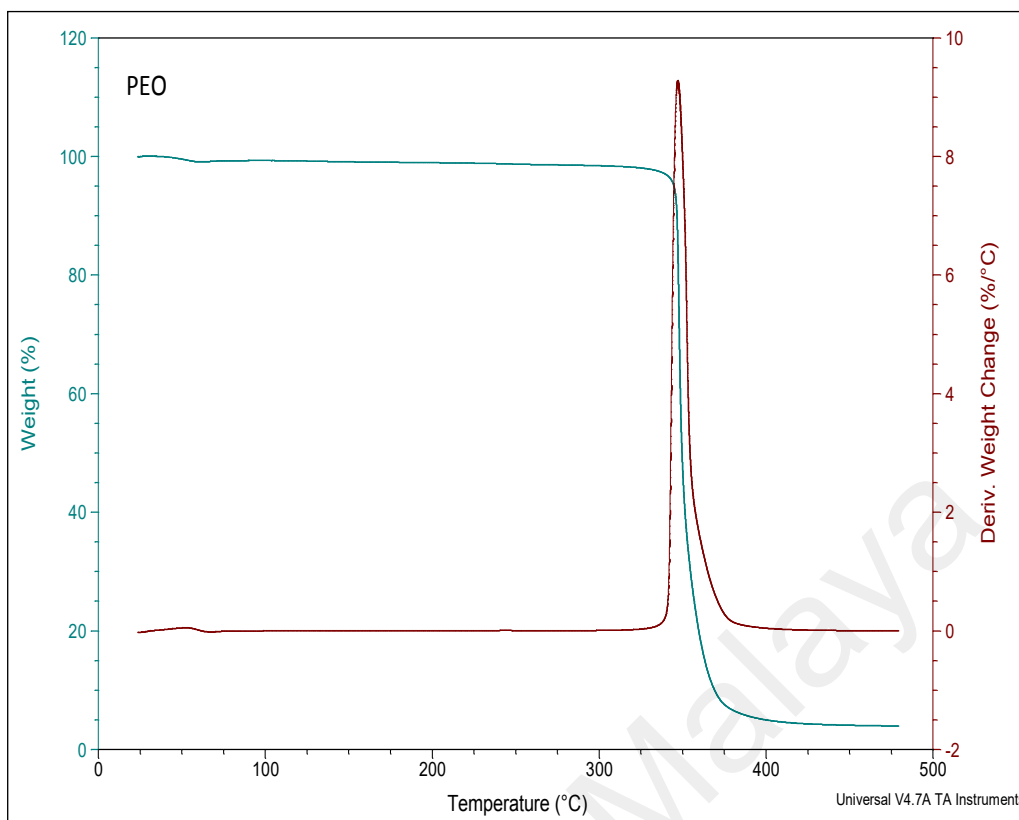


Figure 3.22: TG and its DTG curves of pure PEO.

The thermograms of MWCNT/PEO composites and the DTG curves (figure 3.22) display two main stages of decompositions which are summarized in table 3.3. The first stage was in a long interval of time with a slow process of weight loss, more obviously in 5%, 15%, 25% and 33% samples, the DTG of this first transition yielded more than one peak for all samples, except for 5wt%. The peaks have intensities increasing with the increase of the CNT weight concentration. The presence of more than one peak in the DTG curve indicates the presence of multiple components which confirms the occurrence of different carbonaceous structures in the samples, the weight loss augmented from 2.4% for 5% composite and to 56% for 50% composite, in the temperature intervals ($238^{\circ}\text{C} - 256^{\circ}\text{C}$) and ($139^{\circ}\text{C} - 300^{\circ}\text{C}$) respectively. This can be explained by the interaction between the CNTs and the polymer chains which produce amorphous carbon and graphitic nanoparticles. This result is emphasized by the Raman spectroscopy, it displayed a relatively high ratio of ID/IG observed. Thus, indicates the

formation of sp^3 hybridized carbon on CNTs with PEO modification. The presence of the amorphous layer demonstrates the success bonding of PEO chains onto CNT sidewall (Liu, Chang et al. 2008). This is also emphasized by the SEM results.

Table 3.3: Summary of the prepared composites along with pure PEO thermal degradation.

Sample	First stage		Second stage		
	wt%	temp range °C	weight loss %	temp range °C	weight loss %
5%		238 - 256	2.4	309 - 367	86.6
15%		195 - 335	31	359 - 392	50.8
25%		181 - 326	36.2	365 - 411	36.5
33%		191 - 326	49.4	368 - 395	25.7
40%		189 - 308	55.7	383 - 404	9.4
50%		139 - 300	56	381 - 411	3.1
PEO		/	/	335 - 401	93.6

The second stage was abrupt and steep, having the same shape as the PEO decomposition curve. All the samples present a DTG single, sharp and symmetric with a high magnitude peak between 300-400°C except for the 50% sample which exhibits a broader peak. The sharp peak indicating the homogeneity of the samples at this region as the full width at half maximum (FWHM) of the DTG peak is an indicative of the sample homogeneity (a lower FWHM indicates a sharper and more discrete event, characteristic of more uniform sample) (Moraes, Matos et al. 2011). The intensity of the peaks decreased with the increase of the MWCNT concentration. This indicates that more reactions were held when the amount of nanotubes is becoming higher. The TGA results suggest that there is a good interaction between PEO and CNT.

On the other hand, the second transition displayed at 309-411°C is due to the breaking main chain of PEO composite, the total weight loss corresponds to this stage was about 86.6, 50.8, 36.5, 25.7, 9.4 and 3.1 of the weight percentage for 5%, 15%, 25%, 33%, 40% and 50% composites respectively. Obviously, the second main weight loss is less intense whenever the quantity of CNT in the samples is elevated compared to the pure PEO polymer, which had a total weight loss of 93.6% at 335-40°C.

From the TGA curves, it is also noted that the thermal decomposition temperature (T_d , defined as the temperature at 3% weight loss) of the raw PEO was around 340°C is remarkably much higher than the prepared composites. For instance the highest T_d was 251°C and the lowest was 154°C attained for 5% and 50% respectively. These indicating the low thermal stability exhibited by the composites in the first stage of degradation. Whereas, the situation is inversed in the second stage of the decomposition, where the DTG peaks show considerable shift of the weight loss towards higher temperatures. The peak shifted from 346°C (PEO) to around 376°C, 388°C and 381°C in 33%, 40% and 50% respectively. 5% sample displayed a lower peak at about 323°C. Because the thermal stability of the nanocomposites depends on the interfaces between the CNTs and the surrounding polymer matrix (Yu, He et al. 2011). These results suggests a formation of chemical bounding between the PEO main chain and MWCNT which reduced the thermal resistance and smooths the heat transfer from the polymer to the nanotube (Barick and Tripathy 2011).

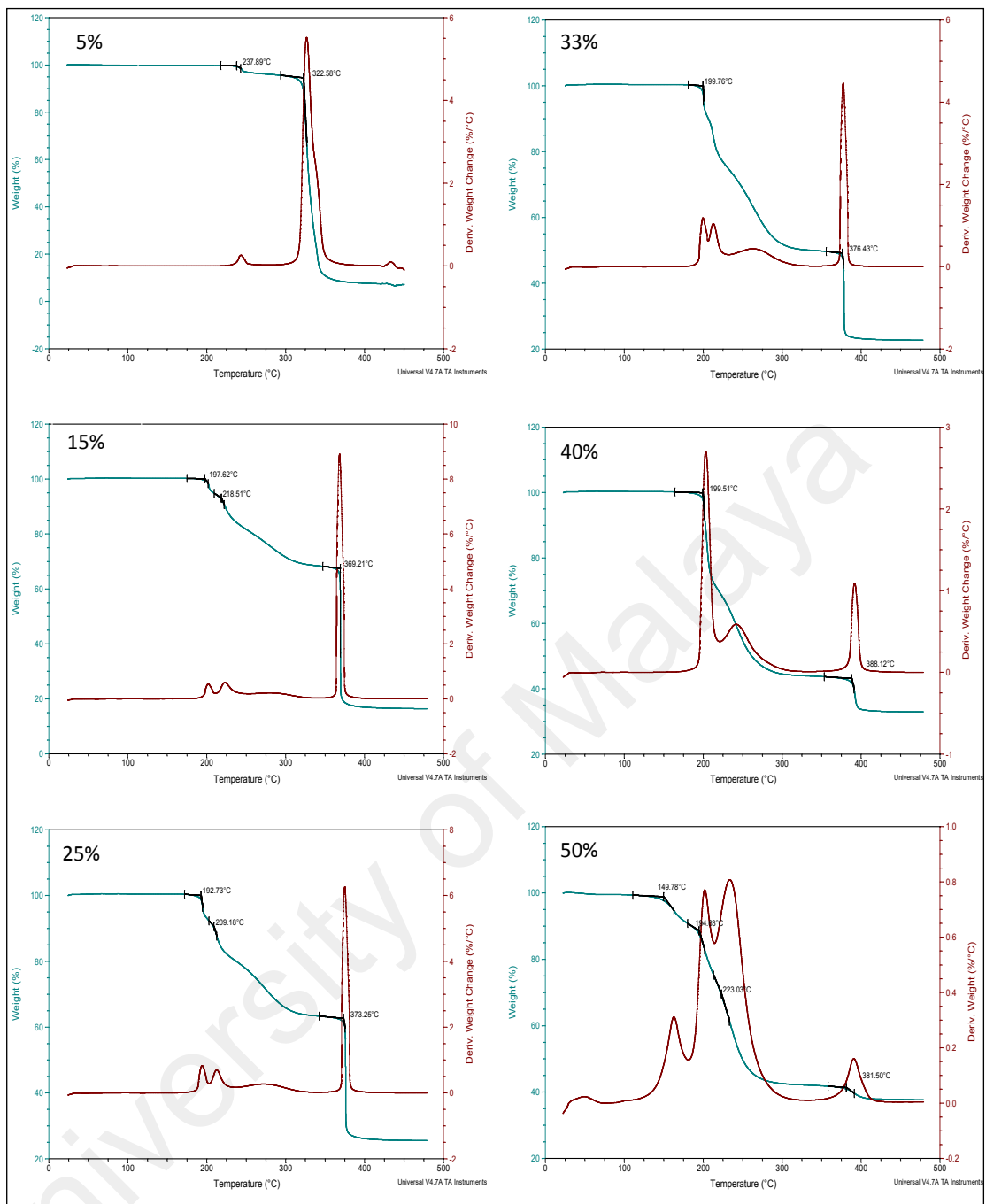


Figure 3.23: The TG and DTG curves of each MWCNT/PEO composite.

A key factor that may determine the two stages degradation, is the nature of the Polyethylene oxide; PEO is a semicrystalline polymer, essentially a two phase material consisting of spherulitic crystals embedded in an amorphous continuum (Crowley, Zhang et al. 2002). Thus provides a hint that different reactions can take place when the later component plays the role of the host.

3.8.4 Thick Films Field Electron Emission

In this part of the work, we report the field emission characteristics of multiwall carbon nanotube- polymer composites as a function of nanotube loading of the thick films group, the gap between the anode and cathode was kept 0.1 mm and the anode bias was changed from 100 to 1100 V. Figure 3.24 illustrates the emission current density (A/cm^2) versus electric field (V/cm) for the prepared thick.

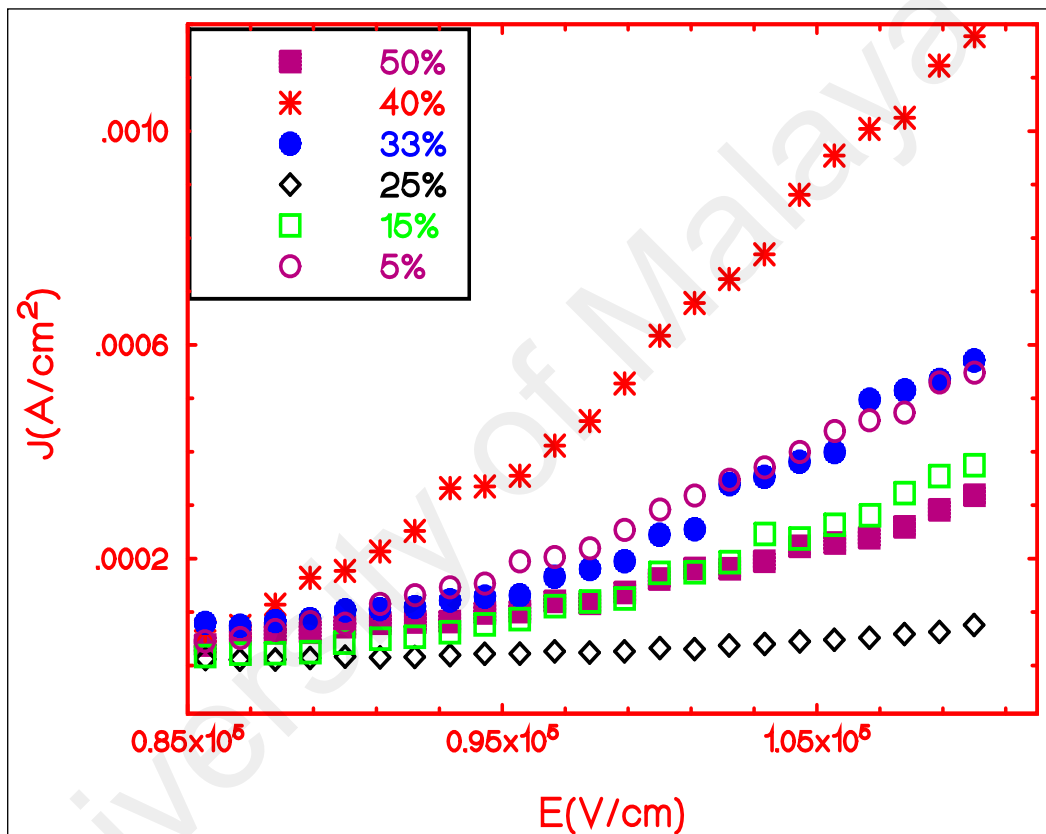


Figure 3.24: Current density versus the electric field applied for Thick films with different MWCNTs weight concentrations.

The turn on field (for $10 \mu m/cm^2$) and the threshold field (for $0.1 mA/cm^2$) in addition to the field enhancement factor (β) parameters are stated in table 3.4.

Table 3.4: Field emission characteristics of PEO/MWCNT thick films composites.

Thick films	Turn on field (V/μm) (10 $\mu\text{A}/\text{cm}^{-2}$)	Threshold field (V/ μm) (0.1mA/ cm^{-2})	\hat{a}
5wt%	7.64 \pm 1.15	9.10 \pm 1.37	979 \pm 147
15wt%	8.16 \pm 1.22	9.61 \pm 1.44	720 \pm 108
25wt%	8.26 \pm 1.24	/	1162 \pm 174
33wt%	6.51 \pm 0.98	9.07 \pm 1.36	1853 \pm 278
40wt%	8.36 \pm 1.25	8.76 \pm 1.31	817 \pm 123
50wt%	7.35 \pm 1.10	9.54 \pm 1.43	1187 \pm 178

The 33% composite displayed the lowest turn on field of 6.51 V/ μm . Whereas, the highest current density achieved was 1.17 mA/ cm^2 , produced by the 40% composite. The latest showed 8.36 V/ μm and 8.76 V/ μm turn on and threshold fields respectively. There is a slight difference in the emission threshold fields of all the samples. The corresponding Fowler–Nordheim plot is shown in figure 3.25, the approximately linear behavior of the FN curve confirms that the observed current is generated by field emitted electrons. 33% showed almost perfect linearity.

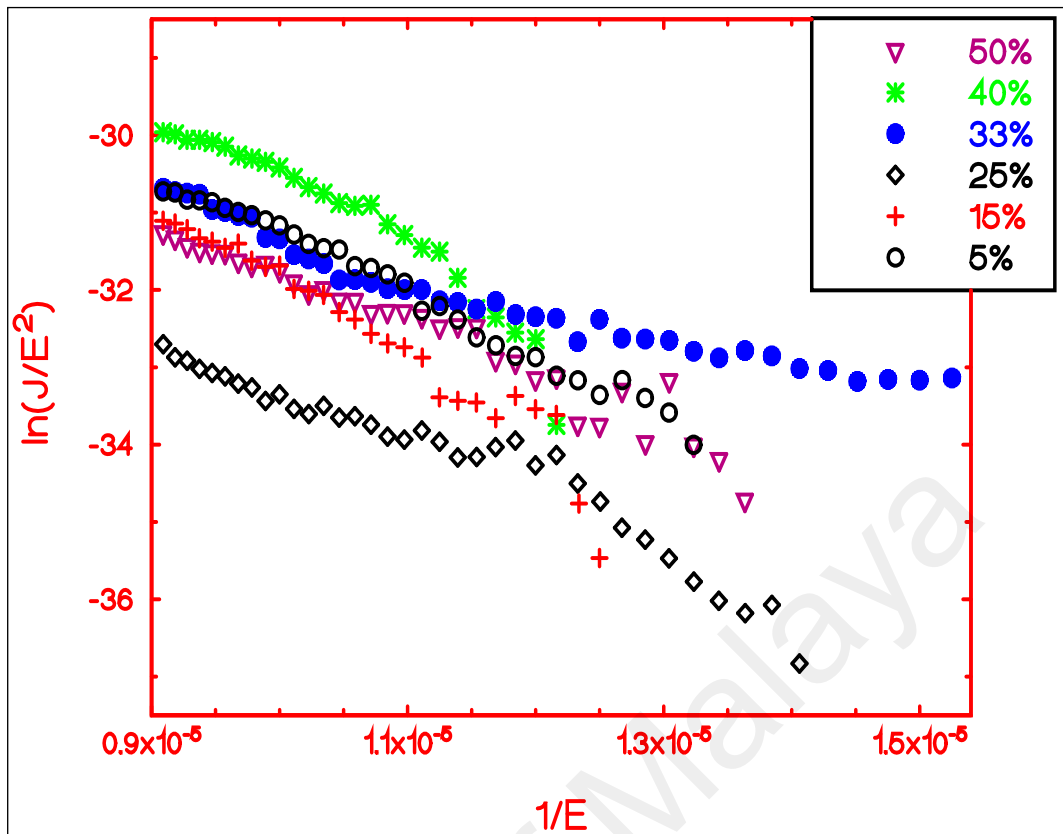


Figure 3.25: Fowler- Nordheim plot of Thick films with different MWCNTs weight concentrations.

Figure 3.26 presents the enhancement factor (β), calculated using the FN equation. It is obvious that there is a non-linear relationship between the enhancement factors and the increasing filler loading fractions, which can be attributed to the non-homogeneous dispersion of CNTs within polymer matrices, in addition to the surface morphology and the work function of the different composites prepared.

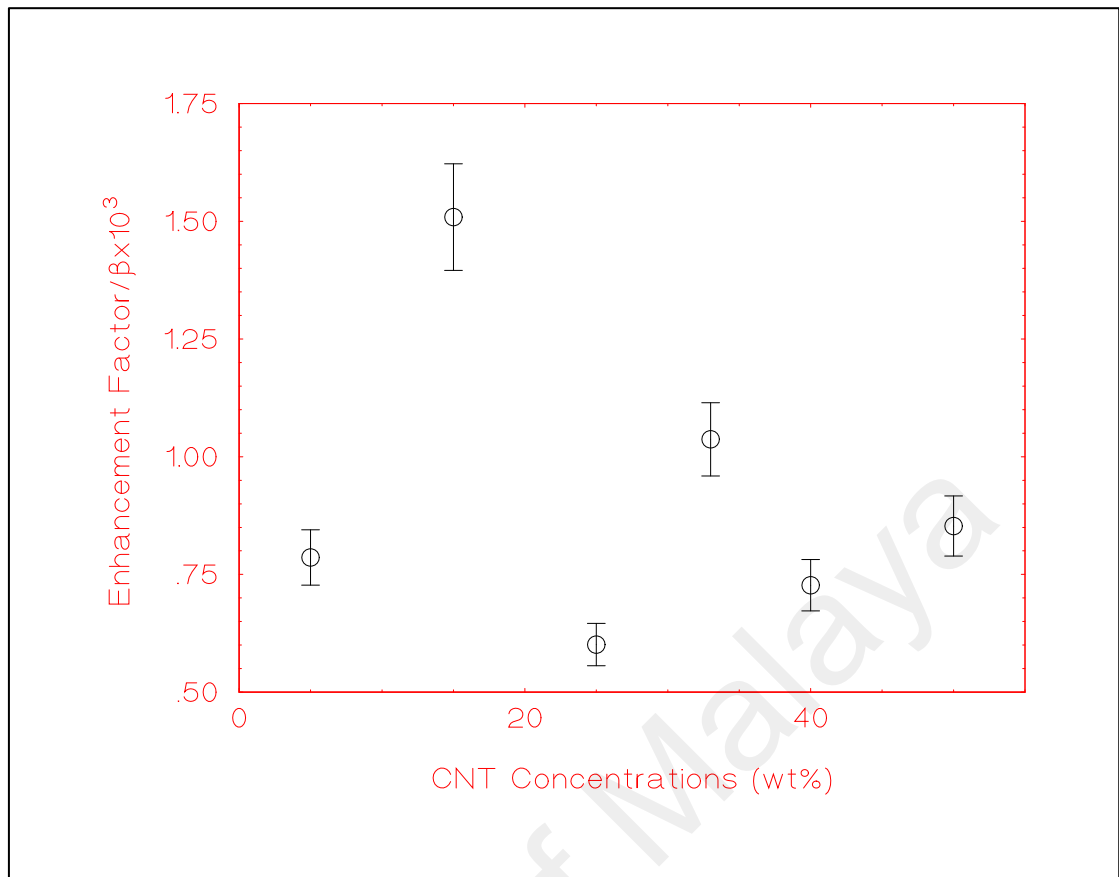


Figure 3.26: Enhancement factors for films with different MWCNTs weight concentrations.

In a previous study, carbon nanotube-polymer composites (MWNT/PmPV), the enhancement factor did not vary significantly with mass fraction of nanotubes, it increased only moderately from 330 (0.44% loading) up to 390 (7% loading). Over the same range of nanotube loading, E_{th} (defined as the applied electric field which gives an emission current of 10 nA), decreased from 14.5 V/ μm (0.44% loading) to 8.4 V/ μm (7% loading) (Smith, Carey et al. 2005).

In a 2000 s (~34min) current stability test, voltage was set to a constant for each sample and the correspondent current intensity is depicted in figure 3.27. Sample with 25% MWCNT showed a great stability for the whole period of 34 min, followed by 33% sample. The latest had some fluctuations in the first 5 min. After 7 min measurement, 5% and 15% maintained a significant stability, whereas before this point of time, the first sample exhibited an increasing trend with peaks reached to 7 mA at 36

s. We believe that the evaporation of the composites material to the anode was the main reason behind the instability. The current of 50% had dramatic up and down fluctuations. The normal trend in decreasing current and some fluctuations might be dynamic rearrangement of emission sites.

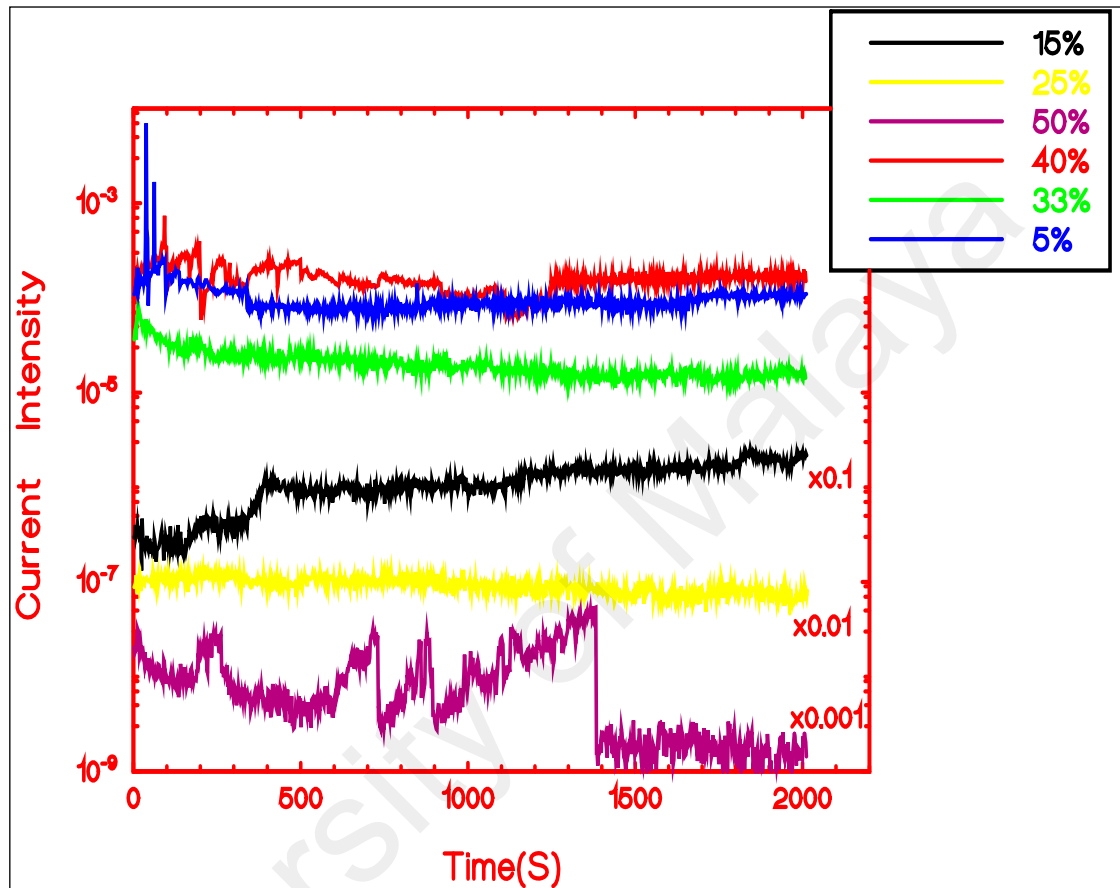


Figure 3.27: Current stability in about 34 min period time for thick films with different MWCNTs weight concentrations.

The greatest enhancement factor is 1853, recorded by 33% loading composite. The measurement of the current density versus the electric field of the latest sample, for before and after the stability test is plotted in figure 3.28.

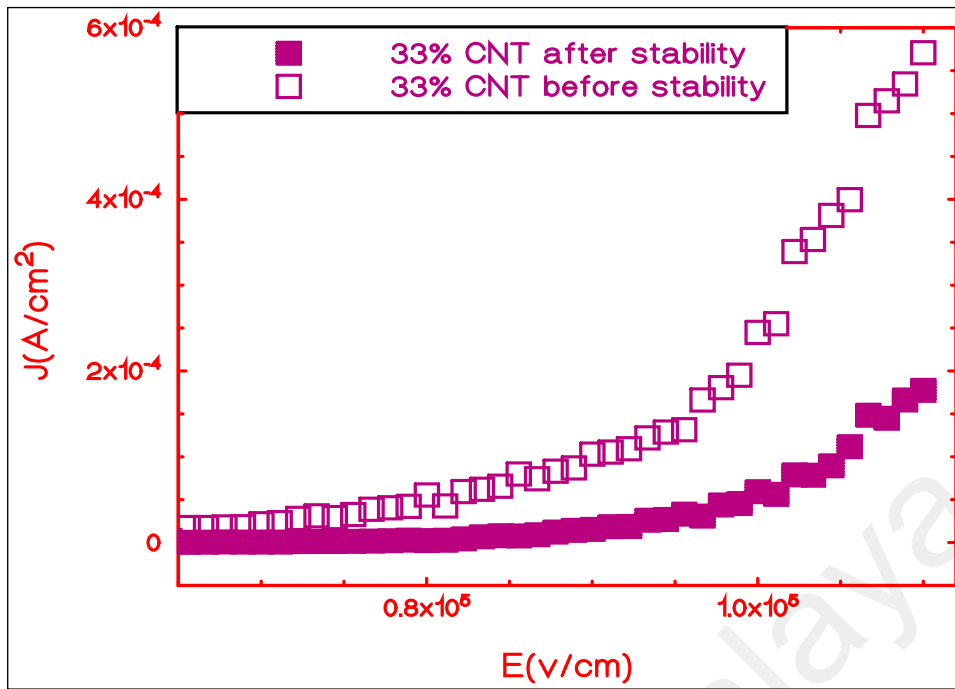


Figure 3.28: Current density versus applied electric field for before and after stability test for 33wt% thick film.

It is obvious that the yield of the current density of the sample was affected and decreased from $570 \mu\text{A}/\text{cm}^2$ to $177 \mu\text{A}/\text{cm}^2$. The turn on and threshold fields augmented from $6.51 \text{ V}/\mu\text{m}$ to $8.77 \text{ V}/\mu\text{m}$ and from $9.07 \text{ V}/\mu\text{m}$ to $10.53 \text{ V}/\mu\text{m}$ respectively, indicating the affection of the composite whether by the strong electrostatic force exerted during the emission (it can peel off the CNTs from substrate, causing current decay and arcing) or by the local Joule heating produced. The temperature at the tip of a MWCNT could go up to 2000 K, which was induced by an emission current of $1 \mu\text{A}$ (Purcell, Vincent et al. 2002, Vincent, Purcell et al. 2002). In addition, PEO polymer has a low melting point of $57\text{-}73^\circ\text{C}$ (Crowley, Zhang et al. 2002). The structural modification of the nanotubes tips by the ion bombardment of residual gases could reduce the emission current at the high electric field region.

3.9 MWCNT/ZnO and MWCNT/TiO₂ hybrid films as electrophoretic deposition

3.9.1 Introduction

Field Emission scanning electron microscope (FESEM) will be used to study structure MWCNT/ZnO and MWCNT/TiO₂ composites. Energy dispersed x-ray spectroscopy is employed to determine the chemical composition of the different composites. Raman spectroscopy will be used to investigate detailed bonding structure and to distinguish various bulk materials without any sample preparation. The structural properties results of the MWCNT/ZnO and MWCNT/TiO₂ hybrid films are reported in section 3.9.2. In section 3.9.3 the Raman spectroscopy results are presented. Finally, the field electron emission results of hybrid films are conducted in section 3.9.4

University of Malaya

3.9.2 Field emission scanning electron microscope (FESEM)

The structure and morphology of the samples were characterized by Field emission scanning electron microscope (FESEM) and Energy dispersive x-ray spectroscopy. Energy dispersed x-ray spectroscopy is employed to determine the chemical composition of the different composites. Figure 3.29 (a), (b) and (c) shows the FESEM images of the MWCNT film for 1 minute, 2 minutes and 3 minutes deposited on silver substrates by electrophoretic deposition. The surface morphologies of other electrodes basically remain the same. The CNT_s entangle with each other and show a good network microstructure with many meso pores with average size of $\sim 2\mu\text{m}$.

Figure 3.29 (d), (e) and (f) shows the FESEM images of MWCNT/ZnO hybrid film and figure 3.29 (f), (g) and (h) shows the FESEM images of MWCNT/TiO₂ for 1 minute, 2 minutes and 3 minutes of times respectively. The MWCNT/ZnO and MWCNT/TiO₂ were deposited onto electrodes. The MWCNT/ZnO hybrid films have bonded together. Such a network structure provides more tunnels for the entering of the solution and allows hydrated ions easily to move onto the surface of the film, which favours the electrosorption. But for MWCNT/TiO₂, the CNT entangle with each other and show a good network microstructure with many mesopores with average of $\sim 10\text{ nm}$, which is derived from Ti physical adsorption measurement.

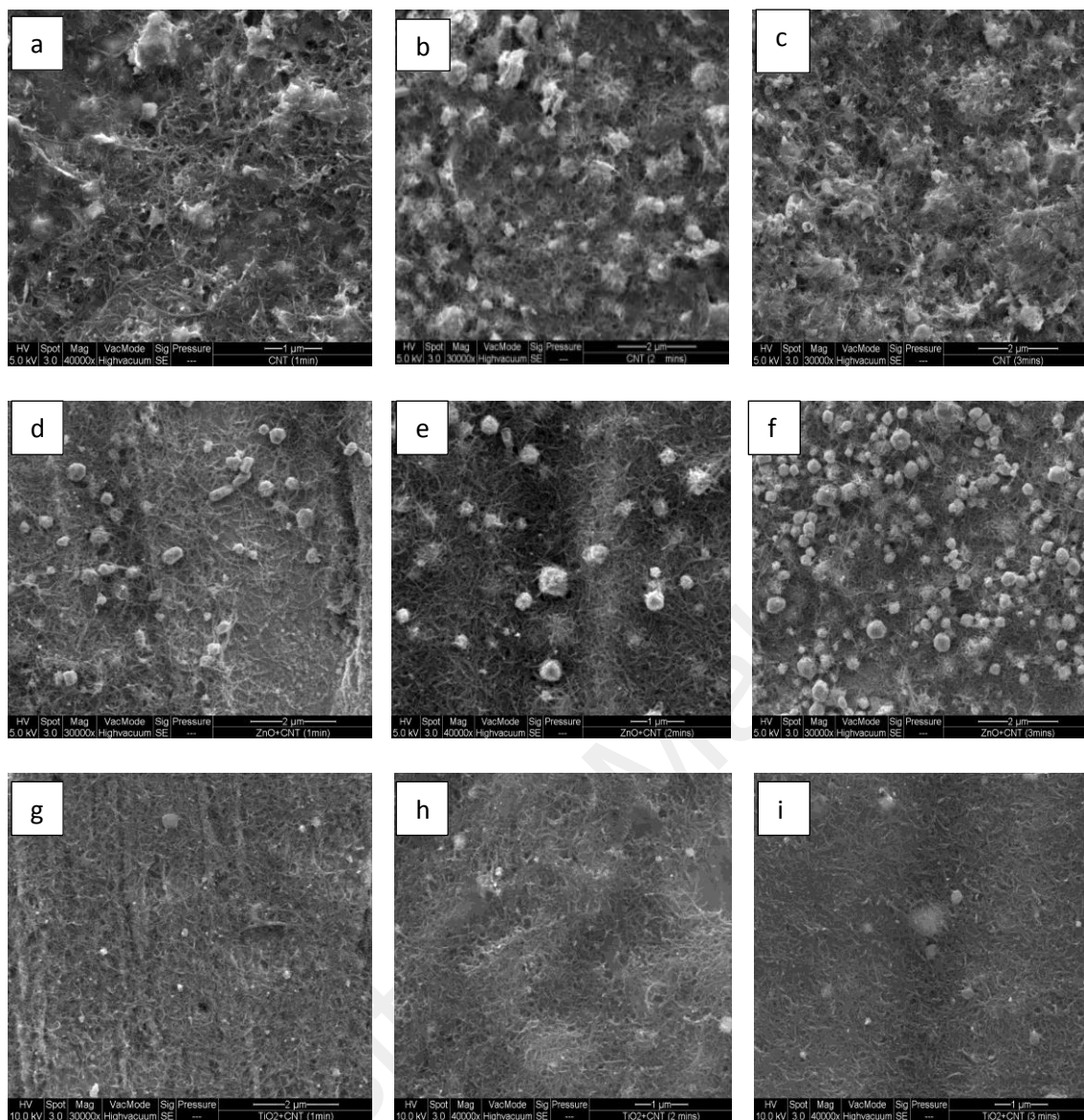


Figure 3.29: FESEM images of (a) 1 minute of MWCNT, (b) 2 minutes of MWCNT, (c) 3 minutes of MWCNT, (d) 1 minute of MWCNT/ZnO, (e) 2 minutes of MWCNT/ZnO, (f) 3 minutes of MWCNT/ZnO (g) 1 minute of MWCNT/TiO₂, (h) 2 minutes of MWCNT/TiO₂ and (i) 3 minutes of MWCNT/TiO₂, were deposited on silver.

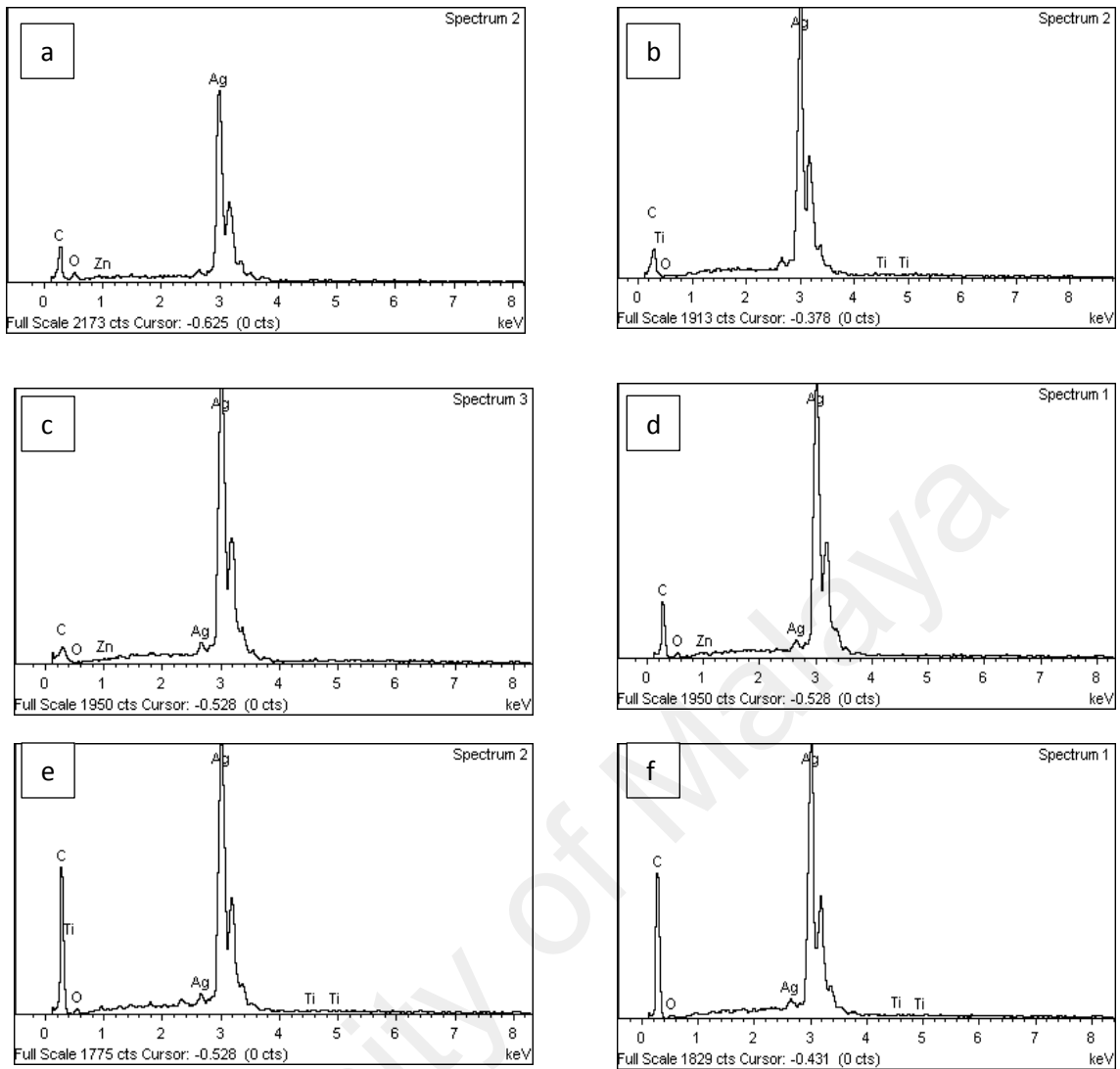


Figure 3.30 (a), (b) and (c) shows the EDX spectra of MWCNT/ZnO. The spectra exhibited the existence of carbon, oxygen, titanium and argentum. Argentum is the major composition and has the highest concentration comparing it to other elements. Zinc and oxygen are resulted from the using of Zinc Oxide. Figure 3.30 (d), (e) and (f) shows the EDX spectra of MWCNT/TiO₂. The highest concentration and the major composition is still Argentum. Titanium and oxygen are produced from the using of Titanium Oxide.

	Element	Weight%	Atomic%		Element	Weight%	Atomic%
a	C K	2.08	17.33	d	C K	6.75	38.12
	O K	-1.51	-9.41		O K	0.89	3.75
	Zn K	0.12	0.19		Ti K	0.13	0.18
	Ag L	99.30	91.90		Ag L	92.23	57.95
	Totals	100.00			Totals	100.00	
b	C K	15.02	55.38	e	C K	29.97	74.53
	O K	4.06	11.23		O K	3.79	7.07
	Zn K	0.65	0.44		Ti K	0.15	0.09
	Ag L	80.28	32.96		Ag L	66.10	18.30
	Totals	100.00			Totals	100.00	
c	C K	11.91	42.29	f	C K	31.00	79.06
	O K	10.01	26.70		O K	0.80	1.53
	Zn K	0.53	0.35		Ti K	0.11	0.07
	Ag L	77.55	30.67		Ag L	68.09	19.33
	Totals	100.00			Totals	100.00	

Figure 3.31: EDS spectra of MWCNT/ZnO hybrid film of (a) 1 minute, (b) 2 minutes (c) 3 minutes and EDS spectra of MWCNT/ZnO hybrid film of (d) 1 minute, (e) 2 minutes (f) 3 minutes respectively.

3.9.3 Raman spectroscopy

Figure 3.32(a) shows the typical spectrum of MWCNT film which is dominated by two intensity peaks at 2680 and 2917 cm^{-1} , which are referred as D line and G line, respectively. The D line is attributed to the presence of amorphous carbons or defects in curved graphite sheets. The G line shows the presence of tubular structure in the CNT_s . The ratio of the intensity of the D peak and G peak (I_D/I_G) is related to the amount of disorder in the carbon products. The (I_D/I_G) values of all CNT_s films are almost the same (~ 0.9), indicating that the electrophoretic deposition (EPD) has not damaged the structure of CNT_s and there exists some defects in the CNT_s films.

Figure 3.32(b) and (c) gives the Raman spectroscopy of MWCNT/ZnO and MWCNT/TiO₂ hybrid films. The G line and D line modes of MWCNT/ZnO and MWCNT/TiO₂ at about 1582 and 1345 cm^{-1} and 2929 and 2692 cm^{-1} respectively and are clearly observed from figure 6.3(b) and (c). The peak at 1582 cm^{-1} and 2929 cm^{-1} (G line) results from graphite sheet of MWCNT/ZnO and MWCNT/TiO₂ wall, which consists of carbon, zinc and titanium atoms all arranging in the form of hexagon, while the peak at 1345 cm^{-1} and 1582 cm^{-1} (D line) represents the impurity and the defects of atomic structure in the MWCNT/ZnO and MWCNT/TiO₂ samples.

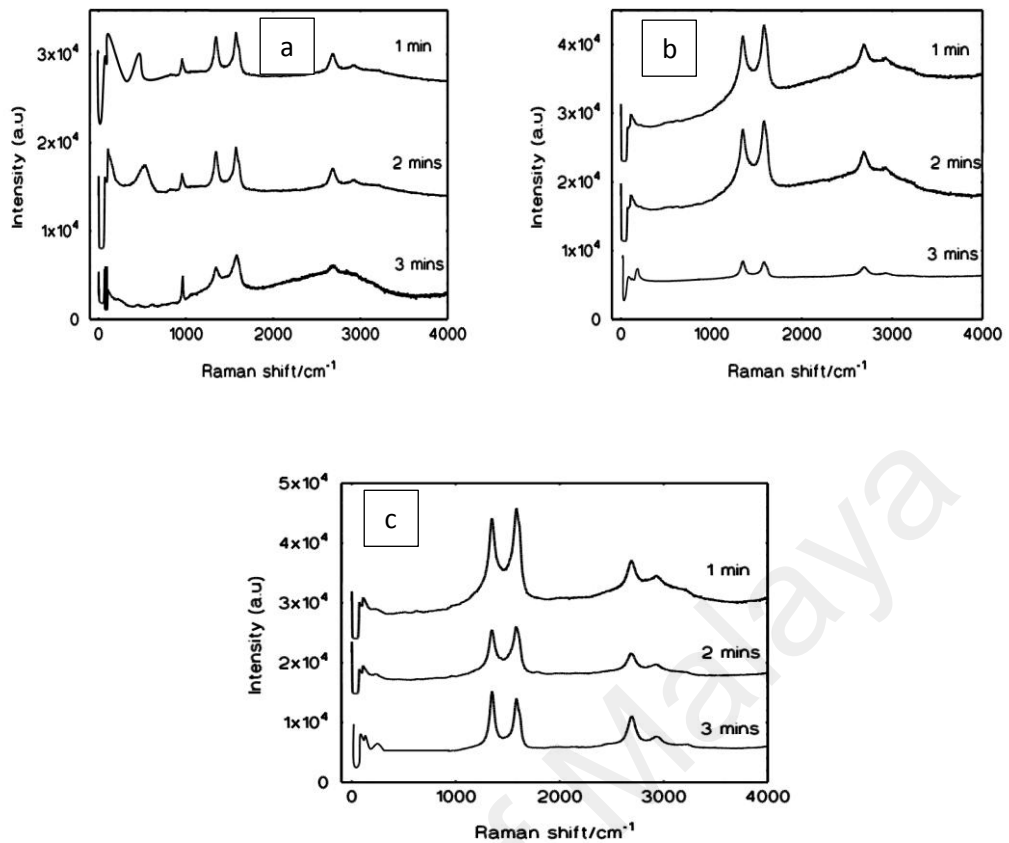


Figure 3.32: Typical raman spectra of (a) MWCNT (b) MWCNT/ZnO (c) MWCNT/TiO₂.

3.10 Field Electron Emission Properties of MWCNT, MWCNT/ZnO and MWCNT/TiO₂ films

The measured field emission current density plotted as a function of the applied field for the thin films of MWCNT, MWCNT/ZnO and MWCNT/TiO₂ deposited on a silver substrate is shown in figure 3.33. For MWCNT films shown in figure 3.33(a) a trend of increasing maximum current density yield with decreasing deposition time was observed. The highest value of the current density for the MWCNT film sample was $4.5 \times 10^{-5} \text{ A/cm}^2$ at $13.8 \text{ V}/\mu\text{m}$ obtained from the film deposited for 1 minute. The turn-on field, at which the emission current density reaches $1 \mu\text{A/cm}^2$, is $8.1 \text{ V}/\mu\text{m}$ and the

threshold field which produced the emission current density of $10 \mu\text{A}/\text{cm}^2$ was $13 \text{ V}/\mu\text{m}$.

The JE curves for the MWCNT/ZnO hybrid films is shown in figure 3.33(b). A similar trend of increasing maximum current density with decreasing deposition time was observed. However, the maximum current density obtained with the sample deposited for 1 minute was significantly higher than that obtained from MWCNT films, at $0.9 \times 10^{-3} \text{ A}/\text{cm}^2$ at $13.8 \text{ V}/\mu\text{m}$. Similarly, films deposited for 2 and 3 minutes yielded much higher current densities than the corresponding pure MWCNT films.

The results obtained from the MWCNT/TiO₂ films are shown in figure 3.33(c). Again, a similar trend of increasing maximum current density with decreasing deposition time was observed. However, the values of the current densities obtained from MWCNT/TiO₂ films, while higher than those obtained from pure MWCNTs were lower than those obtained from MWCNT/ZnO samples. The maximum current density of $2.5 \times 10^{-4} \text{ A}/\text{cm}^2$ at $13.8 \text{ V}/\mu\text{m}$ using films deposited for 1 minute was observed.

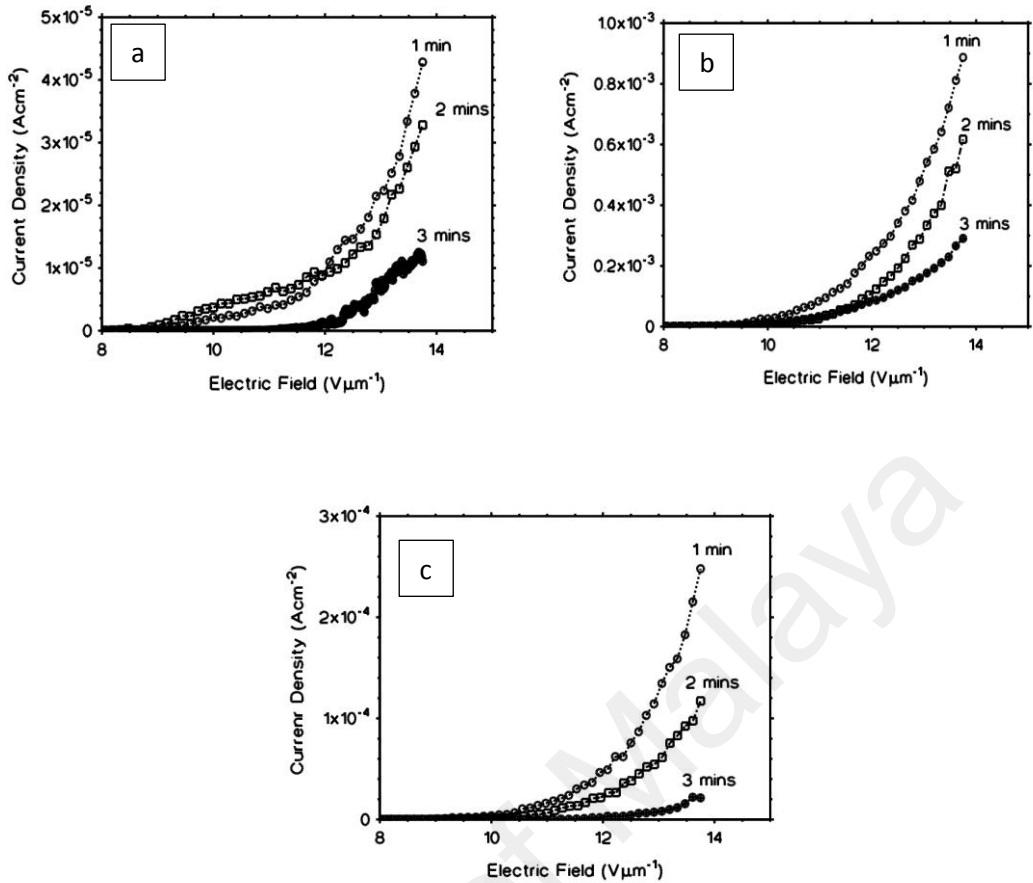


Figure 3.33: Typical field emission current density vs. the applied electric field for (a) MWCNT film (b) MWCNT/ZnO and (c) MWCNT/TiO₂.

Comparing the results of the JE curves for pure MWCNTs, MWCNT/ZnO and MWCNT/TiO₂ film a number of observations can be made. Firstly, better field emission performance were afforded with thinner films, based on the trend of higher current densities with shorter deposition for all types of films. Here, the reason can be that thicker films with higher MWCNT density induced shielding effect during the field emission process. As the MWCNTs bunched together in the thicker films, the cathode surface were smoothed out, thus eliminating the sharp structure effects of the MWCNTs. Comparing the results of pure MWCNTs, MWCNT/ZnO and MWCNT/TiO₂, significant enhancement was observed when hybrid films were used. It

is evident here that the oxide particulates with sizes of about 1 μm functioned as spacers for the MWCNTs. While the oxides themselves were not expected to contribute much in the field electron emission current, the presence on the surface, reduced the agglomeration of the MWCNTs, thus presented the shielding effect.

Figure 3.34 shows the corresponding Fowler-Nordheim (F-N) plots for the MWCNT films, MWCNT/ZnO and MWCNT/TiO₂ hybrid films field emission. Fowler and Nordheim modeled the phenomenon of field emission on the basis of quantum mechanical tunneling of electrons due to the bending of the potential barrier in the presence of an external electric field. According to their prediction, the linear relationship between $\ln (J/E^2)$ and $1/E$ is expected for the voltages above the turn-on voltage. The emission data from experiments generally agree with the linear F-N relationship corresponding to the classical electron tunneling mechanism of field emission. The value for the work function of MWCNT taken at 5 eV was used. The linear curves in figure 3.34 were fitted to a straight line and from the gradient the field enhancement factor, β were calculated. The values obtained for all samples are summarized in table 3.5. For pure MWCNT films, almost similar β values are obtained for films deposited for 1 and 2 minutes at 5680 and 5560 respectively. A slight decrease in β value was observed for the pure film deposited for 3 minutes providing further evidence of shield effect due to thicker films.

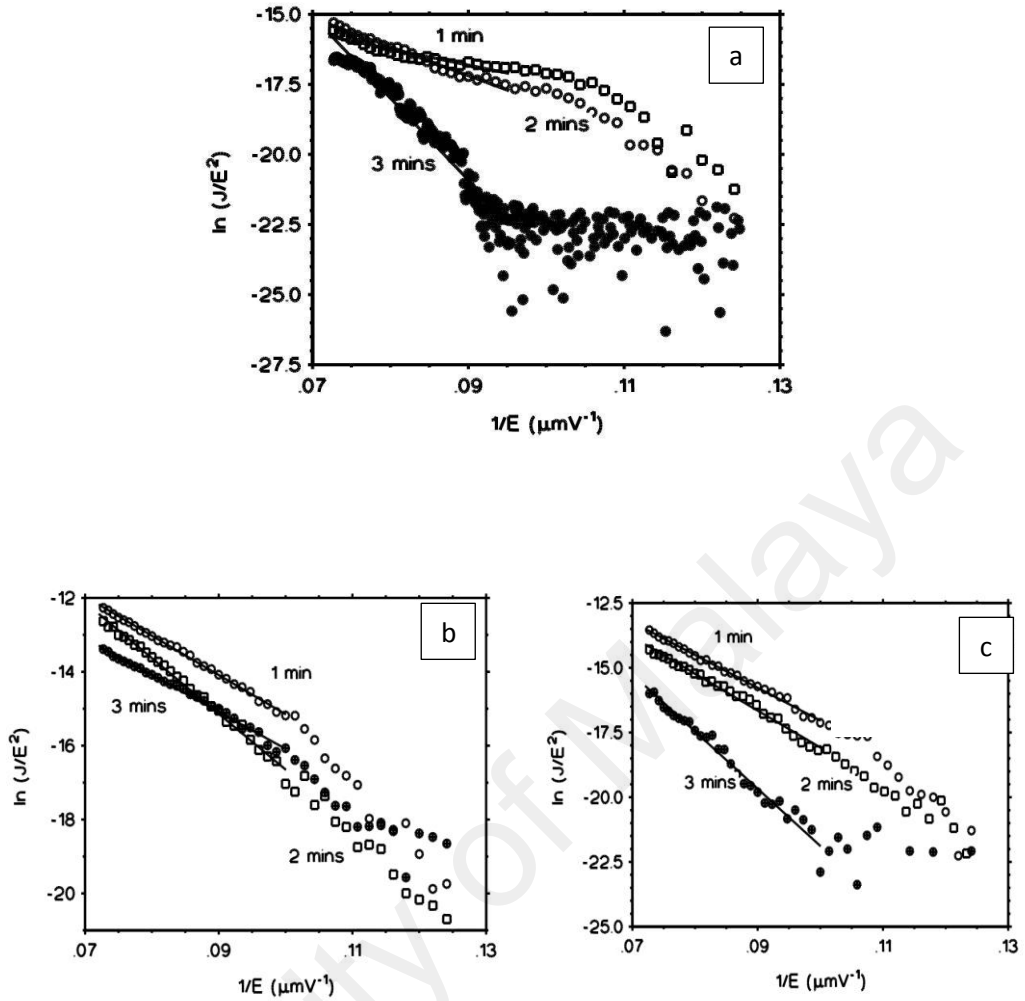


Figure 3.34: The corresponding Fowler-Nordheim (F-N) plots ($\ln(J/E^2)-(1/E)$) with the field emission characteristics of the (a) MWCNT film (b) MWCNT/ZnO hybrid film and (c) MWCNT/TiO₂ hybrid film.

Table 3.5: β value for MWCNT, MWCNT/ZnO and MWCNT/TiO₂.

Deposition Time	MWCNT	MWCNT/ZnO	MWCNT/TiO ₂
1 Minute	5680±852	5790±869	5460±819
2 Minutes	5560±834	5570±836	5390±809
3 Minutes	4570±686	5880±882	5320±798

As for the MWCNT/ZnO films, almost similar β values were observed at 5790, 5570 and 5880 for films deposited at 1, 2 and 3 minutes, respectively. Similarly, MWCNT/TiO₂ films showed little variation at 5460, 5390 and 5320 for films deposited at 1, 2 and 3 minutes, respectively. Again it is evident that the inclusion of the oxide particles in the field electron emission cathode films appeared to curtail the shielding effect due to MWCNT density.

3.11 Conclusions

Raman spectroscopy results emphasized the good adhesion of the polymer chains to the nanotubes walls. All the thick films exhibited higher disorder after the FEE measurement except for 25% film. Thin films reacted in the opposite way, where the disorder was reduced after the FEE test in five out of six samples. The peaks of the Si substrate appeared below 1000 cm⁻¹ frequency in the thin films whereas in the thick films were smoother in this area since the laser waves were absorbed by the thick films. The SEM micrographs indicated that the nanotubes were well dispersed and embedded within the polymer matrix. The microscopy did not exhibit much difference between the thin and thick films. The TG analysis was the same for the two sets of the samples, obviously indicated that the thermal stability of PEO was linearly improved by the incorporation of CNTs in the polymer matrix. Generally, the thin films yielded higher turn on and threshold fields compared with the thick ones. Half of the thin films did not reach the current density of 0.1 mAcm⁻².

Meanwhile all the thick films exceeded this value except for 25%. A non-linear relationship between the enhancement factors and the increasing filler loading fractions was in all the composites.

The best β obtained was 1509 and 1853 in 15% thin and 33% thick films. In 2000 measurement, all the composites showed a considerable stability in current yield, thin films were rather more stable. And the two best field enhancer films presented a degradation in current density supply after the stability test. Generally, the attained results are promising for FEE and multi-functioning MWCNT/PEO devices, more obviously in thick films.

University of Malaya

CHAPTER 4: MWCNT/PEO COMPOSITES AS ACETONE AND ETHANOL SENSORS

4.1 Introduction to Volatile Organic Compound Sensors

Sensors are devices that detect or measure physical and chemical parameters such as temperature, pressure, sound and concentration. The main requirements of a good sensor are high sensitivity, fast response, low cost, high volume production, and high reliability. Gas sensors are developed based on their response to the gases through altering of one of the physical or chemical properties of the sensing material. Thus, they are generally divided into two types, namely; physical gas sensors and chemical gas sensors. Chemical gas sensors usually utilize an electrical or optical response by adsorption of gas molecules on the surface of an active layer (Kim 2006). In this case, it is difficult to detect some gases which have low chemical adsorption energy, like inert gases. Metal-oxide gas sensors (Shimizu and Egashira 1999, Lee and Meyer 2000, Varghese and Grimes 2003) are representative examples of chemical gas sensors. Physical gas sensors which operate by ionization mechanism (Yang, Zhou et al. 2007) work by fingerprinting the ionization characteristics of distinct gases. Although these ionization sensors have better selectivity and response time, but the ones with traditional electrodes are still huge and bulky. Sensors continue to make significant impact in everyday life with applications ranging from biomedical to automotive industry where, the detection of NO₂ is important for monitoring automotive emissions (Cho, Lee et al. 2007). Sensors and biosensors have been widely used in food industry to provide safety and quality control of food products as the contamination of foods caused by bacterial pathogens may result in numerous diseases (Ivnitski, Abdel-Hamid et al. 2000).

4.2 Types of Sensors

Metal oxides are the most widely used for chemiresistors (Kolmakov and Moskovits 2004). They consist of SnO₂, ZnO or TiO₂ as active layer, where the adsorption of gas molecules leads to a large change in its electrical resistivity. They have merits of low cost, good sensitivity, and convenient form of response (a simple change in resistance). But in order to achieve enhanced chemical reactivity between gas molecules and active layer, the sensors need a high temperature of 200-500°C which causes problems in term of high power consumption and pre-heating time. A general problem in the use of high temperature operated gas sensors are the eventual catalytic activity of the surface. In such a gas phase, the possibility of chemical reactions is elevated, resulting in undesirable products. Since the sensors generally are made small in size, the catalytic reactions on their surfaces are hard to be measured (Bene, Perczel et al. 2000).

In addition to metal oxides, a variety of materials have been investigated for sensing so far. Conducting polymers (CP) have been tested for their applications in energy storage (Novák, Müller et al. 1997) and sensing chemical vapors (Bartlett and Ling-Chung 1989, Bartlett and Ling-Chung 1989). Among these polymers, polyaniline (PANi) (MacDiarmid and Epstein 1989, MacDiarmid 1997), polythiophene (Kreja, Kurzawa et al. 1997, Gallazzi, Tassoni et al. 2003) and polypyrrole (Kawde, Laxmeshwar et al. 1995, Kreja, Kurzawa et al. 1997, MacDiarmid 1997, Gallazzi, Tassoni et al. 2003) have been extensively examined in both of the previous applications. These sensors have the potential to function at ambient temperatures. Several organic conducting polymers such as polyaniline have been used as sensing elements for organic and inorganic components (Santhanam, Sangoi et al. 2005). Conducting-polymer sensors made with poly(pyrrole) (PPY) have attracted attention because of their advantages including easy synthesis and micro fabrication, low voltage actuation, wide range of dopant species, high tolerance to electrode materials and

electrolytes, good environmental stability, and biocompatibility with physiological environments (Williams and Doherty 1994, Schmidt, Shastri et al. 1997). Generally, the conducting polymers employed in sensor applications are sensitive to a wide variety of organic vapors and hence their selectivity is relatively poor. Another drawback of these polymers is that they acquire problems of the environmental stability.

The e-nose instruments employed especially for medical applications, including Amperometric Gas Sensors (AGS), Conducting Polymers (CP), Metal-Oxide Semiconductors (MOS), Quartz Microbalance (QMB), and Surface Acoustic Wave (SAW) sensors, represent a relatively small number of e-nose technology types that are available (Wilson and Baietto 2011). Composites with nanofillers also presented their role in sensing field. There have been a series of electronic sensors which utilized ZnO– TiO₂ composites or SnO “nanobelts” to detect the presence of volatile organics, including acetone, ethanol and carbon monoxide as well as WO₃- SnO₂ composites to detect the presence of ethylene gas; a hormone responsible for fruit ripening (Duncan 2011). A series of nanomaterial-based ion-sensitive field-effect transistors (ISFET) were reported as pH and acetylcholine sensors (Lee and Cui 2012). Conductive polymer composites (CPC) are insulating polymers filled with conducting nanoparticles (Kumar, Castro et al. 2012). A variety of them showed acceptable sensitivity, reproducibility and fast response to different kinds of organic vapors in addition to their low temperature and stable performance (Chen, Hu et al. 2004, Dong, Fu et al. 2004, Chen, Hu et al. 2005, Zhang, Fu et al. 2005, Chen, Hu et al. 2006, Chen, Hu et al. 2006, Eastman, Hughes et al. 1999, Chen and Tsubokawa 2000, Cakar, Moroglu et al. 2010).

4.3 Carbon Nanotubes Based Sensors

Carbon nanotubes have fascinating electrical, physical, mechanical, electronic and chemical properties. They possess high mechanical strength, persistence to chemical erosion, high electron field emission characteristics, and a one dimensional electrical transport (L.W. 2008) CNTs also have nanometer range diameters and all the atoms exposed on the surface. The high surface area to volume ratio (Iijima 1991, Dresselhaus 1992) provides plenty of sites and makes CNT well suited for physical adsorption or chemical interaction (Snow, Perkins et al. 2005, Lan, Tung et al. 2011), the nanotube electronic state is a strong function of its atomic structure, therefore; mechanical deformations (Yang and Han 2000) or chemical doping can induce strong changes in conductance. Such changes can be easily detected by electron current signals, and these properties make CNTs extremely small sensors serve as the materials which offer the possibility of excellent sensitivity and rapid response time (Peng, O'Keeffe et al. 2001), Sinha et al. (Sinha, Ma et al. 2006) have presented an extensive survey where they highlighted the CNT-based sensors application in a variety of areas, such as biomedical industry, automotive industry, food industry, environmental monitoring, agriculture and fishing industry, manufacturing industry, security and others. So far, a variety of gases such as NO_2 , NH_3 , CH_4 , O_2 , organic and inorganic vapours, have been successfully detected by SWNT-based sensors (Nguyen and Huh 2006). Someya et al. (Someya, Small et al. 2003) reported alcohol vapour sensors based on SWNT field effect transistors (FETs) and Kong et al. (Kong, Franklin et al. 2000) showed that the electrical resistance of SWCNTs was modified when exposed to gaseous molecules such as NO_2 or NH_3 . CNT based carbon monoxide (CO) sensor (Varghese, Kichambre et al. 2001, Da Silva, Fagan et al. 2004) can be used to control ventilation system in car parks.

Carbon nanotube field-effect transistors have been studied as chemical sensors (Snow, Perkins et al. 2005). They have been shown to act as promising sensing

elements in transducers based on FET architecture, e.g., pressure sensors (Stampfer, Helbling et al. 2006) and chemical sensors (Someya, Small et al. 2003, Hierold, Jungen et al. 2007).

Multi-wall CNT grown on silicon and porous array has been used as a humidity sensor (Jiang, Xiao et al. 2007). Besides medical and domestic applications for human comfort, another significant application of CNT-based humidity sensors is to monitor humidity in agriculture green house. Humidity and temperature conditions impact the quantity and quality of the product directly. In 2006, chemiresistors based on CNT/Polymer systems have been reported (Wei, Dai et al. 2006). Figure 4.1 is a diagram of a CNT sensor in acetone and water vapor atmosphere.

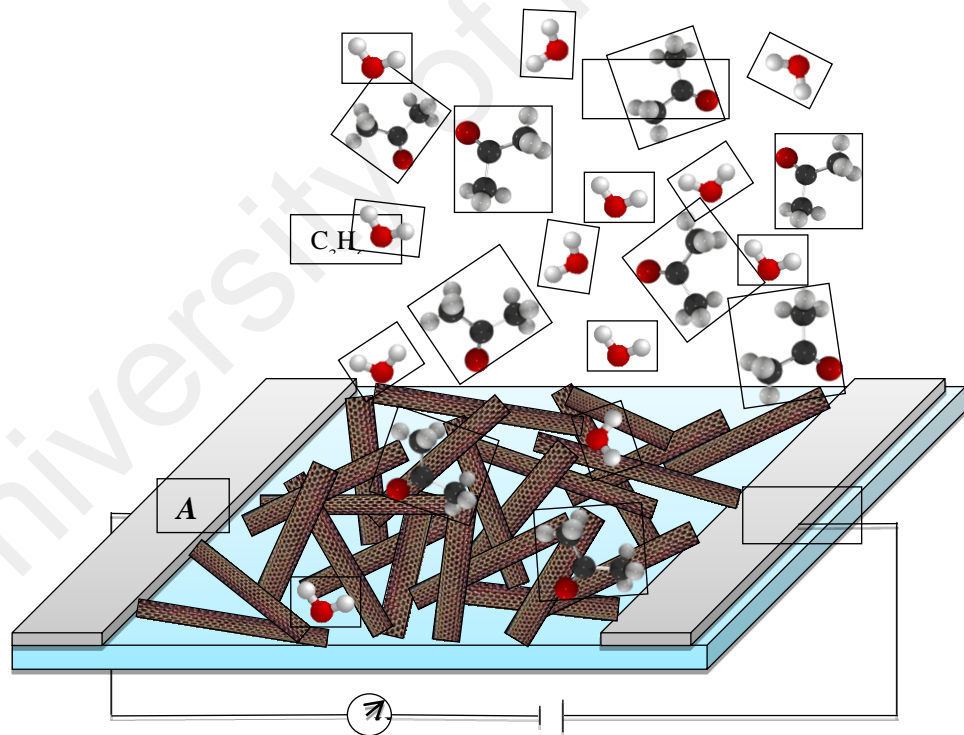


Figure 4.1: Carbon nanotube based sensor in acetone and water vapor environment.

It has been shown that CNT based biosensors may also be used to detect DNA sequences in the body (Wang, Liu et al. 2004). These instruments detect a very specific piece of DNA that may be related to a particular disease (He and Dai 2004). Pressure

sensors can be used in eye surgery, hospital beds, respiratory devices, patient monitors, inhalers, and kidney dialysis machines. These biosensors can be used to detect diseases at the ports of entry. CNT based chemical sensors can be used as electronic noses to detect hidden bombs, chemical weapons in luggage, vehicles, and aircraft (Snow, Perkins et al. 2005, Staii, Johnson et al. 2005), as these electronic noses can sense the vapors emitted by explosives and chemical weapons. They are smaller and less expensive than training bomb-sniffing dogs, which are presently used in airport, maritime ports and borders. Beside the above mentioned applications, CNT-based acoustic and optical sensors can be used for breath alcohol detection at room temperature (Penza, Cassano et al. 2004). Nano scale gas sensors have been attracting considerable attention in recent years as miniaturized sensors can lead to reduced weight, lower power consumption, and low cost. Implantable devices like future autonomous micro robots or multifunctional endoscopes (Kim, Kim et al. 2005) for minimal invasive diagnostics (Allen 2005) health monitoring, drug delivery and many other intra-corporal tasks need ultra-miniature sensors to fulfill their missions; Carbon nanotubes are very promising for the further miniaturization of sensors (Hierold, Jungen et al. 2007).

4.4 Detection of Acetone or Propanone

The organic compound acetone or propanone is the simplest ketone, it is a colorless, mobile, flammable, with a distinguished odor and taste, miscible with water and widely used in laboratories for cleaning purpose (Abdelhalim A. et al. 2015). Acetone has C_3H_6O chemical formula, it exists in nature and meanwhile it can be manufactured (Qi H. et al. 2015). By virtue of the net dipole exists in the carbon-oxygen double bond, acetone possesses most of its chemical and physical properties such as dissolving a wide range of organic chemicals (Kaur et al. 2015 and Salehi S. et al. 2014).

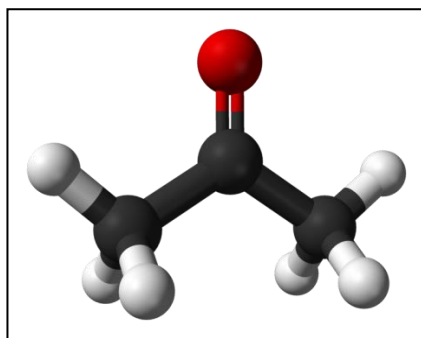


Figure 4.2: Acetone chemical structure (2013)

Acetone is susceptible an important chemical marker detected in the exhaled breath of diabetic patients (Wilson and Baietto 2011) and lung cancer (Kumar, Park et al. 2012). Hyperketonaemia disease associated with cattle can be detected by monitoring the concentrations of breath acetone (Mottram, Dobbelaar et al. 1999). As such the techniques for the monitoring of acetone are of great interest. Different methods have been used to assess breath acetone, such as semiconductor gas sensor, gas chromatography (Rezlescu, Iftimie et al. 2006), GC-Ion mobility spectrometry (GC-IMS) (Lord, Yu et al. 2002). Laser spectroscopic techniques based on cavity ringdown spectroscopy (CRS) (Wang and Mbi 2007, Wang and Sahay 2009) in addition to MOS e-nose (Ping, Yi et al. 1997).

An ample quantity of materials were recently tested for acetone gas detection, metal oxides constitute a large portion of them (Naghadeh S.B et al. 2016). For instance, tin oxide (SnO_2) based thin films prepared by different methods such as (Gong, Wang et al. 1999, Zhao, Huo et al. 2006, Patil, Patil et al. 2007, Song, Wang et al. 2012).

Zinc oxide (ZnO) prepared as thin films (Sahay 2005), hollow, solid nanofibers (Wei, Zhou et al. 2011) and quantum dots incorporated in Poly vinyl pyrrolidone (PVP) (Nath, Choudhury et al. 2010), tungsten trioxide (WO_3) thick films (Khadayate, Sali et al. 2007). In addition to $\text{Cr}_{2-x}\text{Mn}_x\text{O}_3$ powders (Pokhrel, Ming et al. 2007) and $\text{La}_{1-x}\text{Pb}_x\text{FeO}_3$ (Zhang, Qin et al. 2006), $\text{LaNi}_{1-x}\text{Ti}_x\text{O}_3$ (Yang, Huo et al. 2009)

perovskite systems. With regard to CNTs, a set of acetone sensors were built on its basis; an electrostatic layer by layer system (eLbL) formed of poly(diallyldimethylammonium chloride) (PDDA), sodium deoxycholate (DOC) and SWNT was reported by Kumar et al. (Kumar, Park et al. 2012). An array of 32 units prepared from SWCNTs doped and coated with different metals and polymers was produced for the detection of acetone and other gases in parts per million concentrations (Lu, Partridge et al. 2006). The existence of acetone and several organic vapors were estimated applying MWCNTs/Polyurethane (PU) composites (Luo, Wang et al. 2011), SWCNTs bundles planted on flexible substrates (Parikh, Cattanach et al. 2006), MWCNTs functionalized with amino-groups (Xie, Sheng et al. 2012) and others.

4.5 Experimental Details

This part presents an overview of the experimental techniques and technological pathways used to obtain MWCNT/PEO composites and fabricate samples with forms suitable for gas sensing. The instrumentation employed for the vapor production and gas sensing measurements are also introduced. The MWCNT/PEO composites were previously analyzed using a variety of techniques, including TGA and SEM techniques. Raman spectroscopy for before and after gas sensing in addition to various peaks of the composites by Fourier Transform Infra-red Spectrum (FTIR) technique have been further studied.

4.5.1 Fabrication of MWCNT/PEO Composites Sensors

MWCNT of 95% purity, >50 nm diameter and lengths between 10 and 15 μm were obtained from Chengdu Organic Chemicals Limited, China, and was used as received. The MWCNT was dispersed ultrasonically using SDS solution and thick films with 5%, 15%, 25%, 33%, 40% and 50% MWCNT/PEO loadings were fabricated as explained in chapter 3. The dried thick films were further analyzed using Raman at 532 nm and FTIR spectroscopy. To establish the acetone sensors, silver paint electrodes were applied at the edges of films of typical dimensions of 1.3 cm x 0.9 cm and about 60 μm thicknesses, the specimens were supported by glass substrates.

4.5.2 Sensing Measurement Techniques

A vapor delivery system (see figure 4.2) was used and air at different flow rates was passed through mixtures of 0%, 25%, 50%, 75% and 100% acetone/water, the purchased acetone had the molar mass of 58.08 g/mol and the density of 0.789 kg/l. The volume flow rate was increased from 10 sccm (Standard Cubic Centimeters per Minute) to 100 sccm in 10 sccm increment steps. The set-up was connected to a sourcemeter unit (Keithley -Model 2410 supported by a Labtracer 2.0 software) and the electrical responses of MWCNT/PEO composites were recorded when submitted to 20 seconds successive cycles. In each cycle, the film was exposed for 3s to the Acetone/water vapor and then left in the ambient air. The vapor was applied manually at room temperature (25°C).

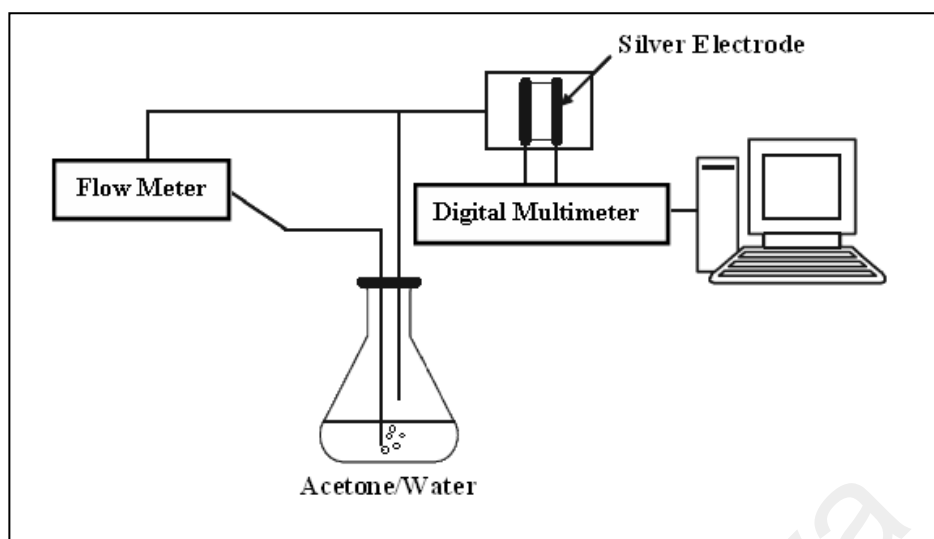


Figure 4.3: A scheme for vapor delivery and gas sensitivity measuring systems.

The previous flow rates were converted to part per million (ppm) using Raoult's law and an estimated volume chamber of 100 cm^3 .

Raoult's Law states:

The partial vapor pressure of a component in a mixture is equal to the vapor pressure of the pure component at that temperature multiplied by its mole fraction in the mixture.

This is explained for a mixture of two liquids A and B by the following equations:

$$p_A = x_A \times P_A^\circ \quad 4-21$$

$$p_B = x_B \times P_B^\circ \quad 4-22$$

P_A and P_B represent the partial vapor pressures of the constituents A and B, P_A^0 and P_B^0 , x_A and x_B are their pure vapor pressures and mole fractions respectively. To compare the sensing properties of composites with different MWCNT loadings independently of their initial resistance, the sensor response was normalized and the relative differential resistance responses (A_r) were calculated according to equation (4.3):

$$A_r = \frac{(R - R_i)}{R_i} \quad 4-23$$

Where R_i is the resistance before exposure to chemical vapor and R resistance after exposure to the chemical vapor. In order to diminish the errors, the average of five cycles for each measurement was calculated. The detailed calculation for the acetone/ethanol concentrations is shown in Appendix B.

4.5.3 Fourier Transform Infrared Spectroscopy (FTIR) Basics

Fourier Transform Infrared Spectroscopy (FTIR) is a powerful tool for identifying types of chemical bonds in chemical molecules which is either organic or inorganic. Molecular bonds vibrate at various frequencies depending on the elements and the type of bonds. The covalent bonds in molecules are usually simulated to stiff springs that can be stretched and bent, at the same time; any given bond has several specific frequencies at which it can vibrate.

When an infrared light interacts with the matter, photon energies associated with the infrared electromagnetic radiation are not large enough to excite electrons, but may induce vibrational excitation of covalently bonded atoms and groups. As a result, chemical bonds will stretch, contract and bend. The energy corresponding to these transitions between molecular vibrational states is generally 1-10 kcal/mole which corresponds to the infrared portion of the electromagnetic spectrum. A chemical functional group tends to adsorb infrared radiation in a specific wavenumber range

regardless of the structure of the rest of the molecule. Thus, the plot of a compound's IR absorption versus frequency is its "fingerprint" which identifies the material structure.

In this view, it is also important to note that:

- a) Infrared spectra can be applied to solids, liquids, and gasses. Liquids are usually examined as a thin film sandwiched between two polished salt plates (NaCl is transparent to IR radiation unlike glass).
- b) The strength of the absorption is proportional to the concentration; FTIR can be used for some quantitative analyses.
- c) The greater the masses of attached atoms, the lower the IR frequency at which the bond will absorb.
- d) Stretching frequencies are higher than corresponding bending frequencies (It is easier to bend a bond than to stretch or compress it).
- e) Because each interatomic bond may vibrate in several different motions (stretching or bending), individual bonds may absorb at more than one IR frequency.
- f) Symmetrical vibrations do not cause absorption of IR radiation. For example, neither of the carbon-carbon in ethene or ethyne absorbs IR radiation.

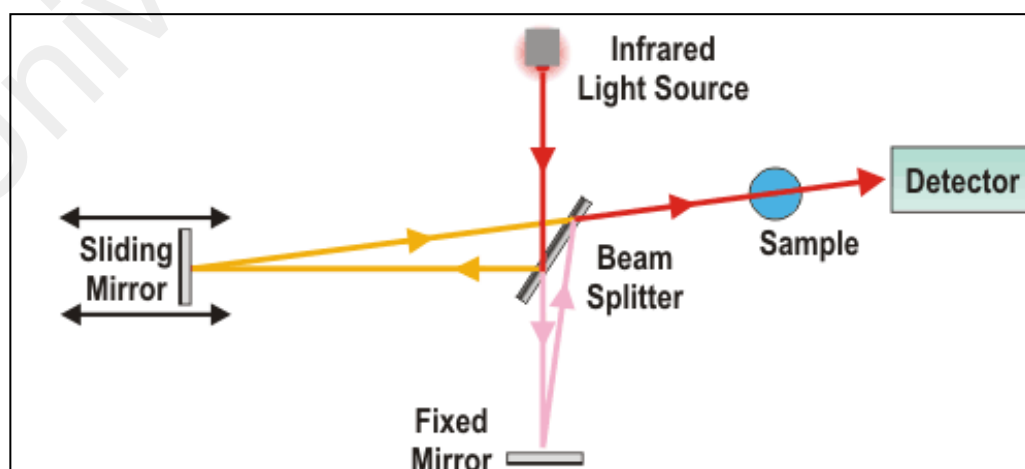


Figure 4.4: Schematic illustration of FTIR system.

The core of the FTIR synthesis an infrared light source generates an infrared beam, a beamsplitter splits the incoming infrared beam into two optical beams. One beam is reflected of a flat fixed mirror. Another beam is reflected of a flat mirror which travels a very short distance (a few millimetres) away from the beamsplitter. The two reflected beams are recombined when they meet together at the beamsplitter. The recombined signal results from the interfering with each other and contains every infrared frequency. After interaction with the sample, some specific frequencies of energy are adsorbed. The beam finally arrives at the detector and a computer performs the decoding of the transmitted signal with a well-known mathematical technique based on Fourier transformation (see figure 4.4). A sophisticated Thermo Scientific Nicolet iS10 FT-IR spectrometer furnished with fast recovery deuterated triglycine sulfate (DTGS) detector was utilized in the present analysis.

A typical infrared spectrum can be divided into two regions, the right half of the spectrum, below 1500 cm^{-1} , which is labeled as the fingerprint region and has a complex looking. The fingerprint region contains bond stretches between backbone atoms and is mostly ignored. Almost every organic compound produces a unique pattern in this complex lower region. In contrast, the second region which is the left half of the spectrum above 1500 cm^{-1} , contains peaks that correspond to stretches in functional groups, and is all that is usually needed to determine molecular structure. It is significant for the identification of the source of an absorption band to analyze the band's intensity (weak, medium or strong), shape (broad or sharp), and position (cm^{-1}) in the spectrum. Figure 4.5 presents a summary of bond types and their appearance in the spectrum.

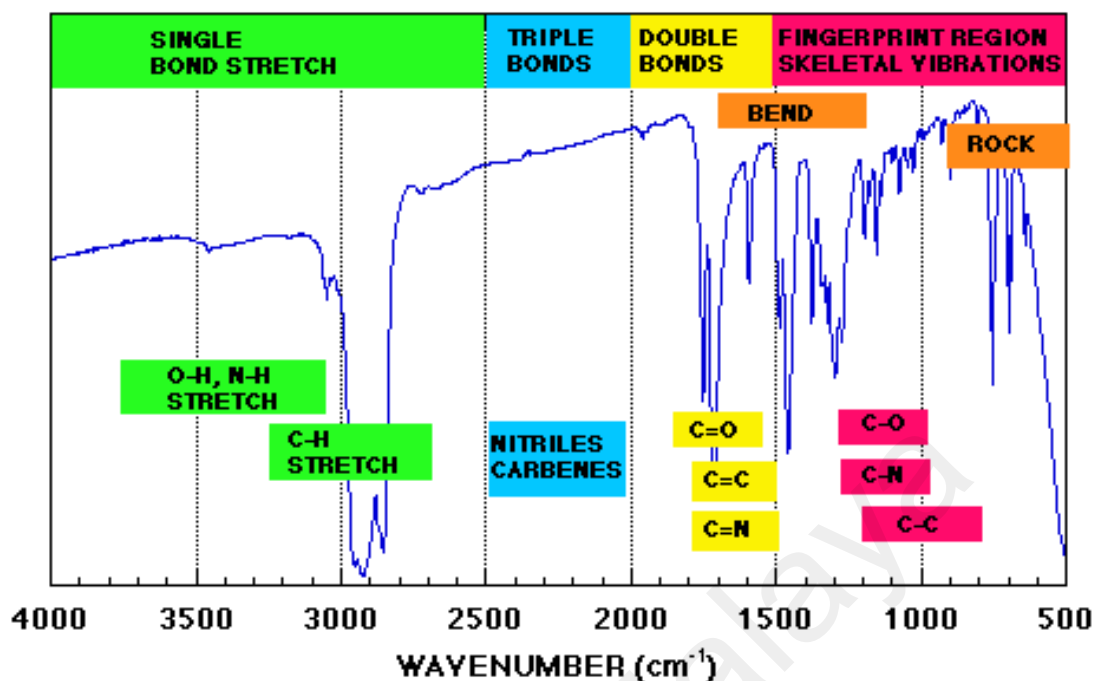


Figure 4.5: A typical FT-IR spectrum (2012).

4.6 Thick Films Characterization

4.6.1 Raman Characterization

Figure 4.6 shows the Raman spectra for PEO/MWCNT acetone sensors before (figure 4.6(a)) and after (figure 4.6(b)) sensing measurements. Before sensing (figure 4.6(a)) for the prepared film, a previous discussion was deliberated in chapter 3.

After sensing (figure 4.6(b)), illustrates the same features as (figure 4.6(a)). However D-band showed no frequency shifting whereas, G and G' exhibited a slight down-shifting from 1583.3 cm^{-1} to 1576.1 cm^{-1} for G peak and from 2699 cm^{-1} to 2691 cm^{-1} for G' peak. The G' down shifting is a result of tensile strain deformation (Ma, Liu et al. 2009). This is usually a sign of matrix swelling. Interestingly, 25wt.% film showed much higher crystallinity after sensing operation, where I_d/I_g decreased from 0.60 to 0.47. Whereas, the rest of the sensors showed higher disorder after sensing.

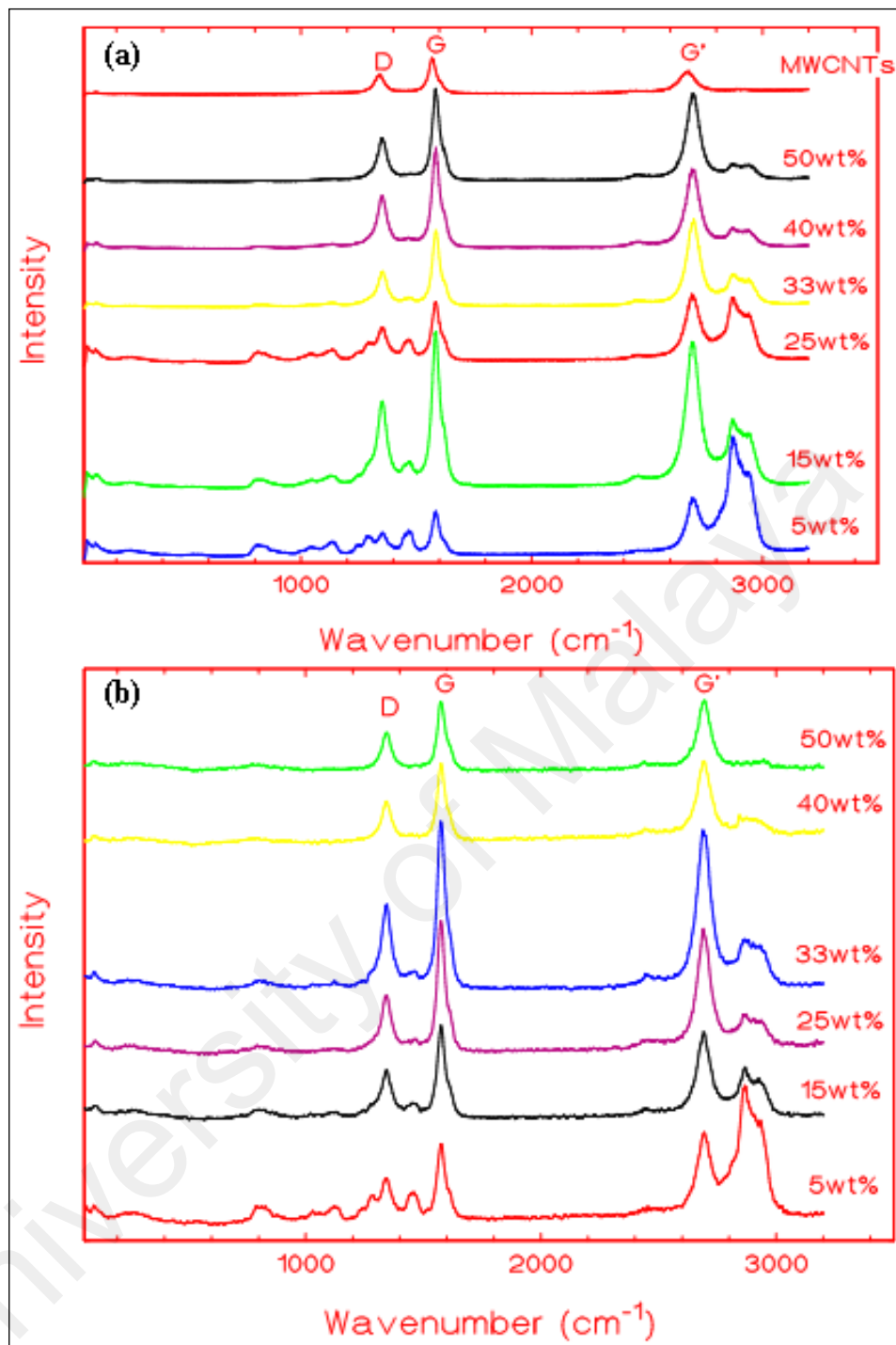


Figure 4.6: Raman spectroscopy of MWCNT/PEO films (a) Before sensing measurements. (b) After sensing measurements.

4.6.2 Fourier Transform Infra-Red (FTIR) Characterization

Figure 4.7 shows the FTIR spectra before sensing measurements, Figure 4.7(a) obtained for MWCNT, SDS, PEO and (5%, 15%, 25%, 33%, 40% and 50%) MWCNT/PEO composites in the wavenumber range 650 to 4000 cm⁻¹ and (figure

4.7(b)) is a clearer picture of the same components; PEO and (5%, 15%, 25%, 33%, 40% and 50%) MWCNT/PEO composites in the wavenumber range 650 to 1600 cm^{-1} . The right half of the spectra, below 2000 cm^{-1} , normally contains many peaks of varying intensities, many of which are not readily identifiable. The lowest spectrum in figure 4.7(a), presents pristine MWCNT, generally it does not show obvious absorption peaks in FTIR analysis, this result is consistent with previous researches (Muraliganth, Murugan et al. 2008, Morávková, Trchová et al. 2012). Typical bands of the anionic surfactant SDS were observed at corresponding wavenumbers, such as CH_2 symmetric stretching at 2842 cm^{-1} , CH_2 asymmetric stretching at 2909 cm^{-1} , CH_2 scissoring mode at 1463 cm^{-1} , the SO_2 asymmetric vibrational feature is the most intense band in the SDS spectrum, it is a combination of several overlapping peaks, and it is located at 1216 cm^{-1} and the SO_2 symmetric vibrational feature is observed at 1089 cm^{-1} (Viana, da Silva et al. 2012).

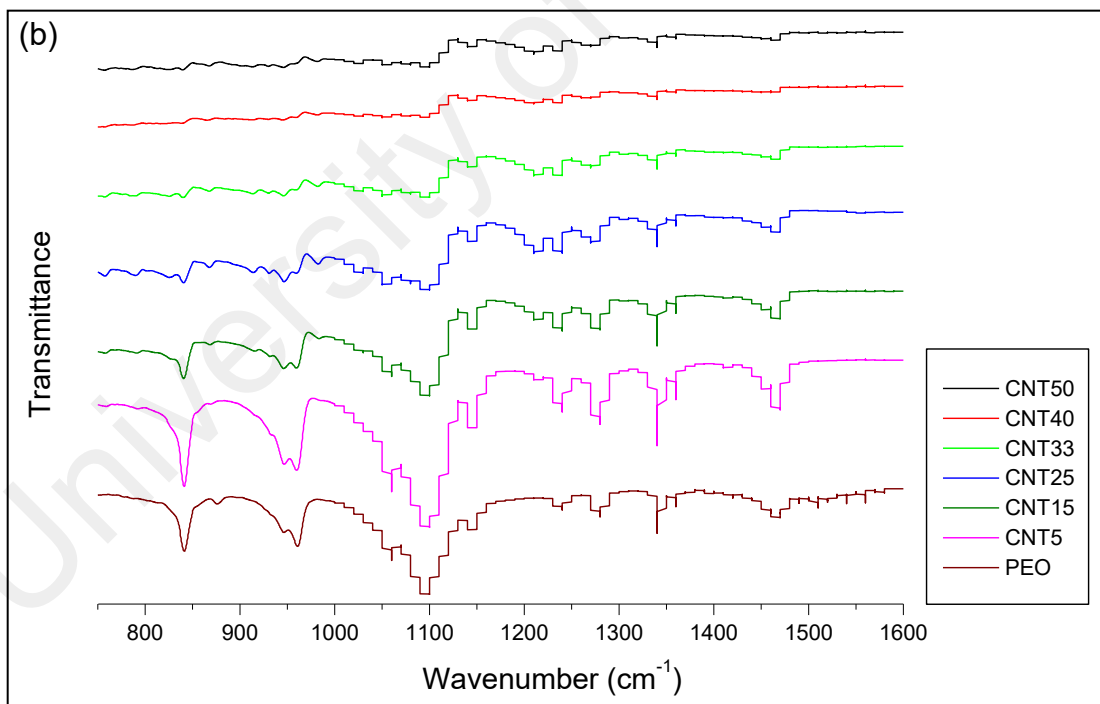
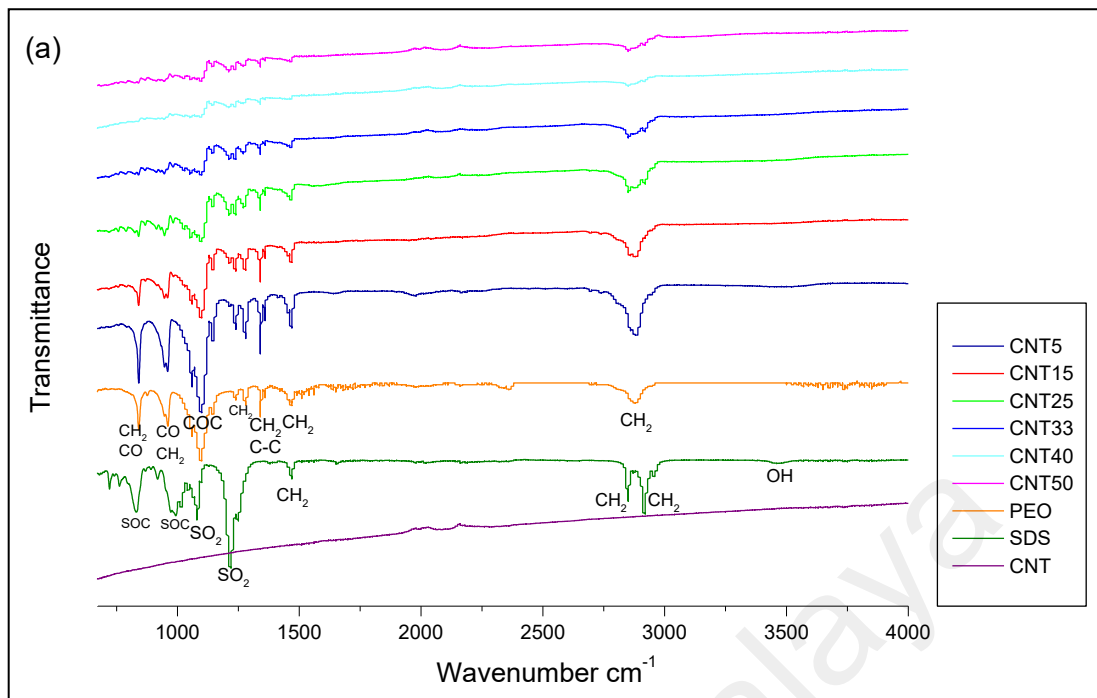


Figure 4.7: FTIR spectra before sensing measurements (a) Obtained for MWCNT, SDS, PEO, and (5%, 15%, 25%, 33%, 40% and 50%) MWCNT/PEO composites in the wavenumber range 650 to 4000 cm^{-1} . (b) A clearer picture of PEO, and (5%, 15%, 25%, 33%, 40% and 50%) MWCNT/PEO composites in the wavenumber range 650 to 1600 cm^{-1} .

The peaks due to -S-O-C- vibration appear at 984 cm^{-1} and 827 cm^{-1} (Antony, Sherine et al. 2010). A slight broad absorption band at 3471 cm^{-1} might correspond to O-H stretching vibration (Coates 2000) of trace water absorbed by the surfactant. Pure PEO shows a large, broad band of CH_2 stretching between 2960 and 2770 cm^{-1} , corresponding to overlapped symmetric and asymmetric CH_2 stretching modes, another two clear CH_2 vibrational modes appear at 1463 cm^{-1} which corresponds to asymmetric CH_2 bending and 1352 cm^{-1} related to symmetric CH_2 wagging and some C-C stretching (Manoratne, Rajapakse et al. 2006). The absorption at 1278 cm^{-1} (Sekhon, Singh et al. 1995) and 1240 cm^{-1} (Kumar, Ravi et al. 2011) represent CH_2 twisting and the strong peak at around 1101 cm^{-1} is identified as the C-O stretching mode of the characteristic of ether linkage (C-O-C) (Kumar, Ravi et al. 2011). The band at 840 cm^{-1} is primarily due to the CH_2 rocking motion with a little contribution from C-O stretching motion of PEO, while the band at 953 cm^{-1} originates primarily in the C-O stretching motion with some CH_2 rocking motion (Intarakamhang 2005). Table 4.1 summarizes SDS, H_2O , PEO and acetone FTIR vibration bands. From the fourth curve (5% CNT) and above, the curves are becoming smoother with the carbon nanoparticles content.

Table 4.1: The assignment of the vibrational bands of SDS, H₂O, PEO and Acetone.

Component	Vibrational bands (cm^{-1})	Assignments	Reference
SDS	2909	CH_2 asymmetric stretching	(Viana, da Silva et al. 2012)
	2842	CH_2 symmetric stretching	(Viana, da Silva et al. 2012)
	1463		(Viana, da Silva et al. 2012)
	1216	CH_2 scissoring	(Viana, da Silva et al. 2012)
	1089	SO_2 asymmetric vibration	(Viana, da Silva et al. 2012)
	984 and		(Antony, Sherine et al. 2010)

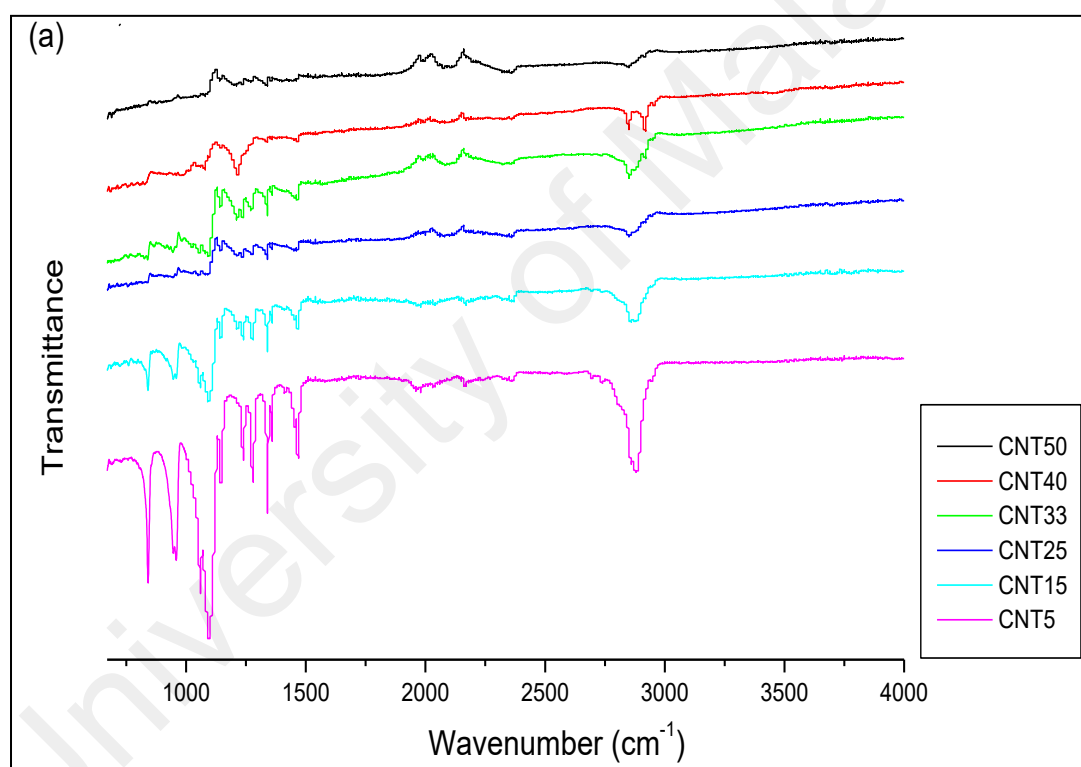
	827	SO ₂ symmetric vibration -S-O-C- vibration	
H₂O	3471	O-H stretching vibration	(Coates 2000)
PEO	2960-2770 1463 1352 1278 1240 1101 953 840	CH ₂ symmetric and asymmetric stretching CH ₂ asymmetric bending CH ₂ wagging and some C-C stretching. CH ₂ twisting CH ₂ twisting C-O stretching C-O stretching and some CH ₂ rocking CH ₂ rocking and some C-O stretching	(Manorathne, Rajapakse et al. 2006) (Manorathne, Rajapakse et al. 2006) (Sekhon, Singh et al. 1995) (Kumar, Ravi et al. 2011) (Kumar, Ravi et al. 2011) (Intarakamhang 2005) (Intarakamhang 2005)
Acetone	<i>In plane</i> 2950 2920 1738 1444 1364 1064 790	CH ₃ asymmetric stretch CH ₃ symmetric stretch C=O stretch CH ₃ asymmetric deformation CH ₃ symmetric deformation CH ₃ in-plane rock	(Badr and Mahmoud 2005) (Badr and Mahmoud 2005)

	488	CH3-C stretch	(Badr and Mahmoud 2005)
	<i>Out of plane</i>	CCC deformation	(Badr and Mahmoud 2005)
	2990	CH3 asymmetric stretch	(Badr and Mahmoud 2005)
	1444	CH3 asymmetric deformation	(Badr and Mahmoud 2005)
	1200	CH3 out-plane rock	

The peak 953 cm^{-1} in PEO is broad ($921\text{-}972\text{ cm}^{-1}$) and formed of two main peaks; 946 and 959 cm^{-1} . In the composites, the intensities of the two peaks are becoming smaller and the second peak is decreasing compared to the first whenever the MWCNT portion is increased. A very small peak at 874 cm^{-1} in PEO spectrum had a slight shifting to 868 cm^{-1} in the composite films. The broad peak ($1006 - 1158\text{ cm}^{-1}$) with the highest peak at 1101 cm^{-1} and representing C-O ether stretching, exhibited smaller intensities in the samples with higher filler percentages. The diminution of the FTIR intensities suggests the change in the dipoles polarities which in turn could be explained by the electron exchange. The CH_2 stretching broad peak at ($2770\text{-}2960\text{ cm}^{-1}$) in PEO showed a deformation in the peak shape and a decrease in the intensity whenever the filler percentage augments. Thus, suggest an interaction and a charge transfer between the two composite constituents; the nanotubes and the polymer matrix (Lefrant, Baibarac et al. 2009). The obtained FTIR results are consistent with the results of SEM, Raman and TGA analysis.

Figure 4.8 presents the FTIR spectroscopy after acetone sensing. Figure 4.8 (a) presents FTIR after sensing of 5%, 15%, 25%, 33%, 40% and 50% MWCNT/PEO composites sensors, whereas figure 4.8(b) shows FTIR spectroscopy before and after sensing of 5%, 15% and 25% composites. Figure 4.8(c) shows FTIR spectroscopy

before and after sensing of 33%, 40% and 50% composites. It is obvious that no new appearing or disappearing peaks are observed after sensing operation. It is worth to notice that most of the acetone peaks (see table 4.1) (Badr and Mahmoud 2005) fall within the composites bands which could be obscured. Three acetone bands, 2990 cm^{-1} assigned for CH_3 out of plane asymmetric stretch, 1200 cm^{-1} assigned for CH_3 out of plane rock and the characteristic 1738 cm^{-1} assigned for $\text{C}=\text{O}$ functional group in addition to the OH band representing H_2O , are not observed in all the spectra after acetone/water vapor sensing.



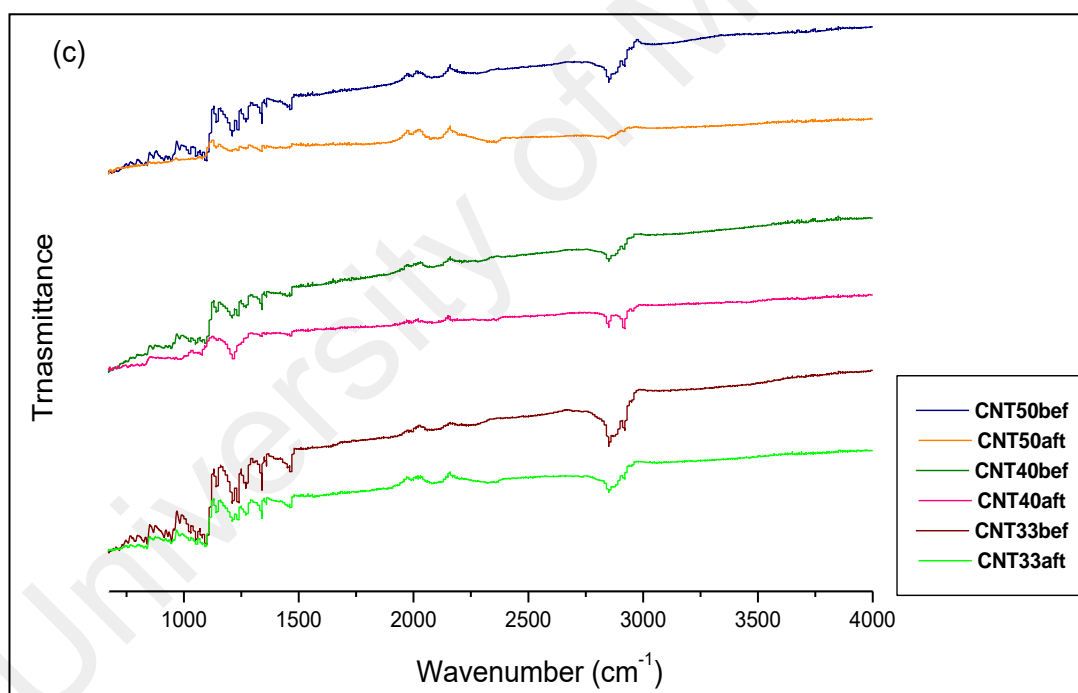
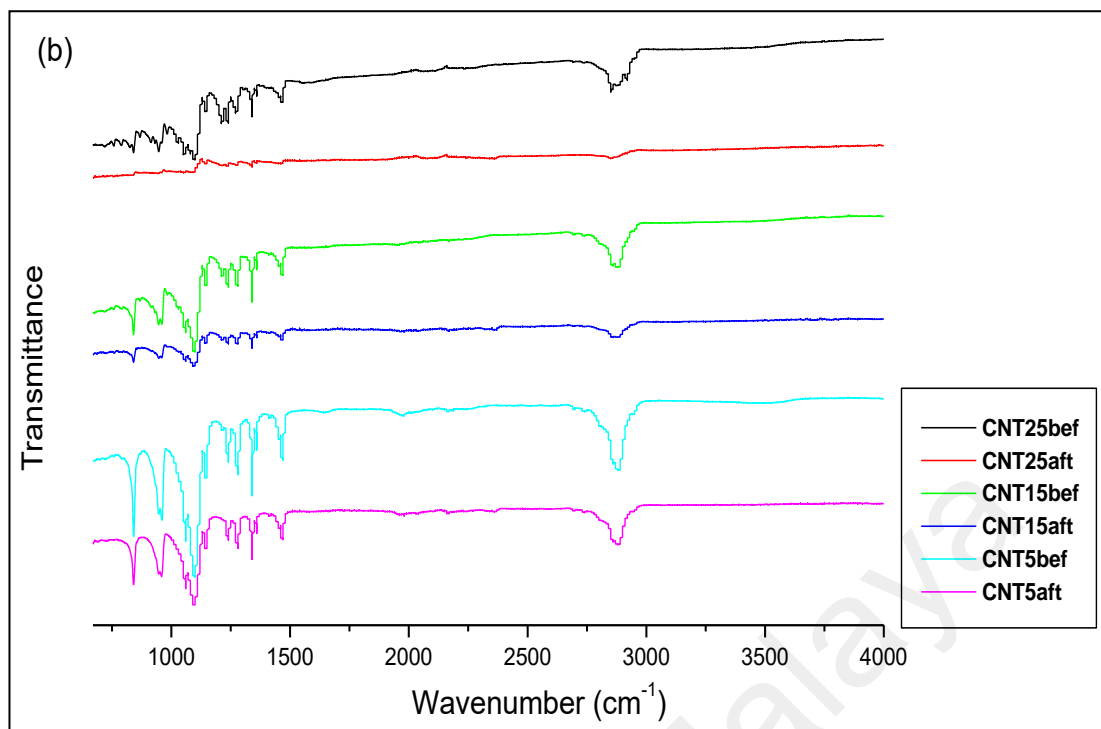


Figure 4.8: FTIR spectroscopy of (a) 5%,15%, 25%, 33%, 40% and 50% MWCNT/PEO after sensing. (b) 5%, 15% and 25% MWCNT/PEO composites before and after sensing (c) 33%, 40% and 50% MWCNT/PEO composites before and after sensing.

The intensity of the C-O ether band showed a decrement, whereas the CH₂ stretching broad band showed a decrease in intensity and deformation in shape in all curves after acetone vapor sensing, more obviously in 40% CNT sensor. The lack of acetone and water peaks in the graph indicates the evaporation of acetone/water gas which proves the reproducibility of the sensors. On the other hand, the reduction of the intensity and the deformation of the shape of the peaks, suggests a decrement in the polarity of the bonds resulted from charge transfer and current circulation through the sensor films.

4.7 Results and Discussion

4.7.1 Acetone Sensing Results and Discussion

Figure 4.9 shows the time-dependent resistance responses of the MWCNT/PEO composites upon exposure to four ranges of acetone parts per million concentrations. The sensors were submitted to 20 seconds successive cycles. In each cycle, they were exposed for 3 s to acetone vapor and then left in the ambient air. Figure 4.9 (a), (b), (c), (d) and (f) are for 5%, 15%, 25%, 33%, 40% and 50% MWCNT/PEO composites, respectively. The resistance variation of each sensor when exposed to three different acetone vapor concentrations was plotted in figure.4.9. Here, the clear reproducible patterns suggest the vapor sensor surface reaction while the gas is on and a fast recovery of a few seconds once it is off. The resistance variation ΔR ($R-R_i$) reached $1.44 \times 10^6 \Omega$ for 5wt% and 1.083Ω for 50wt% in figure 4.9 (a). The value of ΔR depended inversely with the mass of the filler content and proportionally with the vapor concentration in nearly all the films. Kumar et al. built a system based on CNTs built on electrostatic layer by layer technique. This system provided reproducible patterns during acetone sensing with a response of about 0.1 and a recovery time of few minutes (Kumar et al. 2012 and Park et al. 2012).

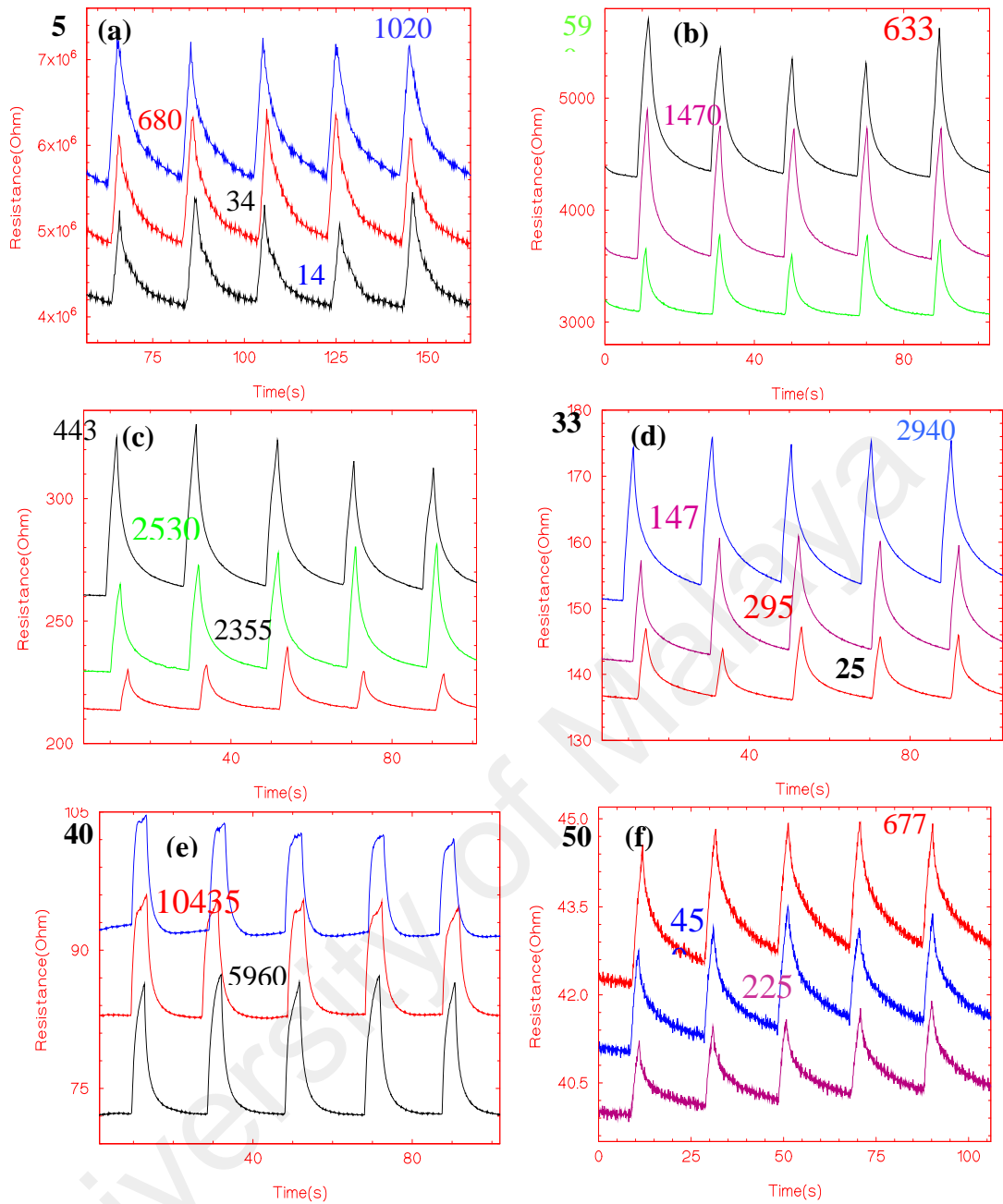


Figure 4.9: Five rounds of electrical response of (a) 5wt%, (b) 15wt% (c) 25wt% (d) 33wt%, (e) 40wt% and (f) 50wt MWCNT/PEO films. Each composite was exposed to three acetone vapor concentrations (The numbers given within the graphs represent the acetone vapor ppm concentration).

In order to compare the degree of resistance modification in all the sensors while the acetone concentration is fixed, the variation of resistance of each sample is measured (figure 4.10 (a) and (b). Figure 4.10 (a) is for the lowest acetone concentration (113 ppm) and figure (b) is for the highest acetone concentration (14900 ppm).

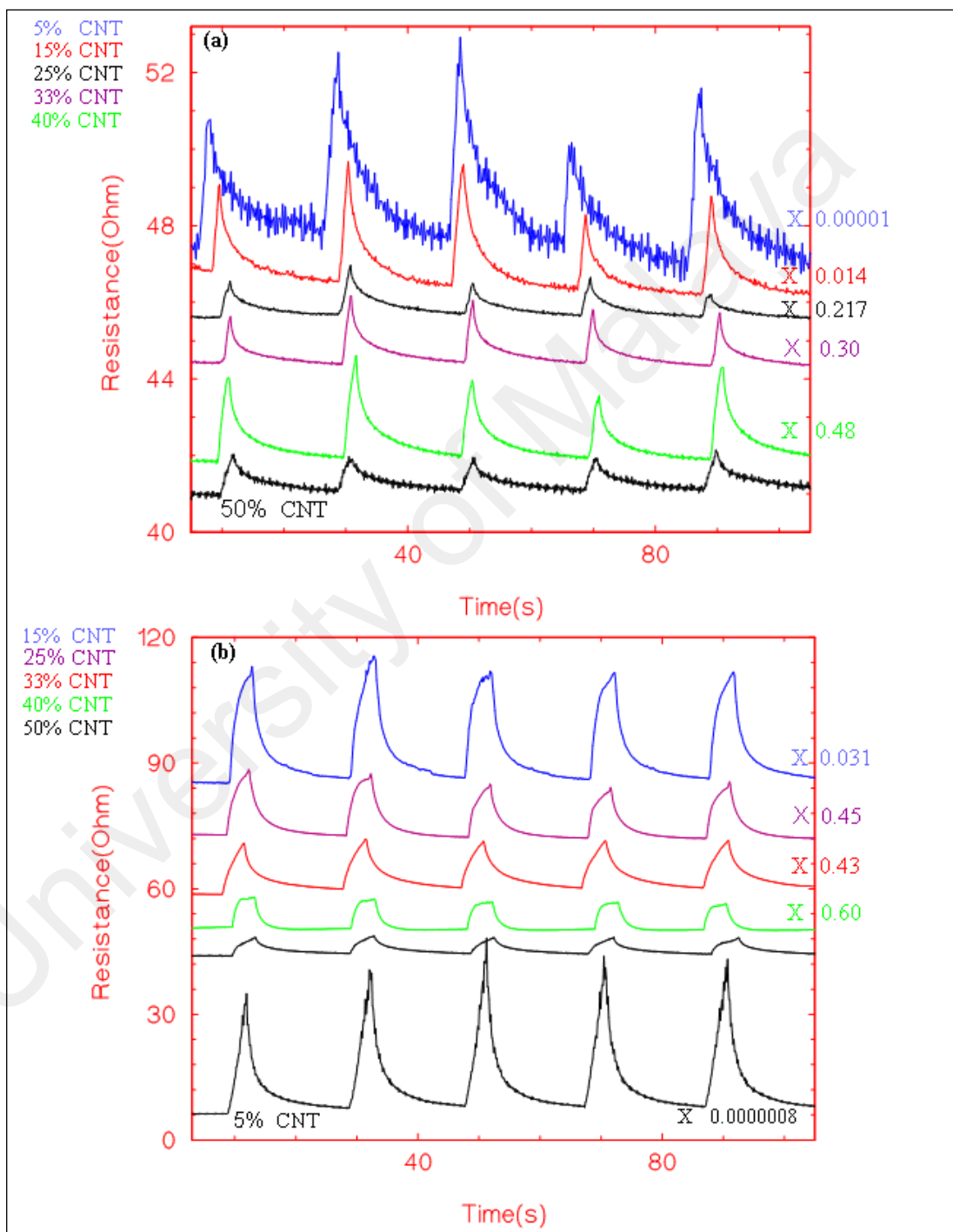


Figure 4.10: Five successive rounds of electrical response of:5wt%, 15wt% and 25wt%.33wt%, 40wt% and 50wt MWCNT/PEO films in (a) low concentration (113 ppm) acetone and (b) high concentration (14900 ppm) acetone. Some adjustments were made in the Y axis in order to obtain a clear view are mentioned at the right side of the curves.

The reproducible response to 7500 ppm acetone gas of three thin films composites of carbon nanotubes/polyurethane (PU) of initial resistances: 63.2, 86.2 and 241.7 Ω and different soft segments are given in (Luo, Wang et al. 2011). Where, acetone gave a much less response compared to chloroform and benzene. Amino-groups functionalized MWCNTs films (18% amino) demonstrated a relative resistance change of slightly more than 1% when exposed to 200 ppb acetone (Xie, Sheng et al. 2012). Figure 4.11 shows the sensing response rates of (5%, 15%, 25%, 33%, 40% and 50%) MWCNTs/PEO thick films sensors as a function of acetone concentration (ppm), each graph represents a certain range of concentration as in table 4.2, variation in acetone concentration was obtained from the different air flow rates through prepared acetone/water solutions.

Table 4.2: Acetone concentration ranges related to figure 4.11 corresponding graphs.

Figure Number	Range Number	Range of acetone concentration (ppm)
Figure.3(a)	Range 1	113 – 1130
Figure.3(b)	Range 2	295 – 2950
Figure.3(c)	Range 3	633 – 6330
Figure.3(d)	Range 4	1490 – 14900

The obvious trend observed was that the response increased with decreasing MWCNT loadings and linearly increased with the acetone concentration. The response and acetone concentration were linearly related when sensed by SnO₂ thin films in 2-8 ppm range (Zhao, Huo et al. 2006), WO₃ thick film showed the same linearity in the range 25-75 ppm acetone (Khadayate, Sali et al. 2007). Meanwhile cobalt-doped SnO₂ thin films response to acetone vapour increased with increment of temperature where the gas concentration was fixed (Patil, Patil et al. 2007).

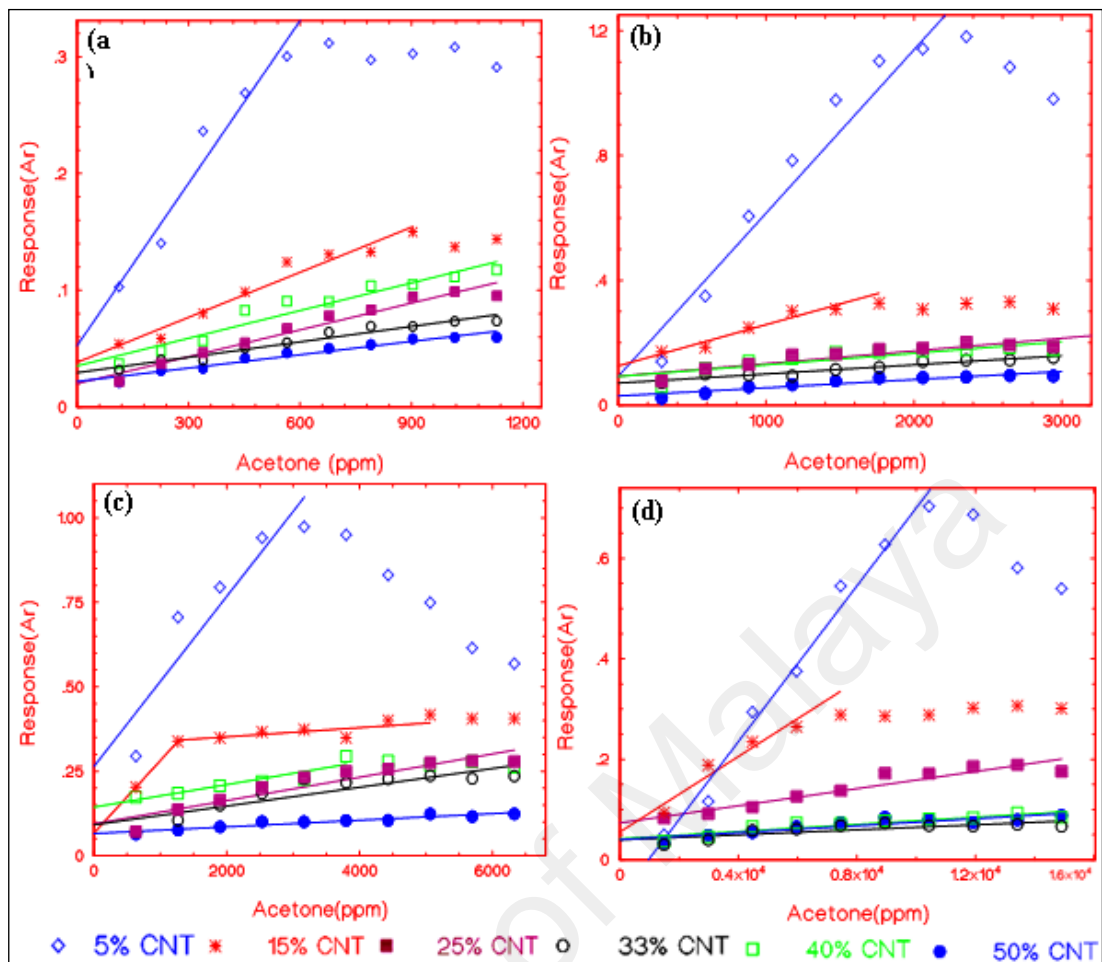


Figure 4.11: Sensing response rates of (5%, 15%, 25%, 33%, 40% and 50%) MWCNTs/PEO thick films versus acetone four ranges of concentration (ppm).

Among our samples, 5wt. % had the top response, which linearly increased with the acetone concentration, its very promising response reached 0.31 at about 680 ppm (figure 4.11 (a)) and saturated beyond that. The current needed, was about 3 μ A. Meanwhile, 15wt. % showed the same trend as 5wt. %. However, its response was less and it saturated at higher point such as in range 1 (790 ppm). When the filler portion increased, the response decreased in all the sensors except for 40wt. % thick film. Accordingly, 50wt. % had the smallest A_r among the other films, it had the response of 0.059 at 1015 ppm and the current needed was 4.9 mA. The saturation level was attained faster in the composites with lower filler loading. However, 33%, 40% and 50wt. % sensors did not show a clear saturation in all graphs. In a previous research, zinc oxide thin films showed saturation at 3000 ppm when exposed to acetone vapor at

275°C. While at higher temperature (350°C) the response increased to a farther point of 4000 ppm, then it declined (Sahay 2005). To this extent, it can be inferred that the tested composites with lower MWCNTs percentages are appropriate for sensitivity estimation, whereas the composites with elevated MWCNTs portion are appropriate for dynamic motion measurements.

As it is obvious in figure 4.11 each sensor response curve fits a straight line function $y=ax+b$, Figure 4.12 depicts $\log(\text{response } (A_r))$ versus acetone concentration. Thus, it emphasizes the linearity of the response increment, notably in the fitted part of the graphs.

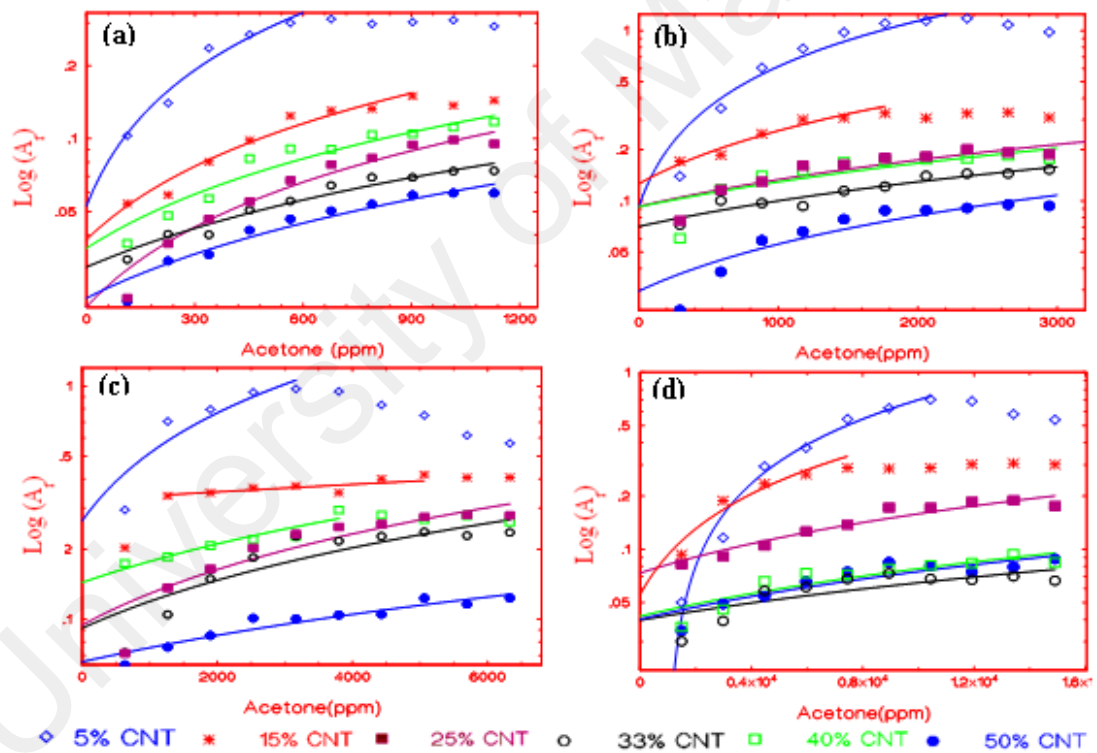


Figure 4.12: Response logarithm of (5%, 15%, 25%, 33%, 40% and 50%) MWCNTs/PEO composites versus acetone four ranges of concentrations (ppm).

The sensor sensitivity is the variation of the response with regard to the concentration of acetone. Hence, the gradient of each straight line defines the sensitivity of the corresponding sensor in the related range of concentration. Figure 4.13 displays the sensitivity of the prepared composites against MWCNT ratios. From the first glance,

5% CNT composite, which possess the lowest CNTs portion has the highest sensitivity in all acetone concentration ranges (reached 4.64×10^{-4} in range 1), followed by 15% CNT with second highest sensitivity in almost all the ranges. Nearly the same trend was in the rest of the sensors, the sensitivity decreased when the filler portion augments. In 50% CNT the sensitivity attained its lowest measure of 3.46×10^{-6} in range 4.

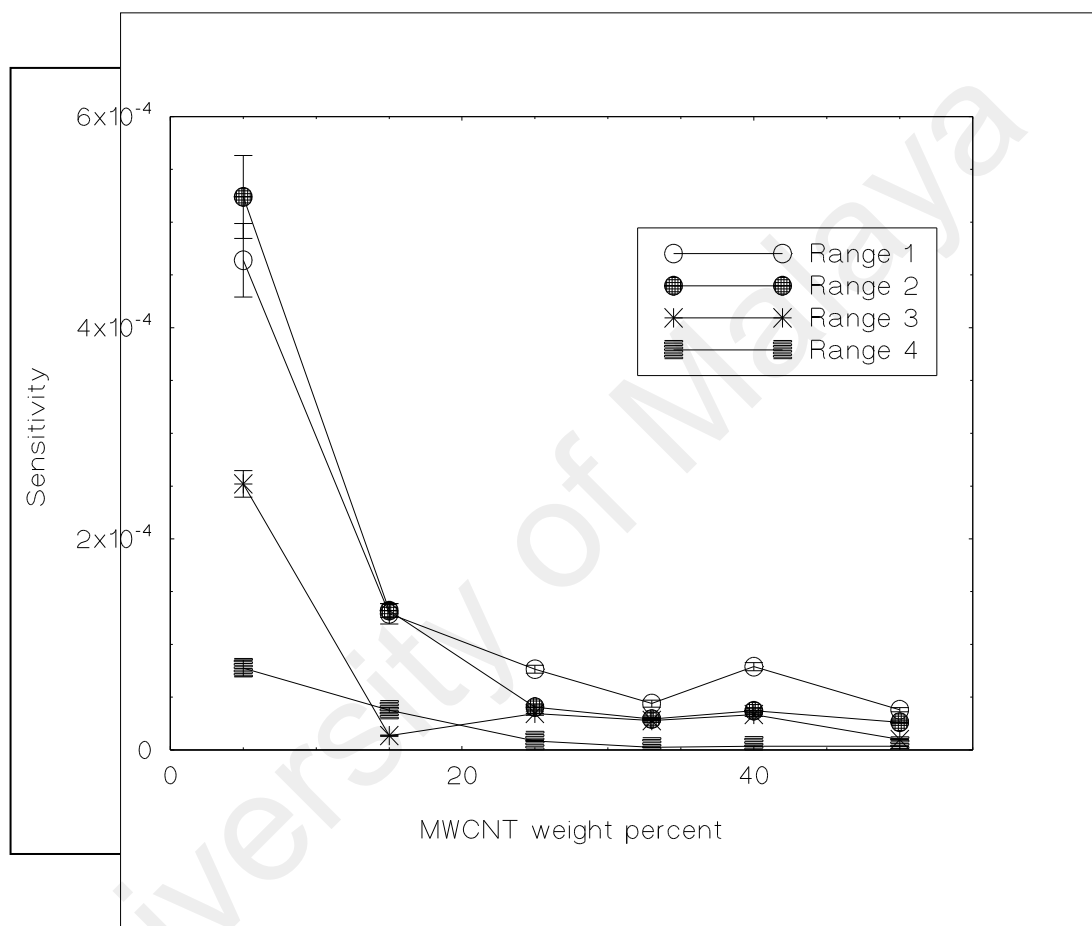


Figure 4.13: Sensitivity versus carbon nanotubes concentration in four ranges of acetone vapour ppm concentrations.

One of the necessary attributes which identifies the capability of a sensor, is its response time, usually expressed as the resistance rise and fall time. In this context, the resistance rise and fall time (is the time to rise to 90%, then fall back to 10% of its maximum value) of MWCNT/PEO composites were calculated for 565 ppm acetone (table 4.3).

Specimen with 15wt% had the shortest response time, 1.82 s to rise and 7.02 s was needed to fall back. Obtaining the signal in less than 2 seconds is absolutely a satisfaction. The time taken for the resistance to fall down equal almost four times the time to rise. This can be predicted since water is much less volatile compared to acetone. The acetone liquid was mixed with water simulating human respiration vapor. Our further investigations revealed that H₂O has its influence on the sensors resistances as well. The time taken by ZnO nanofibers to reach 90% of the entire resistance change was 12-17 s for response and 11-23 s for recovery (Wei, Zhou et al. 2011). Quantum dots of ZnO provided a much shorter response time compared with ZnO thin film in acetone sensing field (Nath, Choudhury et al. 2010).

In thick-film sensors (as in this research) the layer itself is a porous body, so the inner surface also becomes a working surface. Therefore, the gases diffuse into it lead to a good sensitivity. It was reported that conductivity *versus* thickness behavior of SWCNT networks made of four different types of functionalized nanotubes is similar to those of percolating networks (conductivity versus CNT ratio) (Gracia-Espino, Sala et al. 2010).

Table 4.3: The resistance and its rise and fall time in MWCNT/PEO composites (565 ppm).

CNT wt.%	Resistance (Ω)	Rise time-Fall time (s)
5	4 x 10 ⁶	2.34-12.48
15	3332	1.82-7.02
25	209	2.08-10.4
33	138	1.82-9.36
40	87	2.08-8.58
50	41	2.6-14.29

4.7.2 Water Vapor Sensing Results and Discussion

Resistance continual change of (5%, 15%, 25%, 33%, 40% and 50%) MWCNT/PEO composites when 160 ppm flow of water vapour goes on and off on the surfaces of the composites is shown in (figure 4.14). Well reproducible patterns were obtained with no change in the intensity after successive cycles except for 50% CNT which did not reveal a very obvious peaks. 5% CNT curve contains a chain of noise fluctuations while the resistance was in its diminishing period. We rely that to the existence of a small amount of carbon nanotubes in the matrix. Hence, a slight change in the surface environment affects the current circulation.

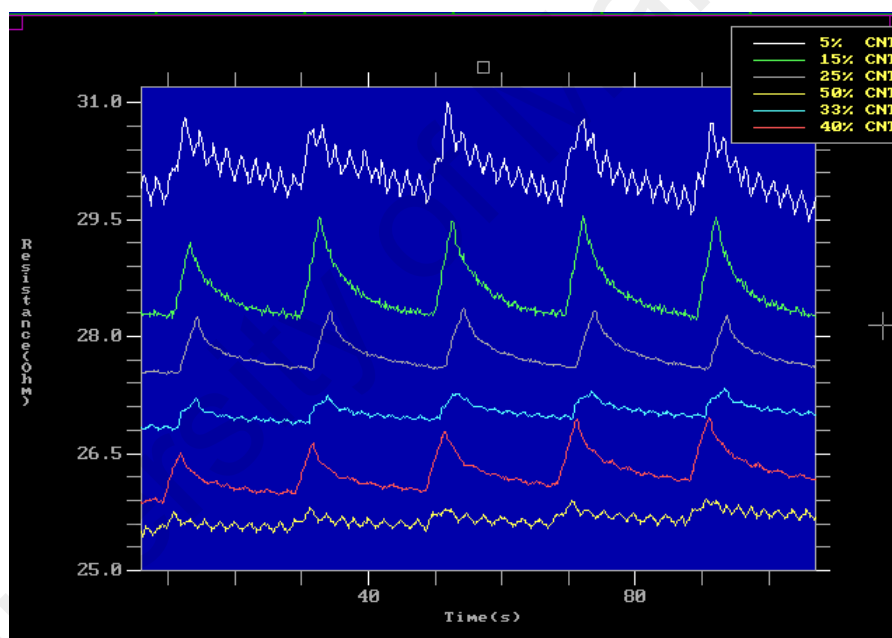


Figure 4.14: Five successive rounds of electrical response of: 5wt%, 15wt% and 25wt%. 33wt%, 40wt% and 50wt MWCNT/PEO film sin 160 ppm water vapour. Some adjustments were made in the Y axis in order to obtain a clear view are mentioned at the right side of the curves.

The response of MWCNT/PEO sensors to H₂O vapour is given in figure 4.15.

They exhibit the same trend as acetone vapor.

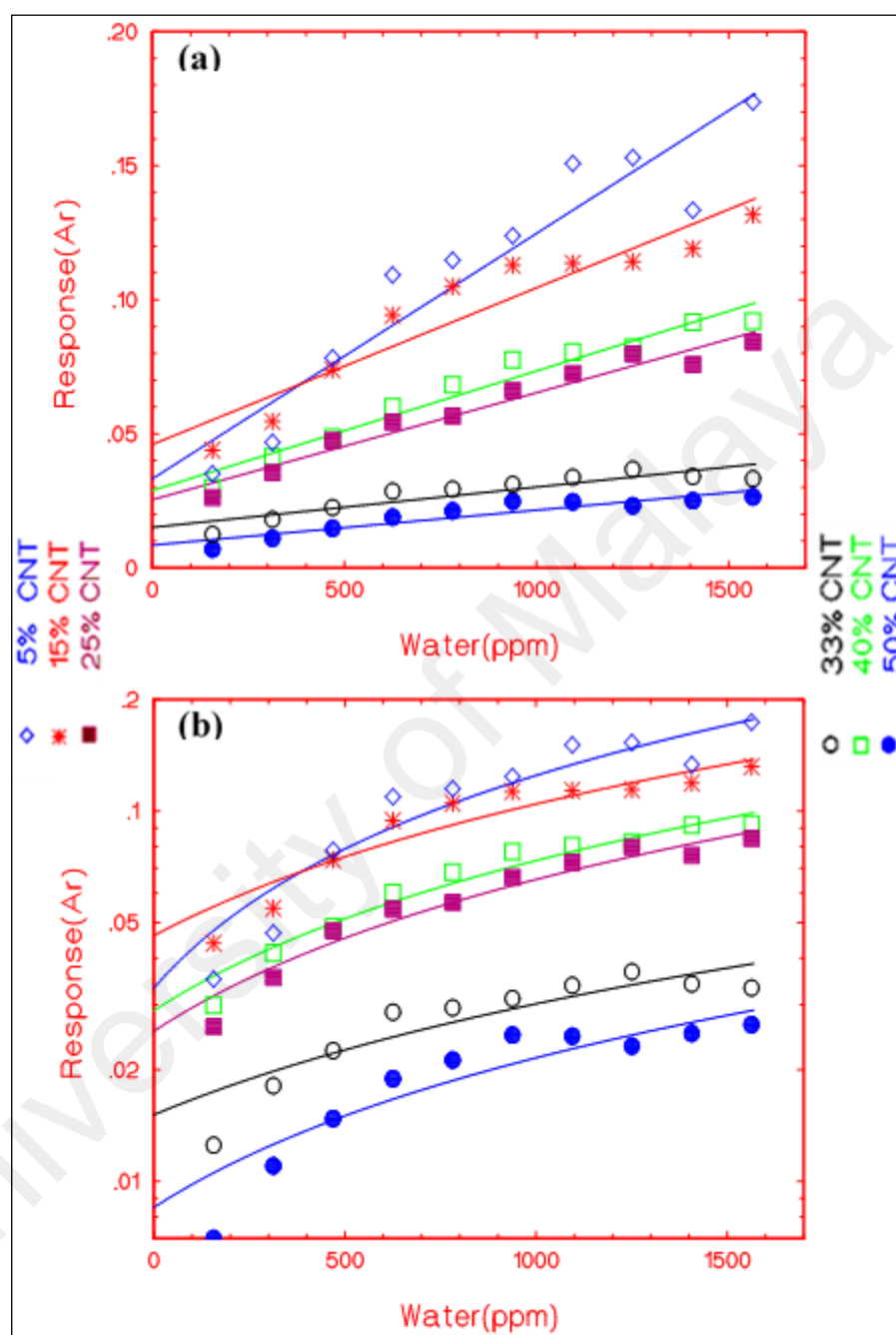


Figure 4.15: Response of MWCNT/PEO sensors to H₂O vapour (a) Response versus water concentration. (b) Response logarithm versus water concentration.

However, the response was much power and the sensitivity was roughly one order of magnitude greater than in acetone case. Whereas, previously studied nanotubes polyelectrolyte sensors showed a higher response for water compared with acetone

(Kumar et al. 2012 and Park et al. 2012). The 5% CNT film has the greatest response values with around 0.03 and 0.17 concerning 160 and 1560 H₂O ppm respectively and 9.15×10^{-5} sensitivity for the studied concentration range (160-1560 ppm) (see figure 4.16).

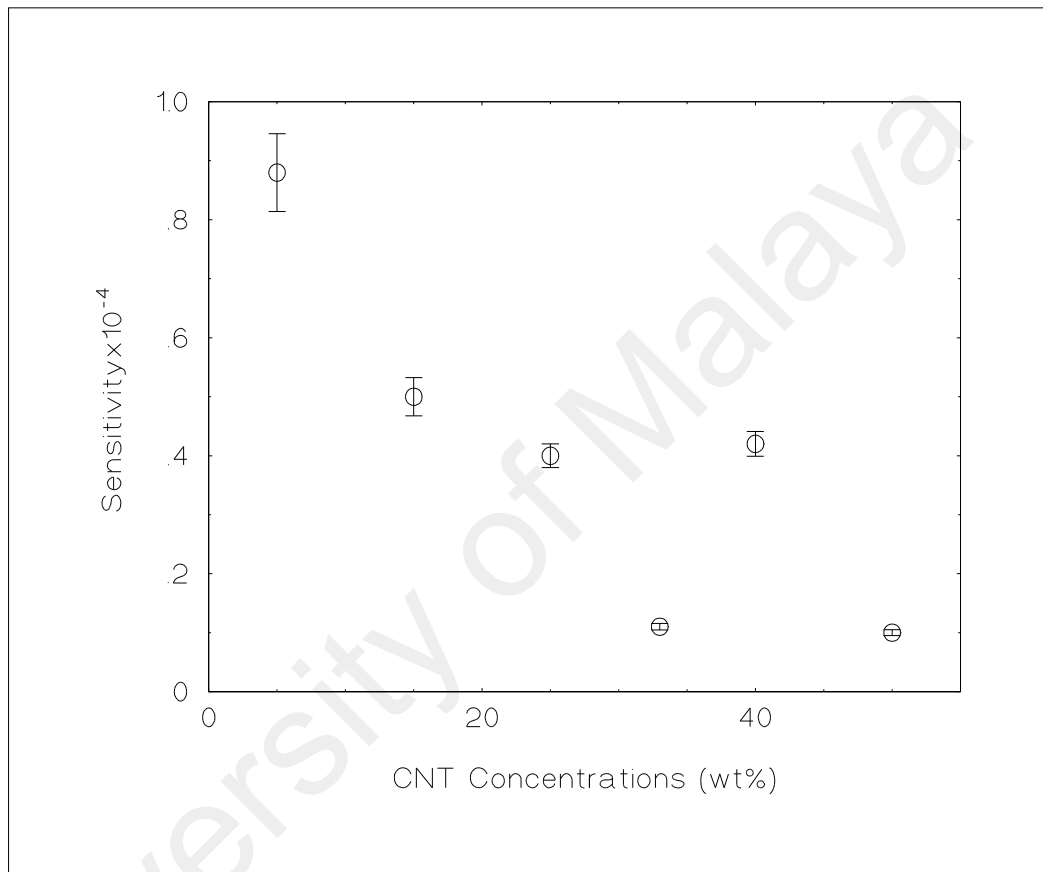


Figure 4.16: Sensitivity versus carbon nanotubes concentration in the range (160-1560 ppm) water vapour.

4.7.3 Sensing Mechanism

As the chemical vapors come into contact with the sensing area of the composite with nanofiller, the current decreases (resistance increases), which is detected by the recording devices. In spite of the seeming simplicity of chemical sensor operation, understanding the mechanisms involved in the process of chemical sensing is usually not so simple.

Different gas sensing mechanisms have been reported (Battie, Ducloux et al. 2011) such as adsorption of gas molecules at the interstitial sites in the SWCNT bundles, direct charge transfer from the gas molecules adsorbed on the SWCNTs and modulation of the schottky barrier (SB) level at the interface between semi-conducting SWCNTs and metallic electrodes or at the contacts between semi-conducting and metallic SWCNTs (Varghese, Kichambre et al. 2001). Some practical works suggested that the tunneling and direct tubes contacts resistances could be neglected in MWCNTs case (Hu, Masuda et al. 2008). Some studies were done based on this suggestion (Foygel, Morris et al. 2005, Ma and Gao 2008). It has also been demonstrated that organic chemicals can be adsorbed by CNTs based on hydrophobic interactions, $\pi - \pi$ bonds, electrostatic interactions, and hydrogen bonds (Pan and Xing 2008). On the other hand, it has been widely accepted that the disconnection of conducting pathways, induced by swelling of polymer matrix due to their adsorption of solvent molecules, is the main reason for the resistance sensitivity in vapors and liquid (Fan, Qin et al. 2011). Here, the weak van der Waals forces between the polymer and the target gas molecules are responsible for the swelling of the sensing layer. This sort of mechanism exists when the host is a conducting polymer. However, the situation is different in the current study since PEO is not electrically conducting.

The sensing mechanism in this research could be explained as follows: since the surface molecules of CNTs are surrounded with δ electrons which are the main cause in graphene and CNTs conductivity, we imply that the adsorbed gas species experience a surface interaction with the carbon nanotubes. This reaction interrupts the δ electrons causing a reduced electron flow in the sensor, resulting in the increased resistance. The portion of the interrupted electrons augments when the number of δ electrons and the quantity of the tubes exposed to the vapor diminishes and verse versa. This can explain the dependence of the sensitivity and saturation on the CNT concentration. Moreover, it stresses the well dispersion of the MWCNTS in the PEO matrix which was previously

inferred from Raman and SEM analysis. Another factor we suppose its contribution to the sensitivity is the microholes observed especially in the sensors with small CNT concentration (SEM chapter 3). The microvoids host the analyte during measurement and induce isolating clusters within the sensing area.

On one hand, acetone has a net dipole and can interact by hydrogen bonding as well as by dipole-dipole interactions, the same types of interactions can be formed by H₂O. On the other hand, PEO is known with its excellent hydrophilic nature, high viscosity and ability to form hydrogen bonds with ether oxygen. It can be inferred that the sensing operation is conducted by both the nanotubes as well as by the PEO matrix. Where most of the signal resulted from physical adsorption, some of the chemical reactions also could have taken place.

4.8 Conclusions

MWCNT/PEO composites have been used to monitor acetone vapor. The electrical responses were reproducible and quick, suggesting an easy disconnection/reconnection of the conductive network. The highest response and sensitivity were obtained from the sample with the lowest concentration of MWCNTs 5wt. However, it showed early saturation (680 ppm). The sensitivity depends linearly with the filler percentage whereas the saturation point depends inversely with the filler concentration. This result is related to the well dispersion of the nanotubes. It is reinforced by Raman and SEM analysis. Thus, revealing a good potential for the fabrication of two types of high sensitive MWCNT/PEO acetone sensors. The first contains low MWCNTs loading and interprets low concentrations of acetone, fits sensitivity measurements. The second type contains high MWCNTs loading and detects the high concentrations of acetone, applicable for dynamic motion testing. MWCNT/PEO composites are also proved to be good water vapor sensors. Yet, their

sensitivity to water vapor is smaller compared to acetone vapor which may be due to the different sticking probabilities of the two vapors on MWCNTs.

University of Malaya

CHAPTER 5: CONCLUSIONS

PEO/MWCNT composite, MWCNT/ZnO and MWCNT/TiO₂ films were fabricated and tested as acetone vapor sensor and field electron emission cathodes. PEO/MWCNT films at different loadings up to 50% weight were fabricated. Characterization using FESEM and Raman spectroscopy showed that the MWCNTs were well distributed in the film. For acetone sensing, the PEO/MWCNT were tested as thick and thin films. For both films, good response was recorded with reasonable rise time of about 2-3second and recovery time of typically 15 seconds. There seemed to be a significant difference in the sensitivity and the saturation point afforded by the different MWCNT loading in the PEO composite. It was observed that composites with the lowest loading of 5% showed the highest sensitivity in all concentration range. At the highest MWCNT loading of 50%, the corresponding lowest sensitivity was observed. However, at the highest MWCNT loading, the measurement dynamic range was highest while at 5% it was the lowest. The tradeoff between the sensitivity and dynamic range indicated that the MWCNT were well disperse in the composite, so that at lower loadings, with less MWCNT there are fewer conduction channels in the sensors. Blocking these channels which produced the sensor responses will give higher sensitivity but will saturate at lower concentration for lower MWCNT contents. When applied as FEE cathodes, the thin films was found to give higher turn on and threshold fields compared to thick films. Half of the thin films did not reach the current density of 0.1 mAcm^{-2} , meanwhile all the thick films exceeded this value except for 25%. A non-linear relationship between the enhancement factors and the increasing filler loading fractions was in all the composites. The composite with 5wt% displayed the turn on field $8.99 \text{ V}/\mu\text{m}$, the threshold field $10.91 \text{ V}/\mu\text{m}$ of with the value of field enhancement factor (β) of 786. The composite with 15wt% displayed the turn on field $8.99 \text{ V}/\mu\text{m}$ with the value of β is 1509. The composite with 25wt% displayed the turn

on field $10.21 \text{ V}/\mu\text{m}$ with the value of β is 601. The best β obtained was 1509 and 1853 in 15% thin and 33% thick films respectively with displayed the turn on field $8.99 \text{ V}/\mu\text{m}$ and $6.51 \text{ V}/\mu\text{m}$, the threshold field $9.07 \text{ V}/\mu\text{m}$. The Turn on field for 40wt% and 50wt% are $9.97 \text{ V}/\mu\text{m}$ and $9.25 \text{ V}/\mu\text{m}$ and the threshold field for 50wt% is $10.71 \text{ V}/\mu\text{m}$ in addition to the field enhancement factor (β) are 727 and 853. In 2000s measurement, all the composites showed a considerable stability in current yield, thin films were rather more stable.

Application of MWCNT/ZnO and MWCNT/TiO₂ hybrid materials films deposited by the electrophoresis method and comparing it with pure MWCNT gave some insight in the effect the oxide particles inclusion into the films. For all film types the effect of deposition time which was translated into film thickness saw the depreciation of the field emission properties. This was due to the shield effect seen when the density of MWCNT increased in thicker films. Most significant was the enhancement of the field electron emission properties in terms of maximum current density, field enhancement factors, turn on and threshold field values with the inclusion of the oxide materials. This phenomenon was due to the oxide particles acting as spacers in the films resulting in some distribution of the MWCNTs, thus reducing the shielding effect.

REFERENCES

- Abdelhalim A., et al. (2015). "Highly sensitive and selective carbon nanotube-based gas sensor arrays functionalized with different metallic nanoparticles." *Sensors and Actuators B*: 1288–1296.
- Adio, A. M. (2009). "(-)-trans- β -Elemene and related compounds: occurrence, synthesis, and anticancer activity." *Tetrahedron* **65**(27): 5145-5159.
- Ajayan, P. and O. Zhou (2001). "Applications of carbon nanotubes." *Carbon Nanotubes*: 391-425.
- Allen, M. G. (2005). Micromachined endovascularly-implantable wireless aneurysm pressure sensors: from concept to clinic. *Solid-State Sensors, Actuators and Microsystems, 2005. Digest of Technical Papers. TRANSDUCERS'05. The 13th International Conference on, IEEE*.
- Antony, N., et al. (2010). "Inhibition and biocide actions of sodium dodecyl sulfate-Zn²⁺ system for the corrosion of carbon steel in chloride solution." *Portugaliae Electrochimica Acta* **28**(1): 1-14.
- B. Philip, A. Chandrasekhar, J. K. A., V.R. Varadan, (2003). "Carbon nanotubes/PMMA composite thin films for gas-sensing applications." *Smart Mater Structure* **12**: 935–939.
- Badr, Y. and M. Mahmoud (2005). "On interaction of 193nm excimer laser with acetone (3s Rydberg state)." *Journal of molecular structure* **748**(1): 189-193.
- Balandin, A. A., et al. (2008). "Superior thermal conductivity of single-layer graphene." *Nano Letters* **8**(3): 902-907.
- Barick, A. K. and D. K. Tripathy (2011). "Preparation, characterization and properties of acid functionalized multi-walled carbon nanotube reinforced thermoplastic polyurethane nanocomposites." *Materials Science and Engineering: B* **176**(18): 1435-1447.
- Bartlett, P. N. and S. K. Ling-Chung (1989). "Conducting polymer gas sensors part II: response of polypyrrole to methanol vapour." *Sensors and Actuators* **19**(2): 141-150.
- Bartlett, P. N. and S. K. Ling-Chung (1989). "Conducting polymer gas sensors part III: Results for four different polymers and five different vapours." *Sensors and Actuators* **20**(3): 287-292.
- Battie, Y., et al. (2011). "Gas sensors based on thick films of semi-conducting single walled carbon nanotubes." *Carbon* **49**(11): 3544-3552.
- Baughman, R. H., et al. (2002). "Carbon nanotubes--the route toward applications." *Science* **297**(5582): 787-792.

- Bene, R., et al. (2000). "Chemical reactions in the detection of acetone and NO by a CeO₂ thin film." *Sensors and Actuators B: Chemical* **71**(1): 36-41.
- Berber, S., et al. (2000). "Unusually high thermal conductivity of carbon nanotubes." *Physical Review Letters* **84**(20): 4613-4616.
- Bonard, J.-M., et al. (2002). "Carbon nanotube films as electron field emitters." *Carbon* **40**(10): 1715-1728.
- Bonard, J.-M., et al. (2001). "Field emission from carbon nanotubes: the first five years." *Solid-state electronics* **45**(6): 893-914.
- Bonard, J.-M., et al. (2003). "Degradation and failure of carbon nanotube field emitters." *Physical Review B* **67**(11): 115406.
- Bonard, J.-M., et al. (1998). "Field emission properties of multiwalled carbon nanotubes." *Ultramicroscopy* **73**(1): 7-15.
- Bonard, J.-M., et al. (2001). "Field emission from cylindrical carbon nanotube cathodes: possibilities for luminescent tubes." *Applied Physics Letters* **78**(18): 2775-2777.
- Bower, C., et al. (2002). "On-chip vacuum microtriode using carbon nanotube field emitters." *Applied Physics Letters* **80**(20): 3820-3822.
- Bozhko, A., et al. (1998). "Resistance vs. pressure of single-wall carbon nanotubes." *Applied Physics A: Materials Science & Processing* **67**(1): 75-77.
- C. Cantalini, I. Armentano, L. V., I., J.M. Kenny, L. Lozzi, S. Santucci, (2003). An innovative approach to gas sensing using carbon nanotubes thin films: sensitivity, selectivity and stability response analysis, *Sensors*, Proceedings of IEEE.
- Cakar, F., et al. (2010). "Conducting poly (ether imide)–graphite composite for some solvent vapors sensing application." *Sensors and Actuators B: Chemical* **145**(1): 126-132.
- Cha, S. I., et al. (2006). "Field-Emission Behavior of a Carbon-Nanotube-Implanted Co Nanocomposite Fabricated from Pearl-Necklace-Structured Carbon Nanotube/Co Powders." *Advanced Materials* **18**(5): 553-558.
- Chai, Y., et al. (2005). "Nanodiode based on a multiwall CN_x/carbon nanotube intramolecular junction." *Nanotechnology* **16**(10): 2134– 2137.
- Chakravarty, P., et al. (2008). "Thermal ablation of tumor cells with antibody-functionalized single-walled carbon nanotubes." *Proceedings of the National Academy of Sciences* **105**(25): 8697-8702.
- Charlier, J. C., et al. (2007). "Electronic and transport properties of nanotubes." *Rev. Mod. Phys* **79**(2): 677-732.
- Charlier, J. R. and J. P. Issi (1996). "Electrical conductivity of novel forms of carbon." *J. Phys. Chem. Solids* **57**(6–8): 957–965.

- Chen, J. and N. Tsubokawa (2000). "Electric properties of conducting composite from poly (ethylene oxide) and poly (ethylene oxide)-grafted carbon black in solvent vapor." *Polymer journal* **32**(9): 729-736.
- Chen, K., et al. (2006). "Field emission image uniformity improvement by laser treating carbon nanotube powders." *Applied Physics Letters* **88**(19): 193127.
- Chen, S. G., et al. (2004). "Gas sensitivity of carbon black/waterborne polyurethane composites." *Carbon* **42**(3): 645-651.
- Chen, S. G., et al. (2005). "Effects of temperature and vapor pressure on the gas sensing behavior of carbon black filled polyurethane composites." *Sensors and Actuators B: Chemical* **105**(2): 187-193.
- Chen, S. G., et al. (2006). "Relationships between organic vapor adsorption behaviors and gas sensitivity of carbon black filled waterborne polyurethane composites." *Sensors and Actuators B: Chemical* **119**(1): 110-117.
- Chen, S. G., et al. (2006). "Improvement of gas sensing performance of carbon black/waterborne polyurethane composites: effect of crosslinking treatment." *Sensors and Actuators B: Chemical* **113**(1): 361-369.
- Chen, Z., et al. (2005). "High emission current density microwave-plasma-grown carbon nanotube arrays by postdepositional radio-frequency oxygen plasma treatment." *Applied Physics Letters* **87**(24): 243104.
- Cheng, Y. and O. Zhou (2003). "Electron field emission from carbon nanotubes." *Comptes Rendus Physique* **4**(9): 1021-1033.
- Cho, T. S., et al. (2007). A low power carbon nanotube chemical sensor system. Custom Integrated Circuits Conference, 2007. CICC'07. IEEE, IEEE.
- Choi, W., et al. (1999). "Fully sealed, high-brightness carbon-nanotube field-emission display." *Applied Physics Letters* **75**(20): 3129-3131.
- Coates, J. (2000). "Interpretation of infrared spectra, a practical approach." *Encyclopedia of analytical chemistry*.
- Coleman, J. N., et al. (2006). "Small but strong: a review of the mechanical properties of carbon nanotube-polymer composites." *Carbon* **44**(9): 1624-1652.
- Collins, P. G. and P. Avouris (2000). "Nanotubes for electronics." *Scientific American* **283**(6): 62-69.
- Collins, P. G. and A. Zettl (1996). "A simple and robust electron beam source from carbon nanotubes " *Appl. Phys. Lett* **69**(13): 1969-1971.
- Collins, P. G. and A. Zettl (1997). "Unique characteristics of cold cathode carbon-nanotube-matrix field emitters." *Physical Review B* **55**(15): 9391.
- Costa, S., et al. (2008). "Characterization of carbon nanotubes by Raman spectroscopy." *Mater Sci-Poland* **26**(2): 433-441.

- Crowley, M. M., et al. (2002). "Stability of polyethylene oxide in matrix tablets prepared by hot-melt extrusion." *Biomaterials* **23**(21): 4241-4248.
- Da Silva, L., et al. (2004). "Ab initio study of deformed carbon nanotube sensors for carbon monoxide molecules." *Nano letters* **4**(1): 65-67.
- Dag, S., et al. (2004). "Theoretical study of crossed and parallel carbon nanotube junctions and three-dimensional grid structures." *Physical Review B* **70**(20): 205407.
- Dai, H. (2002). "Carbon nanotubes: opportunities and challenges." *Surface Sci.* **500**(1): 218–241.
- Dai, H. J., et al. (1996). "Nanotubes as nanoprobe in scanning probe microscopy." *Nature* **384**(6605): 147-150.
- Dai, H. J., et al. (1996). "Probing electrical transport in nanomaterials: conductivity of individual carbon nanotubes" *Science* **272**(5261): 523–526.
- De Heer, W. A., et al. (1995). "A carbon nanotube field-emission electron source." *Science* **270**(5239): 1179-1180.
- De Jonge, N., et al. (2005). "Optical performance of carbon-nanotube electron sources." *physical review letters* **94**(18): 186807.
- De Jonge, N. and J. M. Bonard (2004). "Carbon nanotube electron sources and applications." *Philosophical Transactions of the Royal Society of London A: Mathematical, Physical and Engineering Sciences* **362**(1823): 2239-2266.
- Do, T. M. L., et al. (2013). "New derivatives from the aerial parts of *Boerhaavia diffusa* L. (Nyctaginaceae)." *Phytochemistry Letters* **6**(4): 544-551.
- Dong, X. M., et al. (2004). "Electrical resistance response of carbon black filled amorphous polymer composite sensors to organic vapors at low vapor concentrations." *Carbon* **42**(12): 2551-2559.
- Dresselhaus, M. (1992). "Down the straight and narrow." *Nature* **358**: 195-196.
- Dresselhaus, M. S., et al. (1996). *Science of fullerenes and carbon nanotubes*. New York, NY, San Diego, CA.
- Dresselhaus, M. S., et al. (2005). "Raman spectroscopy of carbon nanotubes." *Physics reports* **409**(2): 47-99.
- Duncan, T. V. (2011). "Applications of nanotechnology in food packaging and food safety: barrier materials, antimicrobials and sensors." *Journal of colloid and interface science* **363**(1): 1-24.
- Durkop, T., et al. (2004). "Properties and applications of high-mobility semiconducting nanotubes." *J. Phys: Condens. Matter* **16**(18): R553–R580.
- E. Kymakis, Amaratunga, G.A.J. (2002). *Synthetic Metals* **127** 59–62.

- E.T. Thostenson, T.W. Chou, Z. R. (2001). *Composites Science and Technology* **61**: 1899–1912.
- Eastman, M., et al. (1999). "Application of the solubility parameter concept to the design of chemiresistor arrays." *Journal of the Electrochemical Society* **146**(10): 3907-3913.
- Ebbesen, T. W., et al. (1996). "Electrical conductivity of individual carbon nanotubes." *Nature* **382**(6586): 54–56.
- Endo, M., et al. (2004). "Applications of carbon nanotubes in the twenty-first century." *Phil. Trans. R. Soc. Lond. A* . **362**: 2223–2238.
- Falvo, M. R., et al. (1997). "Bending and buckling of carbon nanotubes under large strain." *Nature* **389**(6651): 582-584.
- Fan, Q., et al. (2011). "Vapor sensing properties of thermoplastic polyurethane multifilament covered with carbon nanotube networks." *Sensors and Actuators B: Chemical* **156**(1): 63-70.
- Feng, T., et al. (2007). "Effects of plasma treatment on microstructure and electron field emission properties of screen-printed carbon nanotube films." *Physica E: Low-dimensional Systems and Nanostructures* **36**(1): 28-33.
- Fischer, J., et al. (1997). "Metallic resistivity in crystalline ropes of single-wall carbon nanotubes." *Physical Review B* **55**(8): 4921-4924.
- Fowler, R. H. and L. Nordheim (1928). *Electron emission in intense electric fields. Proceedings of the Royal Society of London A: Mathematical, Physical and Engineering Sciences, The Royal Society.*
- Foygel, M., et al. (2005). "Theoretical and computational studies of carbon nanotube composites and suspensions: Electrical and thermal conductivity." *Physical Review B* **71**(10): 104201.
- Frackowiak, E. and F. Béguin (2002). "Electrochemical storage of energy in carbon nanotubes and nanostructured carbons." *Carbon* **40**(10): 1775-1787.
- Fransen, M., et al. (1999). "Field emission energy distributions from individual multiwalled carbon nanotubes." *Applied surface science* **146**(1): 312-327.
- Fröman, N. and P. O. Fröman (1965). *JWKB approximation: contributions to the theory*, North-Holland Pub. Co.;[sole distributors for USA: Interscience Publishers, New York].
- Gallazzi, M., et al. (2003). "Poly (alkoxy-bithiophenes) sensors for organic vapours." *Sensors and Actuators B: Chemical* **88**(2): 178-189.
- Gallazzi, M., et al. (2003). "Poly (alkoxy-bithiophenes) sensors for organic vapours." *Sensors and Actuators B: Chemical* **88**(2): 178-189.
- Gong, H., et al. (1999). "Interaction between thin-film tin oxide gas sensor and five organic vapors." *Sensors and Actuators B: Chemical* **54**(3): 232-235.

- Gracia-Espino, E., et al. (2010). "Electrical transport and field-effect transistors using inkjet-printed SWCNT films having different functional side groups." *ACS nano* **4**(6): 3318-3324.
- Guo, Z., et al. (1999). "Immobilization and visualization of DNA and proteins on carbon nanotubes." *Advanced Materials* **10**(9): 701-703.
- Hamada, N., et al. (1992). "New one-dimensional conductors: Graphitic microtubules " *Phys. Rev. Lett.* **68**(10): 1579–1581.
- He, P. and L. Dai (2004). "Aligned carbon nanotube–DNA electrochemical sensors." *Chemical communications*(3): 348-349.
- Heller, D. A., et al. (2005). "Single-Walled Carbon Nanotube Spectroscopy in Live Cells: Towards Long-Term Labels and Optical Sensors." *Advanced Materials* **17**(23): 2793-2799.
- Hierold, C., et al. (2007). "Nano electromechanical sensors based on carbon nanotubes." *Sensors and Actuators A: Physical* **136**(1): 51-61.
- Hone, J. (2004). *Carbon nanotubes: thermal properties*, London, United kingdom: Taylor & Francis: 603-610.
- Hu, N., et al. (2008). "The electrical properties of polymer nanocomposites with carbon nanotube fillers." *Nanotechnology* **19**(21): 215701.
- Huang, S., et al. (2004). "Growth mechanism of oriented long single walled carbon nanotubes using ‘‘Fast-Heating’’ chemical vapor deposition process." *Nano Lett.* **4**(6): 1025–1028.
- Huang, Z., et al. (2009). " A facile carboxylation of CNT/Fe₃O₄ composite nanofibers for biomedical applications." *Materials Chemistry and Physics* **114** 33–36.
- Iijima, S. (1991). " Helical microtubules of graphitic carbon." *Nature (London)* **354**: 56-58.
- Intarakamhang, S. (2005). "Preparation, characterization and molecular modeling of poly (ethylene oxide)/poly (vinyl pyrrolidone) montmorillonite nanocomposite solid electrolytes."
- Ivnitski, D., et al. (2000). "Application of electrochemical biosensors for detection of food pathogenic bacteria." *Electroanalysis* **12**(5): 317-325.
- Jiang, W. F., et al. (2007). "Resistive humidity sensitivity of arrayed multi-wall carbon nanotube nests grown on arrayed nanoporous silicon pillars." *Sensors and Actuators B: Chemical* **125**(2): 651-655.
- Jung, Y. J., et al. (2006). "Aligned carbon nanotube-polymer hybrid architectures for diverse flexible electronic applications." *Nano letters* **6**(3): 413-418.
- Kaur A. et al. (2015). "Enhancement in the performance of multi-walled carbon nanotube: Poly(methylmethacrylate) composite thin film ethanol sensors

through appropriate nanotube functionalization." *Material Science in Semiconductor Processing* **31**: 166-174.

K. Shen, Y. Jiang, H. X., Y., T. Pietrab, (2004). "The role of carbon nanotube structure in purification and hydrogen adsorption." *Carbon* **42** 2315–2322.

Kawde, R., et al. (1995). "A selective sensing of dopa in the presence of adrenaline." *Sensors and Actuators B: Chemical* **23**(1): 35-39.

Khadayate, R., et al. (2007). "Acetone vapor sensing properties of screen printed WO₃ thick films." *Talanta* **72**(3): 1077-1081.

Khomenko, V., et al. (2005). "Determination of the specific capacitance of conducting polymer/nanotubes composite electrodes using different cell configurations." *Electrochimica Acta* **50**(12): 2499-2506.

Kim, G., et al. (1998). "Magnetoresistance of an entangled single-wall carbon-nanotube network." *Physical Review B* **58**(24): 16064.

Kim, J., et al. (2003). "Ultraviolet laser treatment of multiwall carbon nanotubes grown at low temperature." *Applied Physics Letters* **82**(10): 1607-1609.

Kim, S. (2006). "CNT sensors for detecting gases with low adsorption energy by ionization." *Sensors* **6**(5): 503-513.

Kim, T. S., et al. (2005). Fusion of biomedical microcapsule endoscope and microsystem technology. *Solid-State Sensors, Actuators and Microsystems, 2005. Digest of Technical Papers. TRANSDUCERS'05. The 13th International Conference on, IEEE.*

Kolmakov, A. and M. Moskovits (2004). "Chemical sensing and catalysis by one-dimensional metal-oxide nanostructures." *Annu. Rev. Mater. Res.* **34**: 151-180.

Kong, J., et al. (2000). "Nanotube molecular wires as chemical sensors." *Science* **287**(5453): 622-625.

Kreja, L., et al. (1997). "The influence of steam on the electrical properties of poly (3-alkylthiophenes) and their derivatives." *Sensors and Actuators B: Chemical* **41**(1): 37-43.

Kroto, H. W., et al. (1985). "C₆₀: Buckminsterfullerene " *Nature* **318**: 162 - 163

Kumar, B., et al. (2012). "Poly (lactic acid)–multi-wall carbon nanotube conductive biopolymer nanocomposite vapour sensors." *Sensors and Actuators B: Chemical* **161**(1): 621-628.

Kumar, B., et al. (2012). "Fine control of carbon nanotubes–polyelectrolyte sensors sensitivity by electrostatic layer by layer assembly (eLbL) for the detection of volatile organic compounds (VOC)." *Talanta* **88**: 396-402.

Kumar, K. K., et al. (2011). "Investigations on the effect of complexation of NaF salt with polymer blend (PEO/PVP) electrolytes on ionic conductivity and optical energy band gaps." *Physica B: Condensed Matter* **406**(9): 1706-1712.

- Kuroyanagi, M., et al. (1990). "Structures of sesquiterpenes of *Curcuma aromatica* Salisb. II. Studies on minor sesquiterpenes." *Chem. Pharm. Bull.* **38**(1): 55-58.
- Kyung, S.-J., et al. (2008). "Improvement of electron field emission from carbon nanotubes by Ar neutral beam treatment." *Carbon* **46**(10): 1316-1321.
- L. Jin, C. Bower and O. Zhou, (1998). "Alignment of carbon nanotubes in a polymer matrix by mechanical stretching." *Appl Phys Lett* **73** 1197–1199.
- L.W., C. (2008). "A Sensor for Gas Detection Fabricated by a Circular Single-wall Carbon Nanotube." **91**(4): 91-99.
- Lan, Y.-C., et al. (2011). "A Carbon-Nanotube Resistive Respiratory Sensor by using Dielectrophoresis Technique." *Procedia Engineering* **25**: 868-871.
- Latham, R. V. (1981). *High voltage vacuum insulation: the physical basis*, Academic Press.
- Lee, D. and T. Cui (2012). "A role of silica nanoparticles in layer-by-layer self-assembled carbon nanotube and In₂O₃ nanoparticle thin-film pH sensors: Tunable sensitivity and linearity." *Sensors and Actuators A: Physical* **188**: 203-211.
- Lee, J. O., et al. (2000). "Formation of lowresistance ohmic contact between carbon nanotubes and metal electrodes by a rapid thermal annealing method." *J. Phys. D: Appl. Phys.* **33**(16): 1953–1956.
- Lee, K., et al. (2008). "Origin of enhanced field emission characteristics postplasma treatment of multiwalled carbon nanotube array." *Applied Physics Letters* **93**(6): 063101.
- Lee, M.-S. and J.-U. Meyer (2000). "A new process for fabricating CO₂-sensing layers based on BaTiO₃ and additives." *Sensors and Actuators B: Chemical* **68**(1): 293-299.
- Lin, W., et al. (2012). "Parametric study of intrinsic thermal transport in vertically aligned multi-walled carbon nanotubes using a laser flash technique." *Carbon* **50**(4): 1591–1603.
- Liu, Y.-L., et al. (2008). "Poly (2, 6-dimethyl-1, 4-phenylene oxide)(PPO) multi-bonded carbon nanotube (CNT): Preparation and formation of PPO/CNT nanocomposites." *Polymer* **49**(25): 5405-5409.
- Lord, H., et al. (2002). "Breath analysis and monitoring by membrane extraction with sorbent interface." *Analytical chemistry* **74**(21): 5650-5657.
- Lu, X. (2006). *Field electron emission from diamond and related films synthesized by plasma enhanced chemical vapor deposition*, University of Saskatchewan Saskatoon.
- Lu, Y., et al. (2006). "A carbon nanotube sensor array for sensitive gas discrimination using principal component analysis." *Journal of Electroanalytical Chemistry* **593**(1): 105-110.

- Luo, Y.-L., et al. (2011). "Effect of soft–hard segment structure on vapor responsiveness of polyurethane conducting composite thin films loaded with multi-walled carbon nanotubes." *Sensors and Actuators B: Chemical* **156**(1): 12-22.
- Lyth, S. and S. Silva (2007). "Field emission from multiwall carbon nanotubes on paper substrates." *Applied Physics Letters* **90**(17): 173124.
- M. Moniruzzaman, K. I. W. (2006). "Polymer composites containing carbon nanotubes." *Macromolecules* **39** 5194–5205.
- Ma, H. and X.-L. Gao (2008). "A three-dimensional Monte Carlo model for electrically conductive polymer matrix composites filled with curved fibers." *Polymer* **49**(19): 4230-4238.
- Ma, P.-C., et al. (2010). "Dispersion and functionalization of carbon nanotubes for polymer-based nanocomposites: A review." *Composites Part A: Applied Science and Manufacturing* **41**(10): 1345-1367.
- Ma, W., et al. (2009). "High-strength composite fibers: realizing true potential of carbon nanotubes in polymer matrix through continuous reticulate architecture and molecular level couplings." *Nano letters* **9**(8): 2855-2861.
- MacDiarmid, A. G. (1997). "Polyaniline and polypyrrole: where are we headed?" *Synthetic Metals* **84**(1): 27-34.
- MacDiarmid, A. G. and A. J. Epstein (1989). "Polyanilines: a novel class of conducting polymers." *Faraday Discussions of the Chemical Society* **88**: 317-332.
- Manorathne, C., et al. (2006). "Ionic conductivity of poly (ethylene oxide)(PEO)-montmorillonite (MMT) nanocomposites prepared by intercalation from aqueous medium." *Int J Electrochem Sci* **1**(1): 32-46.
- McNally, T., et al. (2005). "Polyethylene multiwalled carbon nanotube composites." *Polymer* **46**(19): 8222-8232.
- Menon, M., et al. (2003). "Carbon nanotube ‘‘T Junctions’’: formation pathways and conductivity." *Phys. Rev. Lett.* **91**(14): 145501.
- Meyyappan, M. (2005). *Carbon nanotubes: science and applications*. Boca Raton, CRC Press.
- Milne, W., et al. (2006). "Carbon nanotubes as electron sources." *Physica Status Solidi-A-Applications and Materials Science* **203**(6): 1058-1063.
- Mingo, N. and D. Broido (2005). "Carbon nanotube ballistic thermal conductance and its limits." *Physical Review Letters* **95**(9): 96105-96101-96104.
- Moraes, R. A., et al. (2011). "The effect of different chemical treatments on the structure and stability of aqueous dispersion of iron-and iron oxide-filled multi-walled carbon nanotubes." *Journal of the Brazilian Chemical Society* **22**(11): 2191-2201.

- Morávková, Z., et al. (2012). "Enhanced thermal stability of multi-walled carbon nanotubes after coating with polyaniline salt." *Polymer Degradation and Stability* **97**(8): 1405-1414.
- Mottram, T., et al. (1999). "An experiment to determine the feasibility of automatically detecting hyperketonaemia in dairy cows." *Livestock production science* **61**(1): 7-11.
- Muraliganth, T., et al. (2008). "Nanoscale networking of LiFePO₄ nanorods synthesized by a microwave-solvothermal route with carbon nanotubes for lithium ion batteries." *Journal of Materials Chemistry* **18**(46): 5661-5668.
- Murphy, E. L. (1956). *Phys. Rev.* **102** 1464-1473.
- Naghadeh S.B. et al. (2016). "Functionalized MWCNTs effects on dramatic enhancement of MWCNTs/SnO₂ nanocomposite gas sensing properties at low temperatures". *Sensors and Actuators B*: 252–260.
- Nath, S., et al. (2010). "Acetone sensing property of ZnO quantum dots embedded on PVP." *Sensors and Actuators B: Chemical* **148**(2): 353-357.
- Nguyen, H.-Q. and J.-S. Huh (2006). "Behavior of single-walled carbon nanotube-based gas sensors at various temperatures of treatment and operation." *Sensors and Actuators B: Chemical* **117**(2): 426-430.
- Nilsson, L., et al. (2000). "Scanning field emission from patterned carbon nanotube films." *Applied Physics Letters* **76**(15): 2071-2073.
- Novák, P., et al. (1997). "Electrochemically active polymers for rechargeable batteries." *Chemical Reviews* **97**(1): 207-282.
- O'connell, M. J., et al. (2002). "Band gap fluorescence from individual single-walled carbon nanotubes." *Science* **297**(5581): 593-596.
- Odom, T. W., et al. (1998). "Atomic structure and electronic properties of single-walled carbon nanotubes." *Nature* **391**: 62-64.
- Odom, T. W., et al. (2000). "Structure and Electronic Properties of Carbon Nanotubes " *Journal of Physical Chemistry B* **104**: 2794-2809.
- Pan, B. and B. Xing (2008). "Adsorption mechanisms of organic chemicals on carbon nanotubes." *Environmental Science & Technology* **42**(24): 9005-9013.
- Pariikh, K., et al. (2006). "Flexible vapour sensors using single walled carbon nanotubes." *Sensors and Actuators B: Chemical* **113**(1): 55-63.
- Patil, S. B., et al. (2007). "Acetone vapour sensing characteristics of cobalt-doped SnO₂ thin films." *Sensors and Actuators B: Chemical* **125**(1): 126-130.
- Peng, S., et al. (2001). Carbon nanotube chemical and mechanical sensors. Conference paper for the third international workshop on SHM.

- Penza, M., et al. (2004). "Alcohol detection using carbon nanotubes acoustic and optical sensors." *Applied Physics Letters* **85**(12): 2379-2381.
- Pham, G. T., et al. (2008). "Processing and modeling of conductive thermoplastic/carbon nanotube films for strain sensing." *Composites Part B: Engineering* **39**(1): 209-216.
- Ping, W., et al. (1997). "A novel method for diabetes diagnosis based on electronic nose." *Biosensors and Bioelectronics* **12**(9): 1031-1036.
- Pokhrel, S., et al. (2007). "Cr_{2-x}Ti_xO₃ (x ≤ 0.5) as CH₃COCH₃ sensitive resistors." *Sensors and Actuators B: Chemical* **125**(2): 550-555.
- Pop, E., et al. (2006). "Thermal conductance of an individual single-wall carbon nanotube above room temperature." *Nano Letters* **6**(1): 96-100.
- Purcell, S., et al. (2002). "Hot nanotubes: stable heating of individual multiwall carbon nanotubes to 2000 K induced by the field-emission current." *physical review letters* **88**(10): 105502.
- Qi H., et al. (2015). "Carbon nanotube–cellulose composite aerogels for vapour sensing." *Sensors and Actuators B* **213**: 20–26.
- R. Andrews, M. C. W. (2003). *Solid State and Materials Science*.
- Raffaella, R., et al. (2005). "Carbon nanotubes for power applications." *Materials Science and Engineering: B* **116**(3): 233-243.
- Rao, A., et al. (1997). "Diameter-selective Raman scattering from vibrational modes in carbon nanotubes." *Science* **275**(5297): 187-191.
- Ren, Y. and G. Pastorin (2008). "Incorporation of hexamethylmelamine inside capped carbon nanotubes." *Advanced Materials* **20**(11): 2031-2036.
- Rezlescu, N., et al. (2006). "Semiconducting gas sensor for acetone based on the fine grained nickel ferrite." *Sensors and Actuators B: Chemical* **114**(1): 427-432.
- Rinzler, A., et al. (1995). "Unraveling nanotubes: field emission from an atomic wire." *Science-New York Then Washington-*: 1550-1550.
- Ritter, U., et al. (2006). "Radiation damage to multi-walled carbon nanotubes and their Raman vibrational modes." *Carbon* **44**(13): 2694-2700.
- Riviere, M. N. A., et al. (2005). "Multi-walled carbon nanotube interactions with human epidermal keratinocytes." *Toxicology letters* **155**(3): 377-384.
- Sahay, P. (2005). "Zinc oxide thin film gas sensor for detection of acetone." *Journal of Materials Science* **40**(16): 4383-4385.
- Sahoo, N. G., et al. (2010). "Polymer nanocomposites based on functionalized carbon nanotubes." *Progress in Polymer Science* **35**(7): 837-867.
- Saito, R., et al. (1998). *Physical Properties of Carbon Nanotubes*. London, UK.

- Saito, Y., et al. (1998). "Cathode ray tube lighting elements with carbon nanotube field emitters." *Japanese Journal of Applied Physics* **37**(3B): L346.
- Salehi S., et al. (2014). "Highly sensitive carbon nanotubes–SnO₂ nanocomposite sensor for acetone detection in diabetes mellitus breath". *Sensors and Actuators B*: 261–267.
- Santhanam, K., et al. (2005). "A chemical sensor for chloromethanes using a nanocomposite of multiwalled carbon nanotubes with poly (3-methylthiophene)." *Sensors and Actuators B: Chemical* **106**(2): 766-771.
- Schulz, M. (2012). "Speeding Up Artificial Muscles." *Science* **338**(6109): 893-894.
- Sekhon, S., et al. (1995). "Solid polymer electrolytes based on polyethylene oxide-silver thiocyanate." *Solid State Ionics* **80**(1): 37-44.
- Shaffer, M. and I. A. Kinloch (2004). "Prospects for nanotube and nanofibre composites." *Composites Science and Technology* **64**(15): 2281-2282.
- Shaikh, S., et al. (2007). "The effect of a CNT interface on the thermal resistance of contacting surfaces." *Carbon* **45**(4): 695-703.
- Shakir, M., et al. (2006). "TOPICAL REVIEW: Carbon nanotube electric field emitters and applications." *Nanotechnology* **17**: 41.
- Shimizu, Y. and M. Egashira (1999). "Basic aspects and challenges of semiconductor gas sensors." *Mrs Bulletin* **24**(06): 18-24.
- Sim, H., et al. (2007). "Reliable and flexible carbon-nanofiber-based all-plastic field emission devices." *Applied Physics Letters* **90**(14): 143103.
- Sinha, N., et al. (2006). "Carbon nanotube-based sensors." *Journal of Nanoscience and Nanotechnology* **6**(3): 573-590.
- Sivakkumar, S. R., et al. (2007). "Electrochemical performance of polyaniline nanofibres and polyaniline/multi-walled carbon nanotube composite as an electrode material for aqueous redox supercapacitors." *Journal of Power Sources* **171**(2): 1062-1068.
- Smith, R., et al. (2005). "Charge transport effects in field emission from carbon nanotube-polymer composites." *Applied Physics Letters* **87**(26): 263105.
- Smith, R., et al. (2005). "Interpretation of enhancement factor in nonplanar field emitters." *Applied Physics Letters* **87**(1): 013111.
- Snow, E., et al. (2005). "Chemical detection with a single-walled carbon nanotube capacitor." *Science* **307**(5717): 1942-1945.
- Snow, E. S., et al. (2005). "High-mobility carbon-nanotube thin-film transistors on a polymeric substrate." *Applied Physics Letters* **86**(3): 033105.
- Somani, P. R., et al. (2007). "Field electron emission of double walled carbon nanotube film prepared by drop casting method." *Solid-state electronics* **51**(5): 788-792.

- Someya, T., et al. (2003). "Alcohol vapor sensors based on single-walled carbon nanotube field effect transistors." *Nano letters* **3**(7): 877-881.
- Song, P., et al. (2012). "Preparation, characterization and acetone sensing properties of Ce-doped SnO₂ hollow spheres." *Sensors and Actuators B: Chemical* **173**: 839-846.
- Spires, T. and R. M. J. Brown (1996). "High Resolution TEM Observations of Single-Walled Carbon Nanotubes." Department of Botany, The University of Texas at Austin, Austin, Tx., 78713.
- Staii, C., et al. (2005). "DNA-decorated carbon nanotubes for chemical sensing." *Nano letters* **5**(9): 1774-1778.
- Stampfer, C., et al. (2006). "Fabrication of single-walled carbon-nanotube-based pressure sensors." *Nano letters* **6**(2): 233-237.
- Stetter, J. R. (2004). "Carbon Nanotubes and Sensors: a Review." *Advanced Micro and Nanosystems* **1** 357-382.
- Szleifer, I. and R. Yerushalmi-Rozen (2005). "Polymers and carbon nanotubes-dimensionality, interactions and nanotechnology." *Polymer* **46**(19): 7803-7818.
- Treacy, M. M. J., et al. (1996). "Exceptionally high Young's modulus observed for individual carbon nanotubes." *Nature* **381**(6584): 678-680.
- Varghese, O., et al. (2001). "Gas sensing characteristics of multi-wall carbon nanotubes." *Sensors and Actuators B: Chemical* **81**(1): 32-41.
- Varghese, O. K. and C. A. Grimes (2003). "Metal oxide nanoarchitectures for environmental sensing." *Journal of Nanoscience and Nanotechnology* **3**(4): 277-293.
- Vashist, S. K., et al. (2011). "Delivery of drugs and biomolecules using carbon nanotubes." *C A R B O N* **49**(13): 4077-4097.
- Vincent, P., et al. (2002). "Modelization of resistive heating of carbon nanotubes during field emission." *Physical Review B* **66**(7): 075406.
- Wang, C. and A. Mbi (2007). "A new acetone detection device using cavity ringdown spectroscopy at 266 nm: evaluation of the instrument performance using acetone sample solutions." *Measurement Science and Technology* **18**(8): 2731.
- Wang, C. and P. Sahay (2009). "Breath analysis using laser spectroscopic techniques: breath biomarkers, spectral fingerprints, and detection limits." *Sensors* **9**(10): 8230-8262.
- Wang, J., et al. (2004). "Ultrasensitive electrical biosensing of proteins and DNA: carbon-nanotube derived amplification of the recognition and transduction events." *Journal of the American Chemical Society* **126**(10): 3010-3011.
- Wang, Q. H., et al. (1997). "Field emission from nanotube bundle emitters at low fields." *Appl. Phys. Lett* **70**(24): 3308-3310.

- Wang, W.-Z., et al. (2006). "Aligned ultralong ZnO nanobelts and their enhanced field emission." *Advanced Materials* **18**(24): 3275-3278.
- Wang, W. and L. Cao (2001). "Transformation of carbon nanotubes to diamond at high pressure and high temperature." *Russian Physics Journal* **44**(2): 178-182.
- Wei, B. Q., et al. (2001). "Reliability and Current Carrying Capacity of Carbon Nanotubes." *Appl. Phys. Lett.* **79**(8): 1172-1174.
- Wei, C., et al. (2006). "Multifunctional chemical vapor sensors of aligned carbon nanotube and polymer composites." *Journal of the American Chemical Society* **128**(5): 1412-1413.
- Wei, S., et al. (2011). "Improved acetone sensing properties of ZnO hollow nanofibers by single capillary electrospinning." *Sensors and Actuators B: Chemical* **160**(1): 753-759.
- Wildöer, J. W. G., et al. (1998). "Electronic structure of atomically resolved carbon nanotubes." *Nature* **391**: 59-62.
- Williams, R. and P. Doherty (1994). "A preliminary assessment of poly (pyrrole) in nerve guide studies." *Journal of materials science: materials in medicine* **5**(6-7): 429-433.
- Wilson, A. D. and M. Baietto (2011). "Advances in electronic-nose technologies developed for biomedical applications." *Sensors* **11**(1): 1105-1176.
- Xie, H., et al. (2012). "Multi-wall carbon nanotube gas sensors modified with amino-group to detect low concentration of formaldehyde." *Sensors and Actuators B: Chemical* **168**: 34-38.
- Xie, H., et al. (2012). "Multi-wall carbon nanotube gas sensors modified with amino-group to detect low concentration of formaldehyde." *Sensors and Actuators B: Chemical* **168**: 34-38.
- Xu, N. and S. E. Huq (2005). "Novel cold cathode materials and applications." *Materials Science and Engineering: R: Reports* **48**(2): 47-189.
- Xu, Z., et al. (2010). "Morphology, rheology and crystallization behavior of polylactide composites prepared through addition of five-armed star polylactide grafted multiwalled carbon nanotubes." *Polymer* **51**(3): 730-737.
- Yamada, T., et al. (2011). "A stretchable carbon nanotube strain sensor for human-motion detection " *Nature Nanotechnology* **6**(5): 296–301.
- Yamamoto, S. (2006). "Fundamental physics of vacuum electron sources." *Reports on Progress in Physics* **69**(1): 181.
- Yang, L. and J. Han (2000). "Electronic structure of deformed carbon nanotubes." *physical review letters* **85**(1): 154.

- Yang, M., et al. (2009). "Electrical properties and acetone-sensing characteristics of $\text{LaNi}_{1-x}\text{Ti}_x\text{O}_3$ perovskite system prepared by amorphous citrate decomposition." *Sensors and Actuators B: Chemical* **143**(1): 111-118.
- Yang, X., et al. (2007). "A carbon nanotube-based sensing element." *Optoelectronics Letters* **3**(2): 81-84.
- Yang, Z. H. and H. Q. Wu (2001). "Electrochemical intercalation of lithium into raw carbon nanotubes." *Materials Chemistry and Physics* **71**(1): 7-11.
- Ye, F., et al. (2007). "The growth and field electron emission of InGaN nanowires." *Journal of crystal growth* **304**(2): 333-337.
- Yu, C., et al. (2005). "Thermal conductance and thermopower of an individual single-wall carbon nanotube." *Nano Letters* **5**(9): 1842-1846.
- Yu, N., et al. (2011). "High-crystallization polyoxymethylene modification on carbon nanotubes with assistance of supercritical carbon dioxide: Molecular interactions and their thermal stability." *Polymer* **52**(2): 472-480.
- Yue, G., et al. (2002). "Generation of continuous and pulsed diagnostic imaging x-ray radiation using a carbon-nanotube-based field-emission cathode." *Applied Physics Letters* **81**(2): 355-357.
- Zaragoza-Contreras, E., et al. (2009). "Evidence of multi-walled carbon nanotube fragmentation induced by sonication during nanotube encapsulation via bulk-suspension polymerization." *Micron* **40**(5): 621-627.
- Zdrojek, M., et al. (2004). Studies of multiwall carbon nanotubes using Raman spectroscopy and atomic force microscopy. *Solid State Phenomena*, Trans Tech Publ.
- Zhang, B., et al. (2005). "Preparation and characterization of gas-sensitive composites from multi-walled carbon nanotubes/polystyrene." *Sensors and Actuators B: Chemical* **109**(2): 323-328.
- Zhang, H. Y., et al. (2007). "Screening and analysis of bioactive compounds in traditional Chinese medicines using cell extract and gas chromatography-mass spectrometry." *Journal of Pharmaceutical and Biomedical Analysis* **43**(1): 151-157.
- Zhang, L., et al. (2006). "Electric properties and acetone-sensing characteristics of $\text{La}_{1-x}\text{Pb}_x\text{FeO}_3$ perovskite system." *Materials chemistry and physics* **98**(2): 358-362.
- Zhao, J., et al. (2006). "Alcohols and acetone sensing properties of SnO_2 thin films deposited by dip-coating." *Sensors and Actuators B: Chemical* **115**(1): 460-464.
- Zheng, L. X., et al. (2004). "Ultralong single-wall carbon nanotubes" *Nat. Mater.* **3**(10): 673-676.
- Zhi, C., et al. (2002). "Enhanced field emission from carbon nanotubes by hydrogen plasma treatment." *Applied Physics Letters* **81**(9): 1690-1692.

- Zhou, G., et al. (2001). "Electronic structure and field-emission characteristics of open-ended single-walled carbon nanotubes." *physical review letters* **87**(9): 095504.
- Zhu, W., et al. (1999). "Large current density from carbon nanotube field emitters." *Applied Physics Letters* **75**(6): 873-875.
- Zhu, Y., et al. (2005). "Effects of CF₄ plasma on the field emission properties of aligned multi-wall carbon nanotube films." *Carbon* **43**(2): 395-400.

University of Malaya

LIST OF PUBLICATIONS AND PAPERS PRESENTED

Journal Papers

1. Advanced Material Research (AMR) – Electrical and alcohol sensing properties of MWCNT/PS composites. Title Book: NANO-SCI TECH 2013, Code number: P013.
2. Advanced Material Research (AMR) – Field electron emission from electrophoretic deposited MWCNT/ZnO hybrid film. Title Book: NANO-SCI TECH 2013, Code number: P017.

Proceeding Conference

1. American Institute of Physics (AIP) Conference proceedings. Electrical and alcohol sensing properties of PEO/MWCNT composites. AIP Conf. Proc. 1502, pp. 495-499; doi:<http://dx.doi.org/10.1063/1.4769168> (5 pages).

Electrical and Alcohol Sensing Properties of MWCNT/PS Composites

Faridah Abdul Razak^{1,a} and Roslan Md. Nor^{2,b}

^{1,2}Department of Physics, Faculty of Science, University of Malaya, 50603 Kuala Lumpur, MALAYSIA

Email : ^afdah03@yahoo.com.my, ^brmdnor@um.edu.my

Keywords: Carbon nanotubes; Nanocomposites; Electrical properties; Polymers.

Abstract. Composites of polystyrene and multiwalled carbon nanotubes were prepared using the solution blending method. Results on the electrical conductivity and alcohol vapor sensing will be presented. Field Emission Scanning Electron Microscopy was used to investigate the structure MWCNT/PS composites. The optical characterization was investigated by Fourier Transform-Infrared Spectroscopy. Thermogravimetric Analysis was used to determine the composition of materials and to predict their thermal stability at temperatures up to 6000°C.

Introduction

Carbon nanotubes are long cylinders of covalently bonded carbon atoms with a diameter ranging from a few angstroms to several tens of nanometers across. These tubes have an extremely desirable combination of mechanical, thermal and electrical behaviors. CNT can transform an insulating polymer into a conducting composite at very low loading because of their extremely high aspect ratio. The simple method to fabricate Polystyrene/Multiwalled carbon nanotubes (MWCNT/PS) composite where the ethanol vapour sensing characteristics were measured.

Materials and methods

Dispersed MWCNT at loading of between 1% to 9% were added to PS to form homogeneous composites, dried in the form of sheets where the ethanol vapour sensing properties was investigated. MWCNT diameter is 10-30nm, length ~5-15µm and 95% pure was dispersed in SDS solution. PS (molecular wt ~2 X 10⁵ g/mol) was dissolved in toluene. MWCNT/PS was fabricated by solution mixing with MWCNT loading of 1%. Ethanol vapour sensing samples were obtained from dried MWCNT/PS composite solutions. Firstly, all apparatus must be clean. 20 ml of deionised water was thoroughly mixed in 0.5 g of PS and stirred about 1 hour until dissolved. 1% to 10% of MWCNT was added to 20ml deionised water. These selected masses are diluted and stir 1 hour. Then, all the mixtures were mixed and put into ultrasonic bath for 30 minutes. The samples were heated for 23°C until the solution was thick around 6 hours. Printed Circuit Board (PCB) was used to test the resistivity of the samples. Samples were dropped to PCB and run using gas sensor. The reading of resistance was taken for 500sec while ethanol gas passing through the tube. The reaction between nanotube and other molecules alter the electrical resistance due to the change in molecule structure. Using this mechanism we can use MWCNT sensors as chemical detector [6,7].

Results and discussion

The electrical response of 1% MWCNT/PS and 50% ethanol concentration in Fig. 1 shows the comparison of electrical response after exposure to different ethanol flow-rates between 20 sccm and 100 sccm. Fig. 2 an example of electrical curves of the 9% MWCNT/PS at different concentrations of ethanol at the same flow-rate (40 sccm). Fig. 1 shows the response and recovery

curves of CNT composite-based sensor under ethanol vapor concentration of 50 ppm at an operating temperature of 38°C.

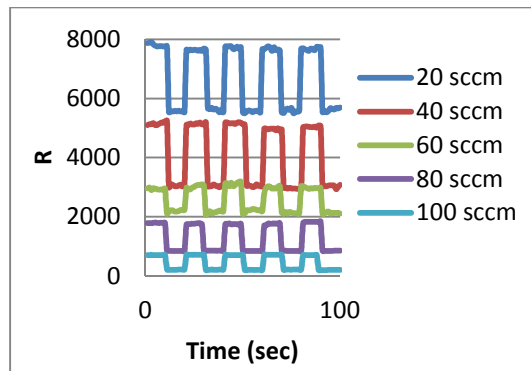


Fig. 1: Electrical response of 1% MWCNT/PS and 50% ethanol concentration at different ethanol flow-rate.

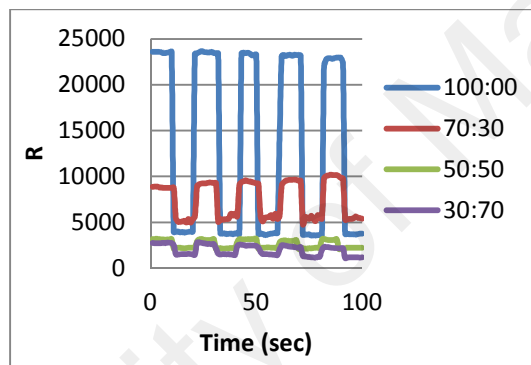


Fig. 2: Electrical response of 9% MWCNT/PS and flow rate=40 sccm at different ethanol concentration.

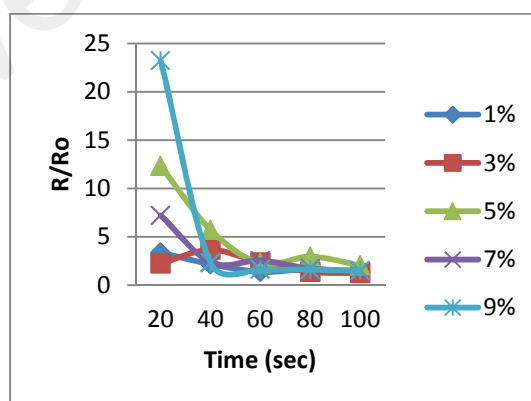


Fig. 3: The response resistance of 1%, 3%, 5%, 7% and 9% MWCNT/PS at 50% ethanol concentrations.

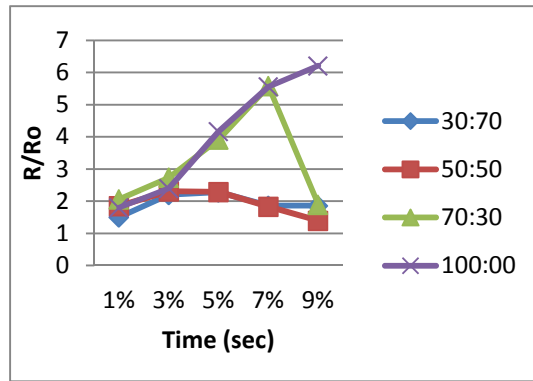


Fig. 4: The response resistance of 1%, 3%, 5%, 7% and 9% MWCNT/PS at different ethanol concentrations.

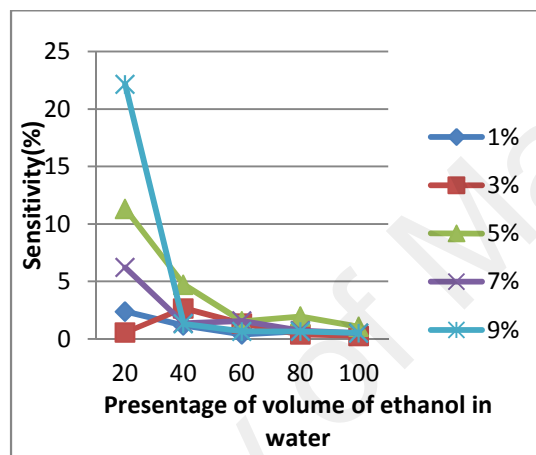


Fig. 5: Response sensitivity of 1% to 9% PS/MWCNT at 50% ethanol concentrations.

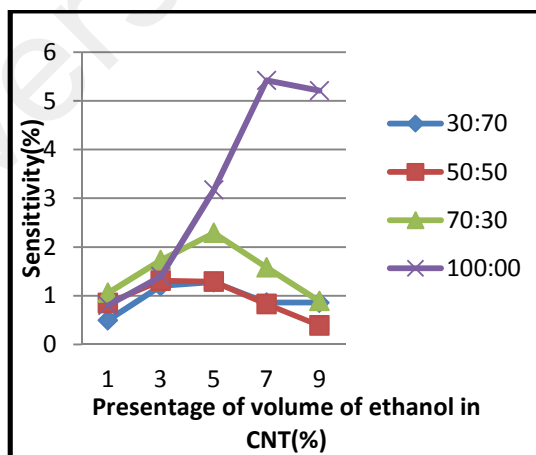


Fig. 6: Response sensitivity of 1% to 9% PS/MWCNT at different concentrations.

Fig. 7 shows the surface morphologies of the MWCNT/PS composite. Fig. 2a and b is the FESEM image at high magnification. These nanoparticles have a narrow size-distribution and average particle size of $\sim 2\mu\text{m}$ and $\sim 1\mu\text{m}$. The image at low magnification (Fig. 2c) shows relatively clean surface with more bitty gullies for the prepared MWCNT/PS nanospheres.

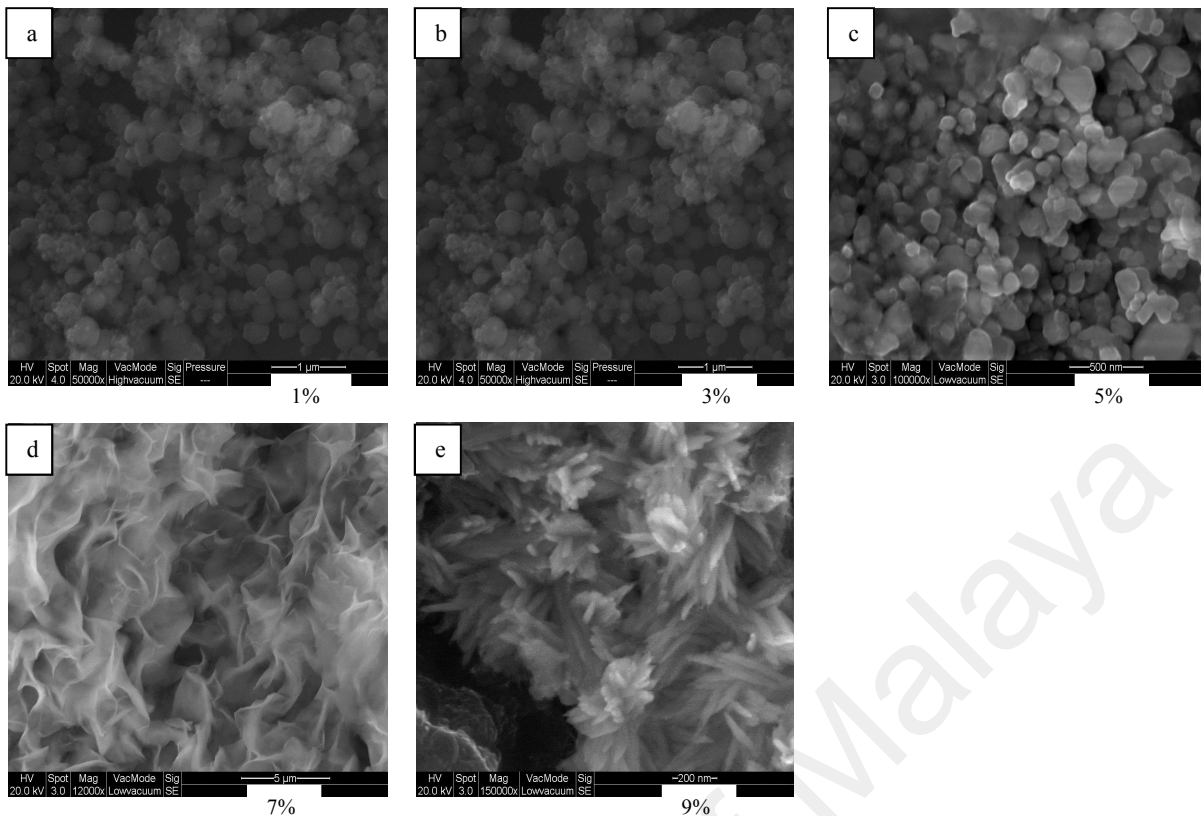


Fig. 7. The FESEM images of 1%, 3%, 5%, 7% and 9% MWCNT/PS at high (a)&(b) and low (c) magnifications.

Fig. 8 shows the FTIR spectrum of 1%, 3%, 5%, 7% and 9% MWCNT/PS. The broad bands in the wavenumber range of $3000-3500\text{ cm}^{-1}$ are related to the trace amount of deionised water in PS used for preparation of the samples whereas the C-H stretching vibrations of the toluene can be observed at 2922 cm^{-1} . The broad absorption band at 1636 cm^{-1} corresponds to the stretching vibration of the C=O group of amide. The broad but relatively weak band at 1492 cm^{-1} is assigned to the stretching vibration of the C-N bond of the amide group.

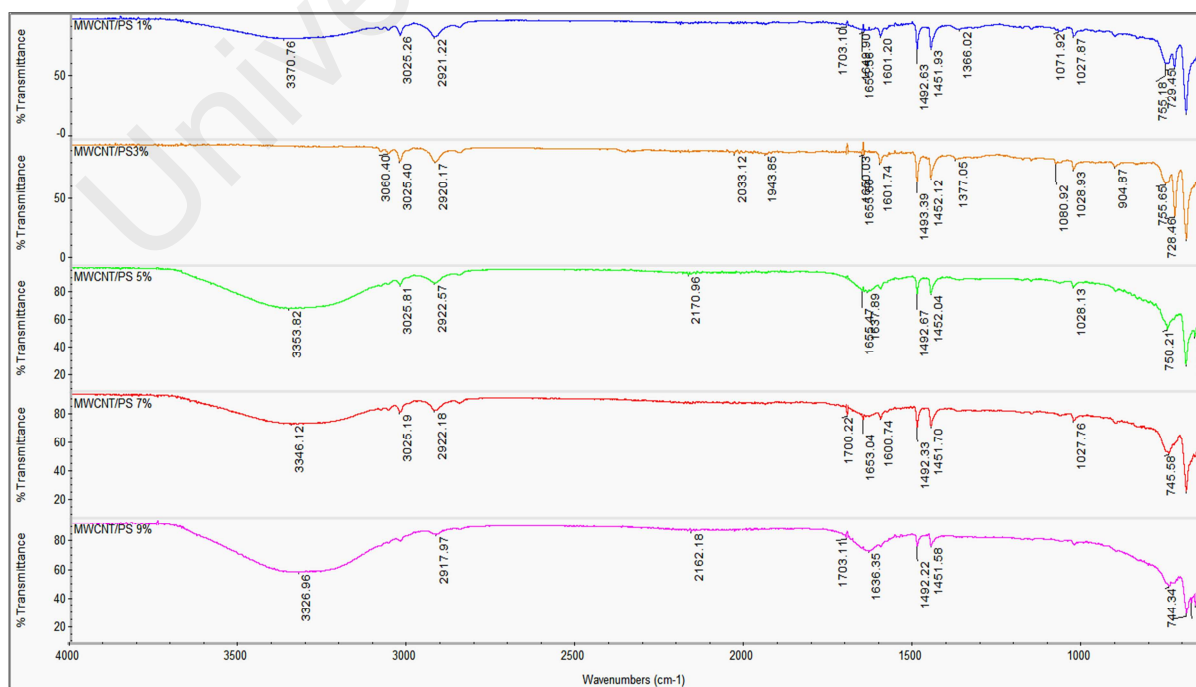


Fig. 8. FTIR spectra of PS-MWCNTs samples.

As shown in Fig 9, only about 1.8 wt% weight loss, mainly contributed by the decomposition of the amorphous carbon or the residual metal catalysts, can be observed for the raw MWCNTs when the temperature is increased to 5000°C, indicating a good thermal stability of the raw MWCNT/PS.

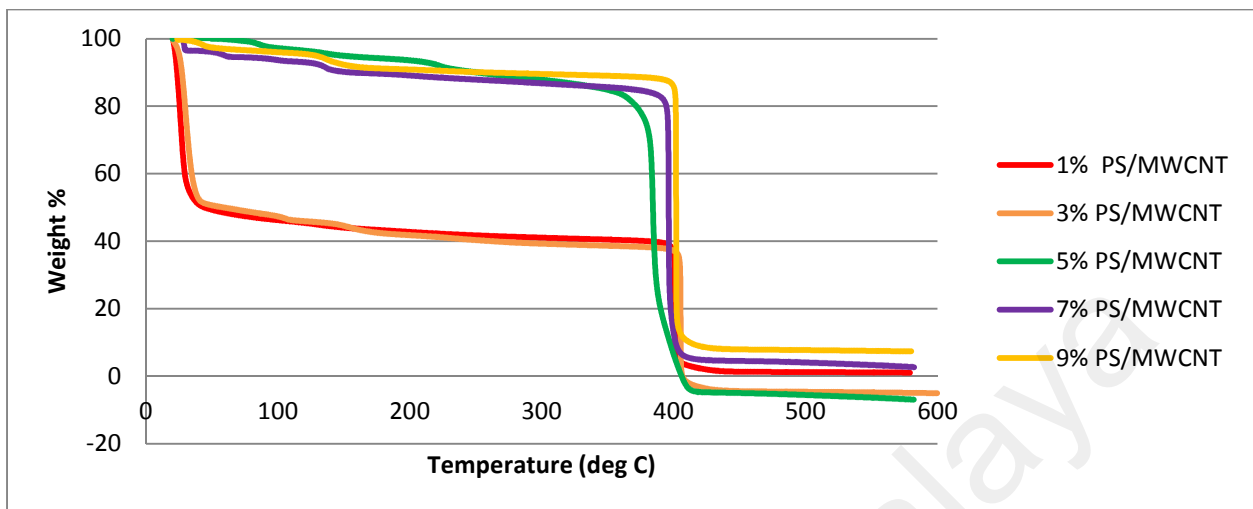


Fig. 9. Temperature dependence of weight loss for the raw 1% to 9% MWCNT/PS composites.

Conclusion

Nanocomposites film of MWCNT/PS was prepared by blending solution providing good nanotube dispersion in polymer. FESEM was employed to determine the nanostructure of nanotube. The sensor sensitivity is increase with increasing the flow-rate of the ethanol vapour.

References

- [1] Y. Gogosti, Nanotubes and nanofibers, CRC Press, 2006.
- [2] A.M. Delores, Focus on nanotube research. Nova Publishers, ISBN 159454851X, 9781594548512, 2006.
- [3] Y-H Liou, Investigation of the dispersion process of SWNTs/SC-15 epoxy resin nanocomposites Structural Materials, 2004, 385, pp 175–181.
- [4] P. Ciselli, The potential of carbon nanotubes in polymer composites, ISBN: 978-90-386-0924-9, 2007.
- [5] A.D, Martin, Focus on nanotube research, Nova Publishers, ISBN 159454851X, 9781594548512. 2006.
- [6] J. Kong, N.R. Franklin, C. Zhou, M.G. Grapline, S. Peng, K. Cho and H. Dai, Nanotube Molecular Witer as Chemical Sensors. Vols. Science, (2000) 287:622. 625.
- [7] M.L.Y. Sin, G.C.T. Chow, C.K.M. Fung, Li, W.J., P. Leong, K.W. Wong, and T, Lee, Ultra-Low-Power Alcohol Vapor Sensors Based on Multi-Walled Carbon Nanotube. In: Proceeding og IEEE-Nano/Micro Engineered and Molecular Systems, Zhuhai, China, 2006, pp 1198-1202.

Nanoscience, Nanotechnology and Nanoengineering

10.4028/www.scientific.net/AMR.832

Electrical and Alcohol Sensing Properties of MWCNT/PS Composites

10.4028/www.scientific.net/AMR.832.178

University of Malaya

Field Electron Emission from Electrophoretic Deposited MWCNT/ZnO Hybrid Film

Faridah Abdul Razak^{1,a} and Roslan Md. Nor^{2,b}

^{1,2}Department of Physics, Faculty of Science, University of Malaya, 50603 Kuala Lumpur, MALAYSIA

Email :^afdah03@yahoo.com.my, ^brmdnor@um.edu.my

Keywords: Carbon nanotubes; Nanocomposites; Field Electron Emission properties.

Abstract. Hybrid film of MWCNT/ZnO was prepared on the silver electrodes using electrophoresis deposition. A constant dc voltage of about 20V was applied to the electrodes and the MWCNT/ZnO was deposited on the surface of the anode electrode as a result. Field Emission Scanning Electron Microscopy was used to investigate the structure MWCNT/ZnO composite. The optical characterization was investigated by Raman Spectroscopy. The MWCNT film exhibits excellent field electron emission properties with high emission current densities, low threshold electric fields and good field emission stability.

Introduction

Carbon nanotubes (CNTs), since their discovery in 1991 [1], have attracted much interests due to their remarkable physical, mechanical, electronic and thermal properties, as well as their potential applications in nano-device. For example, CNTs exhibit promising electron field emission properties, in comparison to the conventional field emitters, with low emission threshold fields, large emission current densities and long emitter lifetime [2], which has prompted many studies on fabricating field emission cathode based on CNT materials.

The CNT-based field emission cathode films have been fabricated mainly by direct growth of CNTs [3] on substrates or by a screen-printing method [4]. The direct growth of CNT such as by CVD process needs high growth temperature (typically >800 °C) [5]. One of the most promising methods of carbon powder-based cold cathode fabrication is the electrophoretic method. But the main difficulty with this method is the weak adhesion of the carbon powder to the substrate. Here, we modify the CNT with SDS surfactant and use electrophoresis deposition to fabricate CNT films, then apply the sinter techniques [6] to make the film adhere strongly [7] to the substrate. The multi-wall carbon nanotube (MWCNT) film developed using this method shows good field emission properties.

Material and methods

The fabrication of composites of carbon nanotubes (CNT) is using dispersion method. 1 gm MWCNT was dispersed in 1% wt SDS aqueous solution by sonication for 2 hours and then ballmilled for 1 hour. The dispersed MWCNT was mixed with 2.5 g ZnO and ballmilled for 5 hours. The resulting solution was centrifuge for 30 minutes at 1000 rpm to separate large agglomerates.

Hybrid film of MWCNT/ZnO was prepared on the silver electrodes using electrophoresis deposition. A constant dc voltage of about 20V was applied to the electrodes and the MWCNT/ZnO was deposited on the surface of the anode electrode as a result.

Field emission scanning electron microscope (FESEM) will be used to analyze the structure of the MWCNT/ZnO composite. Energy dispersed x-ray spectroscopy is employed to determine the

chemical composition. Raman spectroscopy will be used to investigate detailed bonding structure and to distinguish various bulk materials without any sample preparation.

The MWCNT film exhibits excellent field electron emission properties with high emission current densities, low threshold electric fields and good field emission stability.

Field emission experiments were prepared in a vacuum chamber with a 3.5×10^{-7} mbar at room temperature. The distance between an anode and a tip of ZnO hybrid film was $80 \mu\text{m}$. The measured emission area was 0.56 cm^2 . Emission current was monitored with a Keithley 2410 and recorded at intervals of 0.5 s . The emission current-voltage characteristics were analyzed by using the Fowler-Nordheim (FN) eq. 1, for the field emission:

$$J = \frac{AF^2}{\phi} \exp\left(-\frac{0.95B\phi^{3/2}}{F}\right) \quad (1)$$

where J is current density in Am^{-2} , $F = \beta E$, is the local electric field, and E is the average applied electric field, β is the field enhancement factor, A and B are constants, $A = 1.54 \times 10^{-6} \text{ A eV/V}^2$, $B = 6.83 \times 10^9 \text{ VeV}^{-3/2} \text{ m}^{-1}$, and ϕ - work function (4.5 eV for carbon) [8].

Results and discussion

The structure and morphology of the samples were characterized by Field emission scanning electron microscope (FESEM) and Energy dispersive x-ray spectroscopy. Energy dispersed x-ray spectroscopy is employed to determine the chemical composition of the different composites. Fig. 4.1 (a), (b) and (c) shows the FESEM images of the MWCNT film for 1 minute, 2 minutes and 3 minutes deposited on silver substrates by electrophoretic deposition. The surface morphologies of other electrodes basically remain the same. The CNTs entangle with each other and show a good network microstructure with many mesopores with average size of $\sim 2 \mu\text{m}$.

Fig. 4.1 (d), (e) and (f) shows the FESEM images of MWCNT/ZnO hybrid film for 1 minute, 2 minutes and 3 minutes of times. The MWCNT/ZnO was deposited onto electrodes. The MWCNT/ZnO hybrid films have bonded together. Such a network structure provides more tunnels for the entering of the solution and allows hydrated ions easily to move onto the surface of the film, which favours the electrosorption [9].

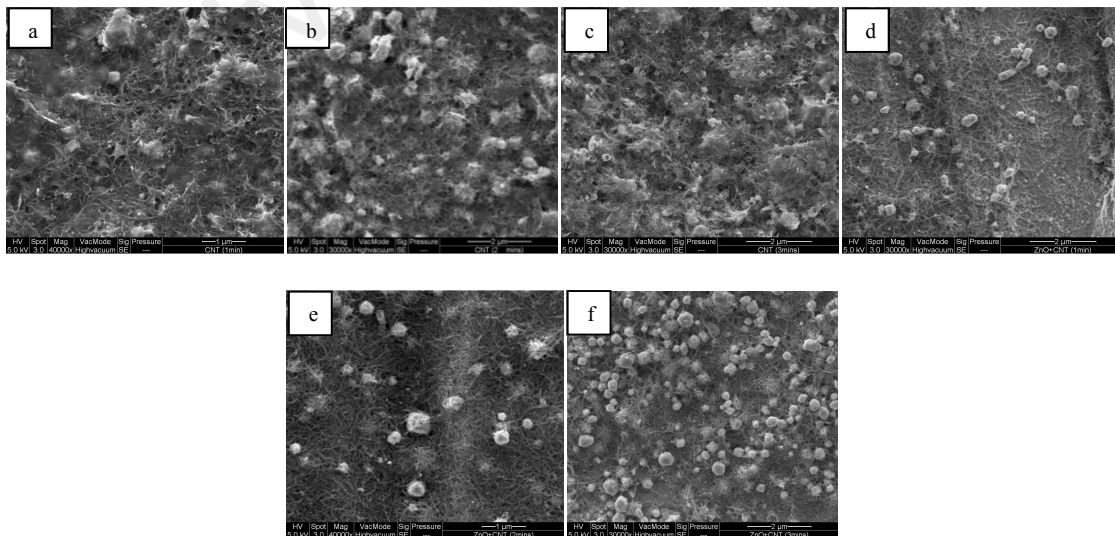
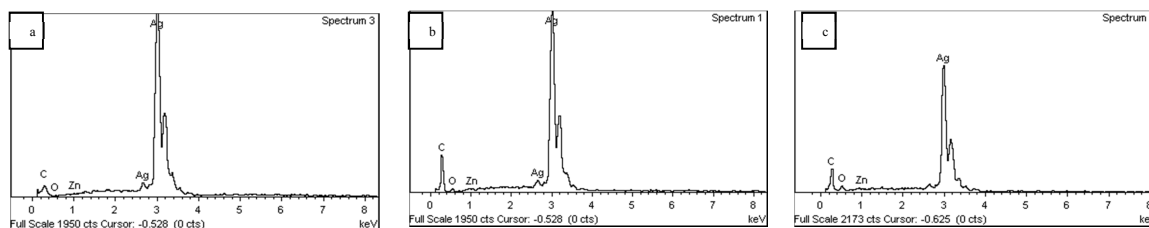


Fig. 4.1: FESEM images of (a) 1 minute of MWCNT, (b) 2 minutes of MWCNT, (c) 3 minutes of MWCNT, (d) 1 minute of MWCNT/ZnO, (e) 2 minutes of MWCNT/ZnO, (f) 3 minutes of MWCNT/ZnO, were deposited on silver.

Fig. 4.2 (a), (b) and (c) shows the EDX spectra of MWCNT/ZnO. The spectra exhibited the existence of carbon, oxygen, titanium and argentum. Argentum is the major composition and has the highest concentration comparing it to other elements. Zinc and oxygen are resulted from the using of Zinc Oxide.



	Element	Weight%	Atomic%
a	C K	2.08	17.33
	O K	-1.51	-9.41
	Zn K	0.12	0.19
	Ag L	99.30	91.90
	Totals	100.00	
b	C K	15.02	55.38
	O K	4.06	11.23
	Zn K	0.65	0.44
	Ag L	80.28	32.96
	Totals	100.00	
c	C K	11.91	42.29
	O K	10.01	26.70
	Zn K	0.53	0.35
	Ag L	77.55	30.67
	Totals	100.00	

Fig. 4.2: EDS spectra of MWCNT/ZnO hybrid film of (a) 1 minute, (b) 2 minutes (c) 3 minutes.

Fig. 4.3(a) shows the typical spectrum of MWCNT film which is dominated by two intensity peaks at 2680 and 2917 cm^{-1} , which are referred as D line and G line, respectively. The D line is attributed to the presence of amorphous carbons or defects in curved graphite sheets. The G line shows the presence of tubular structure in the CNT_s . The ratio of the intensity of the D peak and G peak (I_D/I_G) is related to the amount of disorder in the carbon products. The (I_D/I_G) values of all CNT_s films are almost same (~ 0.9), indicating that the EPD has not damaged the structure of CNT_s and there exists some defects in the CNT_s films.

Fig. 4.3(b) give the Raman Spectroscopy of MWCNT/ZnO. The G and D modes of MWCNT/ZnO at about 1582 and 1345 cm^{-1} and are clearly observed. The peak at 1582 cm^{-1} (G) result from graphite sheet of MWCNT/ZnO wall, which consists of carbon, zinc and argentum atoms all arranging in the form of hexagon, while the peak at 1345 cm^{-1} (D) represent the impurity and the defects of atomic structure in the MWCNT/ZnO sample.

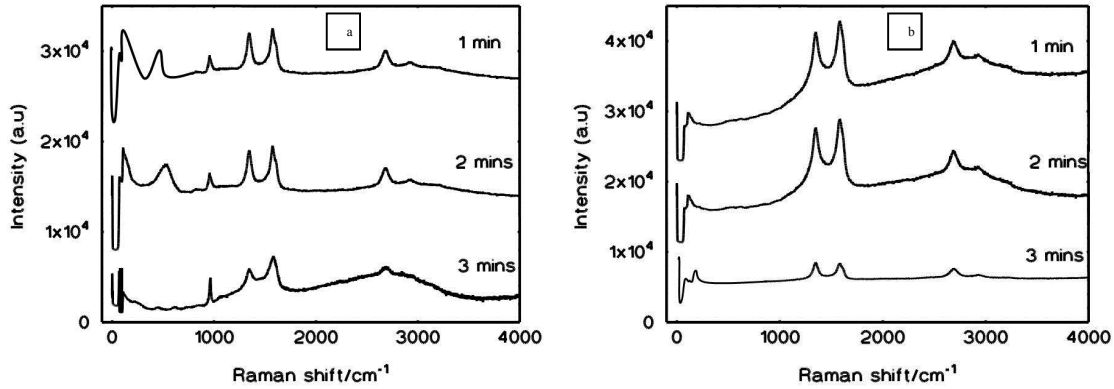


Fig. 4.3: (a)MWCNTand (b)MWCNT/ZnO.

The measured field emission current plotted as a function of the applied field for the thin film of MWCNT deposited on a silver substrate is shown in fig 4.4(a) show the field emission current of $4.5 \times 10^{-5} \text{ A/cm}^2$ is achieved for an applied field intensity of about $13.8 \text{ V}/\mu\text{m}$. The turn-on field, at which the emission current density reaches $2 \mu\text{A/cm}^2$, is $12 \text{ V}/\mu\text{m}$, while a current density of $1 \times 10^{-5} \text{ A/cm}^2$, which is required for flat panel display $13 \text{ V}/\mu\text{m}$.

Then, Fig. 4.4(b) give the field emission current of $0.9 \times 10^{-3} \text{ A/cm}^2$ is achieved for an applied field intensity of about $13.6 \text{ V}/\mu\text{m}$. The turn-on field, at which the emission current density reach $2 \mu\text{A/cm}^2$ is $12.3 \text{ V}/\mu\text{m}$, while a current density of $0.2 \times 10^{-3} \text{ A/cm}^2$, which is required for flat panel display $13 \text{ V}/\mu\text{m}$.

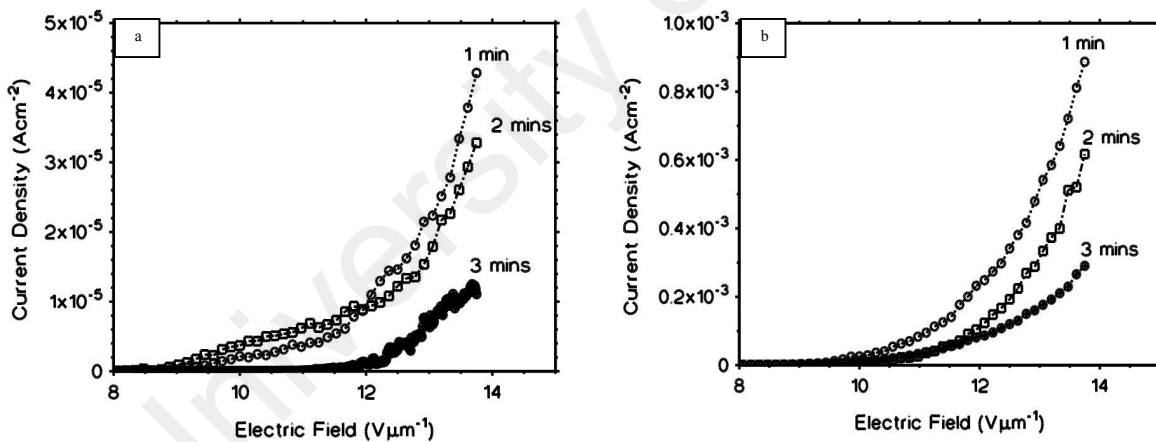


Fig.4.4: Typical field emission current density vs. the applied electric field for (a) MWCNT film and (b) MWCNT/ZnO.

Fig. 4.5 (a) and (b) give the corresponding Fowler-Nordheim (F-N) plots for the MWCNT film and MWCNT/ZnO hybrid film field emission. Fowler and Nordheim explained the phenomenon of field emission on the basis of quantum mechanical tunneling of electrons due to the bending of the potential barrier in the presence of an external electric field. According to their prediction, the linear relationship between $\ln(J/E^2)$ and $1/E$ is expected for the voltages above the turn-on voltage. The emission data from experiments generally agree with the linear F-N relationship corresponding to the classical electron tunneling mechanism of field emission. The measurement value for the work function of MWCNT and MWCNT/ZnO were about 5 eV . From the inset of fig 4.5(a) and (b) the calculated β value in table 1, which is enough for various application of field emission; even though it was much lower than that of CNT_s .

Table 1: β value for MWCNT and MWCNT/ZnO.

	MWCNT	MWCNT/ZnO
1 Minute	-2.48×10^7	-2.41×10^7
2 Minutes	-4.48×10^7	-1.7×10^7
3 Minutes	-8.72×10^6	-2.55×10^7

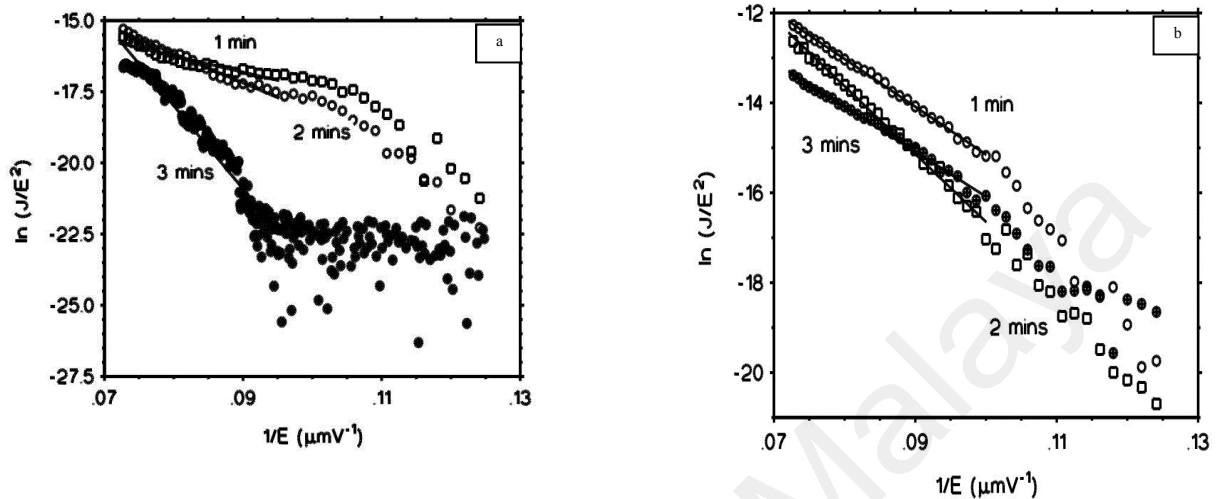


Fig. 4.5: The corresponding Fowler-Nordheim (F-N) plots ($\ln(J/E^2)-(1/E)$) with the field emission characteristics of the (a) MWCNT film and (b) MWCNT/ZnO hybrid.

Conclusions

The method based on electrophoresis deposition for fabricating of MWCNT/TiO₂ hybrid film is presented in this paper. The MWCNT/TiO₂ entangled with each other and shows a good network microstructure. The presence of defects causes an increase in ability for accumulation of charges, which may be beneficial for charge transfer in the adsorption process. The MWCNT/TiO₂ films were very strongly adsorbed onto the substrate, which is very important for the fabrication of a stable field emitter.

Acknowledgements

This work was supported by University of Malaya Research Grant No.: RG008/09AFR and Ministry of Higher Learning of Malaysia Fundamental research grant FRGS FP008/2010C.

References

- [1] S. Iijima, Helical microtubules of graphitic carbon *Nature*, 354 (1991) 56–58.
- [2] S.S. Fan, M.G. Chaplind, N.R. Franklin, T.W. Tomblor, A.M. Cassell, H.J. Dai, Self-oriented regular arrays of carbon nanotubes and their field emission, *Sci.* 283 (1999) 512–514.
- [3] J.Y. Wan, Y.S. Cho, G.S. Choi, Dojin Kim, Patterned carbon nanotube field emitter using the regular array of an anodic aluminium oxide template, *Nanotech.* 16 (2005) S291–S295.
- [4] J.T. Li, W. Lei, X.B. Zhang, Q.L. Wang, Y.N. Zhang, B.P. Wang, Field emission characteristic of screen-printed carbon nanotube cathode, *Appl. Surf. Sci.* 220 (2003) 96–104.

- [5] S.J. Oh, Y. Cheng, J. Zhang, H. Shimoda, O. Zhou, Room-temperature fabrication of high-resolution carbon nanotube field-emission cathodes by self-assembly, *Appl. Phys. Lett.* 82 (2003) 2521–2523.
- [6] B. Gao, Z. Guo, Z. Yue, Q. Qiu, Y.H. Shimoda, L. Fleming, O. Zhou, Fabrication Electron field emission properties of carbon nanotube films by electrophoretic deposition, *Adv. Mater.* 13 (2001) 1770–1773.
- [7] H. Joeong, M.J. Sung, Y.J. Hyun, S.B. Heo, J.H. Shin, J.S. Suh, Fabrication of clean carbon nanotube field emitters, *Appl. Phys. Lett.* 88 (2006) 1131011–1131013.
- [8] H. Araki, T. Katayama, K. Yoshino, *Appl. Phys. Lett.* 79 (2001) 2636.
- [9] X.Z. Wang, M.G. Li, Y.W. Chen, R.M. Cheng, S.M. Huang, L.K. Pan, Z. Sun, *Appl. Phys. Lett.* 89 (2006) 053127-1-053127-3.

Field Electron Emission from Electrophoretic Deposited MWCNT/ZnO Hybrid Film

10.4028/www.scientific.net/AMR.832.183

DOI References

[2] S.S. Fan, M.G. Chaplind, N.R. Franklin, T.W. Tombler, A.M. Cassell, H.J. Dai, Self-oriented regular arrays of carbon nanotubes and their field emission, *Sci.* 283 (1999) 512-514.

<http://dx.doi.org/10.1126/science.283.5401.512>

[4] J.T. Li, W. Lei, X.B. Zhang, Q.L. Wang, Y.N. Zhang, B.P. Wang, Field emission characteristic of screen-printed carbon nanotube cathode, *Appl. Surf. Sci.* 220 (2003) 96-104. a b.

[http://dx.doi.org/10.1016/S0169-4332\(03\)00749-9](http://dx.doi.org/10.1016/S0169-4332(03)00749-9)

[5] S.J. Oh, Y. Cheng, J. Zhang, H. Shimoda, O. Zhou, Room-temperature fabrication of high-resolution carbon nanotube field-emission cathodes by self-assembly, *Appl. Phys. Lett.* 82 (2003) 2521-2523.

<http://dx.doi.org/10.1063/1.1563812>

[6] B. Gao, Z. Guo, Z. Yue, Q. Qiu, Y.H. Shimoda, L. Fleming, O. Zhou, Fabrication Electron field emission properties of carbon nanotube films by electrophoretic deposition, *Adv. Mater.* 13 (2001) 1770-1773.

[http://dx.doi.org/10.1002/1521-4095\(200112\)13:23<1770::AID-ADMA1770>3.0.CO;2-G](http://dx.doi.org/10.1002/1521-4095(200112)13:23<1770::AID-ADMA1770>3.0.CO;2-G)

[8] H. Araki, T. Katayama, K. Yoshino, *Appl. Phys. Lett.* 79 (2001) 2636.

<http://dx.doi.org/10.1063/1.1410874>

[9] X.Z. Wang, M.G. Li, Y.W. Chen, R.M. Cheng, S.M. Huang, L.K. Pan, Z. Sun, *Appl. Phys. Lett.* 89 (2006) 053127-1-053127-3.

<http://dx.doi.org/10.1063/1.2335614>

Electrical and alcohol sensing properties of PEO/MWCNT composites

Faridah Abdul Razak, Nessrin Awadhallah Kattan, and Roslan Md. Nor

Citation: *AIP Conf. Proc.* **1502**, 495 (2012); doi: 10.1063/1.4769168

View online: <http://dx.doi.org/10.1063/1.4769168>

View Table of Contents: <http://proceedings.aip.org/dbt/dbt.jsp?KEY=APCPCS&Volume=1502&Issue=1>

Published by the [American Institute of Physics](#).

Related Articles

Magnetic and electrical properties of PbTiO₃/Mn-Zn ferrite multiphase nanotube arrays by electro-deposition
J. Appl. Phys. **112**, 104310 (2012)

Note: Axially pull-up electrochemical etching method for fabricating tungsten nanopores with controllable aspect ratio
Rev. Sci. Instrum. **83**, 106109 (2012)

Effects of carbon nanofillers on enhancement of polymer composites
J. Appl. Phys. **112**, 074302 (2012)

Improving the field emission of carbon nanotubes by lanthanum-hexaboride nano-particles decoration
Appl. Phys. Lett. **101**, 123116 (2012)

Catalyst-free synthesis of reduced graphene oxide-carbon nanotube hybrid materials by acetylene-assisted annealing graphene oxide
Appl. Phys. Lett. **101**, 123107 (2012)

Additional information on AIP Conf. Proc.

Journal Homepage: <http://proceedings.aip.org/>

Journal Information: http://proceedings.aip.org/about/about_the_proceedings

Top downloads: http://proceedings.aip.org/dbt/most_downloaded.jsp?KEY=APCPCS

Information for Authors: http://proceedings.aip.org/authors/information_for_authors

ADVERTISEMENT

**AIP Advances**

Submit Now

**Explore AIP's new
open-access journal**

- **Article-level metrics
now available**
- **Join the conversation!
Rate & comment on articles**

Electrical and Alcohol Sensing Properties of PEO/MWCNT Composites

Faridah Abdul Razak, Nessrin Awadhallah Kattan, and Roslan Md. Nor

*Department of Physics, Faculty of Science, University of Malaya, 50603 Kuala Lumpur, MALAYSIA
Email: fdah03@yahoo.com*

Abstract. Composites of polyethylene oxide and multiwalled carbon nanotubes were prepared using the solution blending method. Ethanol vapor sensing properties of the composites at different MWCNT loadings were studied. Results on the effect of aligned MWCNT in the composites on the electrical conductivity and alcohol vapor sensing are presented. Field Emission Scanning Electron Microscopy (FESEM) was used to investigate the alignment of PEO/MWCNT.

Keywords: Carbon nanotubes; Nanocomposites; Electrical properties; Polymers.

PACS : 81.07.De

INTRODUCTION

Carbon nanotubes have been shown to be excellent fillers in the fabrication of polymer nanocomposites at much lower loading percentage, compared to particulate fillers such as carbon black [1], where the outstanding properties of carbon nanotubes offer possibilities for developing new strong multifunctional composite materials

[2–5]. Here, we report a simple method to fabricate MWCNT/PEO composite where the ethanol vapour sensing characteristic was measured. In comparison with other nanofillers, carbon nanotubes are excellent candidates for multi-functional nano-reinforcing a variety of polymer matrices because of their high strength (~100 times stronger than steel) and modulus (about 1TPa), high thermal conductivity (about twice as high as diamond), excellent electrical capacity (1000 times higher than copper), and thermal stability (2800 °C in vacuum) [6]. An insulating polymer into a conducting composite can transform at very low loading because of their extremely high aspect ratio. The electrical behaviour is the most outstanding properties of carbon nanotubes. The electrical conductivity of carbon nanotube composite highly depends on its dispersion, aspect ratio, alignment and the type of polymer used as a matrix.

MATERIALS AND METHODS

Dispersed MWCNT at loading of between 1 % to 10 % were added to PEO to form homogeneous composites, dried in the form of sheets where the ethanol vapour sensing properties was investigated. Firstly, all apparatus must be clean. 20 ml of deionised water was thoroughly mixed in 0.5 g of PEO and stirred about 1 hour until it dissolved. 1 % to 10 % of MWCNT was added to 20 ml deionised water. These selected masses are diluted and stirred for 1 hour. Then, all mixtures were placed in an ultrasonic bath for 30 minutes. The samples were heated for 23 °C until the solution was thickened around 6 hours. Printed Circuit Board (PCB) was used to test the resistivity of the samples. Samples were dropped to PCB and tested using gas sensor. The reading of resistance was taken for 500 sec while passing the ethanol gas through the tube. The reaction between nanotubes and other molecules alters the

electrical resistance due to the change in the molecular structure. Carbon nanotube is a new and ideal candidate for gas detection due to the nanometer size, extremely high surface to volume ratio and hollow structure which makes it ideal for gas molecules adsorption. It has been observed that the electrical properties of carbon nanotubes are very sensitive to their chemical environment in which the exposure to gas molecules changes the electrical properties of CNT. These changes attributed to the charge transfer between the molecules and the nanotubes. The gas molecule acts as an electron donors or electron acceptors. Thus, the sensor responses to various gases by decreasing or increasing its resistance. Similar mechanism will be used in fabricating the CNT sensors as chemical detector [7,8]. FESEM was used to study the morphology of the samples.

RESULTS AND DISCUSSION

The electrical response of PEO/MWCNT in Figure 1 shows the comparison of electrical response and recovery curves of the same PEO/MWCNT sheets after exposure to different ethanol flow-rates between 30 sccm and 150 sccm. The results indicate that the sensor sensitivity is increased with increasing flow rate of ethanol vapour. The flow rates at 100 sccm and 150 sccm have almost similar diagram and similar sensing properties which is higher than that when it was exposed to ethanol at 30 sccm and 50 sccm. The higher sensitivity is due to the higher volume of vapour passing through it allowing more gas molecules to react with the nanotube sensor and hence higher electron transfer.

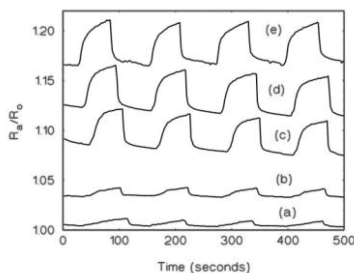


FIGURE 1. Electrical response of PEO/MWCNT sheets at different ethanol flow-rate (a)30 sccm (b)50 sccm (c)75 sccm (d)100 sccm (e)150 sccm.

FESEM images of the aligned nanotubes within the polymer matrix in the same magnification are shown in Figure 2. The nanotubes in PEO are homogenously coated with layer of PEO at 5 % unaligned MWCNT. Composite film for aligned MWCNT at 10 % CNT is shown in Figure 2b.

The grains boundaries reduce the probability of physical contact of MWCNTs which results in less electrons transport through the granular surface.

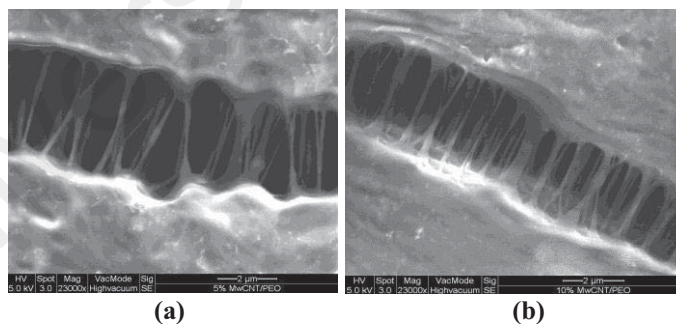


FIGURE 2. The FESEM images of PEO/MWCNT at the same magnification (a) 5% CNT (b) 10% CNT .

CONCLUSION

Nanocomposites film of PEO/MWCNT was prepared by blending solution which provides good nanotube dispersion in polymer matrix. FESEM was employed to determine the alignment of nanotube within polymer matrix. The sensor sensitivity is increased with increasing flow-rate of the ethanol vapour.

REFERENCES

1. G. Yuri, *Nanotubes and Nanofibers*, CRC Press, 2006, pp. 1-36.
2. M. Zhang, K. R. Atkinson and R. H. Baughman, *Science*, **306**, No. 5700, 2004, pp. 1358–1361.
3. C. Velasco-Santos, A. L. Martínez-Hernandez and V. M. Castano, *Carbon Nanotube-Polymer Nanocomposites: The Role of Interfaces, Composite Interfaces*, vol. 11, No. 8-9, 2005, pp. 567–586.
4. Velasco-Santos, A. L. Martínez-Hernandez, and V. M. Castano, *Carbon Nanotube-Polymer Nanocomposites: Principles and Applications, in Focus on Nanotube Research*, D. A. Martin, Ed., Nova Science Publishers, vol. I, Huntington, NY, USA, 2006, pp. 97–126.
5. Y. Dzenis, *Materials Science: Structural Nanocomposites, Science*, **319**, No. 5862, 2008, pp. 419–420.
6. H. Y. Liao, *Nanocomposites Structural Materials*, **385**, 2004, pp. 175–181.
7. Kong, J., Franklin N.R., Zhou, C., Grapline, M.G., Peng, S., Cho, K. and Dai, H., *Science*, **287**, 2000, pp. 622-625.
8. Sin, M.L.Y., Chow, G.C.T., Fung, C.K.M., Li, W.J., Leong, P., Wong, K.W., and Lee, T., *Ultra-Low-Power Alcohol Vapor Sensors Based on Multi-Walled Carbon Nanotube In: Proceeding of IEEE-Nano/Micro Engineered and Molecular Systems*, Zhuhai, China. 2006, pp. 1198-1202.

APPENDIX A – ERROR ANALYSIS

Experimental error was estimated for experimentally determined numerical values related to field electron emission and alcohol sensing studies. For FEE random errors for values of field enhancement factor, β , threshold and turn-on fields. From alcohol sensing studies, errors are estimated for numerical values of the sensor sensitivities.

1. Error Estimation for threshold and turn-on fields from field electron emission measurements.

As described in Section (xxx) on page yyy, field electron emission measurements involved the measurement of field emission current, I at applied voltage ranging from 0 to 1100 volts using a Keithley 2410 source meter unit. Current density was obtained by dividing the current measured by the area of emitting cathode. The applied electric field was obtained by dividing the voltage applied by the inter-electrode distance.

The source of errors is as follows:

- (a) Errors in voltage and current measurements are based on the tolerance as specified by the manufacturer (Keithley) at 0.5% at current and voltages of 10 nA and 0.1 V respectively. At higher current and voltage values the tolerance are smaller. But the higher value is taken for this estimation.
- (b) Errors of measurement of the area of the emitting cathodes. The dimension of the cathode was 5 mm x 5 mm measured using a vernier caliper with an error of 0.1 mm. As such the error for the area was estimated at 4%.
- (c) Error of measurements of the inter-electron spacing was 10% based on the smallest division of the micrometer screw gauge of 10 μm and the fixed inter-electrode spacing of 100 μm .

Fitting these values of estimated errors in to the in Eqn(3.10) on page 39, the estimated errors of the field enhancement factor, β , threshold and turn-on fields are the sums of the individual errors at 15%.

2. Estimation of the errors of the value of sensitivities of the alcohol sensors.

The sensitivity of the alcohol sensors are obtained from the gradient the response curve, that is, the sensor response (A_r) versus acetone concentration in part per million(ppm). Only the linear portion of the curves gave meaningful sensitivity values and the saturation point for the sensors were obtained at the point of departure of the linear curve.

Curve fitting of the linear portion of response curves for all samples were done using a plotting software, Easyplot© by Spiral software. Within the linear curve fitting feature of the software, mean square deviation or error squared was computed automatically, together with the values of the gradient and the intercept. As an example, fittings done for Fig.4.11(a) is shown as Fig.A1. The curve fitting process reported the fractional error squared (mean square deviation) values based on the least square method analysis for the straight line portion of the curves fitted. The results for this example is tabulated in Table A1.

TableA1. Error squared and error based on least square method computation using Easyplot on the linear portion of the response curve.

Sample	Error squared	Error	Percentage error %	Sensitivity($\times 10^{-2}$) \pm error
5% CNT	0.00125	0.035	3.5	5.3 \pm 0.2
15% CNT	0.00013	0.0011	1.1	2.9 \pm 0.3
25% CNT	0.00019	0.0013	1.3	2.6 \pm 0.3
33% CNT	0.0000253	0.0005	0.5	1.500 \pm 0.008
40% CNT	0.000033	0.0005	0.5	2.50 \pm 0.01
50% CNT	0.000026	0.0005	0.5	2.20 \pm 0.01

Generally, the estimated error values were small, highest at about 3.5% in the example shown above and typically less than 1%. This is due to the linear nature of the response in the active region, i.e. before the point of saturation.

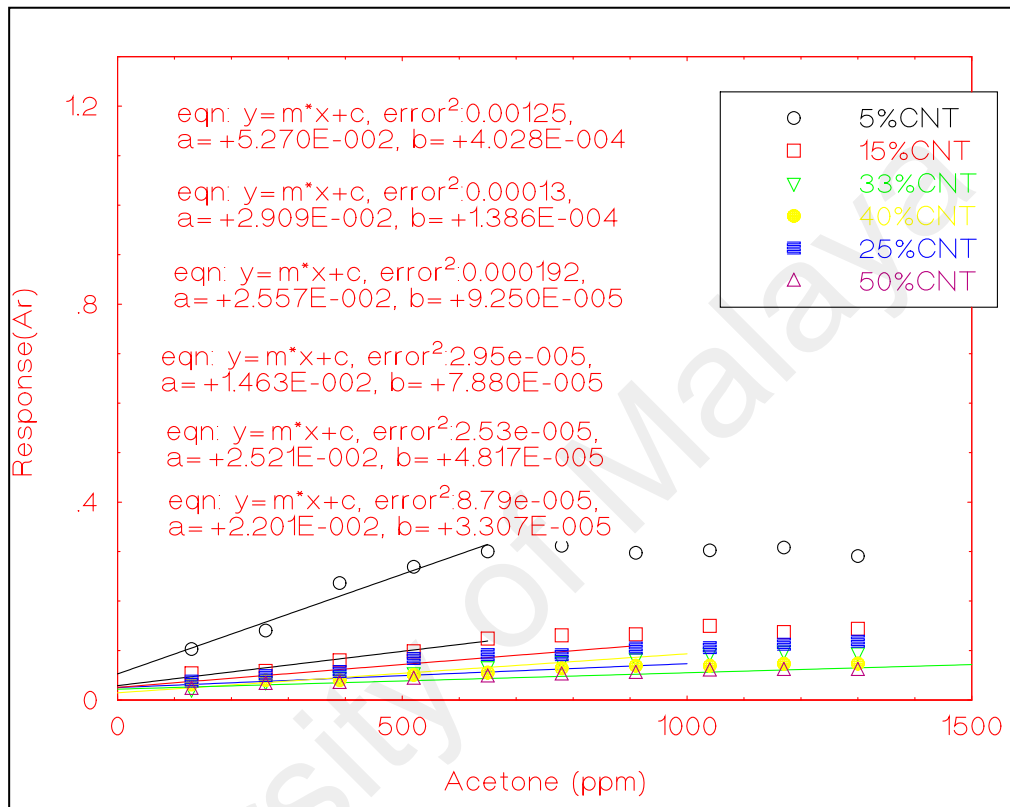


Fig.A1. Figure 4.11 (a) Redrawn showing linear curve fittings and fitting values reports.

APPENDIX B – ESTIMATION OF ACETONE CONCENTRATION TO THE SENSOR

The variation of the acetone concentration on the sensors is determined by the acetone mole fraction in water and the gas flow rate. The acetone concentration delivered on the sensor is estimated as follows.

Considering the experimental setup shown as Figure 4.3 on page 101, a sealed container attached to flowing gas controlled by a precision flow meter formed the source of the acetone vapor dispensed to the sensor.

Acetone and water vapor formed above the liquid mixture in the sealed container and their vapor pressure is given by Rault's equation;

$$p_i = x_i P_i^0 \quad (1)$$

where p_i is the partial pressure of the component of the mixture, x_i is the mole fraction and P_i^0 is the partial pressure of the pure liquid.

Considering the amount of the mixture was 10 to 100% acetone in water so mole fraction of acetone ranged from 0.0345 to 1. Based on Eqn (1), p_i ranged from 8.8 torr to 254 torr at a temperature of 300 K.

Assuming ideal gas the number density in cm^{-3} , n_i , of acetone vapor above the liquid mixture is;

$$n_i = 2.45 \times 10^{19} p_i / p_0 \quad (2)$$

where P_0 is atmospheric pressure (760 torr)

The value of n_i ranged from $2.8 \times 10^{17} \text{ cm}^{-3}$ for 10% vol acetone in water to $2.45 \times 10^{19} \text{ cm}^{-3}$ for pure acetone.

The acetone vapor was delivered to the sensor by flowing gas at flow rates precisely controlled. The flow rates can be varied from 5 to 100 sccm and the flow duration was 5 second. This gives the volume, V , delivered to the sensor between 0.42 to 8.3 cm^3 . Consequently, the actual number of acetone molecules delivered to sensor is given by;

$$N_{\text{ace}} = n_i V \quad (3)$$

The sensor is place in a container with a volume of 14.1 L so the concentration of acetone delivered to sensor in ppm, ρ_{ace} , is estimated as;

$$\rho_{\text{ace}} = N_{\text{ace}} \times 10^6 / (2.45 \times 10^{19} \times 14.1 \times 10^3) \quad (4)$$

University of Malaya